HOKKAIDO UNIVERSITY

Title	Flow and deposition mechanisms of debris avalanches and pyroclastic flows
Author(s)	Takarada, Shinji; 宝田, 晋治
Degree Grantor	北海道大学
Degree Name	博士(理学)
Dissertation Number	乙第4452号
Issue Date	1994-03-25
DOI	https://doi.org/10.11501/3076772
Doc URL	https://hdl.handle.net/2115/50074
Type	doctoral thesis
File Information	000000272850.pdf

Hokkaido University Collection of Scholarly and Academic Papers

Hokkaido University Collection of Scholarly and Academic Papers : HUSCAP

Flow and Deposition Mechanisms of Debris Avalanches and Pyroclastic Flows

Shinji TAKARADA

1994

(1)

Flow and Deposition Mechanisms of Debris Avalanches and Pyroclastic Flows

Shinji TAKARADA

1994

Contents

Abstract 1

Chapter 1. Introduction 5

Chapter 2. Previous works 13

2-1. Debris avalanche 13

2-1-1. Characteristics 13

2-1-2. Mobility 18

2-1-3. Flow and deposition models 18

2-2. Pyroclastic flow 30

2-2-1. Sedimentary structures 30

2-2-2. Flow and deposition models 39

Chapter 3. Terminology 49

Chapter 4. Geologic setting 52

4-1. Tashirodake Volcano 52

4-2. Ontake Volcano 62

4-3. Komagatake Volcano 74

4-4. Unzen Volcano 82

Chapter 5. Debris avalanche deposits 86

5-1. Iwasegawa debris avalanche deposit, Tashirodake Volcano 86

5-1-1. Distribution of the Iwasegawa debris avalanche deposit 86

5-1-2. Debris avalanche block (DB) 88

5-1-3. Debris avalanche matrix (DM) 88

5-1-4. Density grading of clasts and wood fragments 90

5-1-5. Frequency distribution of lineation of wood fragments 93

5-1-6. Captured clasts at the bottom part of the deposit 95

5-1-7. Sedimentary structure of the bottom part of the deposit 95

5-2. Kaida debris avalanche deposit, Ontake Volcano 108

5-2-1. Distribution of the Kaida debris avalanche deposit 108

5-2-2. Debris avalanche block (DB) 110

5-2-3. Debris avalanche matrix (DM) 110

5-2-4. Deformation structures of the DBs 110
5-2-5. Lithic components within the DM 112
Chapter 6. Pyroclastic flows and deposits 124
6-1. Komagatake 1929 pyroclastic flow deposits 124
6-1-1. Outline of the 1929 eruptions 124
6-1-2. Distribution and characteristics 125
6-1-3. Estimation of the yield strength 127
6-1-4. Sedimentary structures 131
6-1-5. Fluidization experiment 136
6-2. Unzen 1991-93 pyroclastic flows and deposits 167
6-2-1. Outline of the 1991-93 eruption 167
6-2-2. Volume estimation 171
6-2-3. Initiation mechanism of the pyroclastic flows on June 3 and June 8, 1991 183
6-2-4. Relationship between volume and H/L ratio of pyroclatic flows 183
6-2-5. Observation of the pyroclastic flows 187
6-2-6. Sedimentary structures of the pyroclastic flow deposit on June 8, 1991 189
6-2-7. Velocity measurement 190
6-2-8. Computer simulations 192
Chapter 7. Discussions 214
7-1. Fundamental clast support mechanisms 214
7-2. Flow and deposition mechanism of the debris avalanches 216
7-2-1. Plug flow model 216
7-2-2. Flow and deposition model of the debris avalanches 219
7-3. Flow and deposition mechanism of the pyroclastic flows 222
7-3-1. Density-modified grain flow model 222
7-3-2. Flow and deposition model of the pyroclastic flows 228
Chapter 8. Summary 233
Acknowledgements 238

References 239

Appendix

Source lists of the program to simulate the pryoclastic flows using the energy line and the Bingham flow models 256

Abstract:

Over the last few decades, the mechanism of flow and deposition of debris avalanches and pyroclastic flows has been the subject of great interest and much debate. The objective of this thesis is to discuss the mechanisms of these gravity currents, based on the detailed field surveys, observation of the currents, fluidization experiment, computer simulations, and critical evaluation of previous models. A plug flow model is used to explain the field evidences of Iwasegawa and Kaida debris avalanche deposits. A density-modified grain flow model is used to explain the characteristics and the results of the laboratory experiment and simulations of Komagatake 1929 and Unzen 1991-93 pyroclastic flow deposits.

The Iwasegawa debris avalanche deposit, ca. 0.1 km^3 in volume, is distributed over the southeastern foot of Tashirodake Volcano, northern Honshu. At least 12 types of fragile debris avalanche block (DB) were identified in this avalanche deposit. Poorly-sorted debris avalanche matrix (DM) fills spaces between them. Normal grading of large clasts and reverse grading of wood fragments were observed. Preferred orientation of 311 pieces of wood fragments within this deposit coincided with the local flow direction. At the bottom part of the deposit, (1) erosion and incorporation of the basement material; (2) higher proportion of the basement materials than the upper part; and (3) reverse grading of the clasts were observed. The Kaida debris avalanche deposit, >0.3 km^3 in volume, is distributed at the eastern foot of Ontake Volcano, central Japan. At least 5 types of fragile DBs were included in this avalanche deposit. Many deformation structures were observed in the DBs such as elongation, folding, conjugate reverse faults and numerous minor faults. Lithic components within the DM tended to have a higher ratio of the material which was captured from the adjacent basement formation during flowage.

The plug flow model is proposed to explain the flow and deposition mechanisms of these debris avalanches as follows. In the inner plug, the fragile DBs were transported without major rapturing due to high yield strength and viscosity of the DM. As the debris avalanches flowed down the steep slope at high speed, basement materials were eroded and incorporated into the laminar boundary layer under a strong shear stress field. The DM was produced by the shear stress between two DBs, and DBs and basement formations. Collision between DB and basement formations resulted in fracturing. Wood fragments included within the DM in the laminar boundary layer were rotated and aligned parallel to the flow direction. The density grading of clasts and wood fragments were formed by the density differences relative to the DM. The elongated DBs were formed by shear stress within the laminar boundary layer, and reverse grading of clasts was formed by the dispersive pressure on collision of each clast at the bottom of the flows. When the shear stress in the laminar boundary layer became smaller than the yield strengths of the flows due to deceleration, the debris avalanches froze and stopped thixotropically.

The Komagatake 1929 pyroclastic flow deposit, ca. 0.14 km^3 in volume, is distributed around Komagatake Volcano, southwestern Hokkaido. Yield strengths were estimated by the measurement of widths and heights of 53 lobes and 37 natural levees of pyroclastic flow deposits at the northwestern slope using methods proposed by Moore et al. (1978). The order of estimated yield strengths were 10^2-10^4 Pa. One flow unit of the pyroclastic flow deposit at the northern slope can be subdivided into three layers: such as (1) fines-depleted layer (DL), (2) fines-rich layer (FL), and (3) pumice-concentrated layer (PL), in ascending order, where the deposit contains many carbonized wood fragments. Fluidization experiments using the material of the pyroclastic flow deposits and the glass beads of various sizes revealed that the formation mechanism of the DL and FL due to concentration of the fine particles toward

the top through the segregation pipes. In this experiment, particles larger than 1 mm were not affected by the upward flow at all. The Unzen 1991-93 pyroclastic flow deposits, ca. 0.2 km^3 in total volume, have been produced by more than 8600 collapses of lava domes extruded at Jigokuato crater. Volume of each pyroclastic flow was estimated using the seismographic record of the tremor produced by the pyroclastic flow. Relationship between the volume and mobility of pyroclastic flows was investigated to predict the disaster area. Observation showed that the pyroclastic flow deposit is composed of a few-meters thick, poorly-sorted, dense basal avalanche deposit and very thin, better-sorted, ash-cloud surge deposit. Video images revealed that the pyroclastic flows descended along the channels, with developing vortices of overlying dilute ash-cloud, but ingestion of air or jetting from the flow head which were proposed by Wilson and Walker (1982) were not observed. Excavation by machines of the toe of the June 8, 1991, pyroclastic flow deposit revealed that the deposit, ca. 4 m thick, was partly fines-depleted and accompanied a <5 cm-thick surge deposit and a 15 cm-thick layer 2a (Sparks, et al., 1973) at the bottom. The measured average velocities of five pyroclastic flows from May 24 to May 29, 1991, were up to 42 m/s. Numerical simulations of pyroclastic flows using energy line/cone (Malin and Sheridan, 1982) and Bingham flow (McEwen and Malin, 1989) models were made to simulate the velocity changes and arrival times of the flows, and to predict the disaster areas. In the simulation using the Bingham flow model, obtained yield strengths and viscosities were 850-2000 Pa and 50-90 Pas, respectively.

The density-modified grain flow model is proposed to explain the flow and deposition mechanisms of these pyroclastic flows. At the measured velocities, the maximum grain size that can be transported by the turbulence is at most 0.1-1.0 cm in diameter. Therefore, grains finer than this size can form the dilute ash-cloud surge/fall, but grains larger than this size must be concentrated on the

bottom and form the poorly-sorted, dense basal avalanche. Theoretical curve of fluidization (Sparks, 1976) shows that the maximum grain size can be fluidized in the basal avalanche is at most 1.0 cm, when no ingestion of air from the flow head occurs. Therefore the transport mechanism of the clasts larger than this size is not fluidization as proposed by Wilson (1980, 1984), but "grain interaction" and "matrix strength". Such a kind of flow is called as "the density-modified grain flow (Lowe, 1976)". The roundness of the clasts in the both pyroclastic flow deposits indicates the severe collision of clasts. Both pyroclastic flows have yield strengths large enough to support the large clasts (10^2-10^4 Pa). The surge deposit at the bottom of the pyroclastic flow deposit may have been formed by ash-cloud surge which was detached from the basal avalanche at the bottom of the steep slopes due to hydraulic jump and proceeded ahead of the tip of the basal avalanche.

Chapter 1. Introduction

Debris avalanches are the large-scale rapid mass movement in dry condition, which is started from the catastrophic landslide of unstable part of the mountain, triggered by the event such as a phreatic explosion and a tectonic earthquake. More than 80 debris avalanche deposits have already been reported in Japan (Ui et al., 1986b). Number of the debris avalanche deposits in the world have also been increased (Siebert, 1986; Siebert et al., 1987). The 1792 Mayuyama debris avalanche, Unzen, Kyushu, 0.34 km^3 in volume, which was triggered by an earthquake, produced a catastrophic tsunami, causing 14500 fatalities, recording the worst disaster in Japan (Fig. 1-1; Katayama, 1974; Siebert et al., 1987). The 1888 Bandai debris avalanche, northeastern Honshu, 1.5 km^3 in volume, which was triggered by phreatic explosions, caused 461 fatalities, forming hummocky surface on the deposit and many damming-up lakes at the northern foot of the volcano (Fig. 1-2; Sekiya and Kikuchi, 1890; Nakamura, 1978). Eye witnesses of the 1980 Mt. St. Helens debris avalanche, USA, 2.8 km^3 in volume, have increased the knowledge of the initiation and the flow mechanisms of the avalanche (Fig. 1-3; Voight et al., 1981; Voight et al., 1983). The small 1984 Ontake debris avalanche, central Japan, 0.034 km^3 in volume, which was triggered by the Naganoken-Seibu Earthquake, M 6.8 on Richter scale, caused devastation along the rivers at the southern slope (Fig. 1-4; Matsuda and Ariyama, 1985; Mimura et al., 1988). Many models have been proposed to explain the great mobility of these catastrophic events, and much debates have been continued (Chap. 2-1-3).

A plug flow model is proposed to explain flow and deposition mechanism of the debris avalanches in this thesis, based on detailed field evidences of the Iwasegawa debris avalanche deposit, Tashirodake Volcano, northern Honshu, and the Kaida debris avalanche deposit, Ontake Volcano, central Japan (Fig. 1-

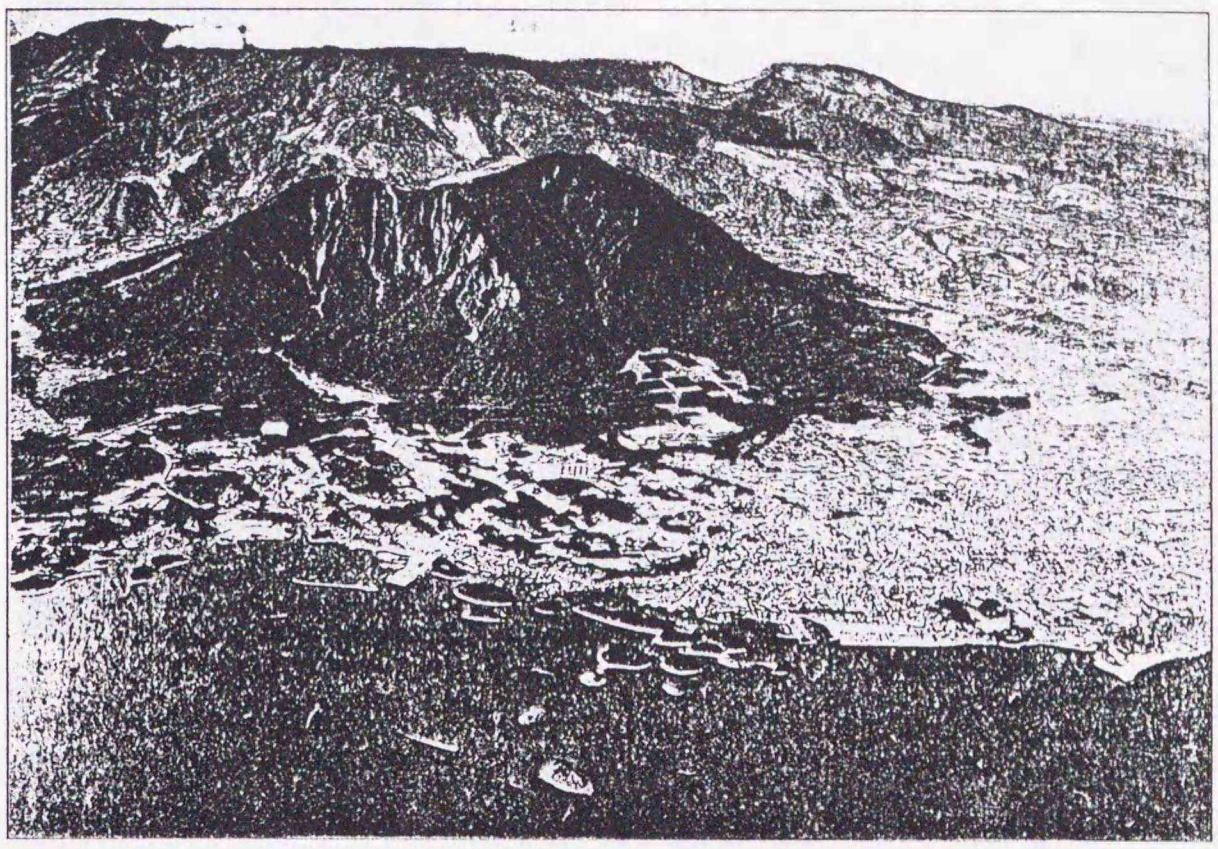

Fig. 1-1. Aerial view of the 1792 Mayuyama debris avalanche deposit, Unzen, Kyushu, and its source amphitheater, which was taken from the east of the volcano (after Miyachi et al., 1987).

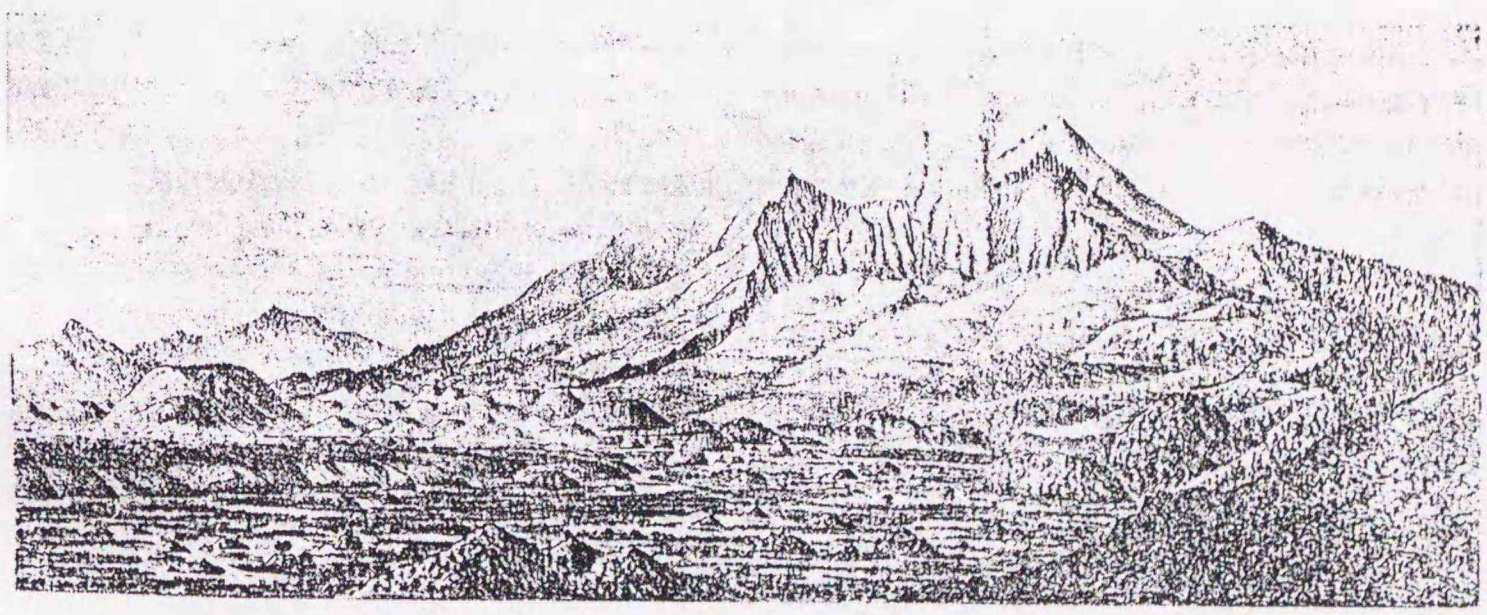

Fig. 1-2. Sketch of the 1888 Bandai debris avalanche deposit, northeastern Honshu, and its hummocky surface. A peak, Ko-Bandai, was lost by this avalanche, forming the amphitheater. After Sekiya and Kikuchi (1890).

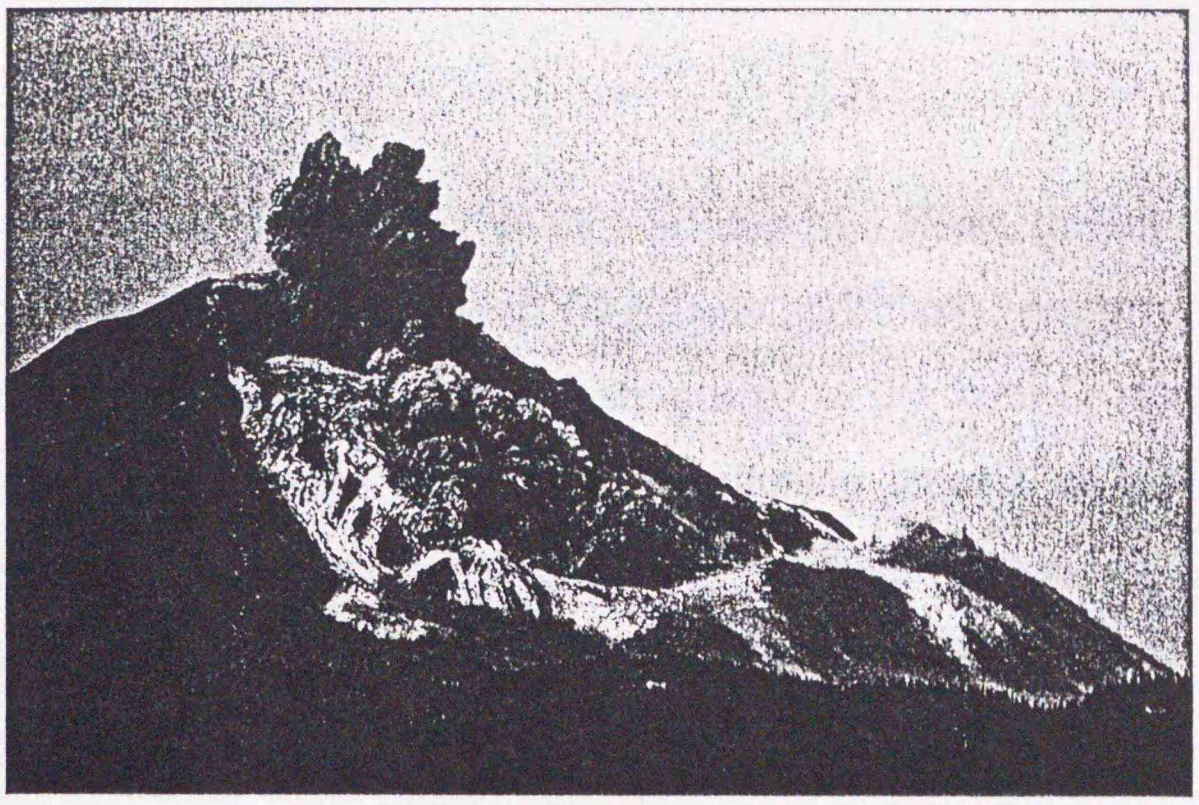

Fig. 1-3. One of the sequence photographs of the initiation of the 1980 Mt. St. Helens debris avalanche, USA, taken by G. Rosenquest. Subsequent blast and plinian column are also observed in the photograph. After Voight (1981).

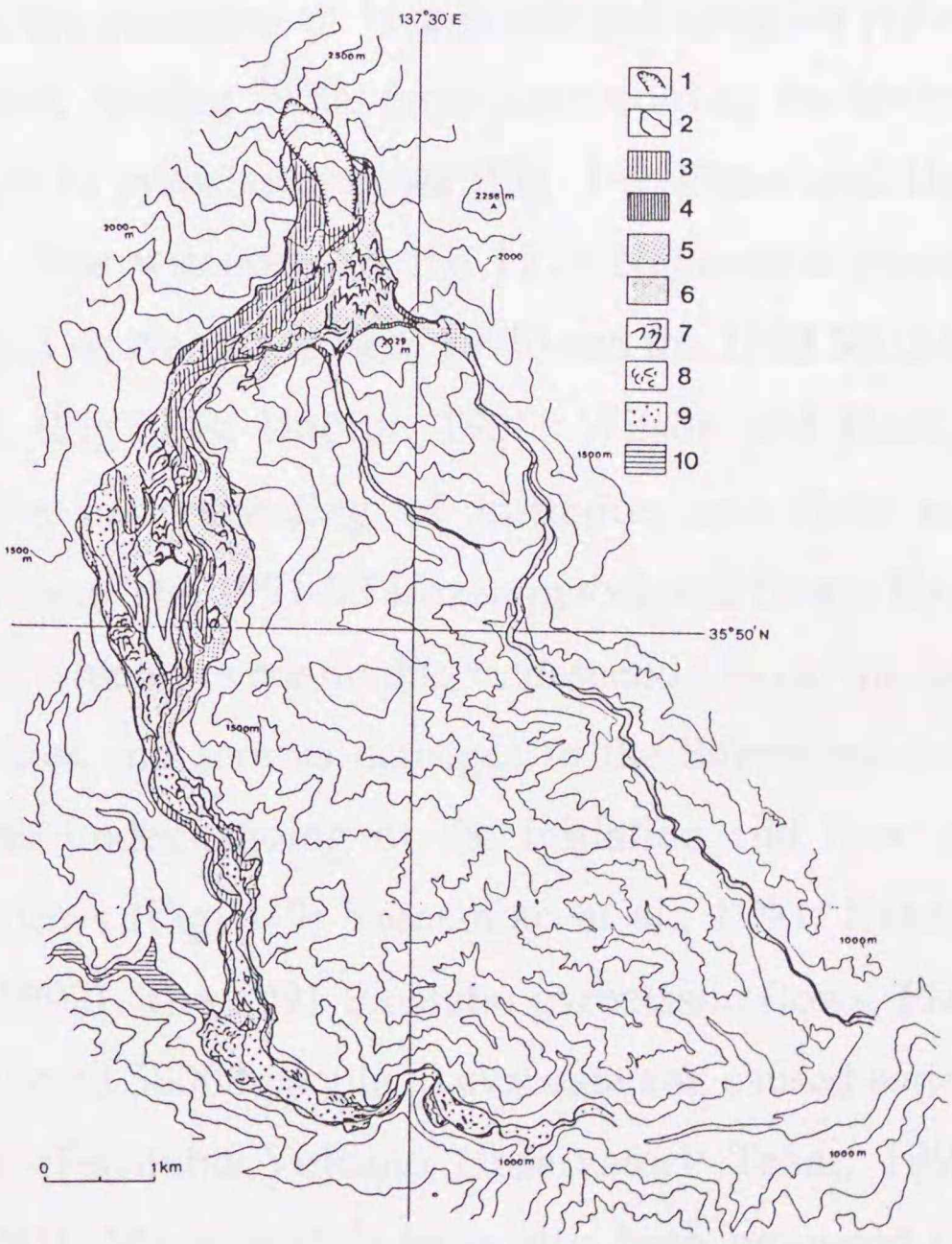

Fig. 1-4. Distribution of the 1984 Ontake debris avalanche deposit at the southern slope of the volcano, central Japan. 1, Source; 2, routes of the debris avalanche and subsequent debris flows and floods; 3, erosion area by the avalanche; 4, area of fallen-trees by the avalanche; 5, erosion area covered with thin avalanche deposit; 6, deposition area of the thick avalanche deposit; 7, colorful streak area by the debris; 8, wrinkle of the avalanche surface; 9, damming-up lake. After Mimura et al. (1988).

5). At the Iwasegawa debris avalanche deposit, characteristics of blocks and matrix, density grading of wood fragments and clasts, preferred orientation of wood fragments, and sedimentary structures at the bottom part of the deposit were investigated. At the Kaida debris avalanche deposit, deformation structures of blocks, and lithic components within matrix were investigated.

Pyroclastic flows are the mass flows of juvenile debris which are potentially the most destructive products of volcanic eruptions due to their high temperature and great mobility. Numerous pyroclstic flows, ranging from 10^{-5} to 10^{2} km^3 in volume, have been reported. The 1902 Mt. Pelée pyroclastic flows and associated pyroclastic surges, Martinique, Lesser Antilles, which occurred by the collapses of lava dome and eruption columns, destroyed the town St. Pierre, causing 29000 fatalities, recording the historic worst disaster in the world due to pyroclastic flows (Fig. 1-6; Fisher and Heiken, 1982; Blong, 1984, p.73). Eye witnesses of the 1975 Ngauruhoe pyroclastic flows, New Zealand (Fig. 1-7; Nairn and Self, 1978) and the 1980 Mt. St. Helens pyroclastic flows, USA (Fig. 1-8; Hoblitt, 1986; Wilson and Head, 1981) have been improved the understanding of initiation and flow mechanisms of the pyroclastic flows. The 1991-93 Unzen pyroclastic flows, Kyushu, ca. 0.2 km^3 in total volume, which are continuing to descend toward the eastern slope, caused the 44 fatalities and serious damages to the Shimabara and Fukae areas, but improved the understanding of the initiation and flow mechanisms of the pyroclastic flows (Fig. 1-9; Yamamoto et al., 1993; Nakada and Fujii, 1993; Sato et al., 1992). The 1991 Pinatubo pyroclastic flows, Philippines, ca. 7 km^3 in volume, forced 58000 people to evacuate and caused serious damages around the volcano (Pinatubo Volcano Observatory Team, 1991; Koyaguchi and Tokuno, 1993). Many models have also been proposed to explain the great mobility of the pyroclastic flows, and much debates have been continued (Chap. 2-2-2).

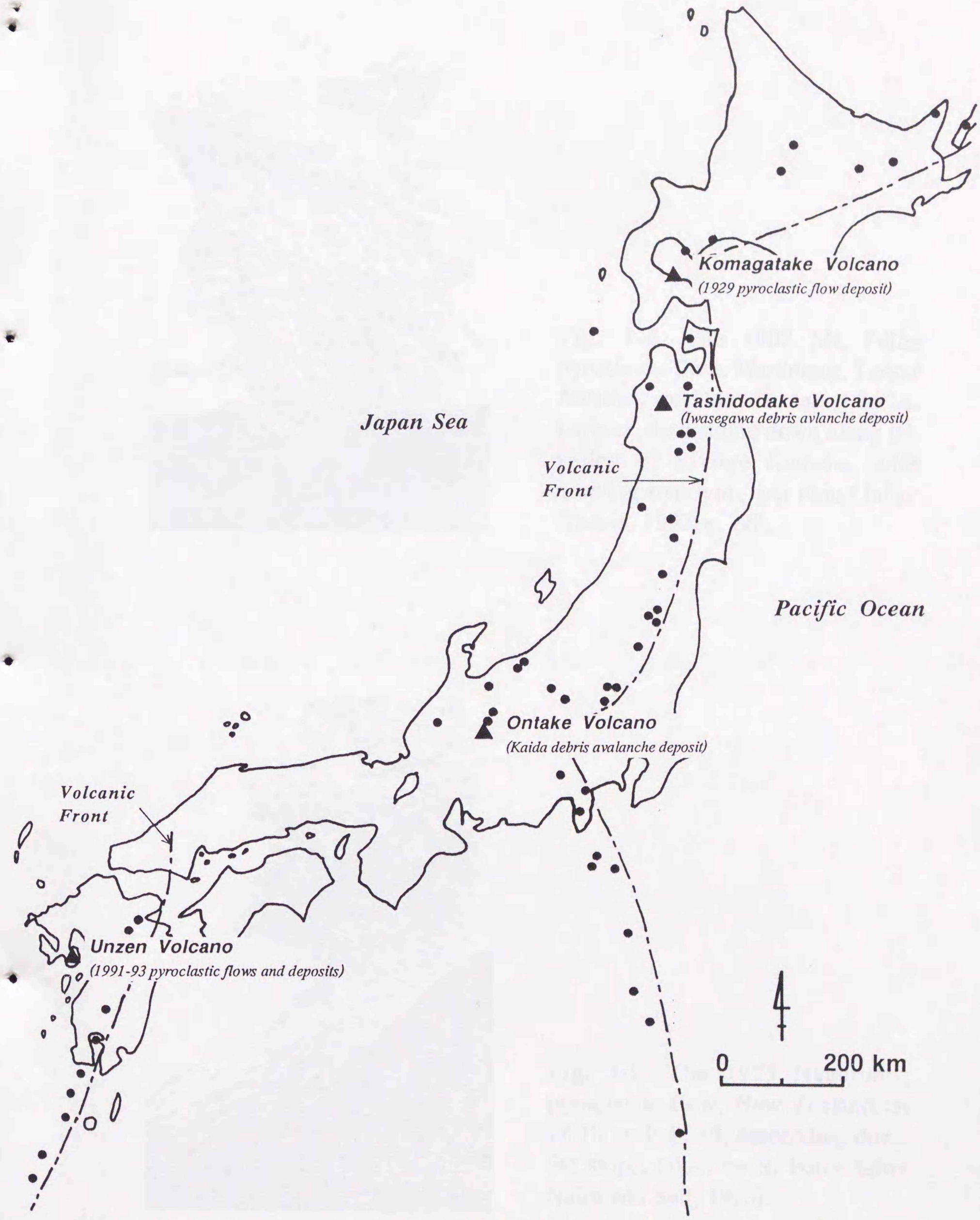

Fig. 1-5. Location map of Tashirodake, Ontake, Komagatake and Unzen Volcanoes (closed triangles). Small closed circles indicate the active volcanoes in Japan. Volcanic fronts are shown after Sugimura (1978).

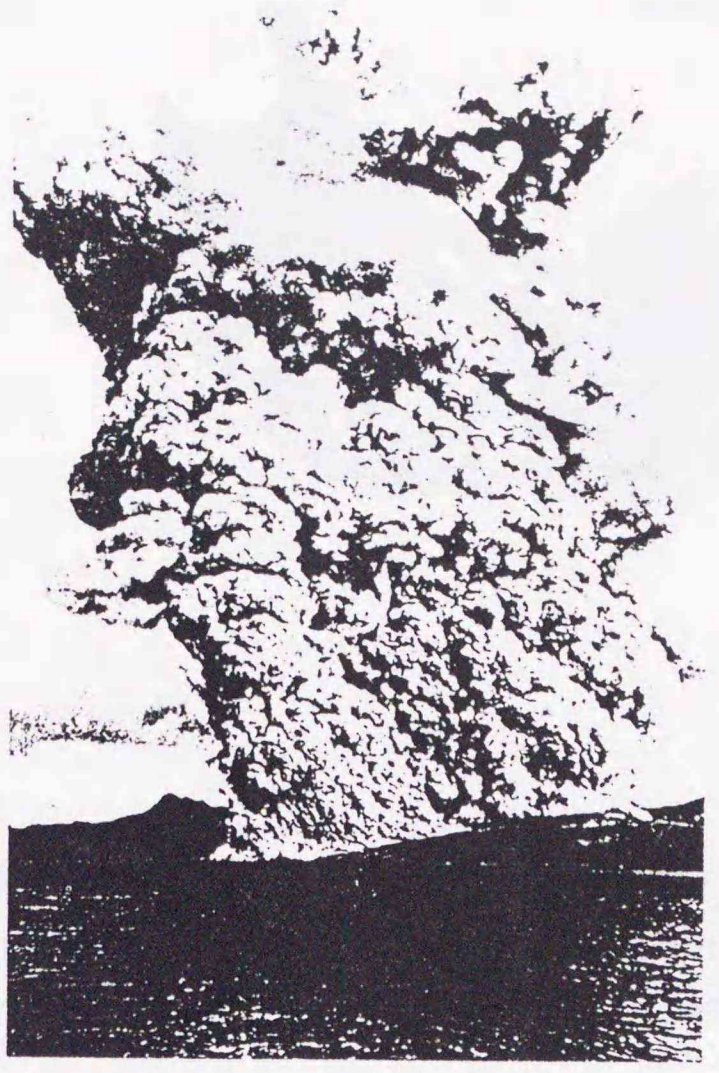

Fig. 1-6. The 1902 Mt. Pelée pyroclastic flow, Martinique, Lesser Antilles, on Dec. 16, taken by A. Lacroix, descending down along the valley of Riviére Blanche, with growing overlying ash cloud (after Francis, 1993, p. 88).

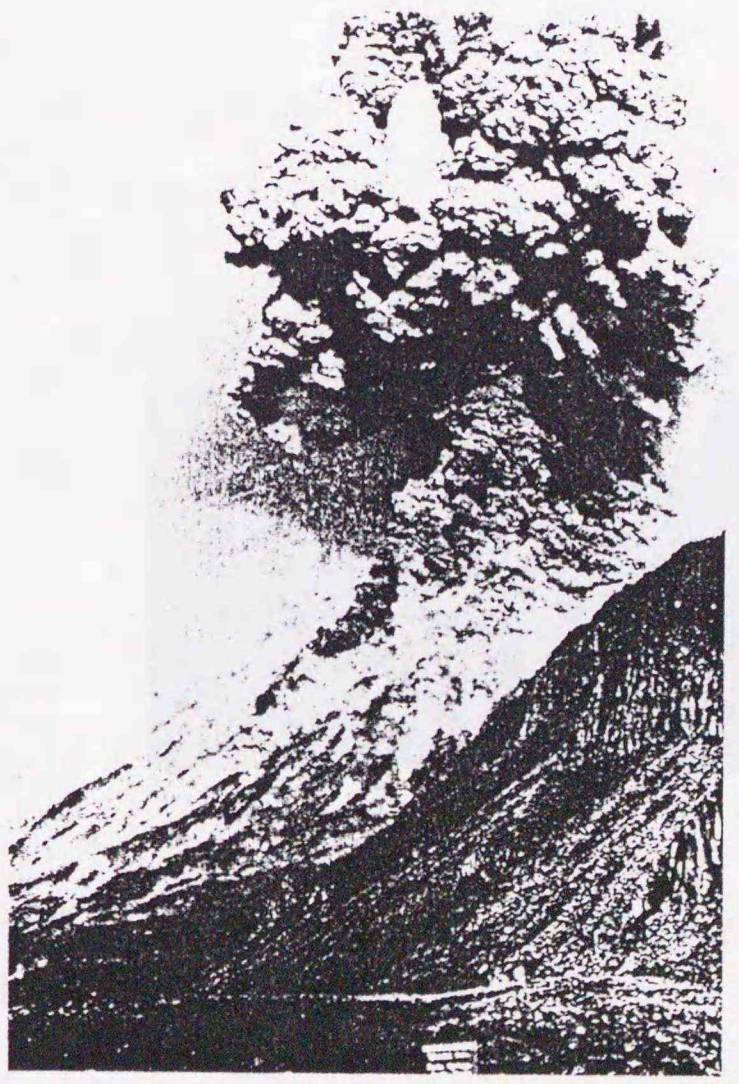

Fig. 1-7. The 1975 Ngauruhoe pyroclastic flow, New Zealand, at 18:10 on Feb. 19, descending down the slope, taken by R. Foley (after Nairn and Self, 1978).

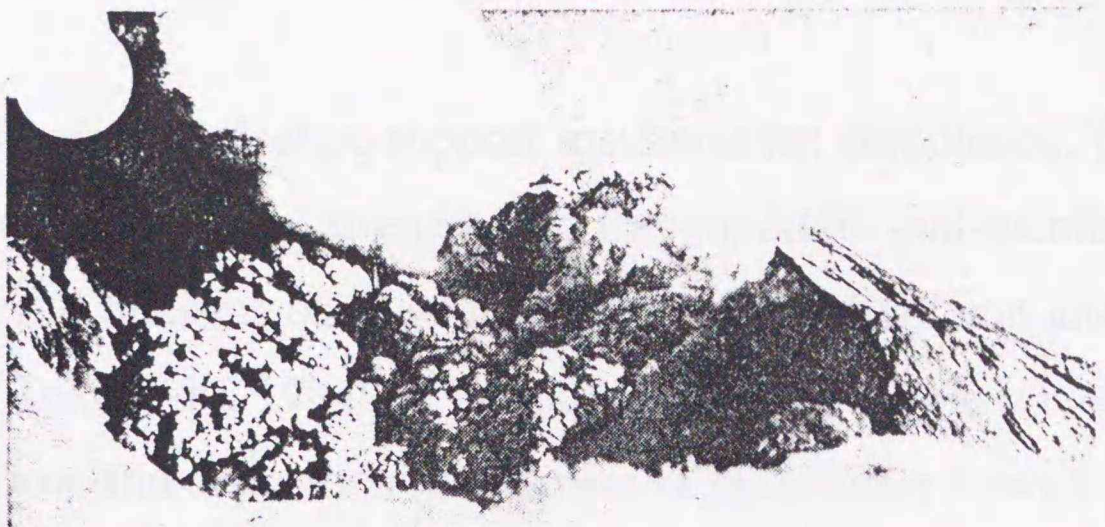

Fig. 1-8. Initiation of the boiling-over type pumiceous pyroclastic flow at Mt. St. Helens, USA, on July 22, 1980, from the amphitheater of the May 18 debris avalanche, taken by H. Gliken (after Cas and Wright, 1987, p. 109).

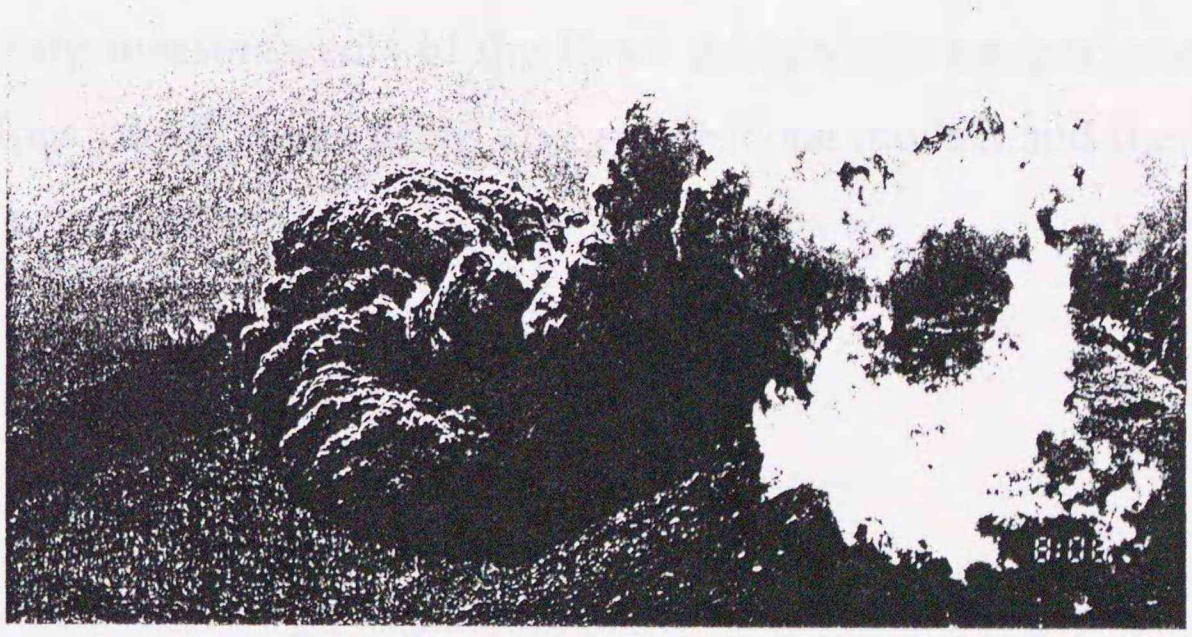

Fig. 1-9. A Unzen pyroclastic flow on Aug. 15, 1991, with growing dilute ash cloud (after Nakada, 1992).

Four fundamental clast support mechanisms: turbulence, fluidization, grain interaction, and matrix strength, are the important end-members to understand the flow mechanisms of general gravity flows (Middleton and Hampton, 1976; Soh and Tokuhashi, 1984). A density-modified grain flow model is proposed to explain flow and deposition mechanism of pyroclastic flows in this thesis, based on the field surveys, observation, and laboratory experimet of the Komagatake 1929 pyroclastic flow deposits, Hokkaido, and the Unzen 1991-93 pyroclastic flows and the deposits, Kyushu (Fig. 1-5). At the Komagatake 1929 pyroclastic flow deposits, (1) estimation of yield strengths using the detail surface morphologies of lobes and levees; (2) observation of one unit of lobe, consisting of fines-depleted, fines-rich, and pumice-concentrated layers; and (3) fluidization experiments using the materials of the deposits and glass bead were performed. At the Unzen 1991-93 pyroclastic flows and the deposits, (1) volume estimation using seismic records by the flows; (2) observation of the pyroclastic flows, consisting of dense basal avalanche and overlying dilute ash-cloud; (3) excavation survey of the June 8, 1991, pyroclastic flow deposit, consisting of the layer 1, 2a, and 2b (Sparks et al., 1973) and segregation pipes; (4) velocity measurements of the flows using video images; and (5) computer simulations of the flows using energy line/cone models and the Bingham flow models were performed.

Chapter 2. Previous works

2-1. Debris avalanche

2-1-1. Characteristics

Source of the debris avalanche is characterized by a breached amphitheater, which was formed by the landslide at the initiation stage of the avalanche (Fig. 2-1; Voight et al., 1981). Typical surface topographies of debris avalanche deposits are hummocks (Fig. 2-2), natural levees, and distal cliffs (Fig. 2-3) (Ui, 1987). A debris avalanche deposit is composed of debris avalanche blocks (Gliken, 1986 MS) and debris avalanche matrix (Takarada, 1991) (see Chap. 3). The debris avalanche blocks characteristically show deformation structures, such as: (1) jigsaw cracks in the massive tough materials (ex. lava; Fig. 2-4a); and (2) several faults in the unconsolidated materials (ex. tuff; Fig. 2-4b) (Ui, 1985).

Mimura et al. (1982) revealed that the debris avalanche blocks (megablocks) were transported rotating mainly with a vertical axis, based on the NRM, natural remanent magnetization, measurement at the Nirasaki debris avalanche deposit, Yatsugatake Volcano, central Japan (Fig. 2-5). This result suggests that the debris avalanche blocks could not move freely in the avalanche during the transportation. Lateral variations of characteristics of the debris avalanche deposits at Mount Egmont, New Zealand (Ui et al., 1986a), and at Mount Shasta, California (Ui and Glicken, 1986), were observed, such as: (1) percentage of the debris avalanche blocks is low; (2) width of jigsaw cracks in the blocks is high; and (3) roundness of the volcanic clasts in the debris avalanche matrix is high at the marginal and distal areas (Fig. 2-6). It is concluded that mobility of the debris avalanches was promoted by production of the debris avalanche matrix produced by collision and abrasion of the debris avalanche blocks. At the bottom of the debris avalanche deposits in dry climate areas, a mixed zone, showing

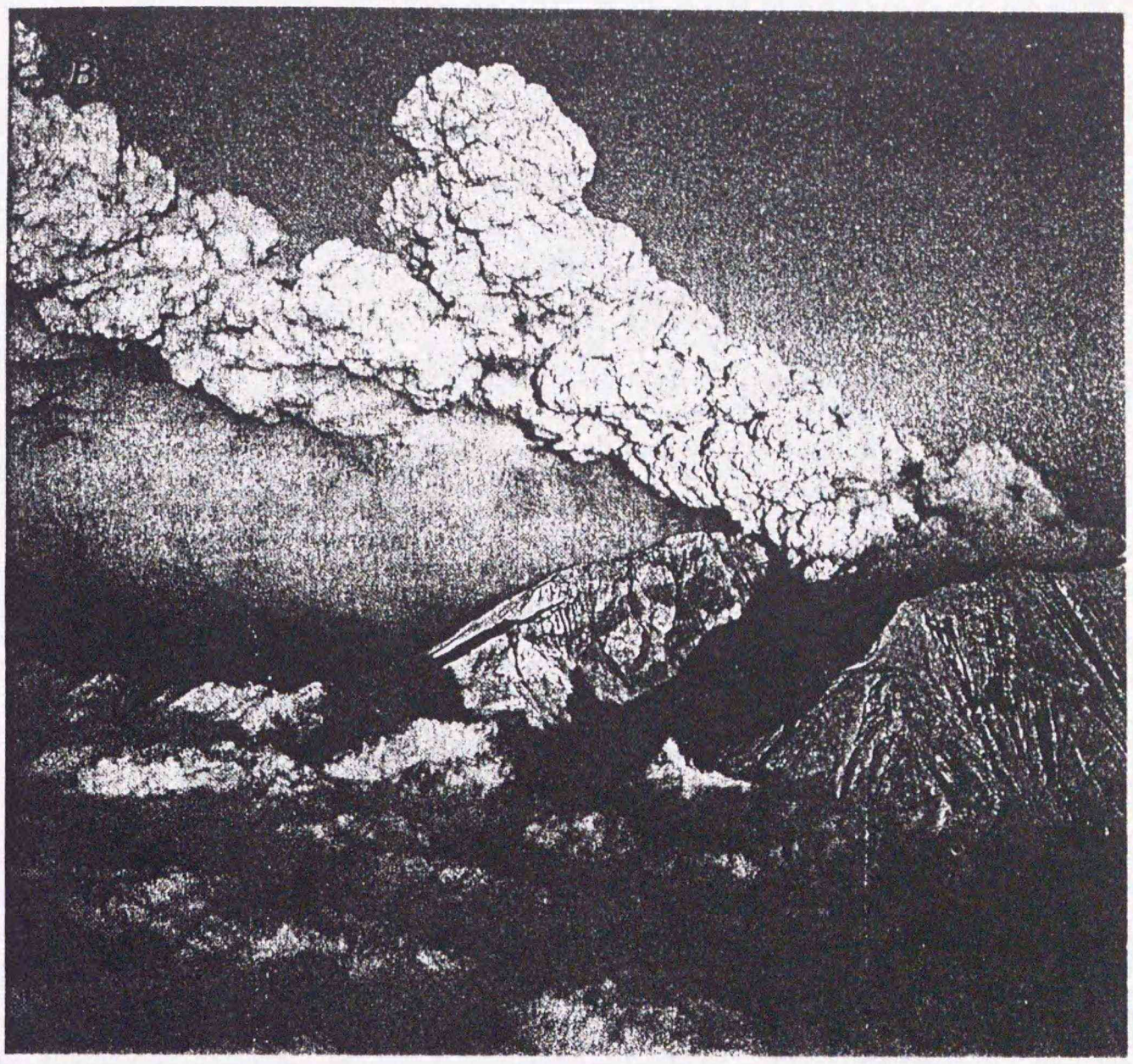

Fig. 2-1. Source amphitheater of the May 18, 1980, Mt. St. Helens debris avalanche (after Foxworthy and Hill, 1982).

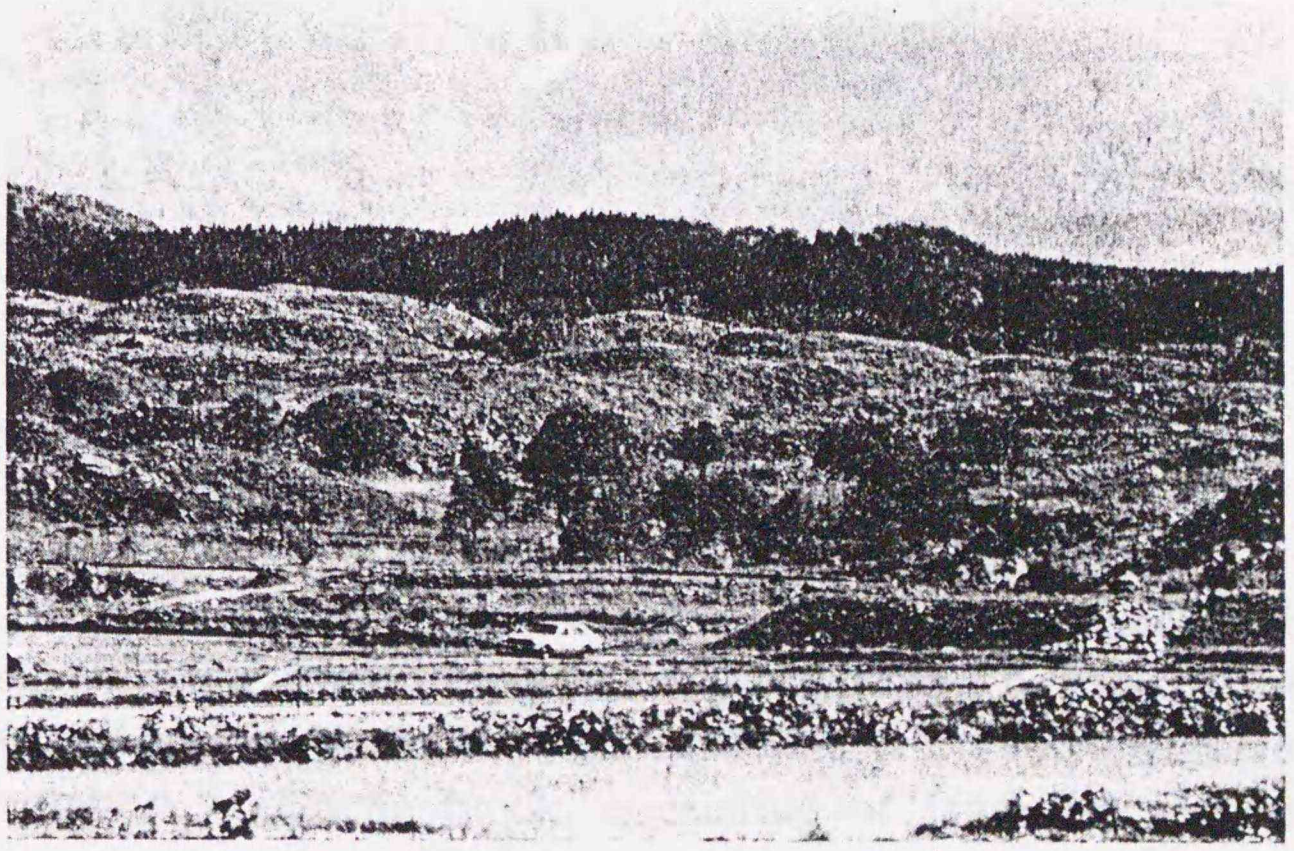

Fig. 2-2. Hummocky surface of the Kisakata debris avalanche deposit, Chokai Volcano, northern Honshu (after Ui, 1983).

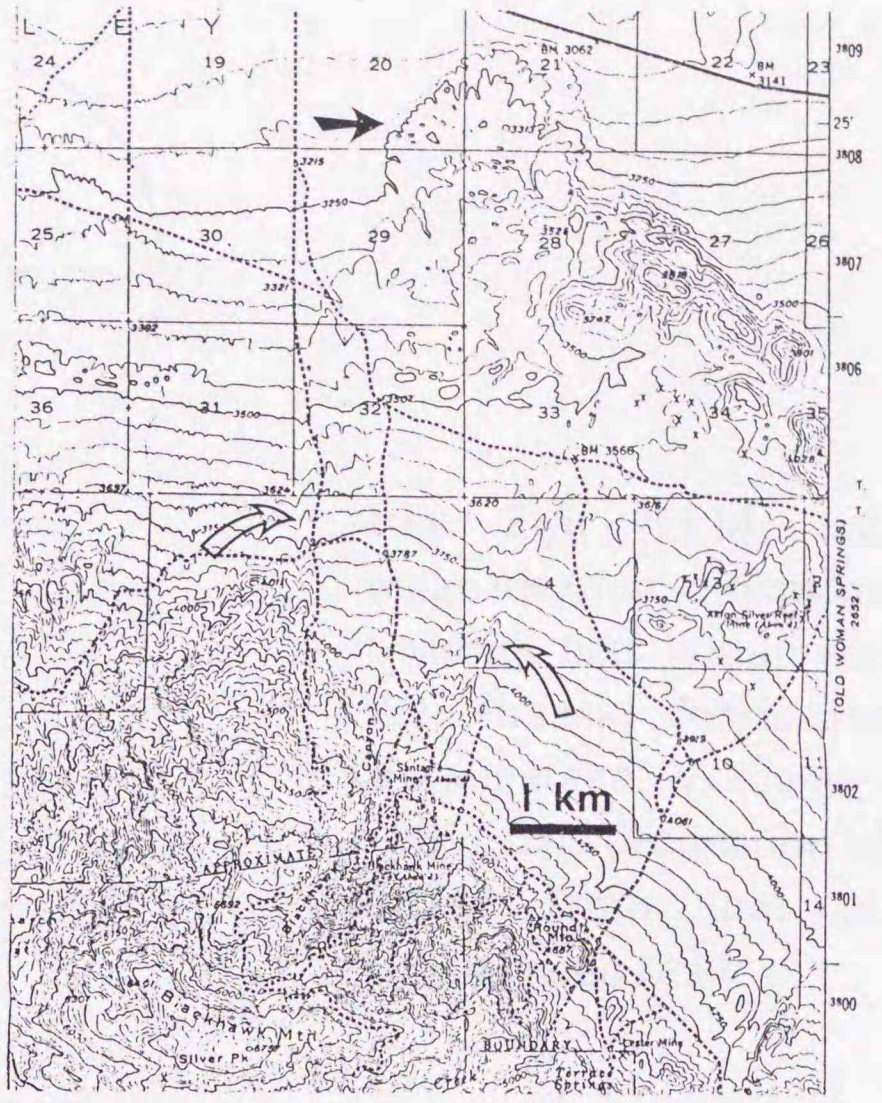

Fig. 2-3. Natural levees (open arrows) and distal cliff (solid arrow) of the Blackhawk debris avalanche deposit, California (after Ui, 1987).

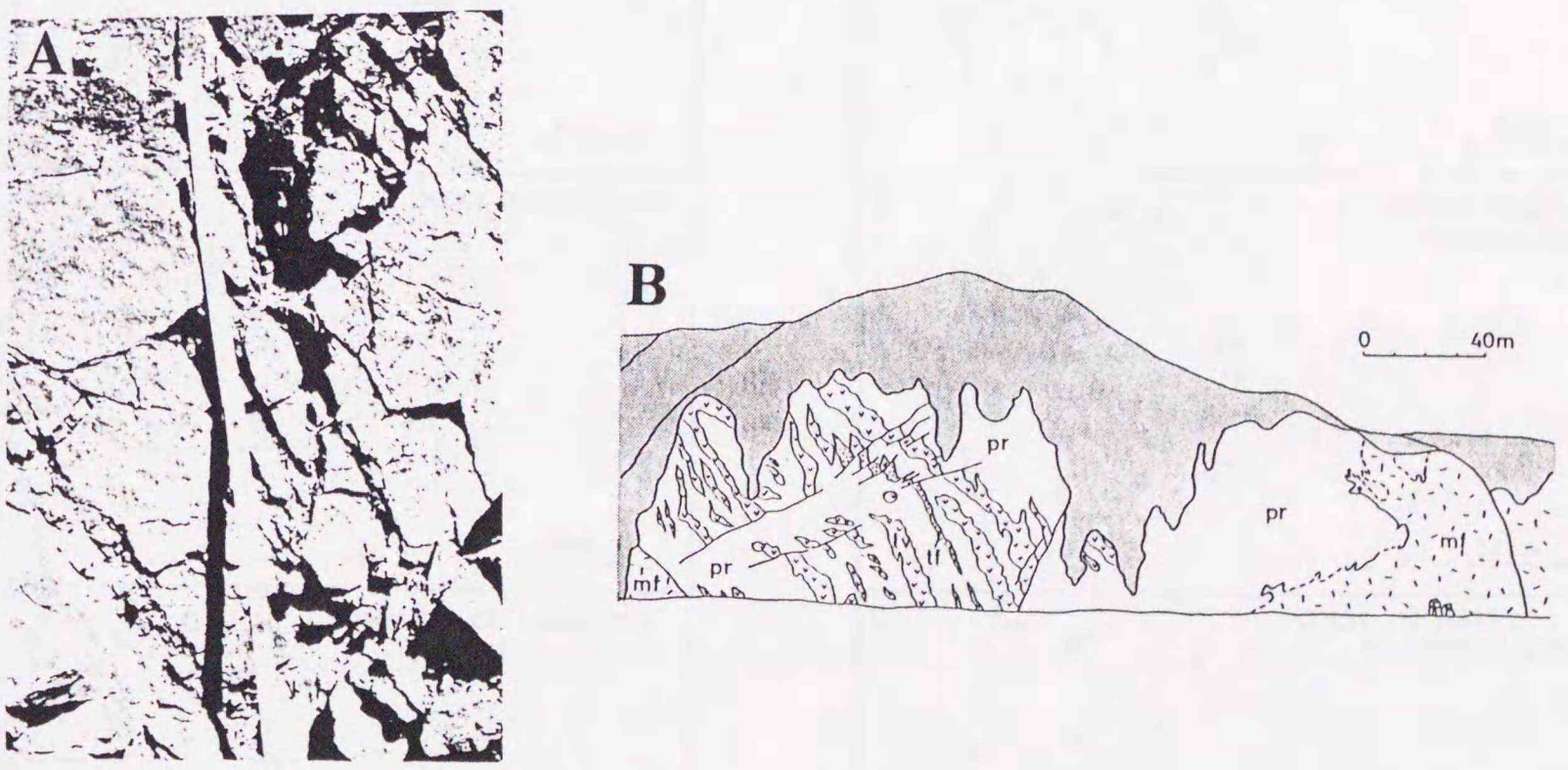

Fig. 2-4A-B. Deformation structures within the debris avalanche blocks. **A.** Jigsaw cracks within a debris avalanche block, consisting of massive lava, in the Mount Shasta debris avalanche deposit, California (Ui, 1985). **B.** Several faults within the debris avalanche block, consisting of lava (lv), coarse-grained pyroclastics (pr), and ash layers (tf), in the Nirasaki debris avalanche deposit, Yatsugatake Volcano, central Japan. mf; debris avalanche matrix. After Mimura (1985).

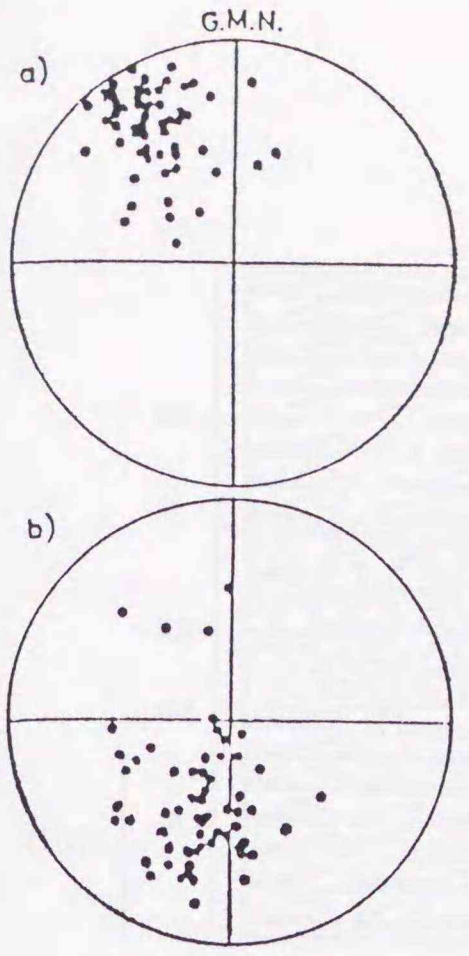

Fig. 2-5. NRM, natural remanent magnetization, directions projected to the Schmidt nets within each megablock of the Nirasaki debris avalanche deposit, Yatsugatake Volcano (after Mimura, 1985). The declination of the megablocks differ from that of the present geomagnetic field.

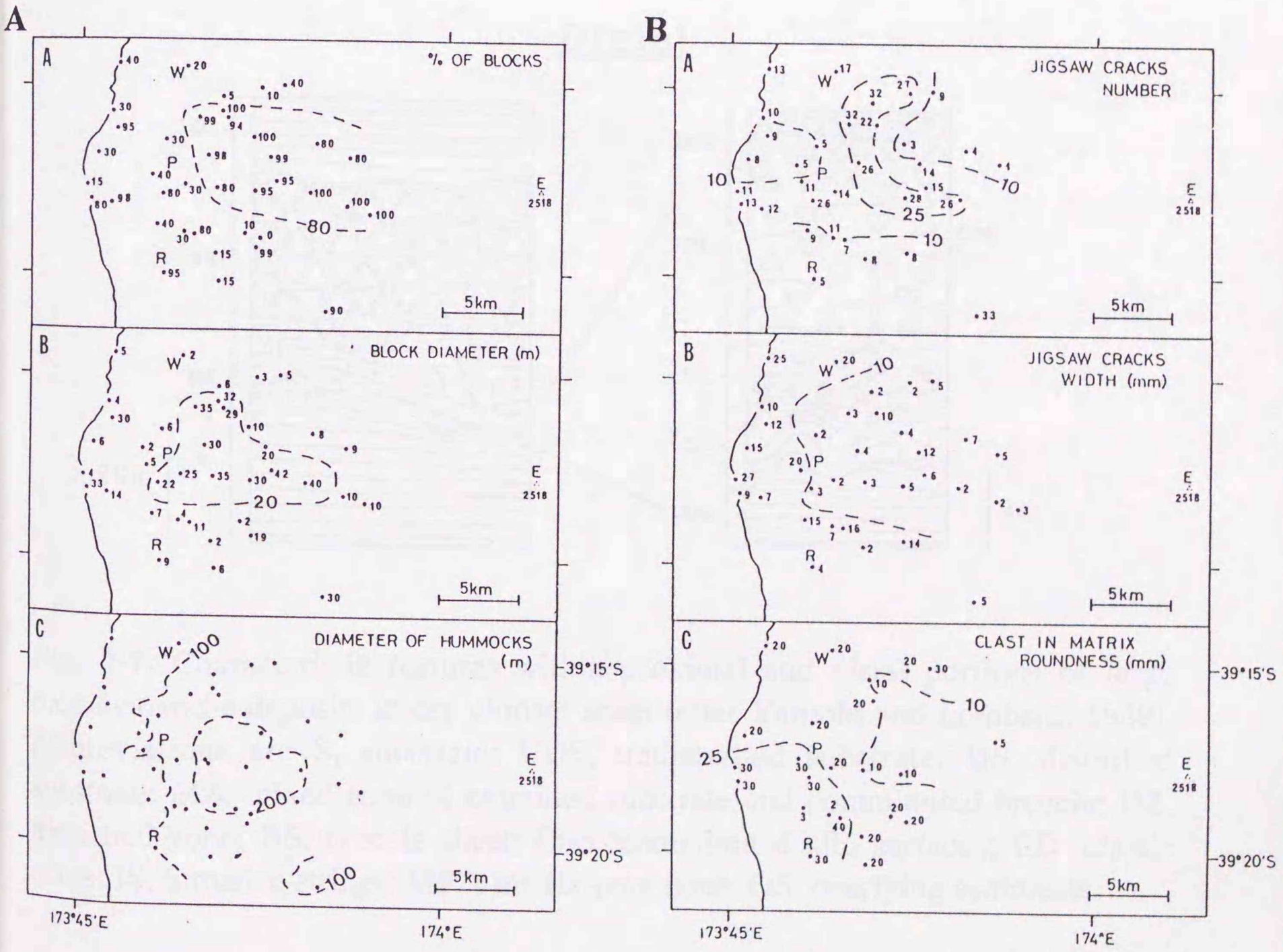

Fig. 2-6A-B. Lateral variations of characteristics of the Pungarehu debris avalanche deposit, New Zealand (after Ui et al., 1986a).

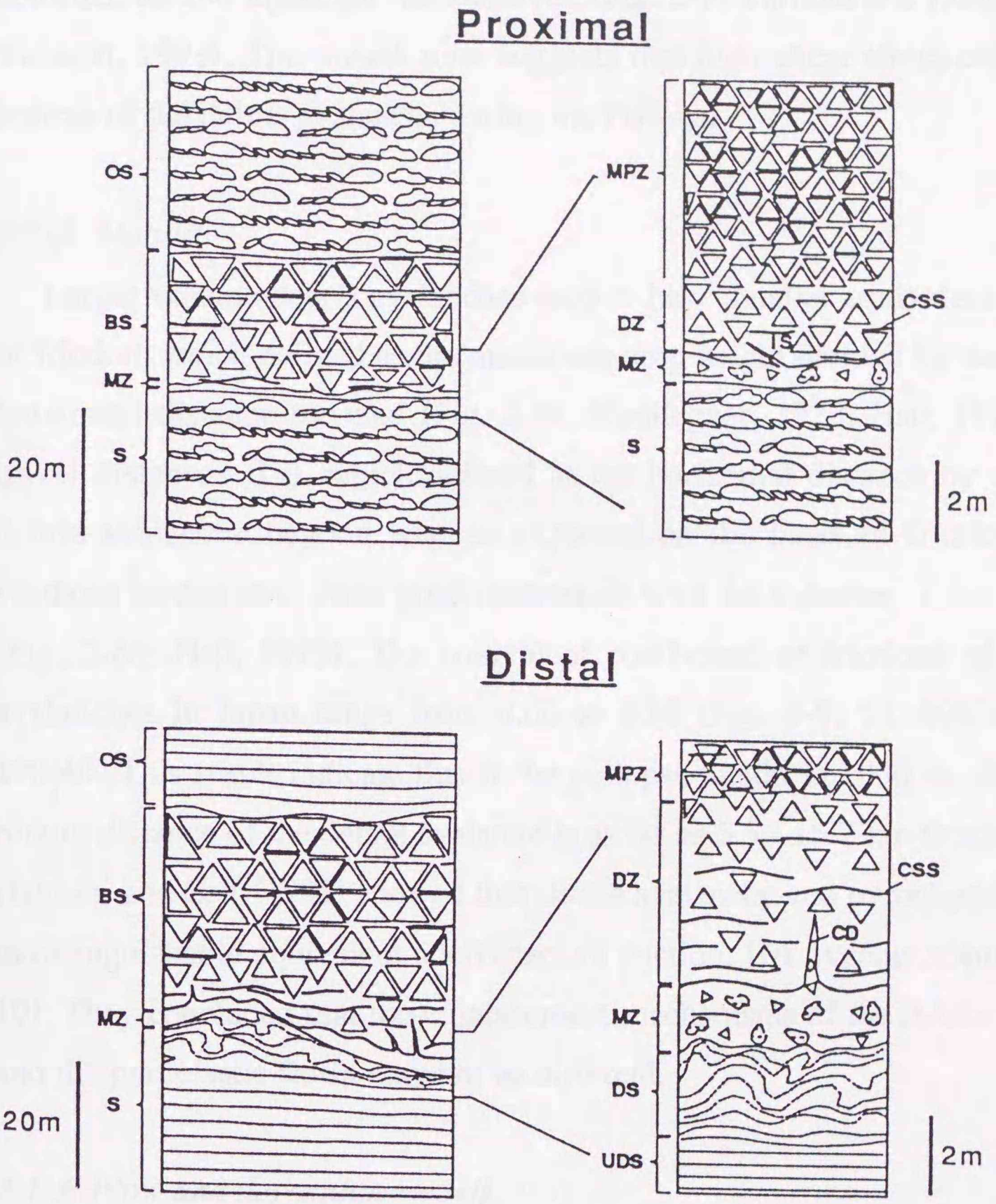

Fig. 2-7. Characteristic features within proximal and distal portions of large rock-avalanche deposits in dry climate areas (after Yarnold and Lombard, 1989). Abbreviations are S, substrate; UDS, undisturbed substrate; DS, disturbed substrate; MZ, mixed zone of entrained substrate and comminuted breccia; DZ, disturbed zone; BS, breccia sheet; CSS, comminuted slip surfaces; CD, clastic dikes; IS, intrusive strings; MPZ, matrix-poor zone; OS, overlying sediments.

deformation and injection, was observed (Fig. 2-7; Yarnold and Lombard, 1989: Yarnold, 1993). The mixed zone suggests that high shear stress existed at the bottom of the debris avalanche during the flowage.

2-1-2. Mobility

Larger volume debris avalanches tend to have smaller equivalent coefficient of friction, which defined as the maximum drop height divided by the maximum horizontal distance traveled (Fig. 2-8a; Sheidegger, 1973; Hsü, 1975). Excess travel distances (L_e), which defined as the horizontal distance by the tip of a debris avalanche beyond what is expected on the basis of frictional sliding (without lubrication), have good correlation with the volumes of the avalanches (Fig. 2-8b; Hsü, 1975). The equivalent coefficient of frictions of the debris avalanches in Japan range from 0.06 to 0.18 (Fig. 2-9; Ui, 1983; Ui et al., 1986b). This result indicate that if the collapse height is 1000 m, the expected runout distance of the debris avalanhe is as far as 5.5 - 16.7 km from the source. Hayashi and Self (1992) showed that debris avalanche and pyroclastic flow have indistinguishable equivalent coefficient of friction, H/L, versus volume (Fig. 2-10). They concluded that the emplacement mechanisms of the debris avalanches and the pyroclastic flows may not be different.

2-1-3. Flow and deposition models

Many emplacement models have been proposed to explain the high mobility of debris avalanches, continuing the much debates of them. Kent (1966) proposed that high speed and high mobility of debris avalanches are due to 'fluidization with air', based on Sadmarreh (Iran), Frank (Canada), and Madison canyon (USA) debris avalanches. But, Shreve (1968a, 1968b) showed that the permeability of Blackhawk debris avalanches, California was less than 1 darcy, and suggested that fluidization of the debris avalanches cannot be the primary

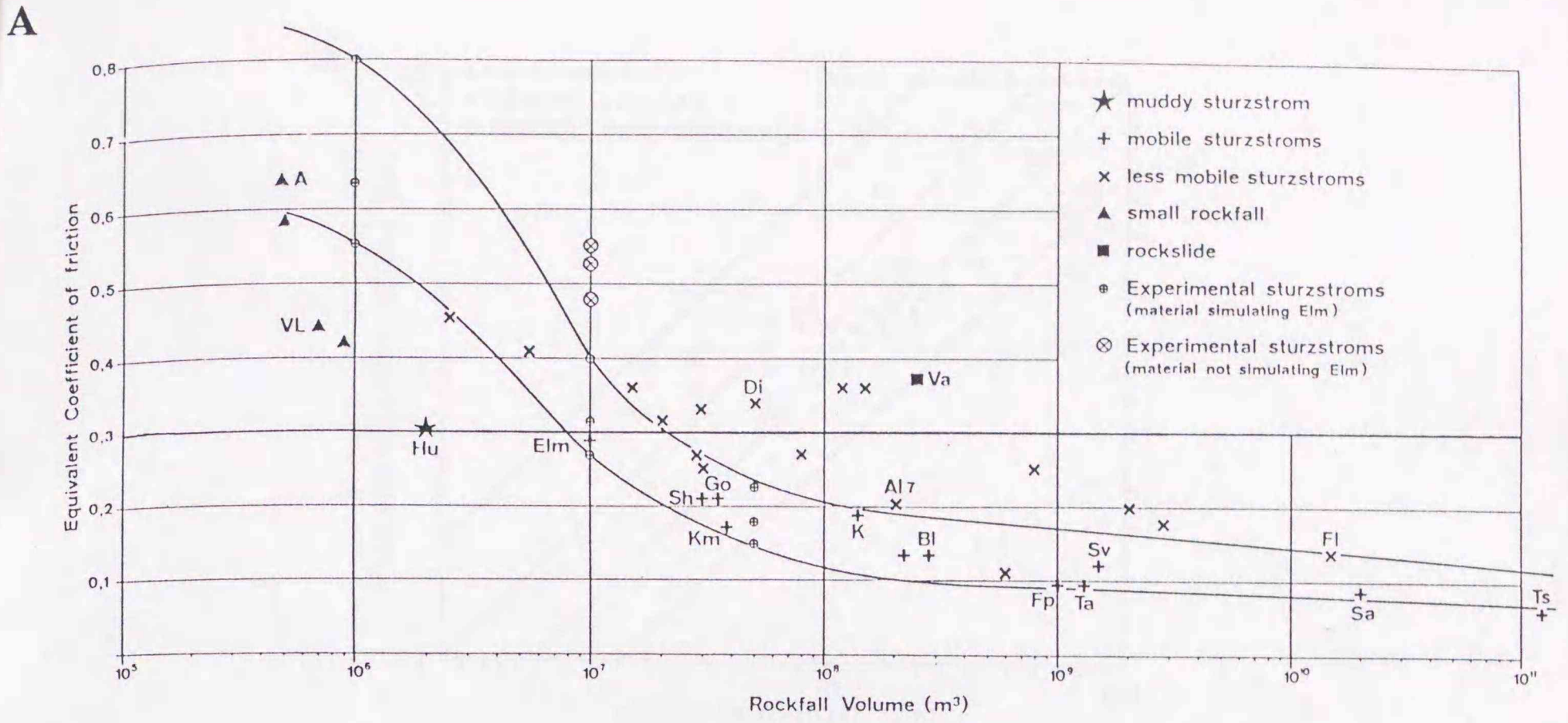

Fig. 2-8A-B. A. Relationship between the equivalent coefficient of friction and the volume of debris avalanches (after, Hsü, 1975). The equivalent coefficient of friction has been defined as the maximum drop height divided by the maximum horizontal distance traveled. There is a general correlation between the coefficient and the size of debris avalanche. **B**. Excess travel distance, L_e, related to debris avalanche volume, V (after Hsü, 1975). The excess travel distance is the horizontal distance traveled by the tip of a debris avalanche beyond what is expected on the basis of frictional sliding (without lubrication). The distance L_e have good correlation with volume of the avalanches.

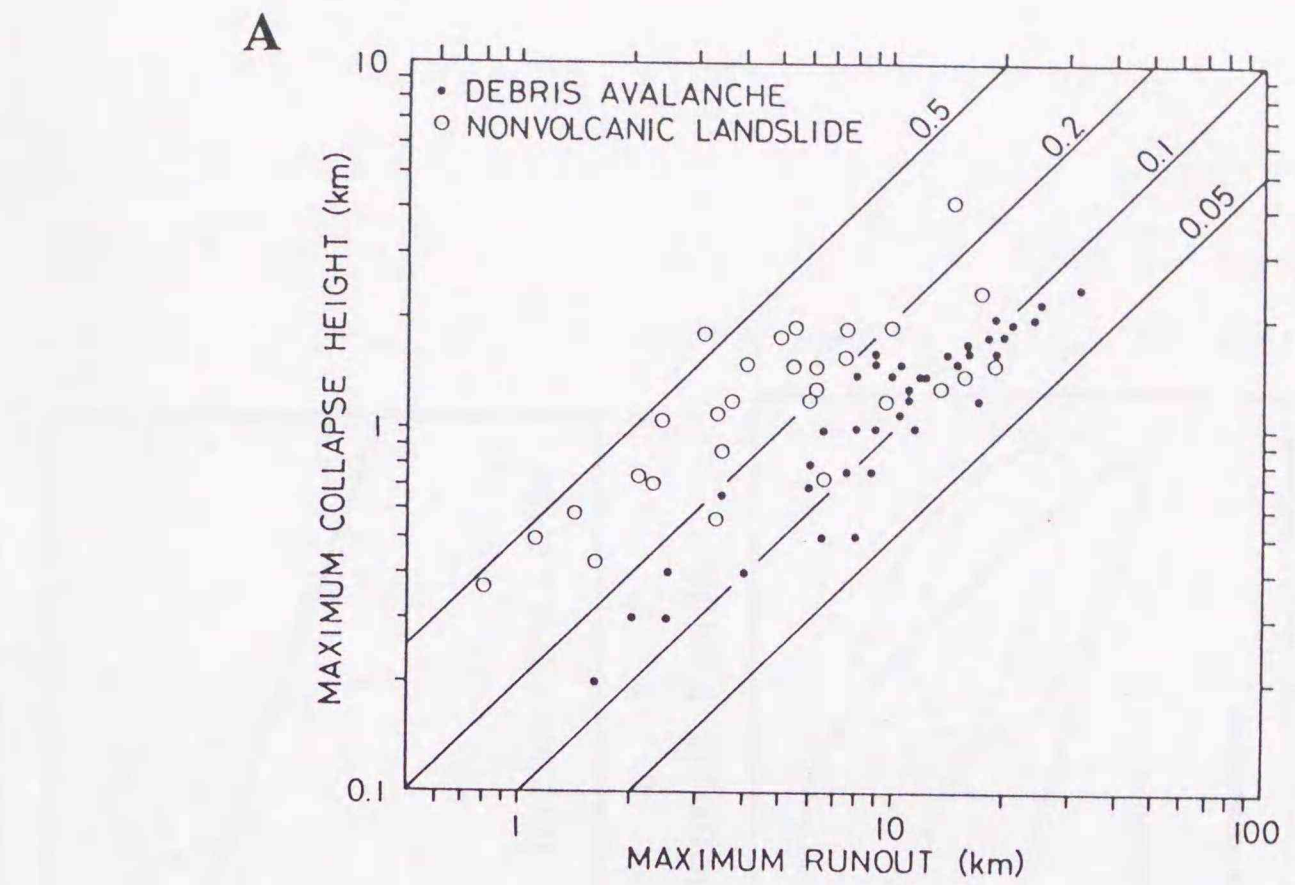

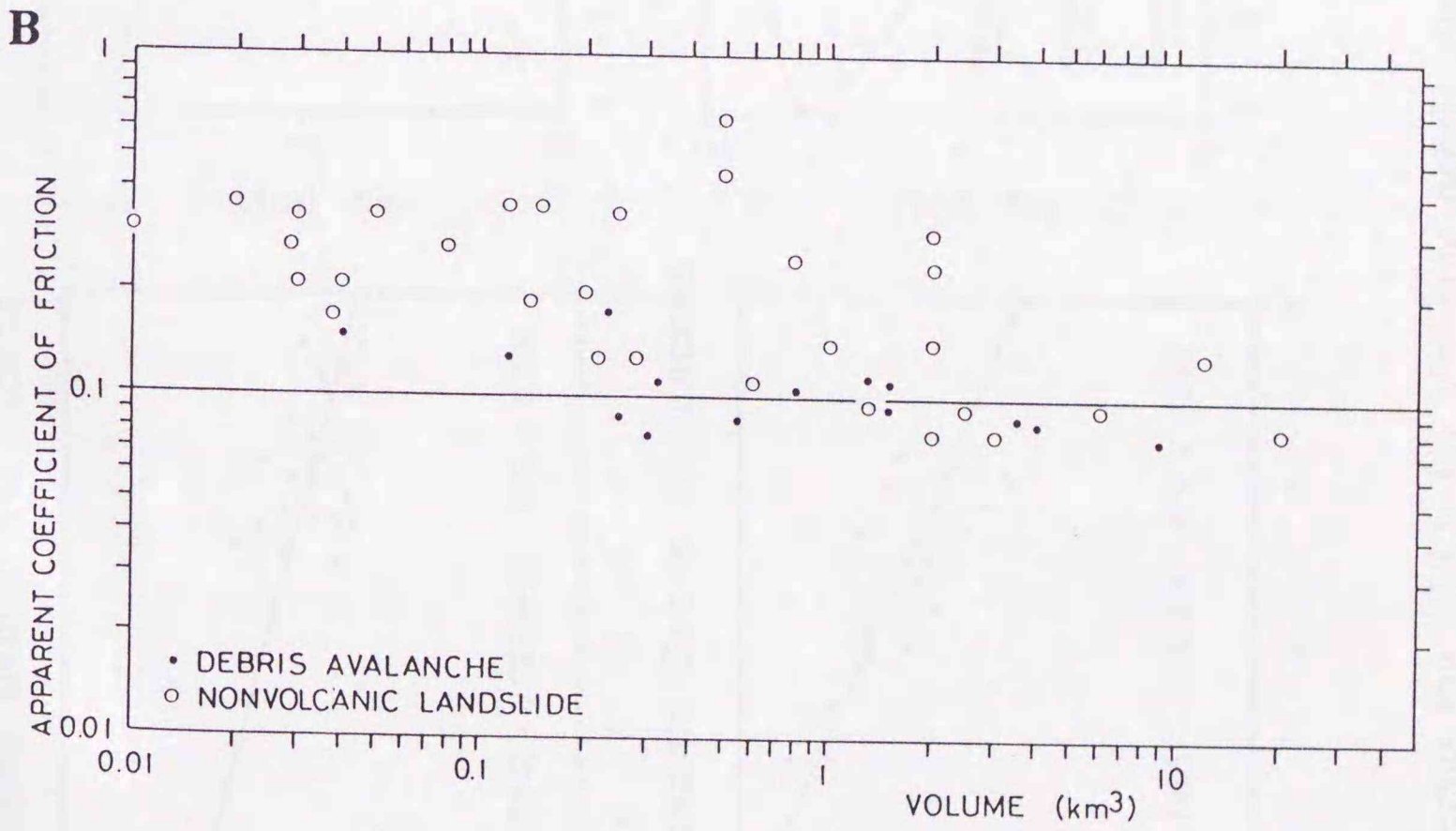

Fig. 2-9A-B. A. Relation between the maximum collapse height of debris avalanche and the maximum runout distance of Japanese debris avalanches (after Ui et al., 1986). Open circles are the data of landslide deposit of non volcanic area. **B.** Relation between the apparent coefficient of friction and the volume of the deposits (after Ui et al., 1986).

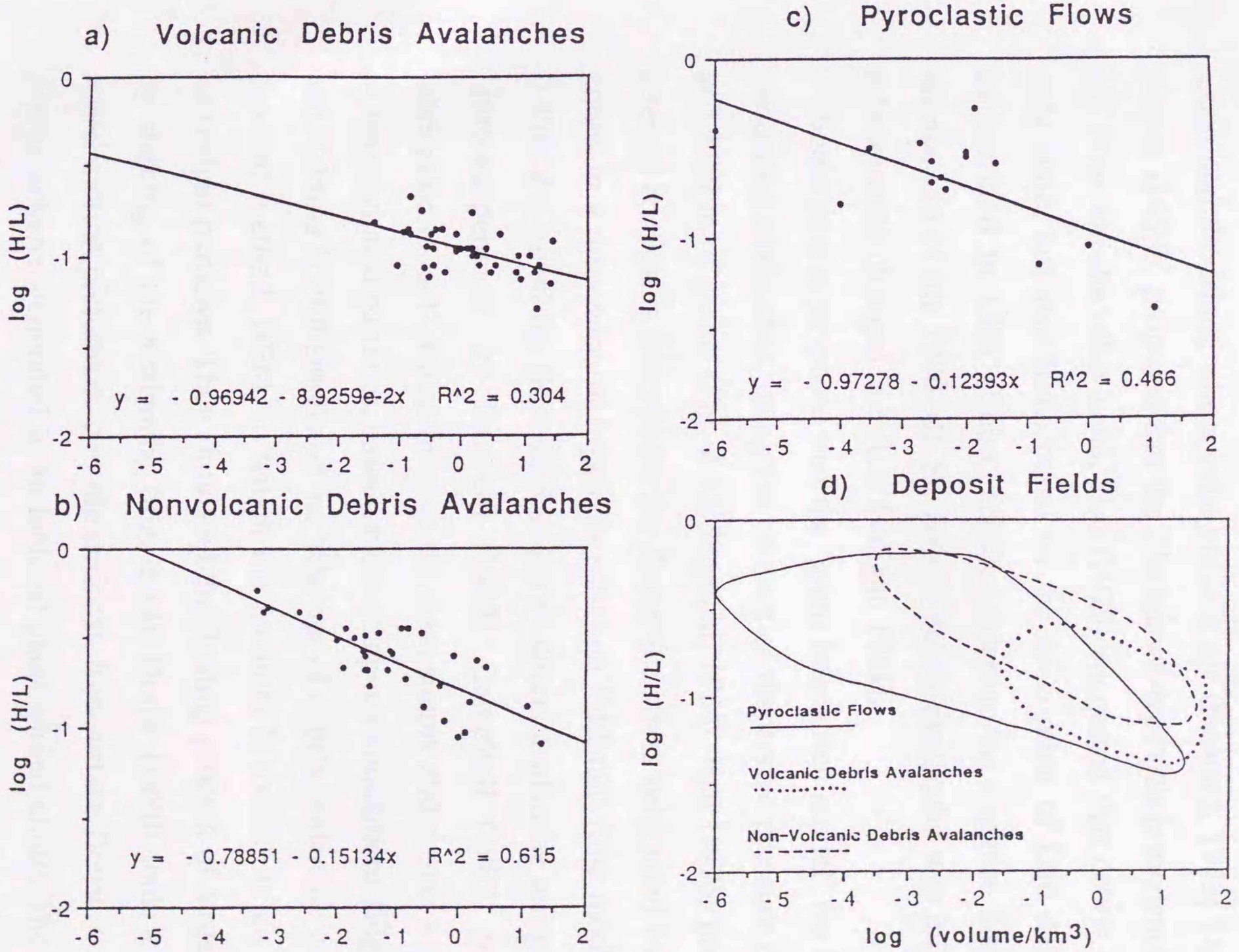

Fig. 2-10. Log (volume) versus log (H/L). (a) Volcanic debris avalanches. (b) Non volcanic debris avalanches. (c) Pyroclastic flows. (d) Deposit fields for all three type of deposits. The debris avalanches and the pyroclastic flows have indistinguishable H/L versus volume (after Hayashi and Self, 1992).

mechanism of lubrication. He proposed such 'an air-layer lubrication model' that the Blackhawk debris avalanche, in initial fall, overrided and trapped a cushion of compressed air upon which they slided at a high speed with little friction (Fig. 2-11). This model, however, cannot explain the debris avalanches on the moon and the Mars, where exist no/little air (Howard, 1973; Lucchitta, 1978). Shreve (1968b) proposed that the Blackhawk-type debris avalanche slide and do not flow. On the other hand, Hsü (1975) suggested that debris avalanches not only slide, but also flow, based on the description of Elm debris avalanche, Switzerland in 1881 (Heim, 1882). Observations suggest that emplacement mechanism of the 1980 Mt. St. Helens debris avalanche was initially slide, but subsequently changed into flow (Voight, 1981).

Some papers proposed that the 'grain interaction model' for the mobility of the debris avalanches, using the concept of dispersive pressure due to collision and friction of grains (Fig. 2-12; Bagnold, 1954). Hsü (1975) proposed that the internal friction is lowered by the dispersive stress originated from collision of grains in a dispersion of high concentration ('dilatant flow model'). Takahashi (1986) discussed the flow mechanism of debris avalanche using the concept of 'auto-suspension' by Bagnold (1962). Campbell (1989) proposed 'self-lubrication model', which most of the mass simply slides over a thin dilute layer of very agitated particles, based on the computer simulations (Fig. 2-13). Uchida and Hakuno (1990) simulated the behavior of debris avalanche using the distinct element method, DEM, in which the medium is treated as an aggregation of individual particles. They simulated the floating process of large rock produced by shaking of the avalanche (Fig. 2-14). Drake (1990) took a series of high-speed motion pictures of two-dimentional, free-surface flows of 6-mm diameter plastic spheres generated in an inclined glass-walled chute. The flows could be divided into a frictional region, in which contacts between neighboring particles are enduring and frictional, and an overlying collisional region, in which binary

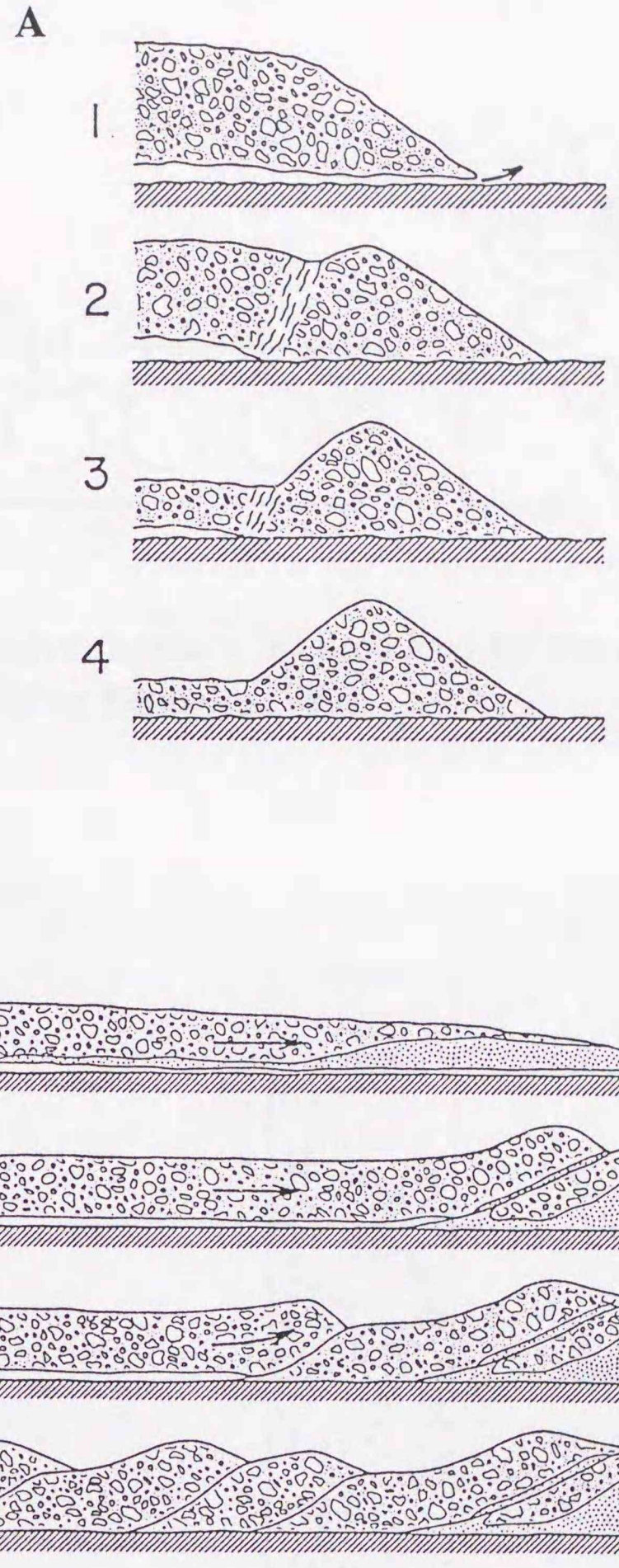

Fig. 2-11A-B. An air-layer lubrication model by Shreve (1968). **A.** Formation of lateral ridges. **B.** Termination of movement, showing formation of distal rim, transverse ridge, and imbricate structure.

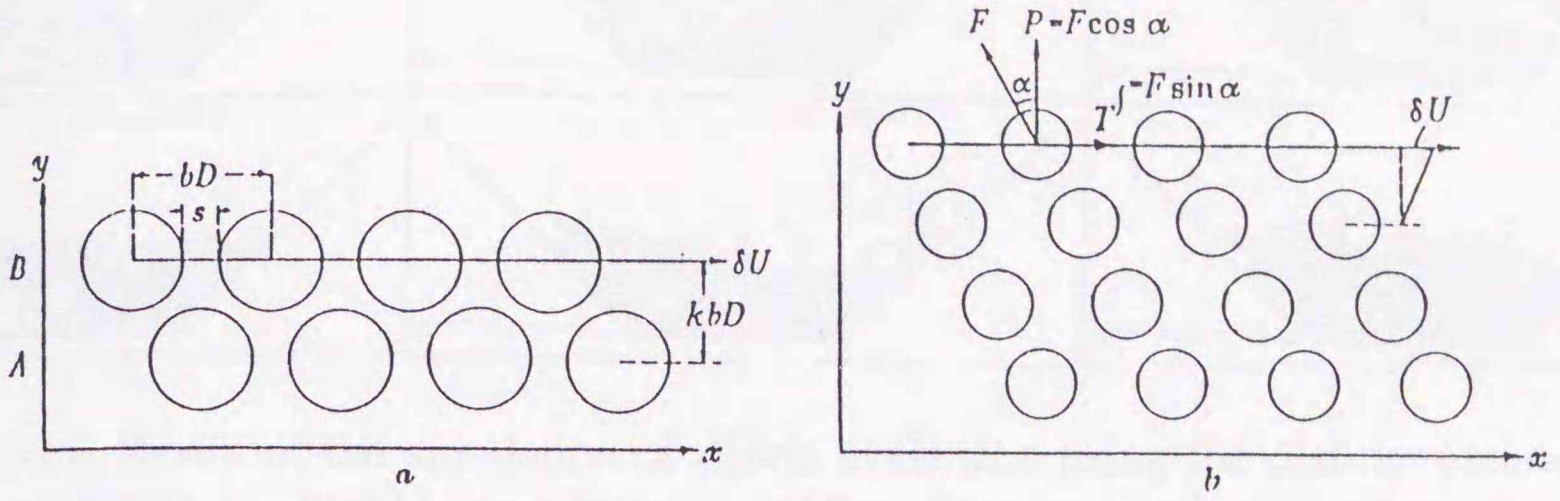

Fig. 2-12. Dispersive pressure, P, produced by the collision of grains within a shear stress field (after Bagnold, 1954).

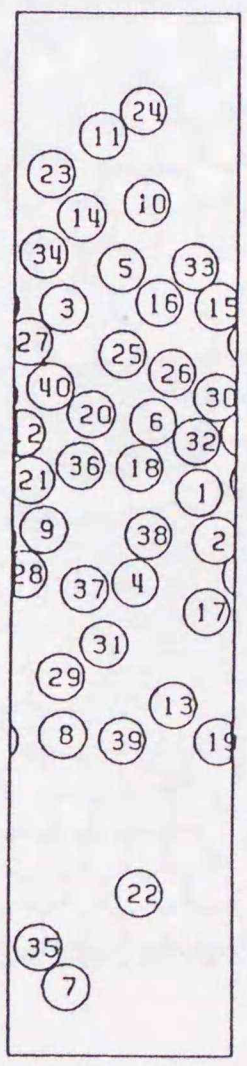

Fig. 2-13. A self-lubrication model proposed by Campbell (1989). The final stage of the 40° chute simulation showing that the bulk of material is riding as a relatively inactive layer supported by only three particles.

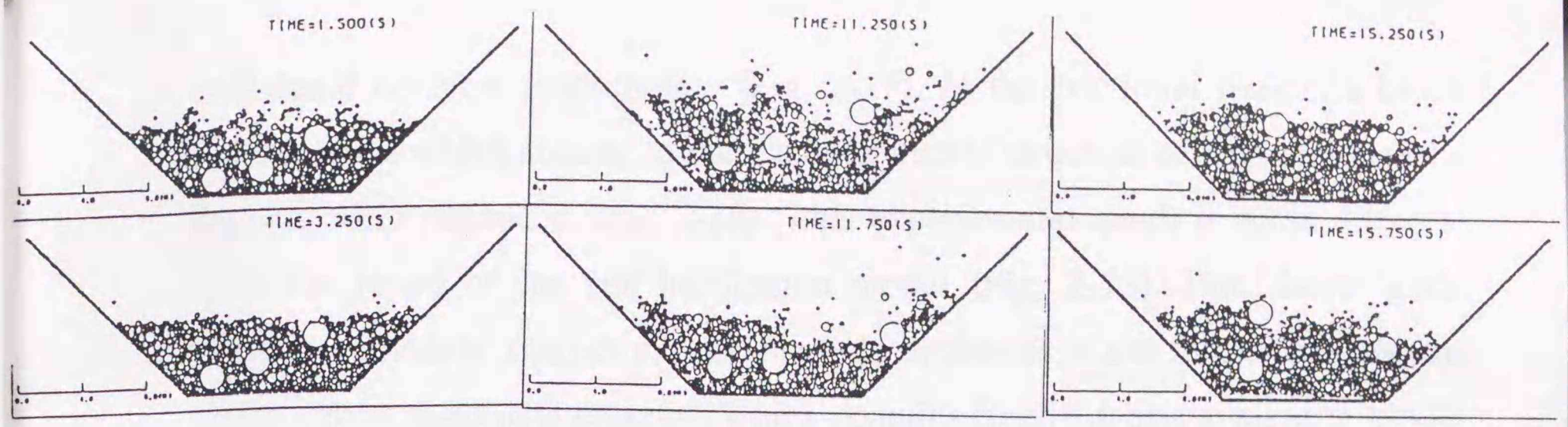

Fig. 2-14. Result of the simulation of debris avalanche using the distinct element method, DEM, by Uchida and Hakuno (1990). Floating processes of the large rocks due to shaking are observed.

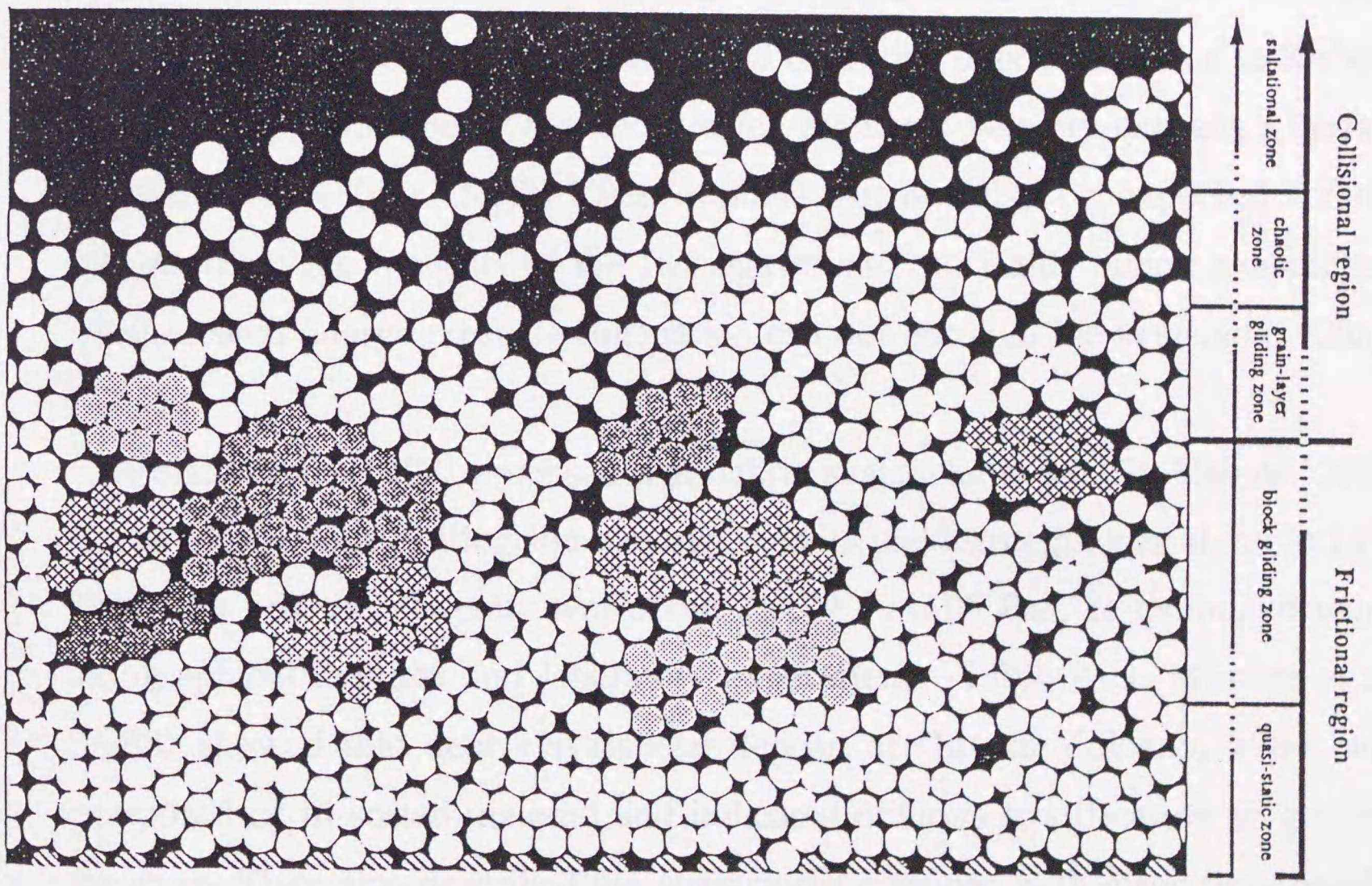

Fig. 2-15. Sketch of the high-speed motion particles of two-dimentional, free-surface flows of 6-mm diameter plastic spheres generated in an inclined glass-walled chute by Drake (1990). Flows can be divided into a frictional region in which contacts between neighboring particles are enduring and frictional and an overlying collisional region in which binary collisional contacts predominate.

collisional contacts predominate (Fig. 2-15). In the frictional region, a block gliding zone, which similar to the block in matrix structure of debris avalanche deposit, were produced (Fig. 2-15). This experimental result is quite different from the result of the self-lubrication model (Fig. 2-13). But, these 'grain interaction models' can not explain the field evidences of the Iwasegawa and the Kaida debris avalanche deposits, which contains fragile debris avalanche blocks (Chap. 5; Chap. 7-2).

Melosh (1979) proposed 'the acoustic fluidization model' that instead of the clasts individually colliding with one another, to stay in contact and move together as parts of elastic wave. Its movement only occurs when the pressure fluctuates and is much lower than the overburden pressure (Fig. 2-16). Kobayashi (1991) postulated 'the basal pressure wave model' that the basal pressure wave between the basal layer and overlying debris mass due to Kelvin-Helmholtz type instability can occur when the shear velocity exceeds a certain threshold value (Fig. 2-17). These models can not also be expected for the emplacement mechanisms of the Iwasegawa and the Kaida debris avalanches, because such a large pressure fluctuation can not occur in the avalanche (Chap. 7-2-1).

Voight et al. (1983) proposed that debris avalanche at Mt. St. Helens, 1980, can be idealized as 'a Bingham material' and its yield strength was about 2×10^3 - 2×10^4 Pa and the viscosity was about 1×10^4 - 7×10^5 Pas, as estimated using topographical features and laboratory experiments (Table 2-1). Mimura et al. (1988) showed that debris avalanche deposit at Ontake Volcano, 1984, was composed of ill-sorted material and indicated obvious stratification or grading structure. They also described the characteristic stripes with clear flow pattern on the surface, which may indicate the blocks rubbed on the basement. They proposed that the debris avalanche behaved as 'a plug flow' (Fig. 2-18; Johnson, 1970). The field evidences of the Iwasegawa and the Kaida debris avalanche

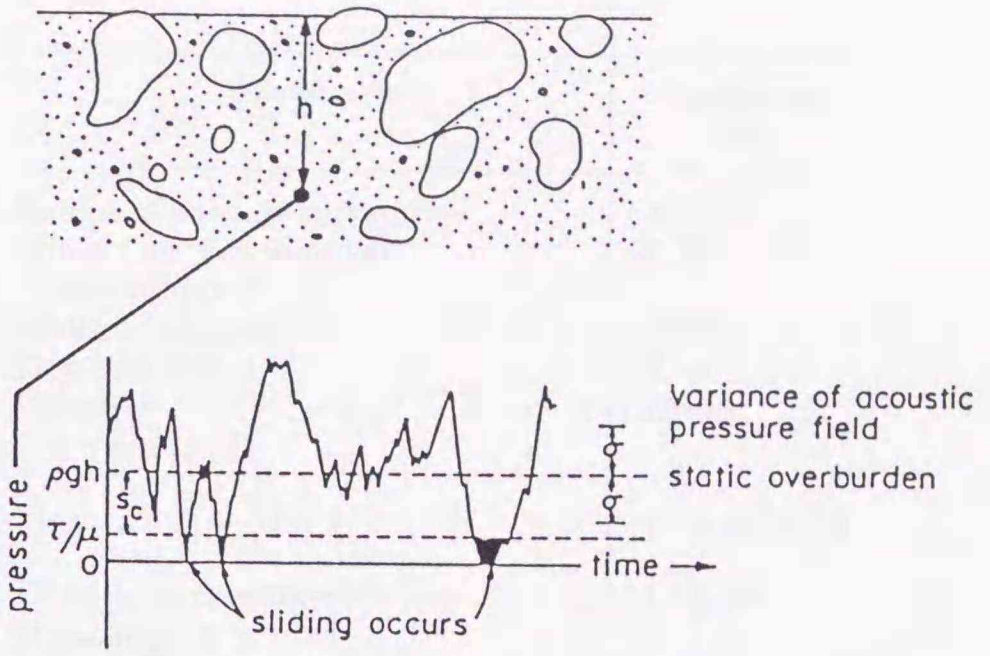

Fig. 2-16. An acoustic fluidization model by Melosh (1979). Schematic diagram of the pressure variations as a function of time at depth h in a mass of rock debris. The static overburden ϱgh about which the pressure fluctuates randomly with variance σ. Sliding occurs when the pressure falls to within τ/μ of zero. S_c is the pressure deviation from the mean when sliding occurs.

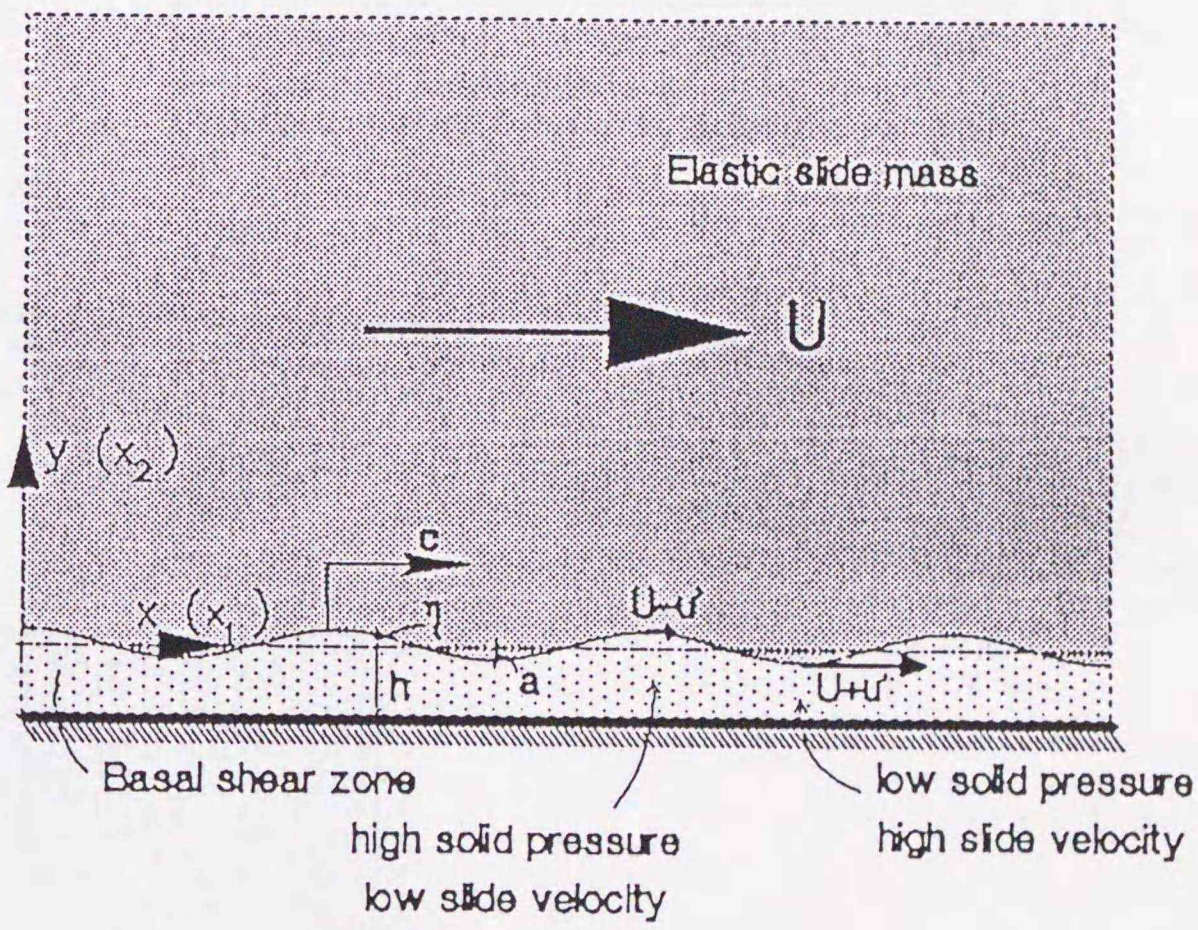

Fig. 2-17. A basal pressure wave model by Kobayashi (1991). Unstable wave can aroused in the basal zone of debris avalanche when the shear velocity exceeds a certain threshold.

Table 2-1. Estimated properties of the 1980 Mt. St. Helens debris avalanche by Voight et al. (1983).

Characteristic	Estimated value
Radius of channel curvature ψ	1270 m
Tilt of flow due to radial acceleration β	0·72°
Width of channel W	1100 m
Depth of flow d	73 m
Velocity† $\bar{v} = (\psi g \tan \beta)^{\frac{1}{2}}$	16 m/s
Flow rate $Q = \frac{\pi}{4} \bar{v} W d$	$1{\cdot}0 \times 10^6$ m^3/s
Density, mobile state γ^*	1·5 g/cm^3
Slope angle δ	1·8°
Critical thickness, mobile state $T_k^* = k/\gamma^* \sin \delta$	4–40 m
Shear strength‡	0·02 – 0·2 bar
Viscosity, Bingham $\eta_b = \frac{1}{v}\left[\frac{\gamma^*}{2} \sin \delta (d^2 - T_k^{*2}) - k(d - T_k^*)\right]$	1×10^5 P to 7×10^5 P
Viscosity, Newtonian $\eta_n = \frac{1}{v}\left[\frac{\gamma^*}{2} d^2 \sin \delta\right]$	$7{\cdot}9 \times 10^5$ P
Bingham number $B = k(d - T_k)/\eta_b \bar{v}$	0·1–3
Reynolds number $Re = \rho^* \bar{v} d/\eta$	22–44

† As a simplification, v is taken equal to $\bar{v}$. Specific weight assumed for mobilized state.
‡ Assumed value of k based on properties for distal end.

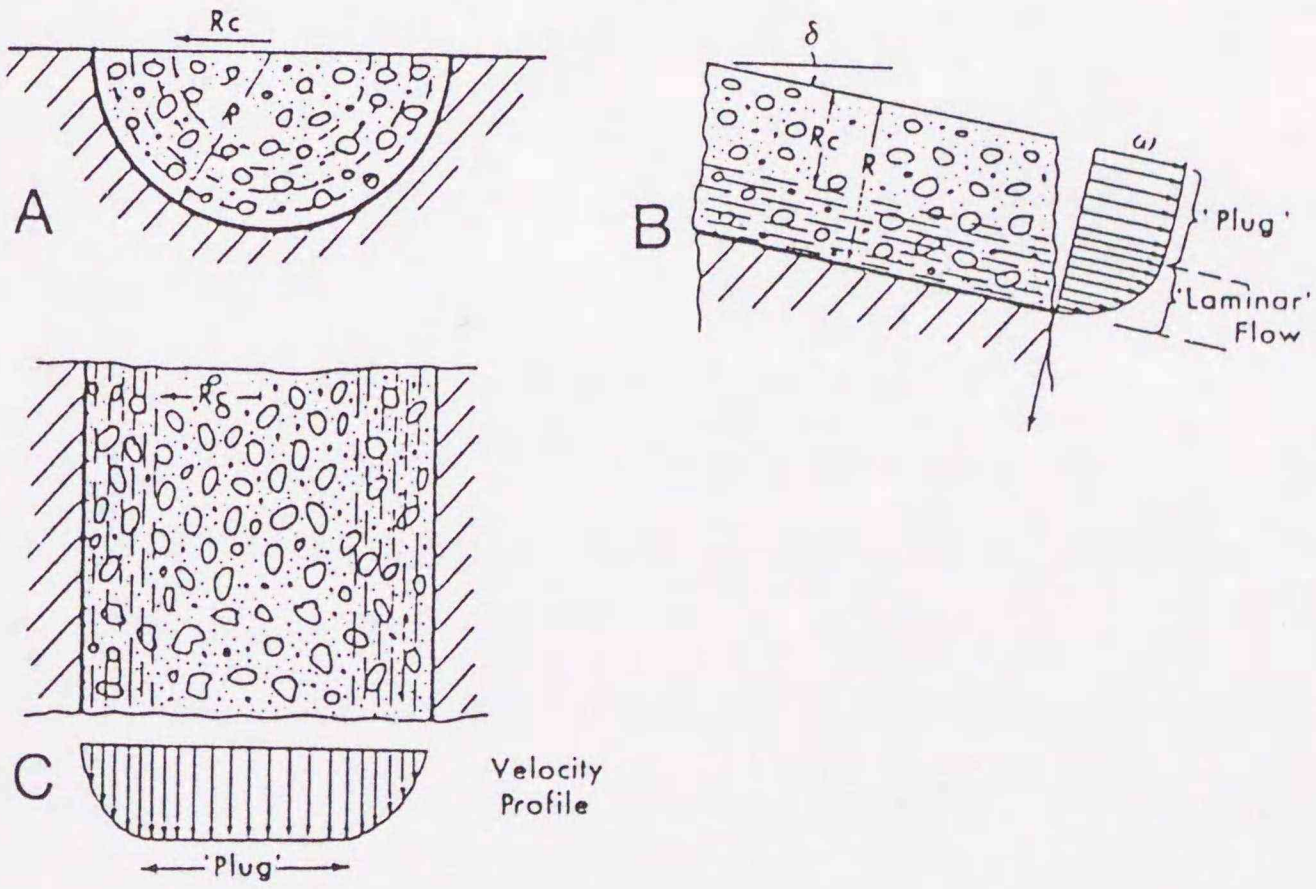

Fig. 2-18. Concept of the plug flow model (after Mimura et al., 1988).

deposits suggest that the plug flow model is suitable for the emplacement mechanism of them (Chap. 7-2).

2-2. Pyroclastic flow

2-2-1. Sedimentary structures

Many papers, describing the sedimentary structures of the pyroclastic flow deposits, have been published. Idealized pumiceous pyroclastic flow deposit (ignimbrite) is composed of layer 1, layer 2a, layer 2b, and layer 3, in ascending order (Fig. 2-19; Sparks et al., 1973; Sparks, 1976). The layer 2b, making up at least 90 percent of its bulk, is relatively homogeneous and poorly sorted, with micron-sized dust and blocks approaching 1 m in size. This layer shows reverse grading of large pumice clasts and normal grading of large lithic clasts (coarse-tail grading, in which clasts beneath a critical diameter are ungraded). The layer 2a, a few centimeter to > 1 m in thickness, is a reversely graded, fine grained basal layer. The layer 1 is the product of a pyroclastic surge (Sparks and Walker, 1973). This layer is seldom more than a few centimeter thick and shows rapid fluctuations in thickness. The layer 1 is well sorted, and often well stratified and contains low-angle cross-bedding. The layer 3 is a fine ash fall or ash cloud surge deposit, consisting largely of vitric material, and much poorer in crystals and lithic fragments than layer 2b. The layer 1 was previously thought that (1) derived directly from the source (ground surge; Fig. 2-28; Fisher, 1979); and (2) segregated from the highly-flidized turbulent head (layer 1 (H); Wilson and Walker, 1982) or jetted from the head (layer 1 (P); Wilson and Walker, 1982). Although the author proposes another origin in this thesis: formed by an ash-cloud surge which was detached from the basal avalanche at the bottom of the steep slope due to hydraulic jump and proceeded ahead of the tip of the basal avalanche (Chap. 7-3-2).

Wilson (1980, 1984) carried out the laboratory fluidization experiment using the pyroclastic flow deposits to explain the sedimentary structures of them (Fig. 2-20). Fluidization is the condition attained when a fluid is passed upwards

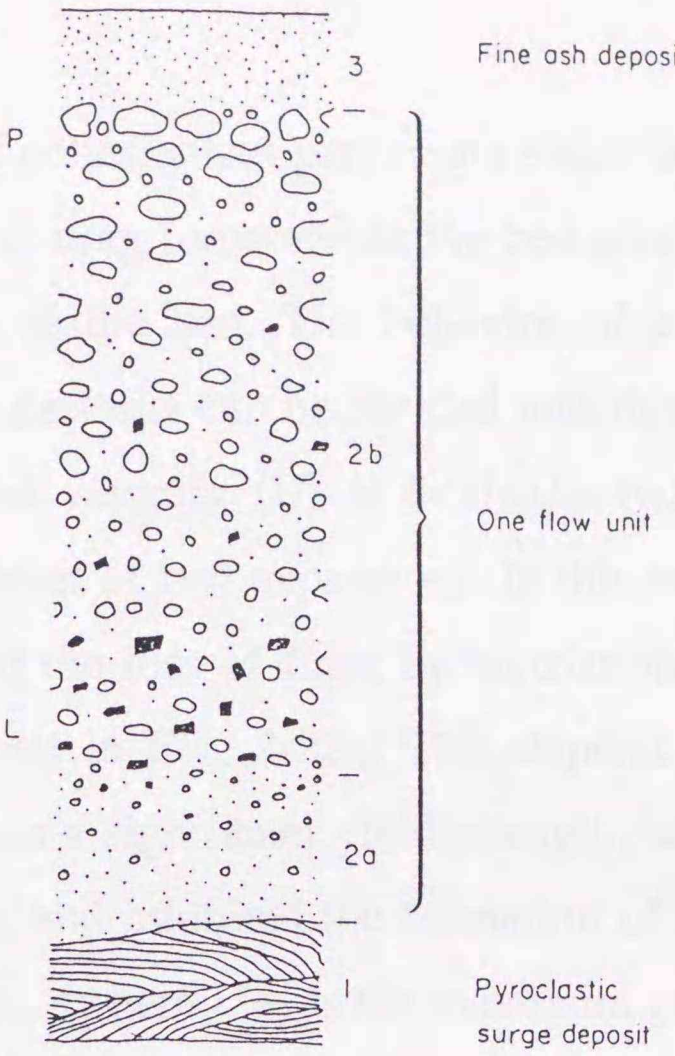

Fig. 2-19. Schematic section of an idealized pumiceous pyroclastic flow deposit (ignimbrite) by Sparks (1976). This figure shows the one flow unit with layer 2a and 2b, underlying pyroclastic surge deposit (layer 1), and fine ash fall/surge deposit (layer 3): P, pumice; L, lithic clast.

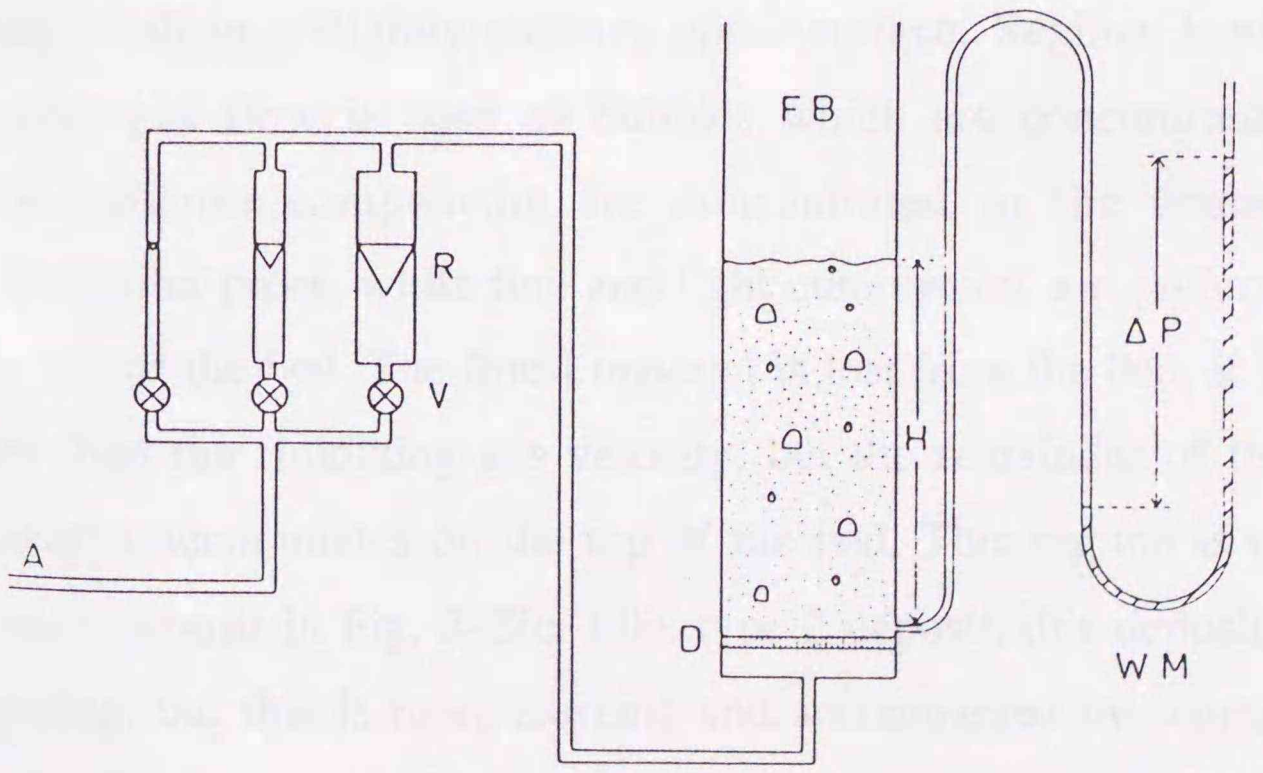

Fig. 2-20. Schematic diagram of the equipment of fluidization experiment by Wilson (1980). A high-pressure air supply (A) is regulated with valves (V), through rotameters (R) and the distributor (D) into the fluidized bed (FB). During runs, the height of the bed (H) is recorded, together with the pressure drop (ΔP) on a water manometer (WM).

through a bed of cohesionless particulate solids in which, at a certain superficial fluid velocity, the drag force across the bed exerted by the fluid is equal to the buoyant weight of the bed. The behavior of a poorly-sorted samples of the pyroclastic flow deposits can be divided into three regimes (Fig. 2-21). Regime 1: where the gas velocity (U) is $0<U<U_{ie}$ (where U_{ie} is defined as the gas velocity at the onset of bed expansion). In this regime, no expansion of the bed has occurred and the loss of fines by elutriation. This regime is correspond to the type 1 deposit in Fig. 2-22a. This deposit is characterized by a lack of expansion and has a significant yield strength, which prevented any gravitaion-induced grading, and inhibited the formation of a separate layer 2a. Regime 2: where $U_{ie} \leq U \leq U_{mp}$ (where U_{mp} is the maximum gas velocity that can be tolerated across the bed, before the channeling begins and segregation structures start to form). In this regime, the bed is partly fluidized and expanded to accommodate the gas flow, but bubbling (and elutriation of fines) are still absent. This regime is correspond to the type 2 deposit in Fig. 2-22b. The expansion allows the characteristic feature of coarse-tail grading to occur. This deposit commonly shows a well developed layer 2a. The post-emplacement deflation of the deposit may result in a slightly concave upper surface. Regime 3: where $U>U_{mp}$, the excess gas flow is seen as bubbles which are concentrated into channels. Coarse/dense components are concentrated in the channels to produce segregation pipes, while fine and light components are preferentially moved to the top of the bed. The finest material is lost from the bed, if its fall velocity is less than the fluidizing gas velocity, but the remainder of the fines and light material accumulates on the top of the bed. This regime is correspond to the type 3 deposit in Fig. 2-22c. Like type 2 deposit, this deposit show coarse-tail grading, but this is more extreme and accompanied by segregation structures. After these papers, many researchers believed that the fluidization is the main transport mechanism of pyroclastic flows. But, the author proposes that the

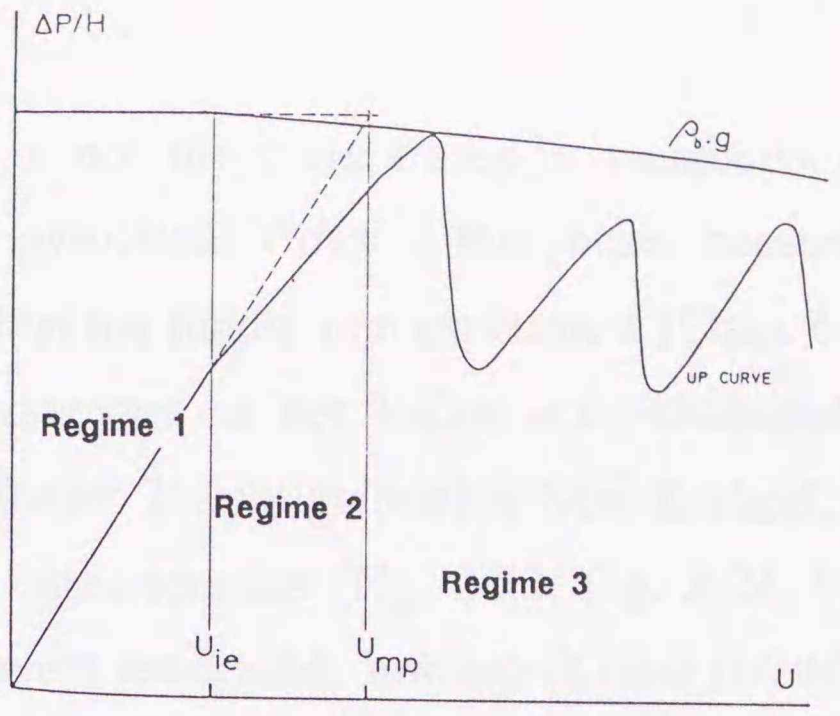

Fig. 2-21. Schematic fluidization plot to show the three regimes of fluidization behavior typical ignimbrite samples by Wilson (1984). U_{ie} is the gas velocity at which expansion of the bed is first observed, and U_{mp} is the gas velocity at the maximum pressure drop that can be tolerated across the bed. Note that U_{mp} is may sometimes be defined by extrapolation if significant expansion occurs. The curve marked $\varrho_b g$ is the bed bulk density times the gravitational acceleration and represents the effective buoyant weight of the bed. ΔP/H in turn measures the amount of support from gas drag. When the two are equal, full bed support is achieved.

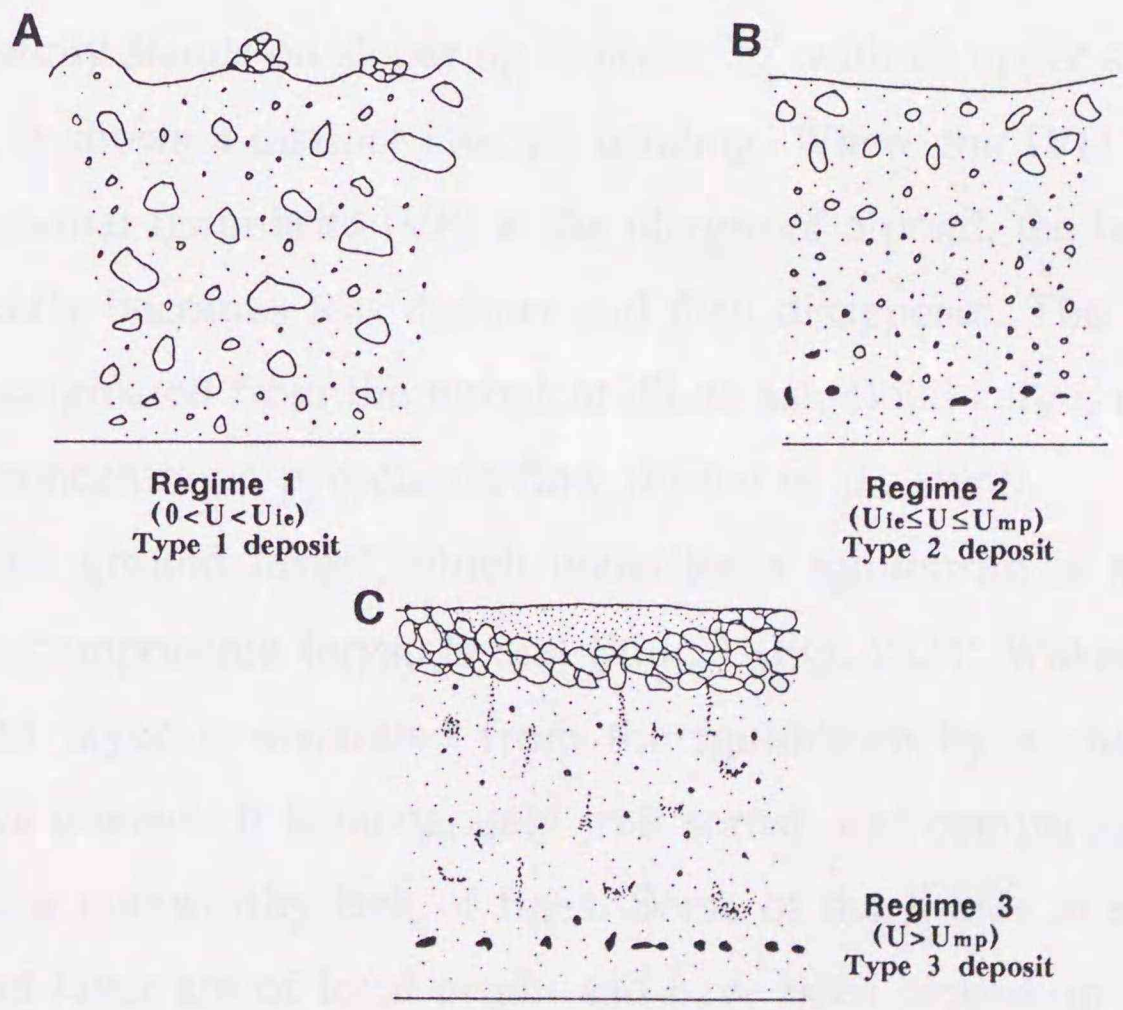

Fig. 2-22. The relationship between the three regimes of fluidization for poorly sorted materials and three proposed types of pyroclastic flow deposit by Wilson (1980). See text for details.

fluidization is not the main transport mechanism for the Unzen and the Komagatake pyroclastic flows in this thesis, because (1) large grains did not affected at all at the fluidization experiment (Chap. 6-1-5); and (2) grains larger than 1 cm in diameter can not fluidize at the measured velocities (Chap. 7-3-1).

The ca. 30 km^3 Taupo ignimbrite, New Zealand, dated ca. AD 186, shows conspicuous characteristics (Fig. 2-23; Fig. 2-24; Fig. 2-25; Fig. 2-26). This ignimbrite have a remarkably low aspect ratio (1:70,000; Walker et al., 1980a). The aspect ratio is that of average thickness to lateral spread such as the diameter of the circle which covers the same area as the rock body. The Taupo flow evidently surmounted and flowed over virtually the entire topography and recorded the fact by the landscape with a thin, but more or less continuous "ignimbrite veneer deposit (IVD)" (Fig. 2-23; Walker et al., 1981a; Walker, 1983). The IVD differs little in grain-size from the associated ignimbrite, but it shows a crude internal stratification. It locally contains laterally-discontinuous lenses of coarse pumice on the far-vent side of topographic obstacles ("lee-side lenses"). The beds in it show more rapid lateral variations in thickness. It commonly stands on slopes up to about 30° with its upper surface parallel to the base. It shows a distinct internal banding. Where the IVD thickens and passed into normal ignimbrite (VP) at the margin of a pond, the banding in the former gradually becomes less distinct and then disappears. The IVD, however, may have originated from the turbulent dilute ash-cloud surge, not from the laminar high-concentraion pyroclastic flow (Fisher et al., 1980).

"The ground layer" which underlies a ignimbrite is strongly enriched in dense components (crystals and lithics) (Fig. 2-24; Waker et al. 1981b). The ground layer is separated from the ignimbrite by a sharp and near-planer erosive contact. It is moderately well sorted, and compared with the ignimbrite shows a noteworthy lack of fines. Some of the lithics in some samples of the ground layer are of local origin and have been picked up from the underlying

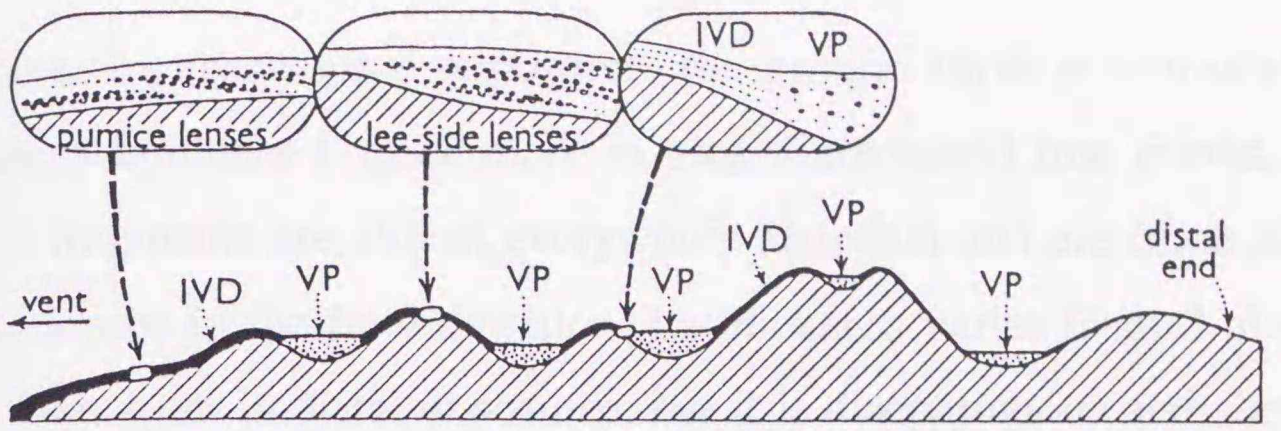

Fig. 2-23. Schematic section across the Taupo ignimbrite from vent (extreme left) to distal end, showing relationship between the ignimbrite veneer deposit (IVD) and the valley pond ignimbrite (VP) by Walker et al. (1981a).

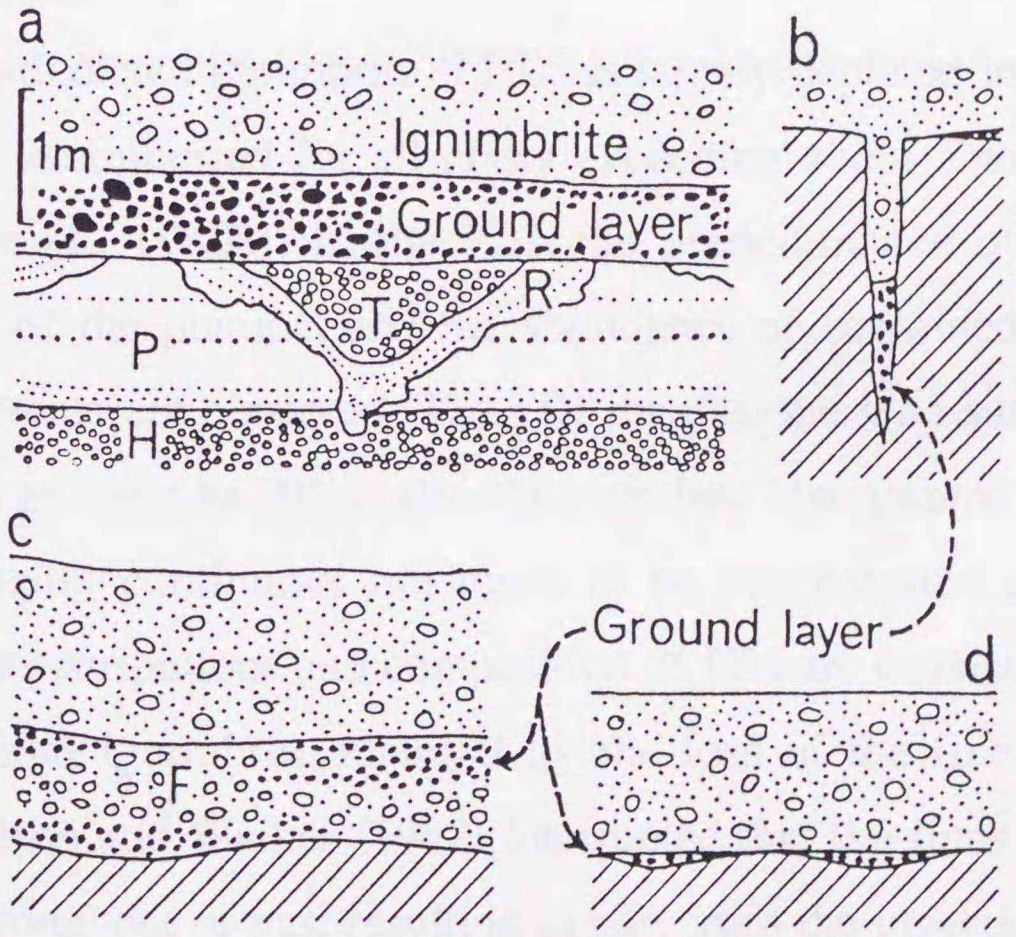

Fig. 2-24. Sketch sections showing typical relationships between the Taupo ignimbrite and its ground layer by Walker et al. (1981b). (a) Ground layer resting on a strongly discordant surface. (b) Fissure penetrating the soil to a depth of ca. 2 m and infilled with ground layer material and ignimbrite. (c) Ground layer interdigitating with fines-depleted and kindred ignimbrite material (F). H, P, R, and T are air-fall deposits of earlier phases of the same eruption.

surface. In near-source exposures, the ground layer is extremely coarse and contains boulders 1 m or more in size. Carbonized tree trunks, branches and wood fragments are almost everywhere abundant and are often aligned radially from source in the flow direction. Its thickness varies from 3 m near source to less than 1 cm in distal exposures, but it is discontinuous and shows rapid local thickness variations. Walker et al. (1981b) proposed that heavies are to settle relatively rapidly in the head as they do in a strongly fluidized experimental fluidized bed, and they accumulated as a ground layer. The ground layer, however, may have formed by change of hydraulic condition of the pyroclastic flow, such as hydraulic jump due to sudden change of slope angle (ex. at the bottom of the steep slope; at the lee side of the mound), not by the segregation from the highly-fluidized turbulent head, because ingestion of air from the flow head to maintain the fluidization can not be expected at the high-density flow (Chap. 7-3-1).

"Fines-depleted ignimbrite (FDI)" is largely depleted in the finer constituents and is clast-supported for all clasts exceeding about 2 mm in size (Fig. 2-25; Walker et al., 1980b). In the FDI, the predominance of pumice, the distinct rounding of the pumice, and the abundance of contained carbonized logs and tree fragments are observed. The FDI mantles the land surface and locally rests on slopes as steep as 30°; it also thickens into topographic depressions. The FDI is not areally continuous but tends to be concentrated in local pockets. The grain-size distributions and composition of FDI are consistent with its derivation from normal ignimbrite material by the loss of the fine constituents (Fig. 2-25b). Wilson and Walker (1982) interpreted that the fines loss was attributed to a high throughput of gas, resulting in part from the ingestion of vegetations, and in part from the effects of ground-surface roughness on an exceptionally fast-moving pyroclastic flow. Although the author proposes that the fines-depletion of the FDI was attributed mainly to the gas from the carbonized vegetation, not

to the high throughput of gas which ingested from the flow head, because ingestion of air from the head can not be expected at the high-density currents (Chap. 7-3-1).

Wilson and Walker (1982) and Wilson (1985) described the two distinct layers at the bottom of the Taupo ignimbrite (Fig. 2-26). The layer 1 (P) is a pumiceous, mildly to strongly fines-depleted unit, and the overlying layer 1 (H) is a thinner, crystal- and lithic-rich, fines-depleted unit. The layer 1 (P) forms the lowest deposit of the ignimbrite. It varies greatly in thickness from a few centimeters up to more than 8 m, and thicken in topographic depressions. It is dominantly pumiceous, commonly containing a fines-grained matrix rich in flidization segregation bodies. Fragments of carbonized vegetation, ranging from leaf fragment to logs, are widely dispersed. Often its fines content decrease upwards, at one extreme forming the FDI. The layer 1 (P) is separated from layer 1 (H) by an erosive contact which may be sharp or sheared. The layer 1 (H) overlies the layer 1 (P). It is thinner but more continuous than the latter. Apart from near-vent location, it is extremely poor in fines and rich in crystals and lithics. Its upper and lower contacts are erosive. It is interpreted that the layer 1 (P) is generated by the expulsion of material from the flow front, and termed the jetted deposits, and the layer 1 (H) is generated by the sedimentation of coarse/dense constituents segregated out by strong fluidization within the flow head and termed the ground layer. But, the layer 1 (P) may correspond to the section of the previous lobe which fines were highly depleted due to the gas from the many carbonized wood fragments during the flowage and after the deposition, based on the observation of the Komagatake 1929 pyroclastic flow deposits, which show similar texture to the layer 1 (P).

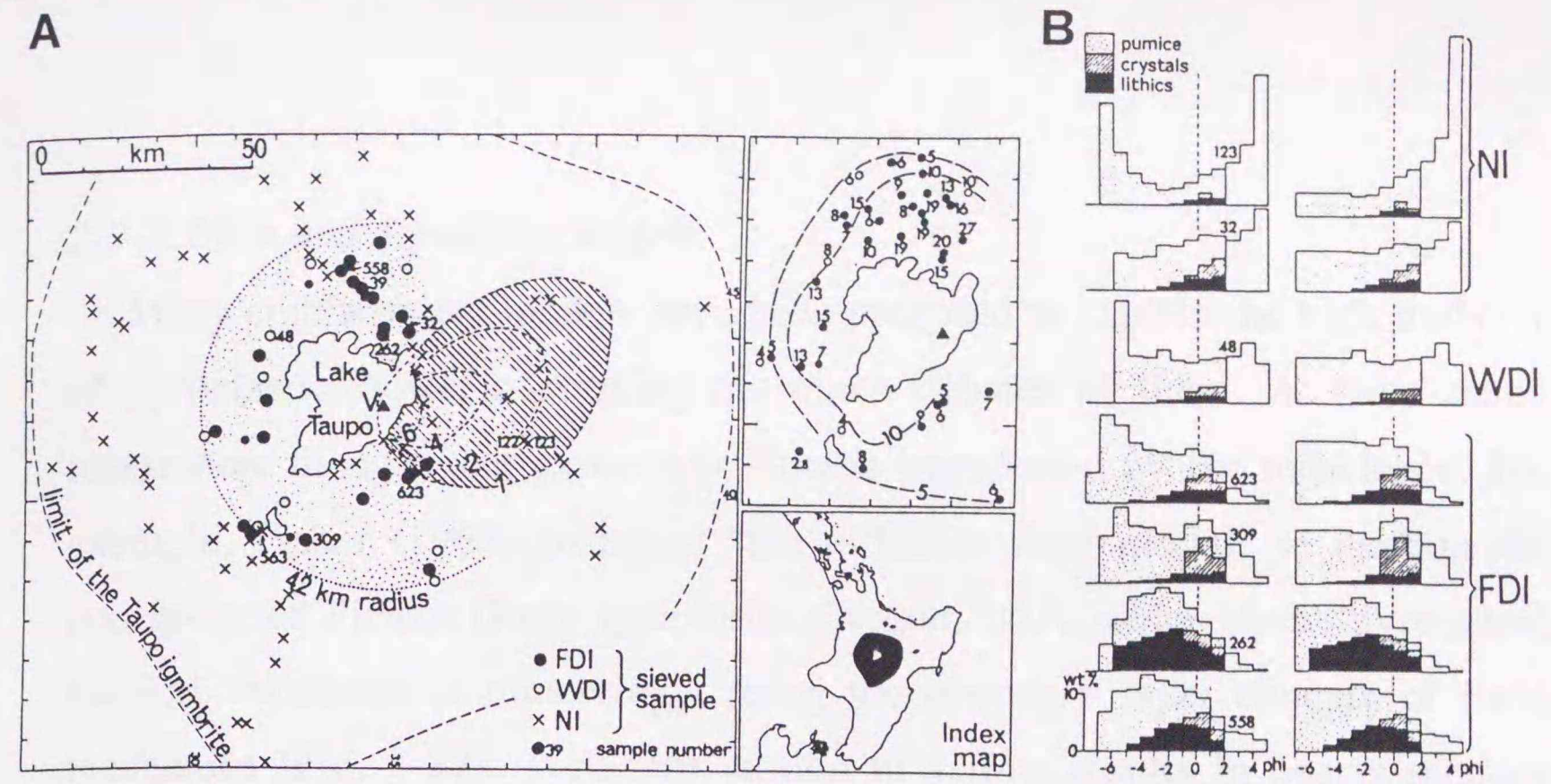

Fig. 2-25A-B. A. Distribution of fines-depleted ignimbrite (FDI; stippled area) within the Taupo ignimbrite by Walker et al. (1980b). WDI, weakly-depleted ignimbrite; NI, normal ignimbrite; V, vent. Ruled area is where the fall deposit immediately predating the ignimbrite exceed 1 m thick; isopachs give the thickness in meters. (Top right) Map on same scale showing average maximum diameter of the three largest lithic fragments in a sample of FDI. **B.** Grain-size histograms of typical examples of the three types of ignimbrite. Grain-classes down to 0.25 mm are subdivided on their weight proportions of pumice, free crystals, and lithic fragments. Left, raw data; right, normalized data.

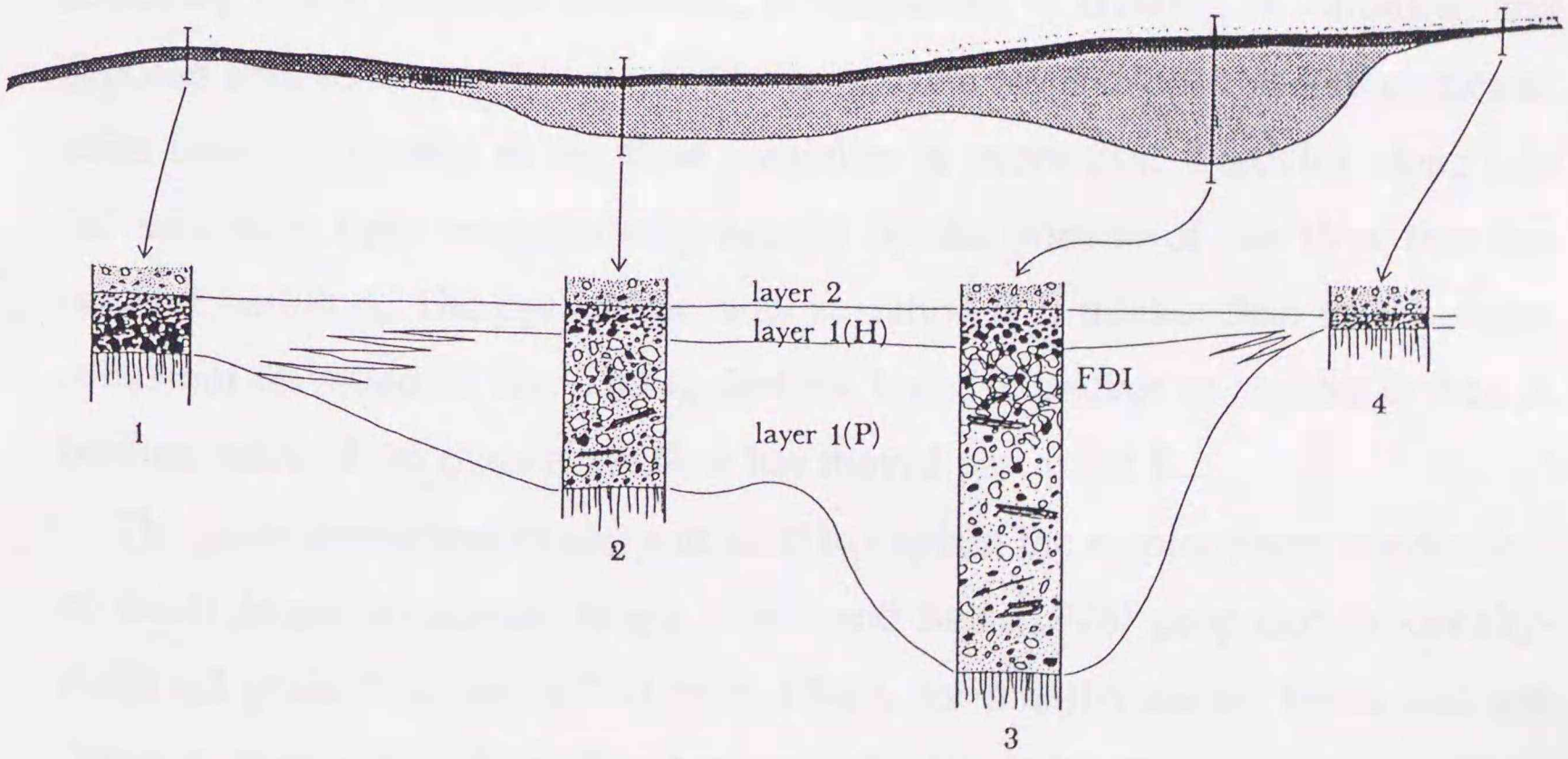

Fig. 2-26. Schematic cross section showing field relationships of layer 1 (P): jetted deposit, and layer 1 (H): ground layer, by Wilson (1985). The upper section illustrates the relatively thickness and lateral continuity of the layers. The lower sections show; 1, typical lithic-rich, normally graded layer 1 (H); 2, layer 1 (P) overlain by layer 1 (H); 3, thicker, near-vent layer 1 (P) in which the fines content decreases upwards to give FDI; 4, thin, fine-grained layer 1(H) forming the entire thickness of layer 1.

2-2-2. Flow and deposition models

Many emplacement models have been proposed to explain the high mobility of pyroclastic flows, continuing the much debates of them. At first, many researchers thought that pyroclastic flow is transported by the turbulence. For example, Fisher (1966) proposed "the turbulent flow model" to explain the poorly-sorted Picture Gorge ignimbrite, Oregon, USA, which shows systematic vertical variations in mineralogy, using the boundary layer concept of fluid mechanics (Fig. 2-27). Turbulent motion in a flow results in nearly random movement for a given suspended particle depending upon (1) the velocity, energy, and directions of current eddies, (2) the settling velocity of the particles, (3) the energy of possible gases escaping from the particles, and (4) the interference of other particles. Deposition of fragments from a rapidly moving turbulent pyroclastic flow may be nearly continuous from near its point of origin to the farthest point reached by the flow (Fig. 2-27). The chance for deposition of a small lightweight particle is nearly as great as for a large and relatively heavy particles; therefore, development of layering is inhibited, and deposits tend to be poorly sorted. The ignimbrite layer deposit at any particular point becomes thicker as the flow continues to move past. Particles along line "a" will have been progressively deposit by the portion of the flow that has reached station A. The pyroclastic flow at station B is thicker than at A because it has not travelled as far. The ignimbrite layer is thicker at station B than A because more of the pyroclastic flow has moved past point B.

The grain interaction model was used to explain the emplacement mechanism of small dense pyroclastic flows. Nairn and Self (1978) proposed "a density-modified grain flow model" (Lowe, 1976), for small-volume, block and ash flows at Ngauruhoe, New Zealand on Feb. 19, 1975. The erosion of chute, relatively slow speeds, short runout distances, deposition of some debris half-way down chutes, and the presence of surface levees and channels all indicate

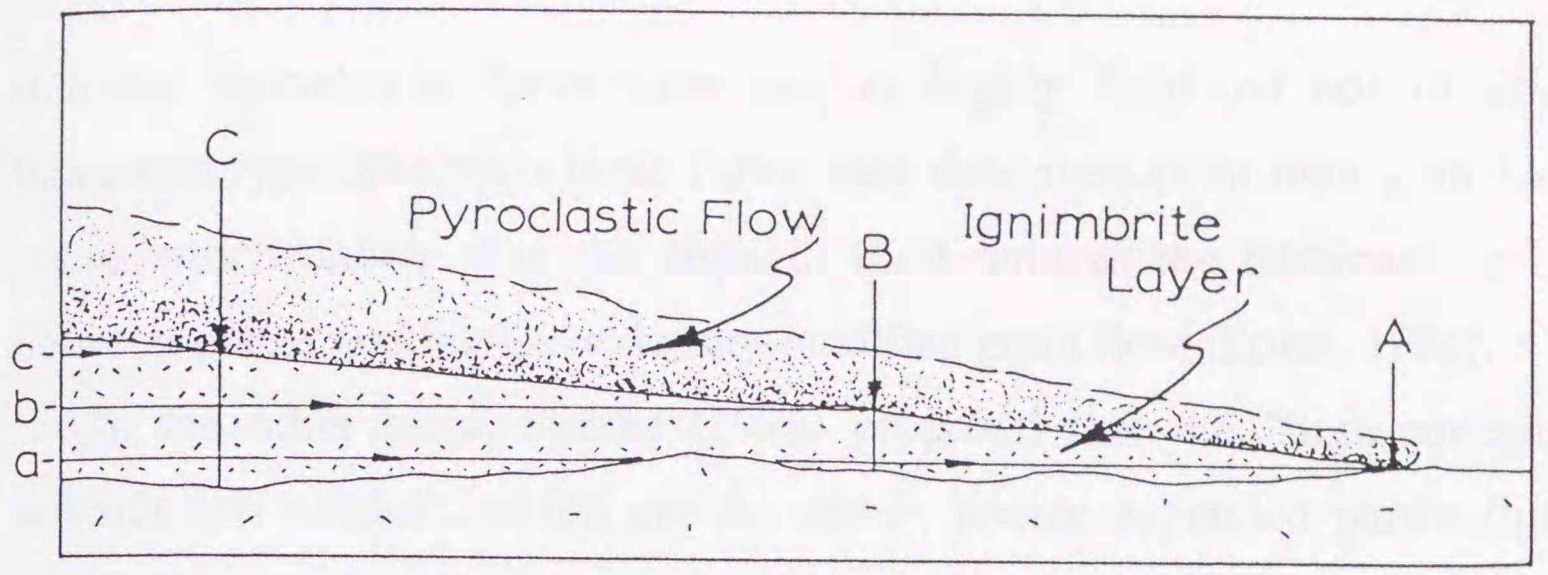

Fig. 2-27. Diagrammatic illustration of a moving turbulent pyroclastic flow and its gradually thickening ignimbrite deposit by Fisher (1966). Particles along line "a" were deposited from the portion of the flow that has reached station A. Particles along line "b" were deposited from the portion of the flow that has reached station B and so on through innumerable theoretical lines parallel to the base of the deposit deposited by innumerable theoretical turbulent "fronts" that follow the leading edge of the pyroclastic flow.

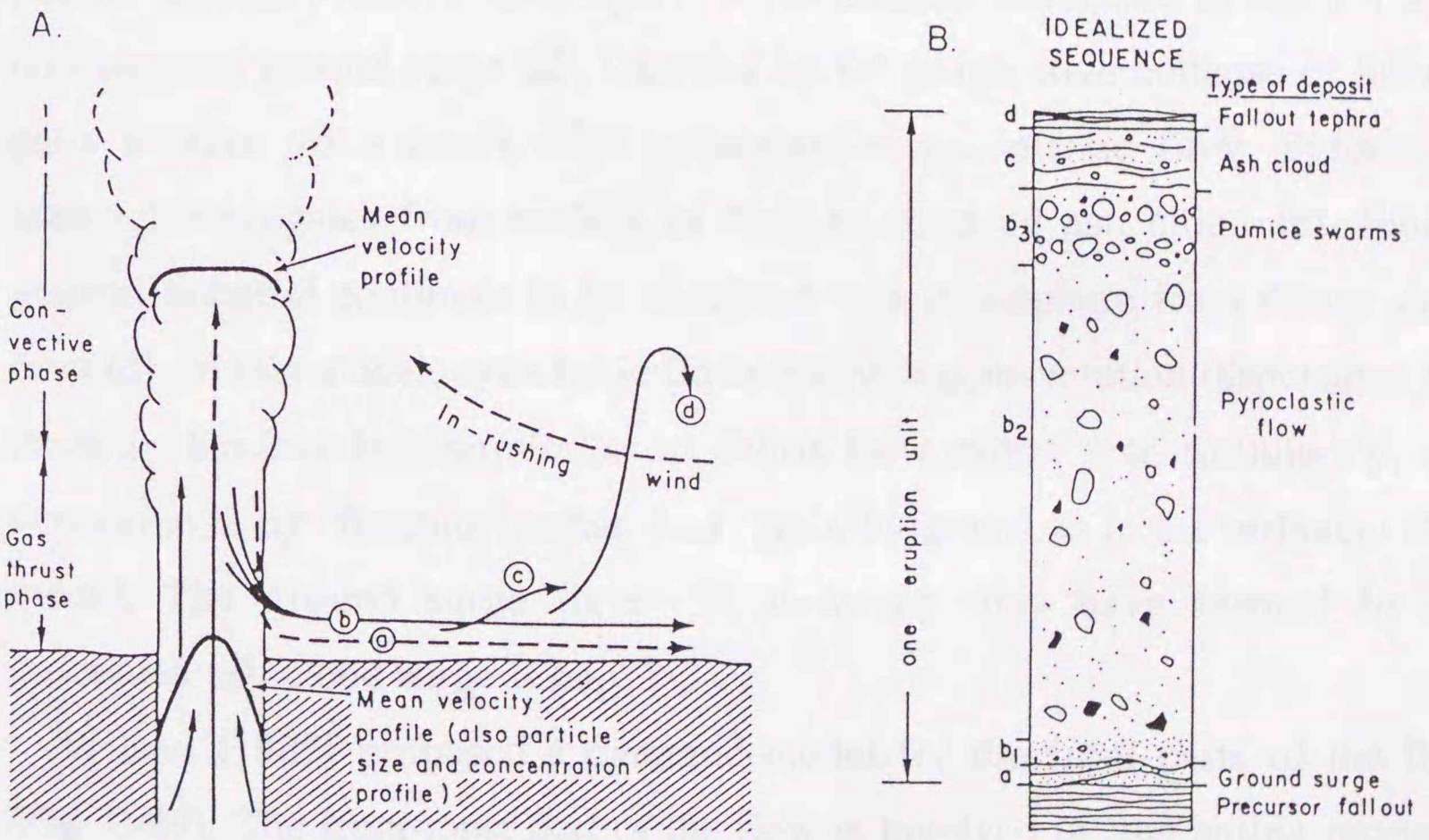

Fig. 2-28A-B. Eruption column collapse related to idealized eruption unit (**B**). Letters a-d in (**A**) correspond to those in (**B**). See text for details.

that the pyroclastic flows were neither highly fluidized nor of air-layer lubricated type. The pyroclastic flows were described as an inter-granular fluid phase which denser than the ambient fluid reduces the frictional resistance between grains and implies a density-modified grain flow (Lowe, 1976).

On the other hand, Sparks (1976) proposed that the "high-concentrated laminar low model", which are the dense, poorly expanded partly fluidized flows. The poor sorting in pyroclastic flow deposit is attributed to high particle concentrations not turbulence. Fisher (1979) proposed the formation processes of the sedimentary structures of the pyroclastic flows, using this high-concentrated laminar flow model (Fig. 2-28). If an eruption column is heavier than air and does not become turbulently mixed with it, collapse occurs (Fig. 2-28; Sparks and Wilson, 1976). In volcanic pipe and in the lower part of vertical eruption column, the large fragments migrates toward the center of the conduit, due to boundary effect. Outer part of the column collapsed to form a low-concentrated ground surge (a); followed by (b) progressive collapse of interior parts to give voluminous, high-concentration pyroclastic flow. Pyroclastic material segregates from surface of flow to form an ash cloud (c). Finest-grained material continues to be elutriated into atmosphere from dilute phase flow (d). In this model, pyroclastic flows are high-concentration dispersions that move in laminar fashion similar to debris flow rather than turbulently, and deposition is by "freezing" rather than "grain-by-grain" as in the turbulent flow model. The ground surge (layer 1), however, may have formed by the proceeded ash-cloud surge (Chap. 7-3-2).

Wilson (1985) proposed a dynamic model for the front parts of the flow (Fig. 2-29). The front-most part of the flow is involved in 'the jetting process', and a larger proportion of the flow is strongly fluidized by heated, ingested air. In this fluidization zone, coarse/dense constituents segregate out and sediment to generate 'the ground layer', while fine/light material is carried upwards, by the

gas flow or buoyancy effects, or both, and rearwards, by air friction or by moving down the slope at the rear of the flow front. The finest fractions are preferentially elutriated into the dilute cloud, but the remaining material accumulates as a coarse-pumice-enriched top plus segregation layer above the flow. Although ingestion of air from the flow front, as proposed by Allen (1971) and Simpson (1987, p.149), was only observed at the dilute currents, which had low density difference between the current and the ambient medium, such as a saline-water current in pure water. In experiment, ingestion of air from the flow front did not observed at the dense current due to the high flow resistance at the flow front (Huppert et al., 1986). Therefore, ingestion of air from the flow front can not be expected at the high density flow, such as the pyroclastic flow, due to the great density difference between the flow and the air. Thus, the model, which was proposed by Wilson (1985), forming the jetted deposit and the ground layer from the highly fluidized turbulent head due to the ingestion of air from the flow front, can not be expected at the pyroclastic flows.

Freundt and Schminke (1985) showed the erosion mechanism and formation processes of ground layer at the flow head of the Laacher See pyroclastic flow, Germany, using "the recycling mechanism" and the results of the flume experiment (Fig. 2-30). The head was inevitably divided into a shifting pattern of lobes separated by clefts and tunnels due to bottom roughness (Allen, 1971; Simpson, 1987, p.141-159). While effective segregation took place above tunnels and formed lapilli-rich ground layer (LaGL), the segregated lapilli may have become partially remixed with unaltered material of lobes. Erosion take place near the very front of the head under most turbulent conditions. Eroded tephra was mixed with the genuine material of the flow inside the head, segregation occurred and large/heavy components were deposited further back from the tip of the head. The greatest volume of tephra was carried up towards the back of

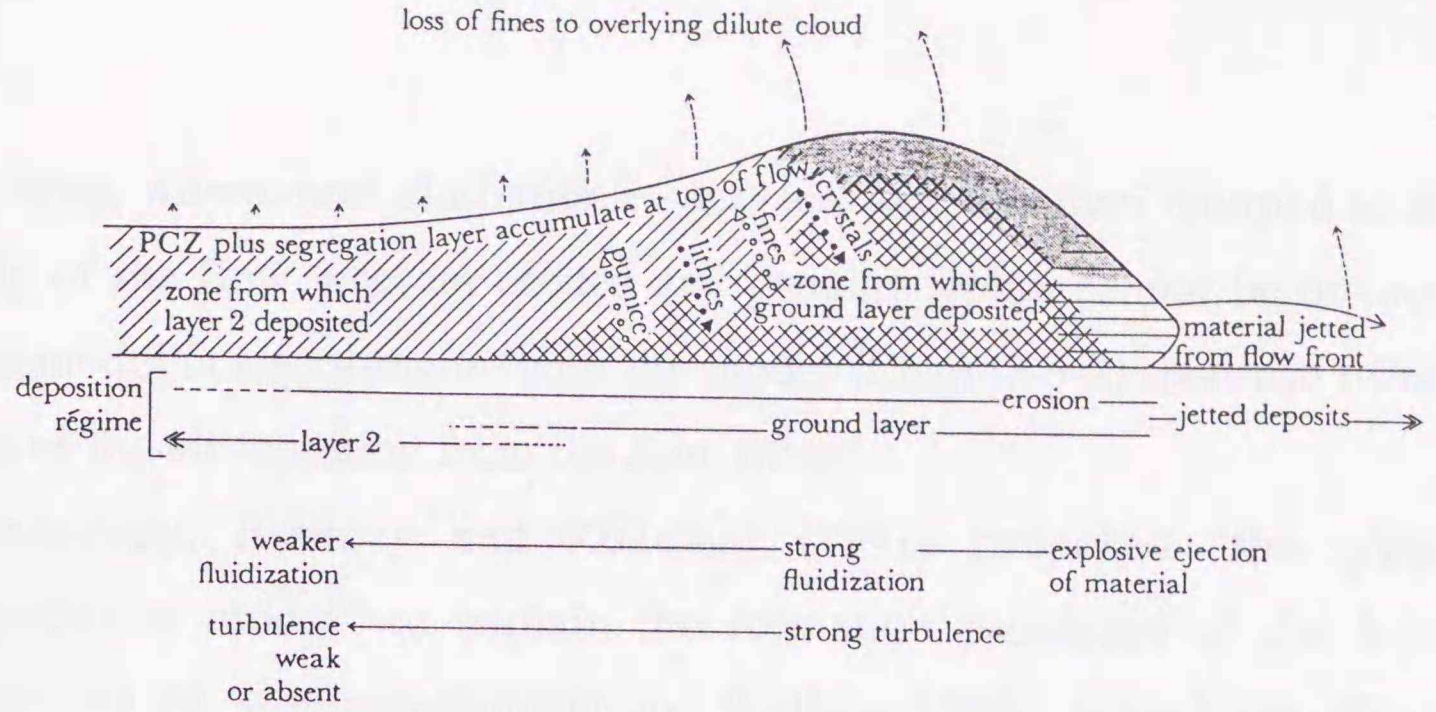

Fig. 2-29. Schematic diagram illustration the processes inferred to have operated at the flow front of the Taupo pyroclastic flow by Wilson (1985). The zones involved in jetting (horizontal hatching), segregation and sedimentation to generate the ground layer (cross hatching), and the generation of layer 2 (diagonal hatching) are indicated. The stippled zone at the top of the flow represents the area where mixing and air drag would have been most strongly developed. The dotted arrows within the flow represent the overall transfer of fine/light components upwards and rearwards and of coarse/dense components downwards. The dashed arrows above the flow represent very fine material elutriated from the flow, which mixes with the atmosphere, rises to form a dilute ash cloud and its eventually deposited as a layer 3 co-ignimbrite ash. The various depositional, fluidization and flow regimes are indicated below the diagram.

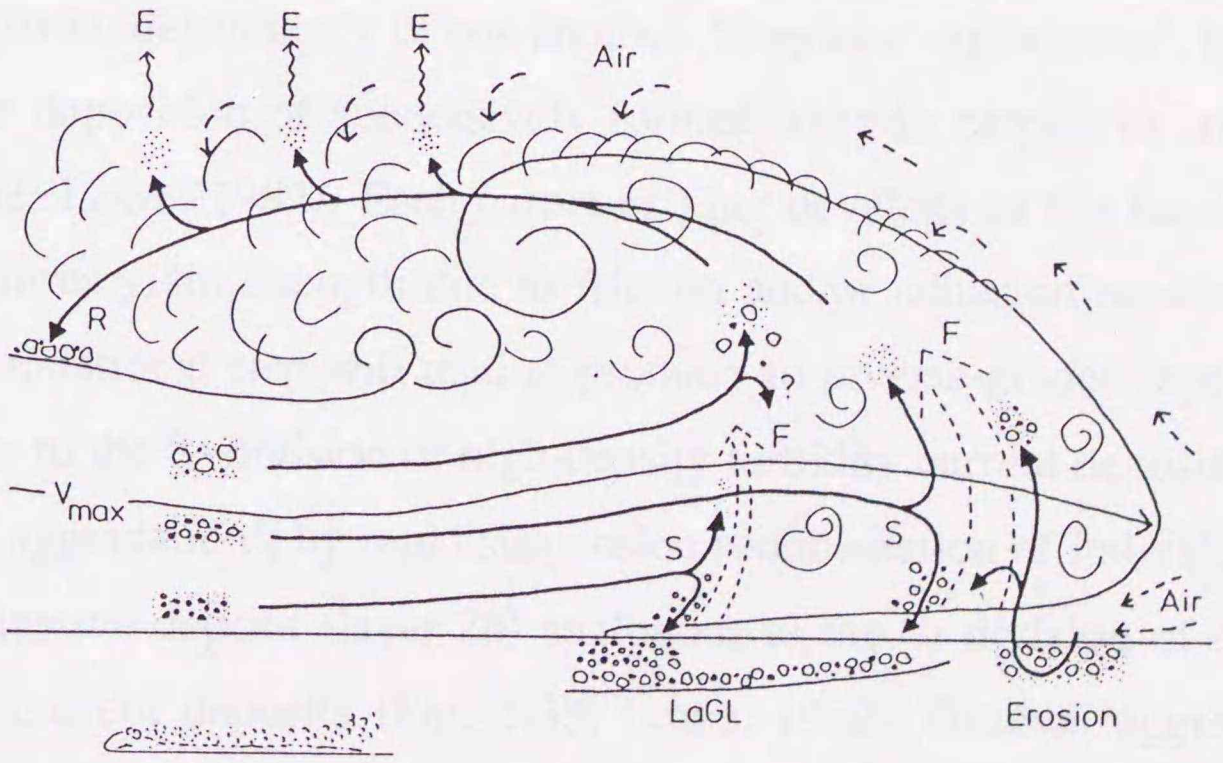

Fig. 2-30. Cartoon of erosion, fluidization (F), segregation (S), elutriation (E), and recycling (R) of material in the head of the Laacher See pyroclastic flow by Freundt and Schminke (1985). V_{max}=streamline of maximum velocity. See text for details.

the head, where most elutriation took place, and was then returned to the main body of the flow wherein eroded and genuine tephra cannot be distinguished. This model is also disagree with my model (Chap. 7-3-2), because of using the idea of the air ingestion from the flow front.

Recently, Branney and Kokelaar (1992) proposed "the progressive aggradation model" to explain the formation processes of the high-grade (=amount of welding-compaction; Walker, 1983) ignimbrite (Fig. 2-31). Massive beds in ignimbrites, and apparently stacked flow units, can be formed by continuous incremental deposition (progressive aggradation); this is in contrast to en masse deposition of high-concentrated, laminar-fashion pyroclastic flow. In this model, the lower part of depositional regime undergoes laminar flow and that material is supplied to it from an overriding, relatively turbulent part of the flow (the transport regime), whose particle concentration probably decreases more or less continuously upwards from the high-concentration near the base. Poor sorting reflects rapid deposition from a high-concentration depositional boundary layer. The particulate to non-particulate (P-NP) transition occurs in and just beneath a depositional boundary layer. 'Non-particulate' include material composed of particles that are stuck together such that they cannot move independently of one another. 'Stepwise aggradation', by successive en masse deposition of successively formed traction carpets or traction plugs (Fig. 2-32; Lowe, 1982). Each carpet or plug develops as the basal part of the flow acquires yield strength due to friction and/or adhesion between particles. Each aggradational step will tend to produce an inverse-graded layer (layer 2a), analogous to the S_2 division of high-density turbidity current deposit (Fig. 2-33). 'Gradual aggradation', by rapid suspension sedimentation of individual grains to form a massive deposit (layer 2b) analogous to the S_3 division of high-density turbidity current deposits (Fig. 2-33; Lowe, 1982). Gradual aggradation of a massive flow occurs during fairly steady flow in which the base of the flow is

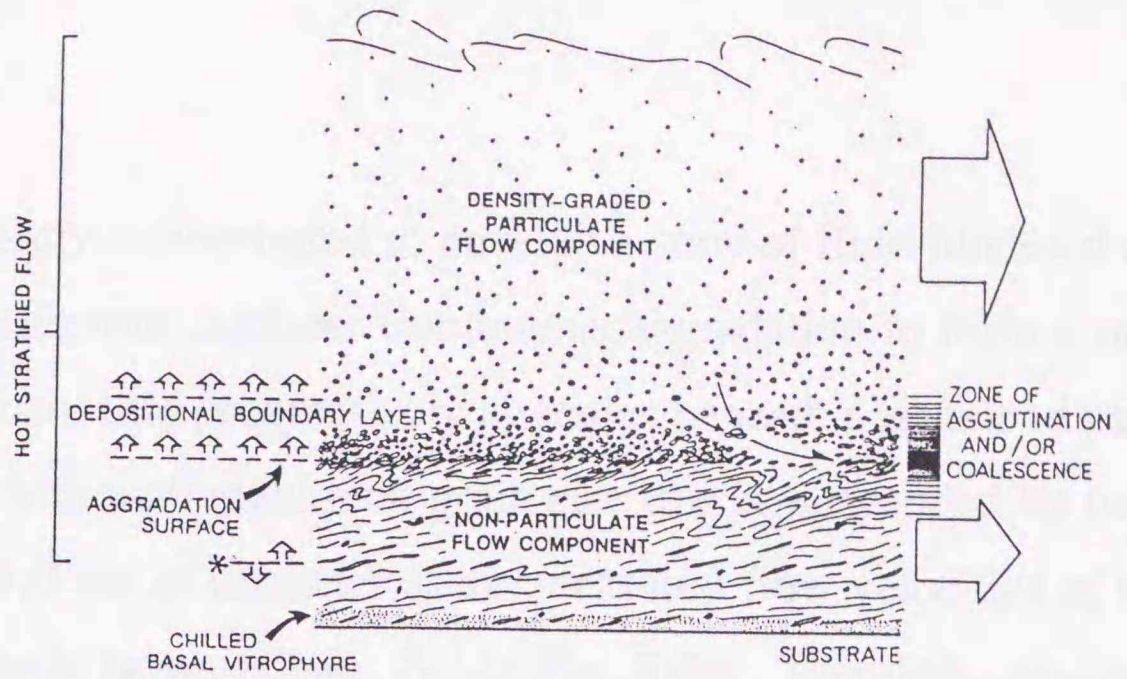

Fig. 2-31. A schematic cross-section showing emplacement and progressive aggradation of an extremely high-grade ignimbrite by Branney and Kokkelar (1992). Hot particles agglutinate and/or coalesce within and just below a depositional boundary layer that migrates progressively upwards from on the substrate to a position between non-particulate and particulate flow components. The asterisk indicates the boundary between the non-particulate flow component and underlying stationary tuff at an instant in time; its vertical position will vary with time.

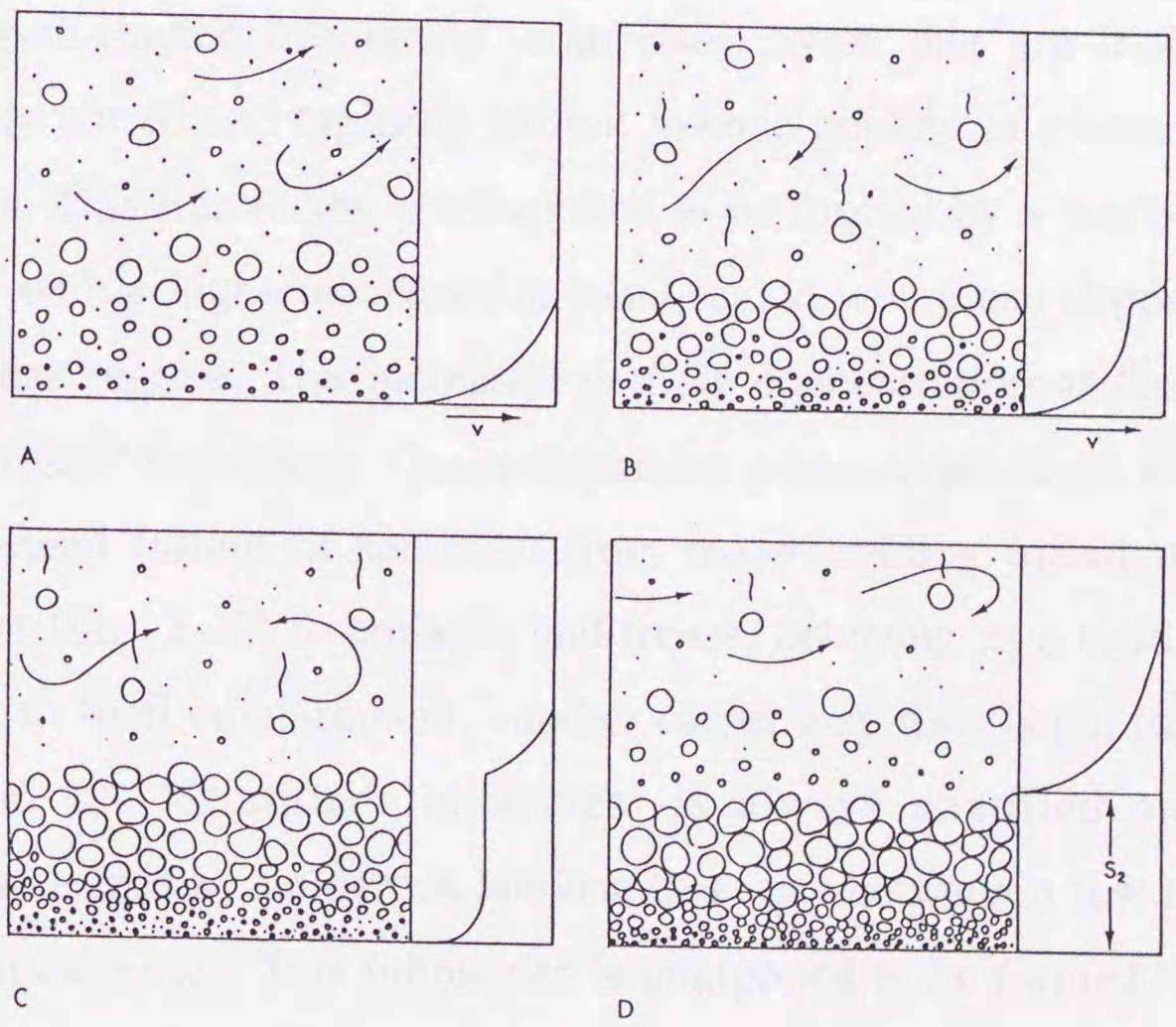

Fig. 2-32A-D. Origin of traction carpet layers by Lowe (1982). (**A**) Basal part of high-density flow shows development of inversely graded zone due to intergranular dispersive pressure. (**B**) Fallout from suspension increases clast concentration in basal layer and results in formation of traction carpet in which grains are fully supported by dispersive pressure. (**C**) Continued fallout from suspension loads traction carpet and causes freezing and plug in formation in the upper part of traction carpet. (**D**) Final freezing of traction of traction carpet results in formation of new inversely graded basal flow layer above deposit.

sufficiently concentrated to develop a zone of fluid-hindered deposition adjacent to the substrate surface. Continuous aggradation to form a non-particulate flow component that progressively aggrades beneath a sustained particulate flow (Fig. 2-31). Although maximum grain size can be suspended by turbulence is at most 0.1 to 1.0 cm in diameter at the measured flow velocities of the Unzen 1991-93 pyroclastic flows (Chap. 7-3-1; Fig. 7-3b). Therefore, grains larger than a few cm can not be transported only by the turbulence even if the flow velocity was 100 m/s. Thus, grain interaction should be the main transport mechanism for large grains up to a few meters.

Cole and Scarpati (1993) also proposed the deposition model from "a laminar boundary layer" which forms beneath the turbulent flow, to explain the lithofacies of the upper part of the Neapolitan Yellow Tuff, Italy (Fig. 2-34). 'Inverse-graded lithofacies' comprises layers that are individually massive, poorly sorted and typically exhibit inverse-grading of coarse pumice and lithic clasts. This lithofacies is interpreted to be formed by a predominantly turbulent flow with a high-concentration basal region where can deposit material from a laminar regime. The increased particle concentration at the base of the flow suppresses turbulence. Grain-dispersive pressure produces inverse-grading and continued fallout of sediment from the overriding turbulent flow causes the carpet (Fig. 2-32) to collapse and freeze, behaving as a rigid plug immediately prior to final emplacement; another carpet may then begin to form on top (Fig. 2-34a, b). 'Stratified lithofacies' is always stratified and poorly sorted, characterized by numerous laminae that vary between a few millimeters and 10 cm in thickness. This lithofacies is interpreted to be formed by deposition from low-concentration, turbulent flows, where deposition was dominantly due to traction sedimentation (Fig. 2-34c). This model is also disagree with my model (Chap. 7-3-2), because large grains from a few centimeters to a few meters can not be transported by the turbulence. Thus, the turbulent flow model, depositing

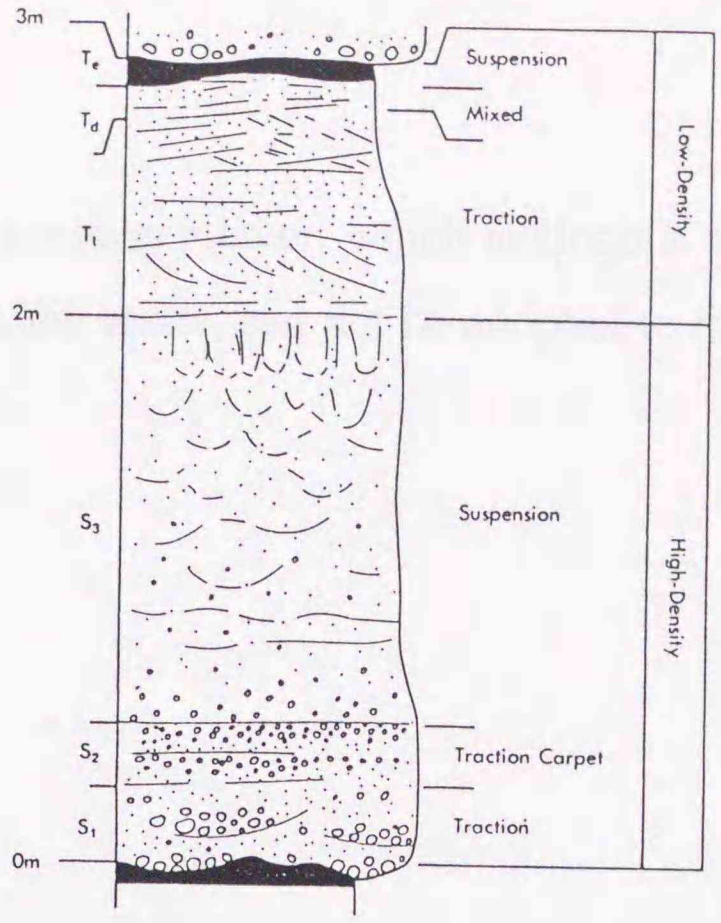

Fig. 2-33. Ideal deposit of a sandy high-density turbidity current showing both high-density (S_{1-3}) and late-stage low-density (T_t, T_{d-e}) divisions by Lowe (1982).

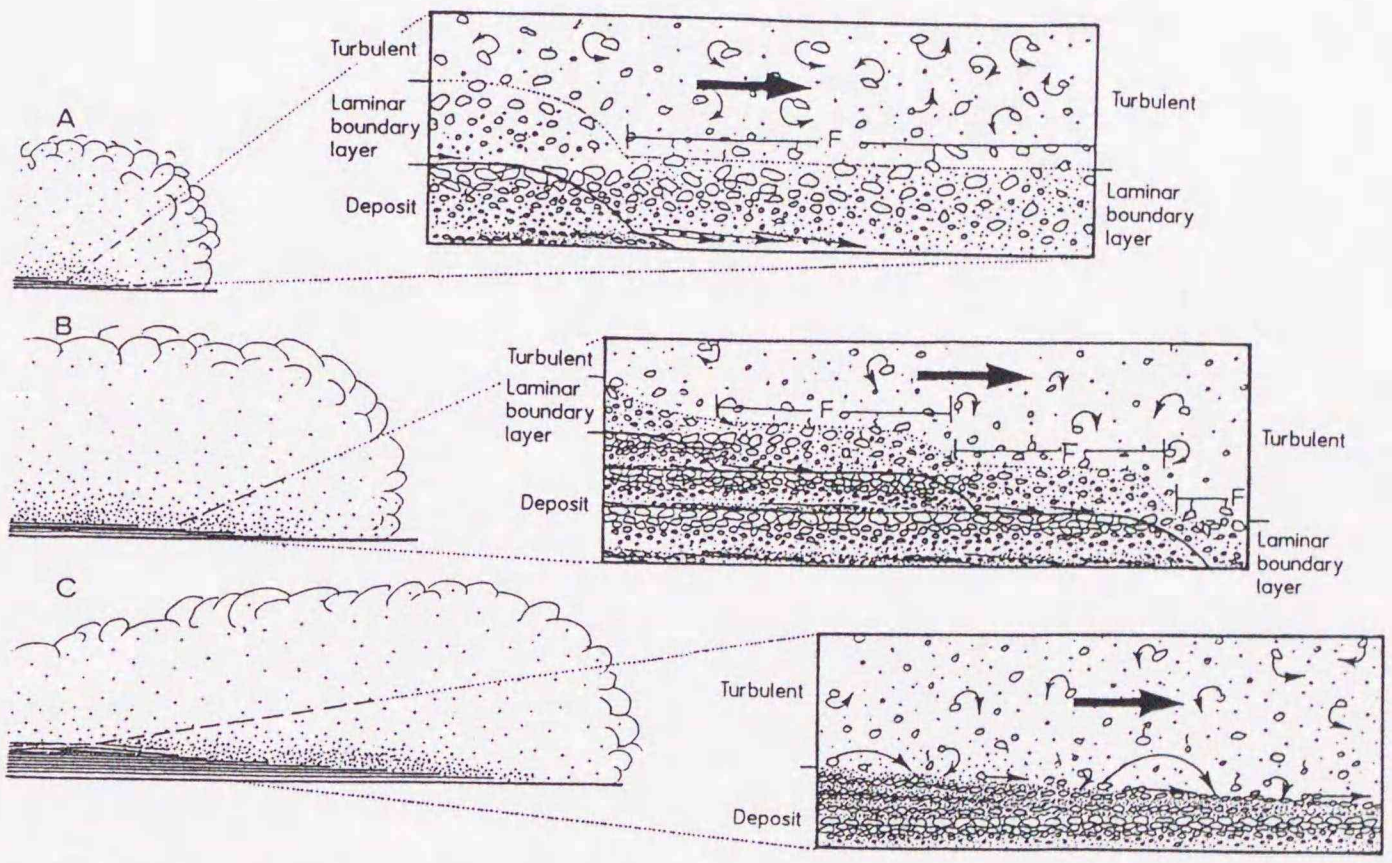

Fig. 2-34A-C. Diagrams showing deposition of inverse-graded facies (**A** and **B**) and stratified facies (**C**) at different times within one flow of the Neapolitan Yellow Tuff, Italy, by Cole and Scarpati (1993). The dotted line marks the transition between turbulent and non-turbulent flow. The solid line marks the boundary between flow and deposit. **A**. The formation by settling of grains in a high particle-concentration, of a non-turbulent 'carpet' layer which develops inverse-grading due to dispersive pressure. F, area of formation. **B**. Shows the formation of several inverse-graded layers simultaneously, but each successive layer is being formed immediately behind the previous one. **C**. Towards the end of the depositional pulse sedimentation occurs directly from the turbulent flow. This deposition occurs by saltation, rolling, and sliding which give rise to a thinly stratified and cross stratified deposit.

from the laminar boundary layer, which analogous to the high-density turbidity current flowing in the water, can not be adopted to the pyroclastic flows flowing in the air.

Chapter 3. Terminology

The terminology related to debris avalanches is still differs between papers. Thus, the terms related to the debris avalanches are defined as follows in this thesis.

Debris avalanche block: This component consists mainly of relatively coherent material derived from the source area and basement formations (Gliken, 1986 MS; Fig. 3-1). For simplicity, 'DB' is used for debris avalanche block. Structures within DBs are sometimes tilted, and deformed with minor faults. Jigsaw cracks which formed by the impact are usually observed in dense DBs. Percussion marks (Ui, 1985) of which removed wedge-shaped small fragment, are usually observed at the junction of jigsaw cracks. In sedimentology, 'block' indicate a large, angular rock fragment, having a diameter greater than 256 mm (American Geological Institute, 1987, p.75). But, DBs are defined by the inner structure or existence of cracks, without relation to the size. Thus, the usage of DB in this thesis is different from that in sedimentology.

Debris avalanche matrix: This component is a blended, unsorted, and unstratified mixture of material ranging from clay to boulders in size (Takarada, 1991; Fig. 3-1). These materials are made of the clast derived from the source area, basement formations, soil, wood fragments, and river deposits. Debris avalanche matrix fills spaces between the DBs. For simplicity, 'DM' is used for debris avalanche matrix. In sedimentology, 'matrix' indicate the finer-grained material enclosing, or filling the interstices between, the larger grains or particles (American Geological Institute, 1987, p.405). But, DM is composed of not only finer-grained material, but also larger-size material. Thus, the usage of DM in this thesis is different from that in sedimentology.

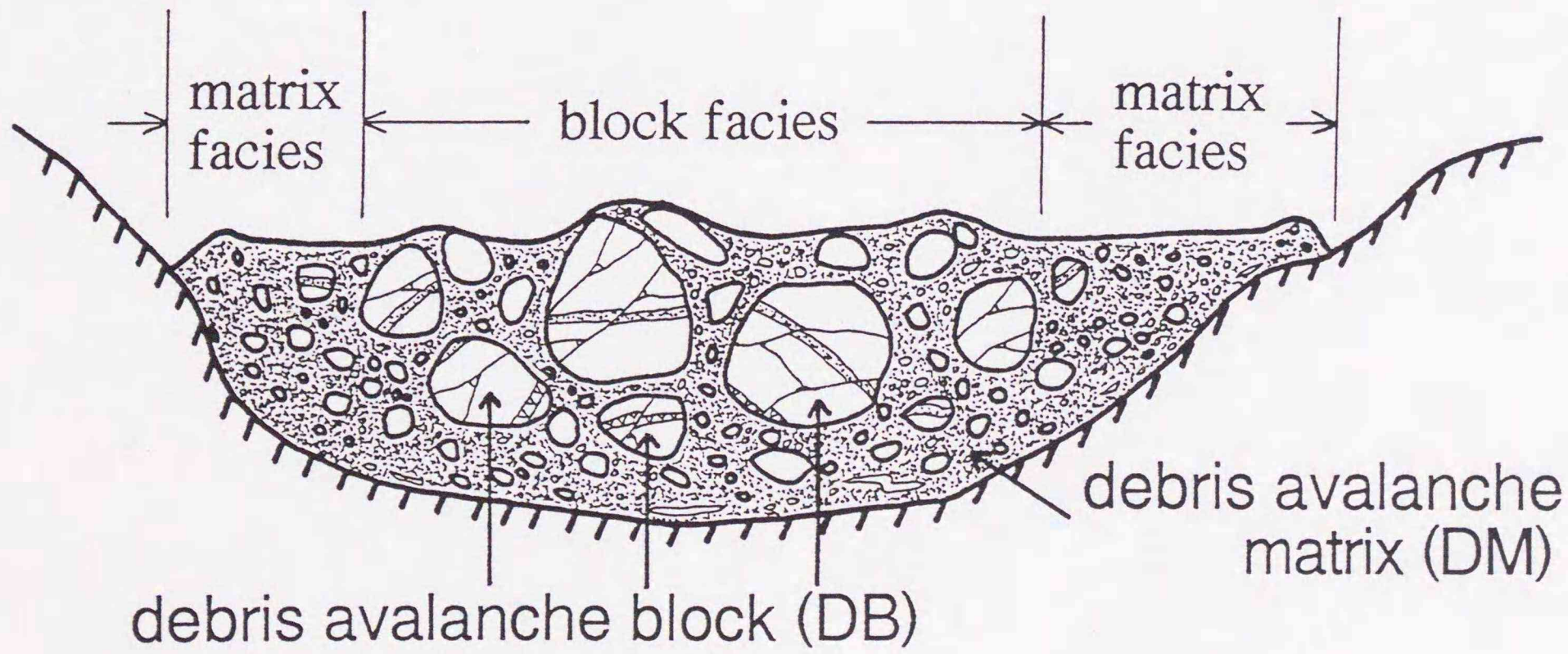

Fig. 3-1. Schematic cross section of a debris avalanche deposit, showing the definition of debris avalanche block (DB), debris avalanche matrix (DM), block facies, and matrix facies (after Takarada, 1991).

Block facies: This facies is composed mainly of DBs and intercalated DM. The surface of block facies usually shows hummocky structures (Ui, 1983). This facies is widespread enough to be shown on a geologic map (Crandell et al., 1984; Fig. 3-1).

Matrix facies: This area is mostly composed of the DM. The surface of the matrix facies is relatively flat. This facies is widespread enough to be shown on a geologic map (Crandell et al., 1984; Fig. 3-1).

Clast: This is one component of DM. The clast is relatively larger particle which preserve no deformation and geologic structures, such as jigsaw cracks, minor faults, successive stratigraphy, and intrusions. Therefore, the features of a clast cannot indicate whether it was transported by the debris avalanche or not. 'Captured clast' is used for the clast incorporated into an avalanche during flowage.

Chapter 4. Geologic setting

4-1. Tashirodake Volcano

Tashirodake Volcano, 1178 meters in height, is a Quaternary stratovolcano, located at the 40 kilometers west of the Towada Volcano (Plate 4-1a; Fig. 4-1). Geology of this area was previously surveyed by Sumi (1962) and Muraoka and Takakura (1988). A geologic map of the southeastern foot of the Tashirodake Volcano, based on the author's field survey, is shown in Fig. 4-2. The description of the formations is described in Takarada (1990 MS) and Takarada (1991) in detail.

The basement formations of the Tashirodake Volcano in this area are composed of pre-Neogene Tertiary metamorphic rocks, Miocene subaqueous volcaniclastics and mudstones, and Pliocene Obirakiyama Tuff (Fig. 4-2). The Obirakiyama Tuff is a large-scale pyroclastic flow deposit consisting of biotite-rhyolite pumice tuff (Plate 4-1b). The tuff can be divided into red-colored welded subaerial deposit, and white-colored non-welded subaqueous deposit. Cholitized pumices due to hydrothermal alteration, a few millimeters to a few centimeters in size, are contained in the subaqueous deposit (Plate 4-1b). The Obirakiyama Tuff is widely distributed in the surveyed area (Fig. 4-2). The Obirakiyama Tuff was erupted from the Valles-type Yunosawa Caldera, which located at the 17 km northeast from the surveyed area (Muraoka and Takakura, 1988; Muraoka and Hase, 1990; Fig. 4-1). The Obirakiyama Tuff is dated at 3.5 Ma by the K-Ar method (Muraoka and Takakura, 1988).

The Quaternary formations are divided into the main volcanic edifice of the Tashirodake Volcano, the Iwasegawa debris avalanche deposit, Ooishiwatari lacustrine deposit, Ofudo pyroclastic flow deposit, Amaike debris avalanche deposit, Hirataki nuée ardente deposit, Hachinohe pyroclastic flow deposit,

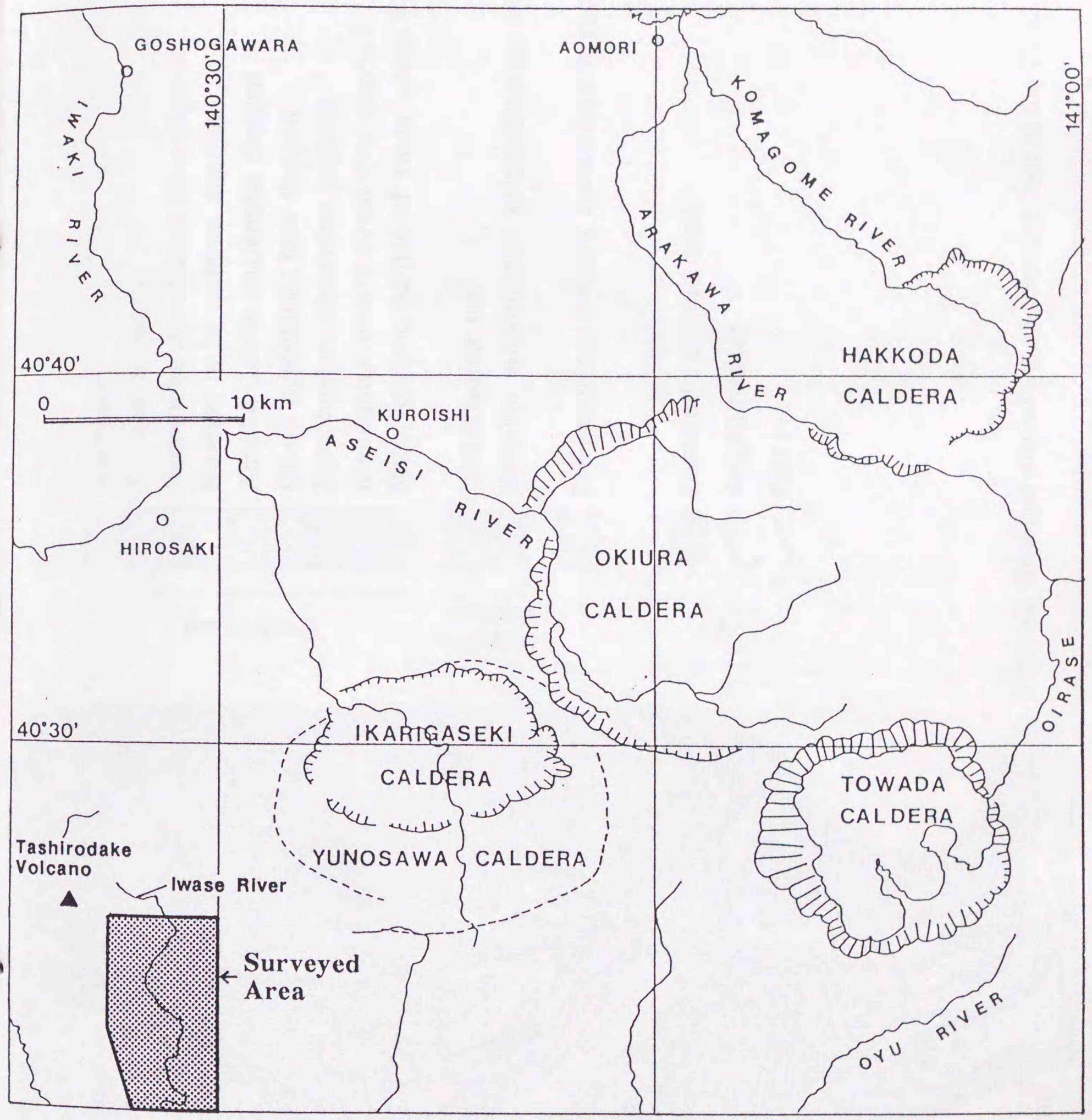

Fig. 4-1. Locations of the surveyed area at the southeastern foot of the Tashirodake Volcano. Five calderas: Towada, Hakkoda, Okiura, Ikarigaseki, and Yunosawa calderas, are located at the northeastern region of the surveyed area (after Muraoka et al., 1991).

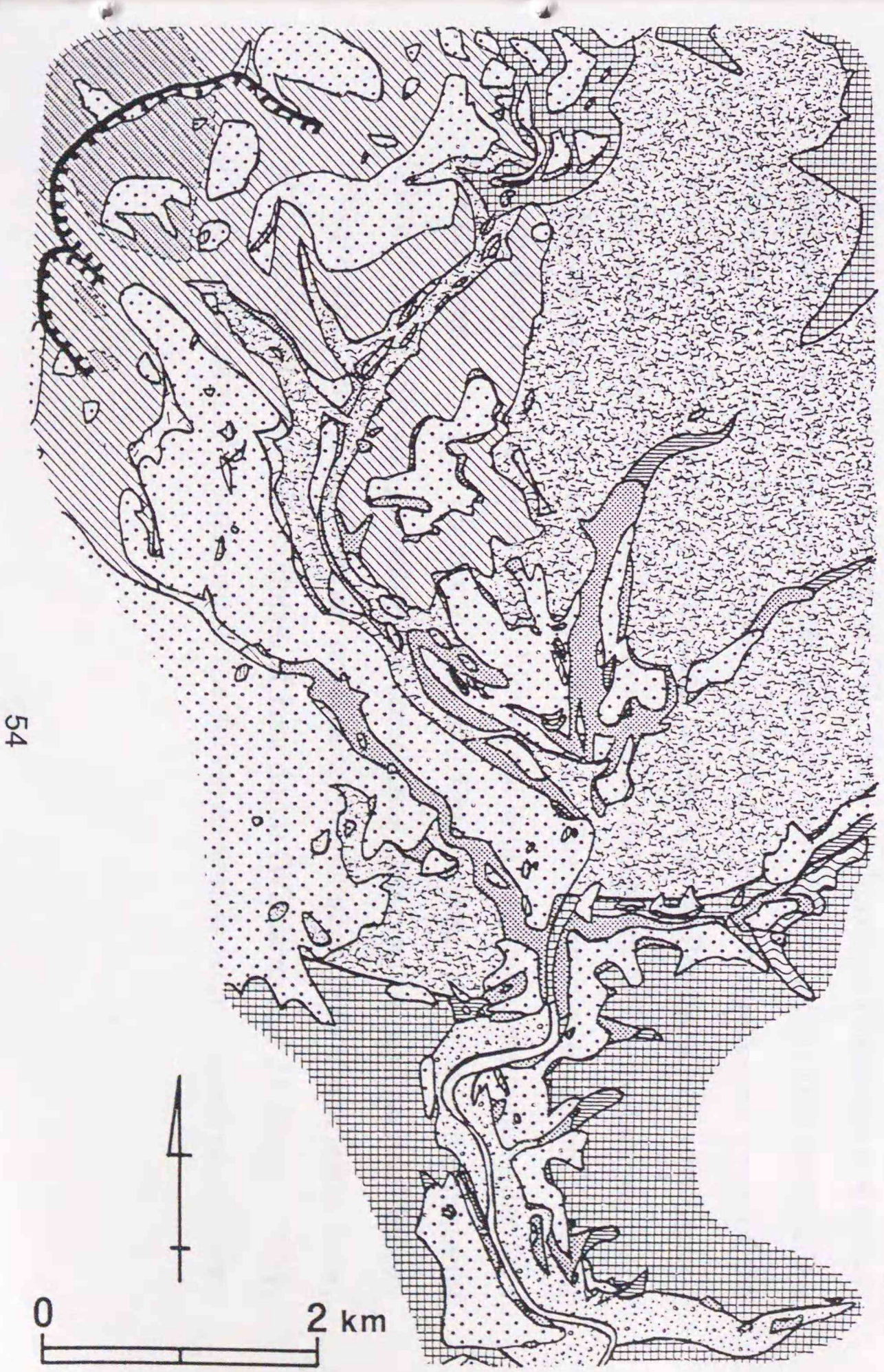

Quaternary
- Alluvium
- Terrace deposits
- Hachinohe pyroclastic flow deposit
- Hirataki nuée ardente deposit
- Amaike debris avalanche deposit
- Ofudo pyroclastic flow deposit
- Ooishiwatari lacustrine deposit
- Iwasegawa debris avalanche deposit
- Main volcanic edifice of Tashirodake Volcano

Neogene Tertiary
- Obirakiyama tuff
- Miocene subaqueous volcaniclastics and mudstones

- Pre-Neogene Tertiary metamorphic rocks
- Fumarolic altered area
- Amphitheater
- Fault

Fig. 4-2. Geologic map of the southeastern foot of the Tashirodake Volcano.

terrace deposits, and alluvium, in ascending order (Fig. 4-2). The main volcanic edifice is composed of hornblende-bearing augite-hypersthene andesite lava and tuff breccia. This formation is distributed at the northwestern part of the surveyed area, forming the eastern slope of the Tashirodake Volcano (Fig. 4-2). The Iwasegawa debris avalanche deposit is distributed mainly along the Iwasegawa River and its tributaries (Fig. 4-2). The sedimentary structures of the Iwasegawa debris avalanche deposit are described in chapter 5-1 in detail. The source amphitheater is located at 2.5 kilometers southeast from the summit of the Tashirodake Volcano (Plate 4-1c). Rocks in the amphitheater is mostly altered by fumarolic activities (Plate 4-1d). The Ooishiwatari lacustrine deposit is silty deposit, a few centimeters to two meters in thickness, which was formed due to damming-up the rivers by the avalanche deposit (Plate 4-1e). The Ofudo pyroclastic flow deposit is composed of well-vesiculated fresh white pumices, fine ash, lithics, and charcoal (Plate 4-1e, f). This deposit is a large-scale pyroclastic flow deposit erupted from the Towada Volcano (Fig. 4-1). This deposit is dated at 25 ka by ^{14}C method (Hayakawa, 1985). The Amaike debris avalanche deposit is composed of DBs made of altered tuff breccia, < 4 meters in diameter, and DM filling spaces between them (Plate 4-1g). This deposit is a small-scale debris avalanche deposit, distributed at the northeastern slope of the surveyed area (Fig. 4-2). The assumed source is a smaller breached area located at the south of the larger amphitheater of the Iwasegawa debris avalanche, based on the observation of aerial photos (Fig. 4-2). The Hirataki nuée ardente deposit is composed of the dense essential blocks made of augite-hypersthene andesite, a few centimeters to five meters in size, and fine-grained altered cognate material (Plate 4-1h, i). Shrinkage crakes are sometimes observed in the essential blocks (Plate 4-1h). The Hirataki nuée ardente is the Merapi type pyroclastic flow, which occurred due to the collapse of lava dome (Williams and McBirney, 1979, p.152). Thickness of the deposit in the surveyed area is from several centimeters

to eight meters. This deposit is widely distributed in the surveyed area (Fig. 4-2). Assumed source of this deposit is lava domes at the summit of the Tashirodake Volcano, because the thickness of the deposit and the size of the blocks increase toward the summit. The Hachinohe pyroclastic flow deposit is composed of fragile yellow pumices, a few centimeter in size, small altered lithics, and charcoal (Plate 4-1j). The pumices typically include hornblende minerals (Takarada, 1988 MS). Thickness of the deposit in the surveyed area is from several centimeters to two meters. This deposit is also a large-scale pyroclastic flow deposit erupted from the Towada Volcano. This deposit is dated at 13 ka by ^{14}C method (Hayakawa, 1985). The terrace deposit is composed of sand and conglomerates up to five meters in diameter, which eroded mainly from the Iwasegawa debris avalanche deposit and the Hirataki nuée ardente deposit. The terrace deposit is distributed along the Iwasegawa River in the downstream area (Fig. 4-2).

A

B

Plate 4-1. A. A summit of the Tashirodake Volcano and the source amphitheater of the Iwasegawa debris avalanche (in front of the summit). **B.** Close-up of the Obirakiyama Tuff which contains a few millimeters to centimeters-size cholitized pumices due to hydrothermal alteration. The Obirakiyama Tuff is a large-scale pyroclastic flow deposit, dated at 3.5 Ma, consisting of biotite pumice tuff, erupted from the Yunosawa Caldera located at 17 km northeast from this point (Fig. 4-1).

C

D

Plate 4-1. C. The source amphitheater from the hill at locality I1 (Fig. 5-1). Size of the amphitheater is 1.75 km across and the scarp is 150 m high. **D.** Altered tuff breccia in the amphitheater due to the past fumarolic processes in this area.

E

F

Plate 4-1. E. Slity Ooishiwatari lacustrine deposit intercalated between the lower Iwasegawa debris avalanche deposit and the upper Ofudo pyroclastic flow deposit. **F.** Close-up of the Ofudo pyroclastic flow deposit which composed of well-vesiculated fresh white pumices, fine ash, and lithics.

G

H

Plate 4-1. G. Amaike debris avalanche deposit. Lower gray-colored part is the DB composed of a little altered tuff breccia. Upper brown-colored part is the DM containing altered rock fragments. **H.** Essential block in the Hirataki nuée ardente deposit. Shrinkage cracks are observed.

I

J

Plate 4-1. I. Hirataki nuée ardente deposit and an overlying Hachinohe pyroclastic flow deposit (yellow part). **J.** Close-up of the Hachinohe pyroclastic flow deposit, which contains a few centimeter-size fragile pumices.

4-2. Ontake Volcano

Ontake Volcano, 3063 meters in height, is a Quaternary stratovolcano, located at the southern part of the North Japan Alps in central Japan (Plate 4-2a). Geology of the Ontake Volcano and basement formations were previously surveyed by Kobayashi (1987) and Yamada and Kobayashi (1988) (Table 4-1a, b).

The basement formations of the Ontake Volcano are composed of Mesozoic strata of the Mino belt, Late Cretaceous-Early Paleogene Noohi Rhyolites, Late-Pliocene Nyukawa pyroclastic flow deposit, and Late-Pliocene Suzurankoogen basalt (Table 4-1a). Products of the Ontake Volcano are divided into Older and Younger Volcanic Rocks. The Younger Volcanic Rocks are further subdivided into rhyolite-dacite Mamahahadake (SiO_2=66-73%) and andesite Marisiten (SiO_2=52-64%) Volcanic Groups (Table 4-1a, b). A large caldera (6x8 km) was formed due to the eruption of Pm-I tephra, 70-100 ka (Kobayashi et al, 1967), at the beginning of stage of the Mamahahadake Volcano Group (Table 4-1b; Takemoto et al., 1987; Machda and Arai, 1992, p.82-83). Kisodani Formation, consisting of rhyolite-dacite conglomerates, sand, and rework deposits of the Mamahahadake Volcano Group, was formed between stages of the two Volcano Groups (Sakai, 1963; Table 4-1a). The Marisiten Volcano Group is composed of the products of Nigorigo (ng), Kongoodo (kn), Okunoin (ok), Kusakidani (ks), Mamakodake (mm), Ichinoike (ic), and Yonnoike (yn) Volcanos, and Sannoike (sn) Lava, in ascending order (Fig. 4-4). The Kaida debris avalanche occurred between the stages of the Mamakodake (mm) and the Icinoike (ic) Volcanos (Yamada and Kobayashi, 1988). The Daisen-Kurayoshi tephra, DKP, ca. 50 ka (Machida and Arai, 1992, p.79-80), was observed beneath the Kaida debris avalanche deposit (Takemoto et al., 1987; Table 4-1b). The Aira-Tn tephra, AT, 22-25 ka (Machida and Arai, 1992, p.60-66), was observed above the products

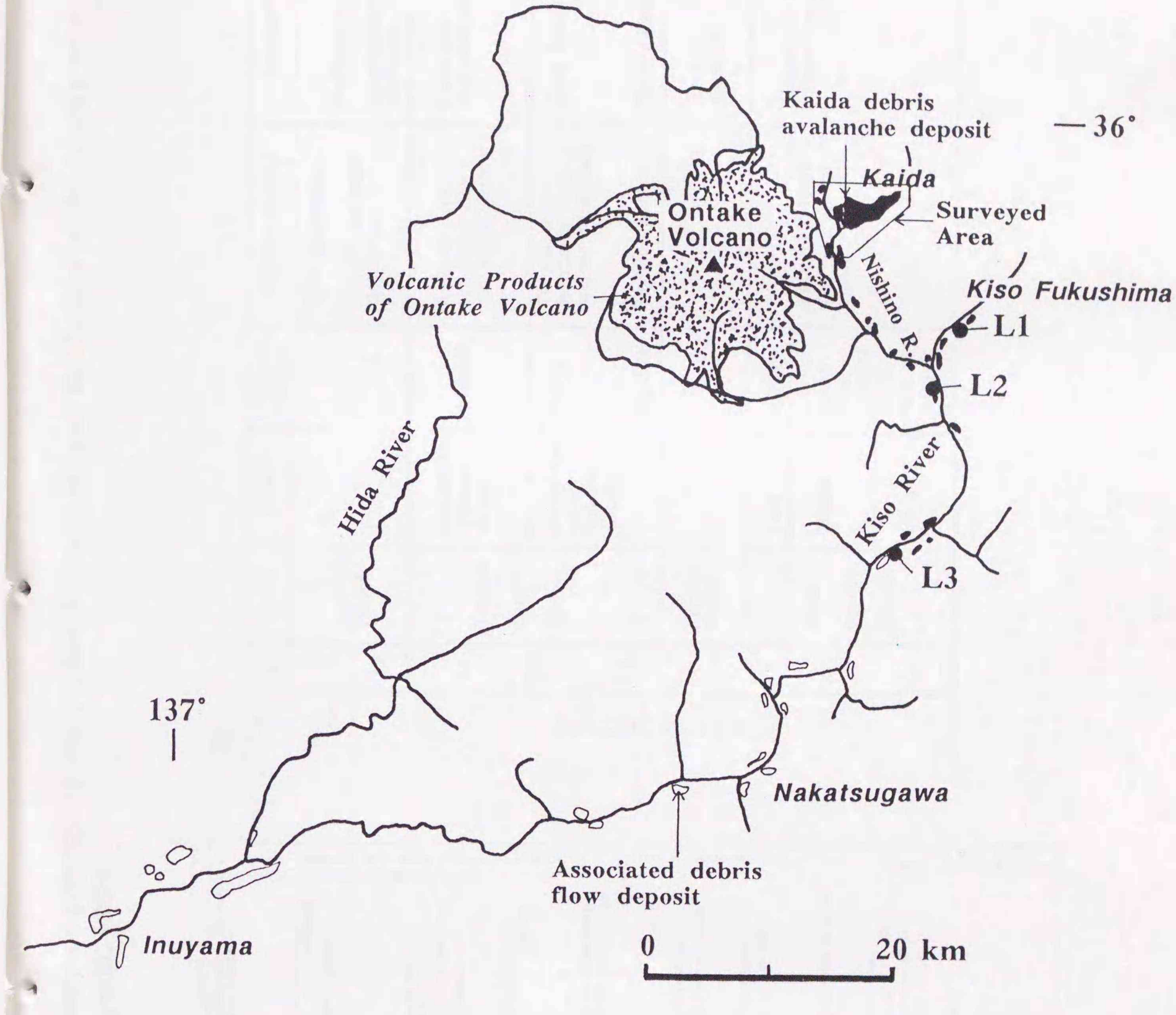

Fig. 4-3. Distribution of the Kaida debris avalanche deposits (solid parts) and the associated debris flow deposits (closed parts). The Kaida debris avalanche deposits can be traced along the Nishino and the Kiso Rivers as far as at least 46 km from the source. The associated debris flow deposits can be traced along the Kiso River up to the Inuyama city as far as 144 km from the source (after Fujii, 1976 and Kobayashi, 1987).

Table 4-1A-B. A. Summary of geology of the Ontake Volcano region. **B.** Outline of the history of the Ontake Volcano (after Yamada and Koabayashi, 1988).

A

Geologic age				Stratigraphic units	Remarks	
Cenozoic	Quaternary	Holocene		1984 Ontake Debris Avalanche Deposit	1984 Naganoken-seibu Earthquake	
				Alluvium	1979 Phreatic Explosion	
				Debris deposits		
				Talus and colluvial deposits	↑	
				Terrace deposits	Erosion of Younger strato-volcanoes	
		Pleistocene	Late	Products of Ontake Volcano — Younger Ontake Volcanic Rocks — Marishiten Volcano Group (andesite)	Younger stratovolcanoes	Ontake volcanism
				Kisodani Formation		
				Mamahahadake Volcano Group (rhyolite-dacite)	Lava domes	
					Pumice eruption and caldera formation	
			Middle	Older Ontake Volcanic Rocks (dacite-basalt)	Erosion of Older stratovolcano	
					Older stratovolcano	
			Early		Intrusions of porphyrite and dacite	Atera fault movement
	Neogene	Pliocene		Suzurankōgen Basalt		
				Nyūkawa Pyroclastic Flow Deposit		
					Formation of the intramountain basins in the northern areas	
		Miocene			↑ Erosion	
	Paleogene				Yakeiwadani Granodiorite	
				Nōhi Rhyolites — Stage V welded tuffs	Intrusions of granite porphyry	
				Stage IV welded tuffs		
				Kurosawa Breccia		
				Shirakawa Formation	Intrusions of granodiorite porphyry	
				Stage III welded tuffs		
				Atera Formation		
				Stage II welded tuffs		
Mesozoic	Cretaceous		Late		Intrusions of pre-Nōhi granitoids	Felsic magmatism
			Early		↑ Upheaval and erosion	
	Jurassic		Late	Mesozoic strata of the Mino Belt — Olistostrome	Regional folding	
			Middle	Sandstone, mudstone, tuffaceous mudstone, conglomerate	Formation of thrust sheets	
			Early		Submarine slumping	
	Triassic		Middle to Late	Bedded chert	Felsic volcanism	Sedimentation-deformation of the Mino Belt
			Early			

B

Age $\times 10^4$ y		Period	Stage	Magmatic products	Volcanic activity	Landform	Remarks
Holocene		Inactive Period			1979 Explosion		1984 Earthquake
							1975-78 Earthq. swarm
					Phreatic explosion	Explosion craters	Akahoya Ash (6,300y.B.P.)
	2.3				Hot spring Fumarole	Large-scale landslides	AT Ash (23,000y.B.P.)
PLEISTOCENE	4.8	Younger Ontake Period	Marishiten Volcano Group	Andesite	Andesite lava, pyroclastic flow and air-fall tephra	Composite stratovolcano	**Kaida debris avalanche**
							DKP Pumice
	5-6		Mamahaha-dake Volcano Group	Dacite	Viscous lava, pyroclastic flow and air-fall pumice	Lava domes	Aso-4 Ash
	7-9			Rhyolite	Rhyolitic pumice	Caldera formation	Pm-I Pumice ($7\text{-}9\times10^4$ y.B.P.)
		Inactive Period				Heavily dissected	Wamura Mudflows
		Older Ontake Period	Late	Andesite	Lava, pyroclastic flow and air-fall tephra	Single cone of stratovolcano	
			Middle	Andesite Basalt Basaltic andesite			
			Early	Dacite Andesite Basaltic andesite			

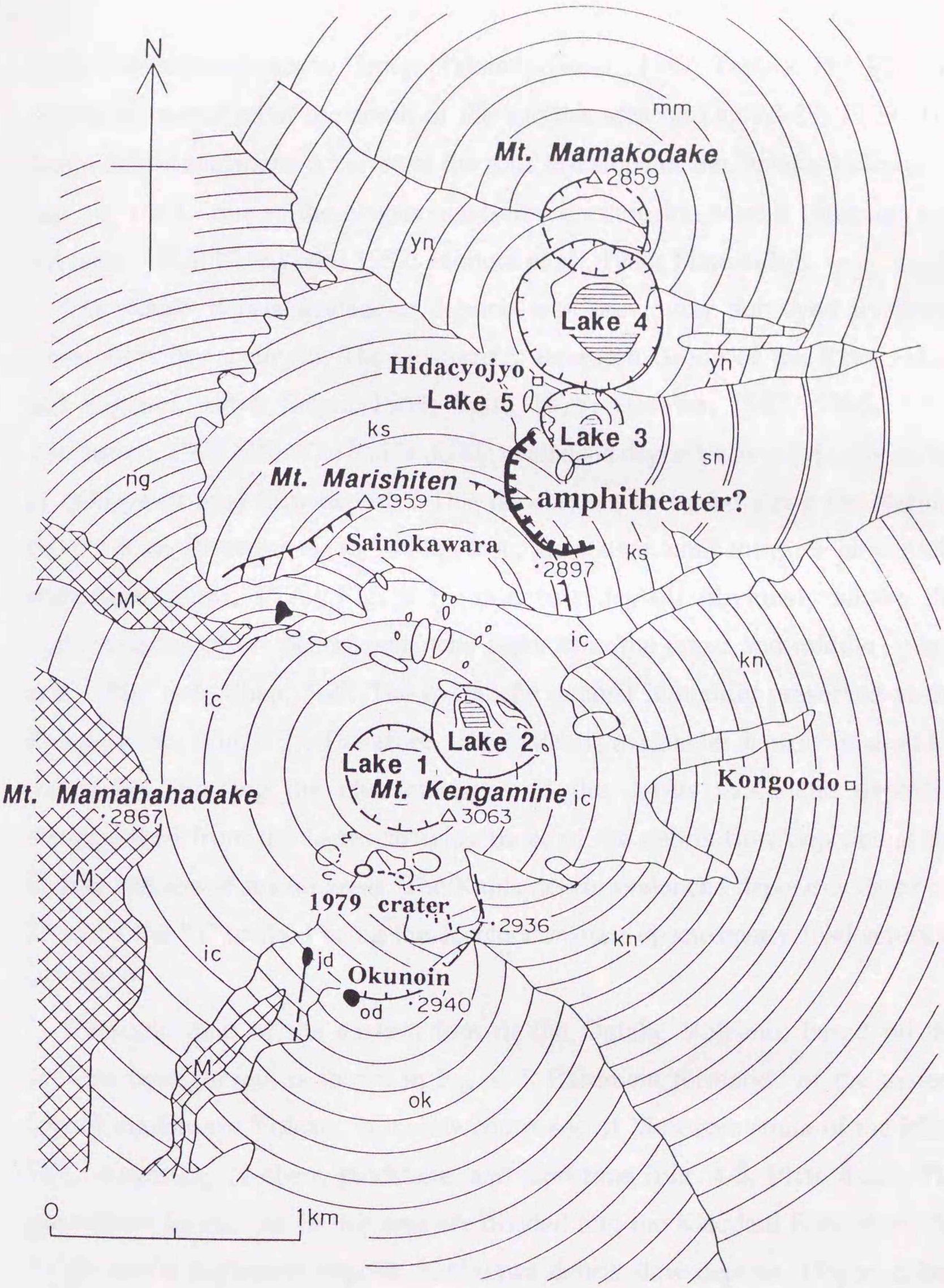

Fig. 4-4. Distribution of the Marishiten Volcanic Group at the top of the Ontake Volcano. This group is composed of the products of Nigorigo (ng), Kongoodo (kn), Okunoin (ok), Kusakidani (ks), Mamakodake (mm), Ichinoike (ic), and Yonnoike (yn) Volcanoes, and Sannoike (sn) lava in ascending order (after Yamada and Kobayashi, 1988). The assumed source amphitheater is located at the eastern scarp of the Mt. Marishiten.

of the Marishiten Volcano Group (Takemoto et al., 1987; Table 4-1b). Phreatic explosions occurred at the south of the summit area on Oct 28-29, 1979. The Denjo debris avalanche occurred at the southern slope of the Ontake Volcano on Sep 14, 1984, due to the Naganoken-Seibu Earthquake, M=6.8 (Matsuda and Ariyama, 1985; Kobayashi, 1987; Mimura et al., 1988; Plate 4-2b).

The Kaida debris avalanche deposit was previously surveyed by many researchers (for example, The Quaternary Research Group of the Kiso Valley and Kigoshi, 1964; Sakai, 1963; Fujii, 1976; Oosawa, 1983, 1986, 1987; Yamamoto, 1990 MS). The Kaida debris avalanche deposit was previously called as 'Kisogawa mud flow deposit'. This deposit can be traced along the Nakano and the Kiso Rivers as far as 144 km from the source, until Inuyama city, Aichi prefecture (Fujii, 1976; Fig. 4-3). But, this deposit obviously shows the characteristics of the debris avalanche deposits at the upper and middle stream areas (Fig. 4-3; Chap. 5-2). The avalanche deposit is mainly preserved at the Kaida district (Fig. 4-3). Therefore, 'Kaida debris avalanche deposit' is used for the facies showing the characteristics of the debris avalanche deposits, distinguished from the facies showing those of the debris flow deposits at the middle and lower stream areas. The Kaida debris avalanche deposit is dated ca. 50 ka by the ^{14}C method using the accelerator mass spectrometry (Nakamura et al., 1992).

Geologic map of the eastern foot of the Ontake Volcano, based on the author's field survey, is shown in Fig. 4-5. Basement formation of the eastern foot of the Ontake Volcano is mainly composed of Mesozoic strata of the Mino belt, consisting of chert, sandstone, and mudstone (Fig. 4-5; Plate 4-2c). The Quaternary formations in this area are divided into the Kisodani Formation, the Kaida debris avalanche deposit, Kudasawa debris flow deposit, Dogoo debris flow deposit, alluvium, and talus, in ascending order (Fig. 4-5). The Kisodani Formation, consisting of dacitic conglomerates, sand, and silty lake deposits, is

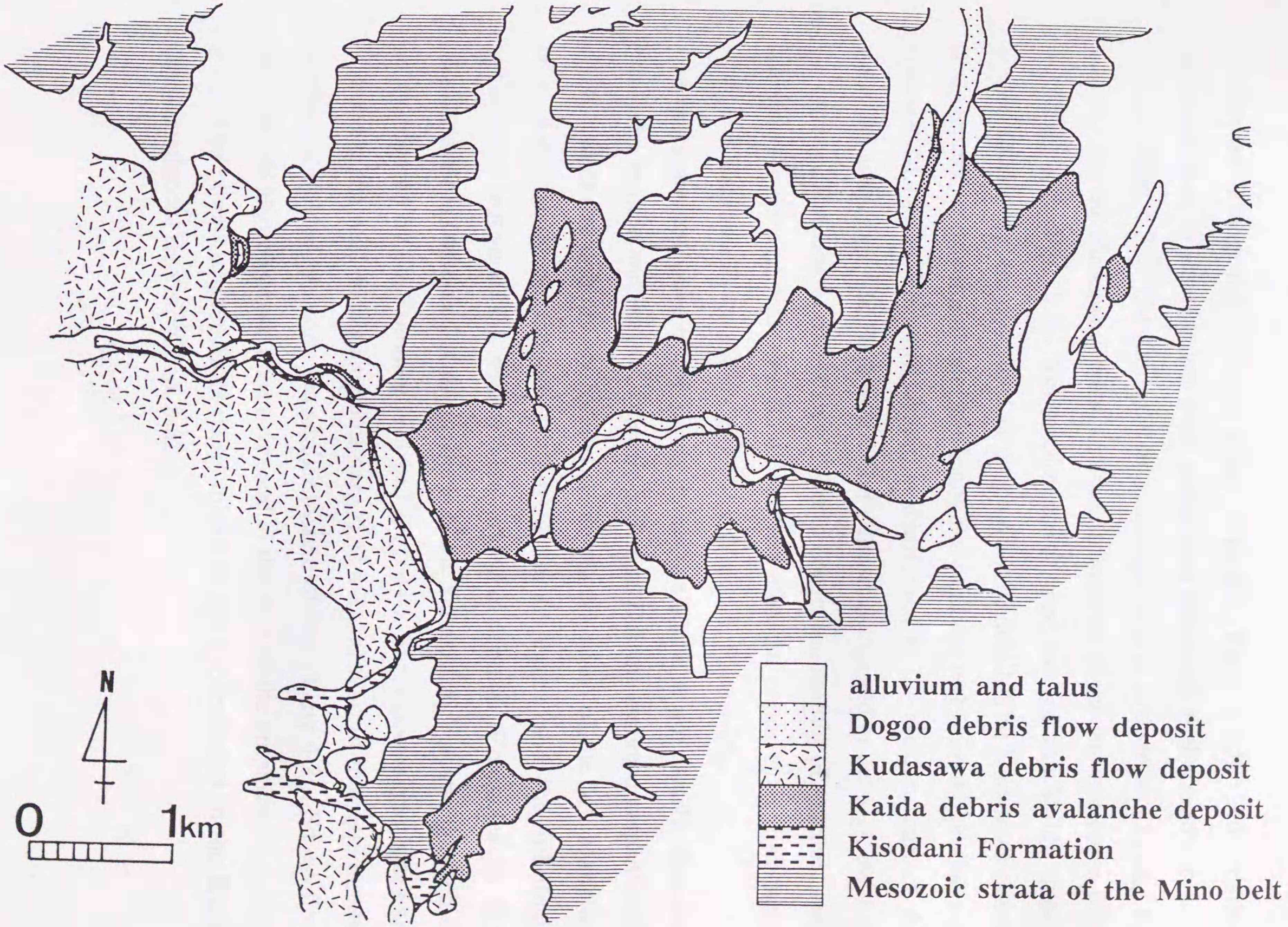

Fig. 4-5. Geologic map of the eastern foot of the Ontake Volcano.

distributed along the Nishino River (Fig.4-5; Plate 4-2d). Deformation structures due to liquefaction were sometimes observed at the sandy to silty deposit (Plate 4-2d). The Kaida debris avalanche deposit is distributed along the Nishino and the Suekawa Rivers, and their tributaries in the surveyed area (Fig. 4-3; Fig. 4-5; Fig. 5-5). The sedimentary structures of the Kaida debris avalanche deposit are described in chapter 5-2 in detail. The Kudasawa debris flow deposit, consisting of conglomerates and sand derived from the products of andesite Marisiten Volcanic Group, is distributed at the western part of the surveyed area (Fig. 4-5; Plate 4-2e). This deposit is exposed at the high level on the terrace. The Dogoo debris flow deposit, consisting mainly of volcanic sand and gravels derived from the Kaida debris avalanche deposits, is distributed along the Suekawa River and its tributaries (Fig. 4-5; Plate 4-2f).

Source amphitheater of the Kaida debris avalanche is not clearly observed due to the erosion and the post volcanic activities. But, the assumed amphitheater of the avalanche is probably located at the eastern scarp of the Mt. Marisiten (Fig. 4-4), based on the observation of aerial photos and the lithologic similarities between the source area and the deposit. Volcanics in this amphitheater is composed of the products of the Kusakidani Volcano (ks), which partly covered by the Sannoike lava (sn) (Fig. 4-4). Successive agglutinates are exposed at the wall of this amphitheater (Plate 4-2g, h). Part of this agglutinates is strongly welded, showing the similar texture of lava (Plate 4-2i). Scoria flow deposits are also observed on the rim and at the wall of the amphitheater (Plate 4-2j). The blocks derived from these volcanics are also included in the Kaida debris avalanche deposit (Chap. 5-2).

A

B

Plate 4-2. A. The Ontake Volcano taken from the Kaida district. **B.** A source amphitheater of the 1984 Denjo debris avalanche.

C

D

Plate 4-2. C. Example of Mesozoic strata of the Mino belt, which composed of sandstone and mudstone. **D.** Kisodani formation consisting of dacitic sandy to silty reworked deposit. Deformation due to liquefaction is observed.

E

F

Plate 4-2. E. Kudasawa debris flow deposits consisting of conglomerates and sand which derived from the products of andesitic Marishiten Volcanic Group. **F.** Dogoo debris flow deposit overlaying on the Kaida debris avalanche deposit. This deposit is composed mainly of gravels and volcanic sand derived from the Kaida debris avalanche deposit.

G

H

Plate 4-2. G. Successive agglutinates at the wall of the eastern scarp of Mt. Marishiten (source amphitheater?; Fig. 4-4). **F.** Close-up of the agglutinate at the scarp.

I

J

Plate 4-2. I. Strongly-welded agglutinate which shows similar texture of lava. **J.** Scoria flow on the rim of the scarp.

4-3. Komagatake Volcano

Komagatake Volcano, 1133 meters in height, facing to the Funka Bay, is a Quaternary stratovolcano, located at the 33 km north of Hakodate city (Plate 4-3a; Fig. 4-6). Geology of the Komagatake Volcano was previously surveyed by Katsui et al. (1975), Katsui et al. (1986), Sagayama (1986), and Katsui et al. (1989)(Fig. 4-6).

The basement formations of the Komagatake Volcano are composed of Miocene Nakanogawa Formation, Pliocene Oshironai Formation, Pliocene Togeshita Volcanic Rocks, Pliocene Tomenosawa Formation, Pleistocene Shikabe and Mori Formations, and intrusive rocks ('Ba' in Fig. 4-6). The Nakanogawa Formation is composed of rhyolite green tuff, siltstone, shale, and altered andesite. The Oshironai Formation is composed of a lower tuffaceous sandstone and an upper siltstone members. The Togeshita Volcaniclastic Rocks are composed of andesite lava, volcanic breccia, and tuff breccia. The Tomemosawa Formation is composed of rhyolite tuff (Plate 4-3b). The Shikabe and the Mori Formations are composed of gravel, sand, silt, clay, and tuffaceous sand. Terrace deposits were developed along the main rivers before the production of the Komagatake Volcano ('t' in Fig. 4-6).

The products of the Komagatake Volcano are divided into four stages. At the first stage, thick pyroxene-andesite Komagatake Lava was extruded and formed the stratovolcano, exposing only at the summit Kengamine (Plate 4-3c) and at the west of Mt. Sahara ('Kl' in Fig. 4-6). At the second stage, Komagatake debris avalanche; Ko-h_2 air fall and pyroclastic flow; and Ko-h_1 air fall and pyroclastic flow were produced (Fig. 4-6). The Komagatake debris avalanche deposit is distributed at the western and the northeastern foot of the Volcano, forming hummocky surface ('Kd' in Fig. 4-6). The Ko-h_2 air-fall deposit, dated at 32-39 ka by the ^{14}C method, is widely distributed around the volcano (Yanai and Ganzawa, 1988; Katsui et al., 1989). The partly welded Ko-h_2 pyroclastic flow

Legend

a	Alluvium
f	Talus and fan deposits
Ex	1942 explosion products
Sp	1929 Ko-a pyroclastic flow deposit
Ss	1929 Ko-a pyroclastic surge deposit
Ko	Air-fall pumice and ash older than 1929
Sw	Pyroclastic flow deposit older than 1929 in the summit area
Ap	1856 Ko-c1 pyroclastic flow deposit
As	1856 Ko-c1 pyroclastic surge deposit
Gp	1694 Ko-c2 pyroclastic flow deposit
Kp	1640 Ko-d pyroclastic flow deposit
Km	1640 mud flow deposit
Kr	1640 Kurumisaka debris avalanche deposit
Kf	Ko-f pyroclastic flow deposit (2.7 ka)
Kg	Ko-g pyroclastic flow deposit (6.1 ka)
Kh	Ko-h2 pyroclastic flow deposit (32-39 ka)
Kd	Komagatake debris avalanche deposit
Kl	Komagatake lava
t	Terrace deposit
Ba	Basement Formations (Shikabe, Mori, Tomenosawa, Togeshita, Oshironai and Nakanogawa Formations)

Fig. 4-6. Geologic map of the Komagatake Volcano (after Katsui et al., 1989).

deposit is distributed at the northern and the eastern foot of the volcano ('Kh' in Fig. 4-6). The Ko-h1 air-fall deposit, dated at 17 ka by the ^{14}C method, is distributed at the northern, western, and southeastern foot of the volcano (Katsui et al., 1989). Between the second and the third stages, the Nigorikawa Caldera, located at the 20 km northwest of the Komagatake Volcano, were formed at 12 ka (Sato, 1969), producing hypersthene-hornblende andesite air fall (Ng-a, b, c), base surge (Ng-b, c), and pyroclastic flow (Ng-a) (Yanai et al., 1992). The Ng-b, c base surge deposits are distributed at the western foot of the Komagatake Volcano (Yanai et al., 1992). The Ng-a pyroclastic flow deposit is distributed around the Nigorikawa Caldera as far as 5 km from the source (Yanai et al., 1992). The air-fall deposits (Ng-a, b, c) are distributed toward the eastern direction (Yanai et al., 1992).

At the third stage, Ko-g air fall and pyroclastic flow (6 ka; Katsui et al., 1989); and Ko-f air fall and pyroclastic flow (2.7 ka; Sasaki, et al., 1971) were erupted. The Ko-g air-fall deposit is distributed toward the eastern direction. The Ko-g pyroclastic flow deposit is exposed at the northern and the northeastern foot of the volcano ('Kg' in Fig. 4-6). The Ko-f air-fall deposit is distributed toward the east-northeastern direction. The Ko-f pyroclastic flow deposit is distributed at the northern and the western foot of the volcano ('Kf' in Fig. 4-6). Between the third and the fourth stages, Ko-e air fall (1.7 ka; Sasaki et al., 1971) and B-Tm air fall (1ka; Machida and Arai, 1992, p.84-85), derived from another volcanoes, were distributed in this area.

At the fourth (historic) stage, 1640 Kurumisaka debris avalanche, 1640 Ko-d air fall, and pyroclastic flow; 1694 Ko-c2 air fall and pyroclastic flow; 1856 Ko-c1 air fall, pyroclastic surge, and pyroclastic flow; 1929 Ko-a air fall, pyroclastic surge, and pyroclastic flow; and 1942 explosion products were produced. The 1640 Kurumisaka debris avalanche deposits, ca. 0.25 km^3 in volume, are widely distributed at the southern, eastern, and northeastern foot of

the volcano, showing the hummocky surface ('Kr' in Fig. 4-6; Plate 4-3d; Katsui et al., 1975). Lake Oonuma and Konuma were formed due to damming-up the rivers by this debris avalanche deposit. This debris avalanche entered the sea from the east-northeastern foot of the volcano, causing catastrophic tsunami (Nishimura and Shimizu, 1993). The 1640 Ko-d pyroclastic flow deposit is distributed around the volcano ('Kp' in Fig. 4-6; Plate 4-3e). The 1640 Ko-d air-fall deposit, ca. 3.5 km^3 in volume, is distributed toward the northwestern direction (Suzuki and Katsui, 1982). The Ko-d air-fall deposit can be divided into eleven fall units (Katsui et al., 1986; Plate 4-3e). The 1694 pyroclastic flow deposit, ca. 0.1 km^3 in volume, is exposed at the northeastern slope of the volcano ('Gp' in Fig. 4-6; Katsui et al., 1975). The 1694 Ko-c2 air-fall deposit, ca. 0.26 km^3 in volume, is distributed toward the eastern direction (Suzuki and Katsui, 1982). The 1856 Ko-c1 air fall, pyroclastic surge, and pyroclastic flow were distributed around the volcano on Sep. 25, causing more than 20 fatalities. The 1856 Ko-c1 pyroclastic flow deposit, ca. 0.1 km^3 in volume, is widely distributed around the volcano, showing red color due to high-temperature oxidization ('Ap' in Fig. 4-6; Katsui et al., 1986; Plate 4-3f). The 1856 Ko-c1 pyroclastic surge deposit is exposed at the southeastern slope, showing dune structure ('As' in Fig. 4-6). The Ko-c1 air-fall deposit is distributed toward the eastern direction. Ansei Crater, 200 meters in diameter, was formed in the amphitheater at this eruption. The 1929 Ko-a air-fall, pyroclastic surge (Ss), and pyroclastic flow (Sp) were distributed around the volcano on June 17 (Fig. 4-6). The characteristics of these deposits are described in chapter 6-1 in detail. The Nov. 16, 1942, explosions produced the breccias around the summit area, consisting of the fragments of the welded 1929 air-fall deposit ('Ex' in Fig. 4-6; Plate 4-3 g, h), forming a 1.6 km-long large fissure in the amphitheater (Fig. 4-6; Fig. 6-1c).

A

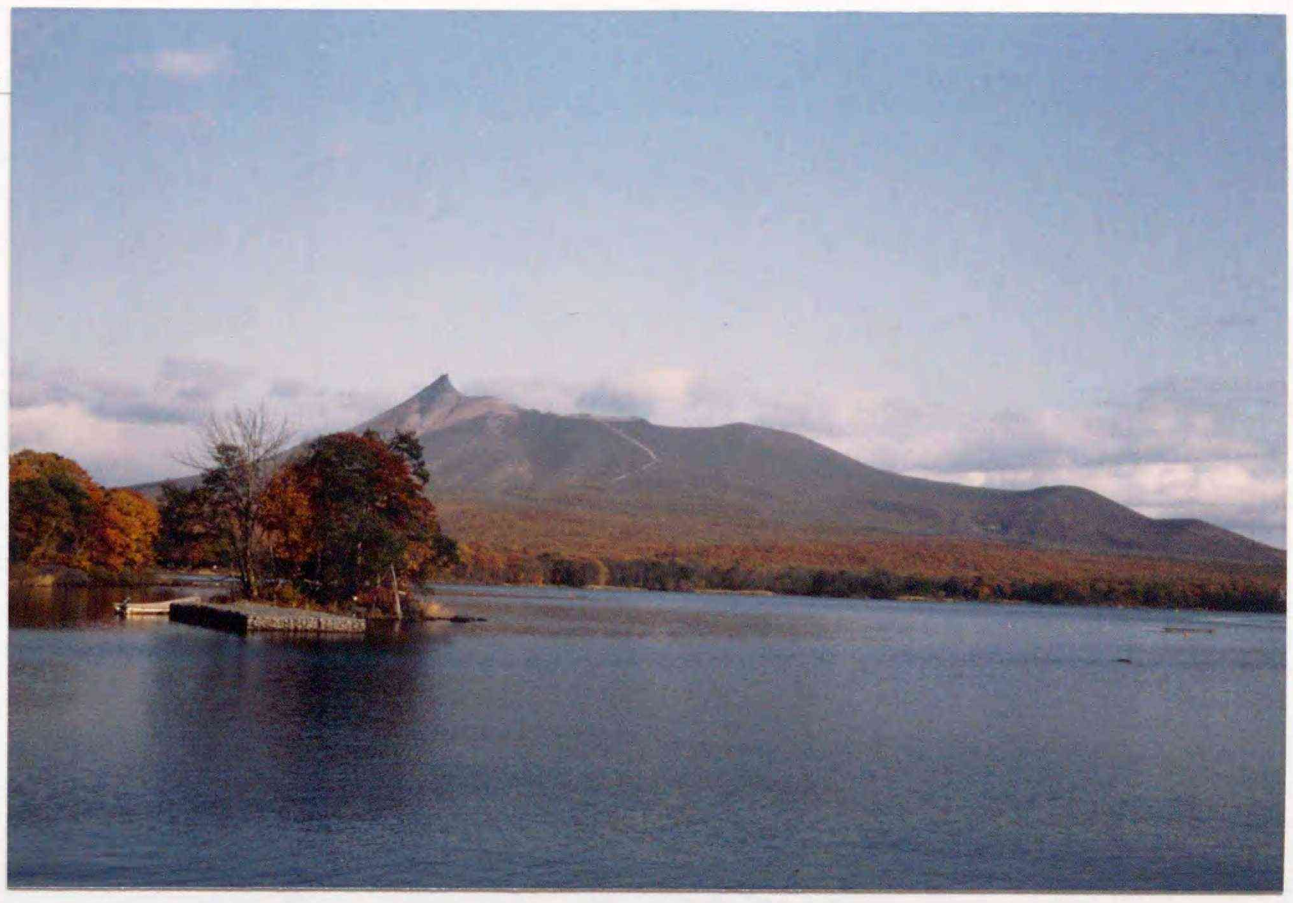

B

Plate 4-3. A. The Komagatake Volcano taken from the southern foot of the Volcano. The lake Oonuma is observed in front of the volcano. A hummock of the 1640 debris avalanche deposit is observed in the lake. **B.** The Pliocene Tomenosawa Formation composed of rhyolite tuff.

C

D

Plate 4-3. C. Komagatake Lava comprising the Mt. Kengamine which located at the western rim of the amphitheater (Fig. 4-6). **D.** The 1640 Kurumisaka debris avalanche deposit overlying on the Tomenosawa Formation.

E

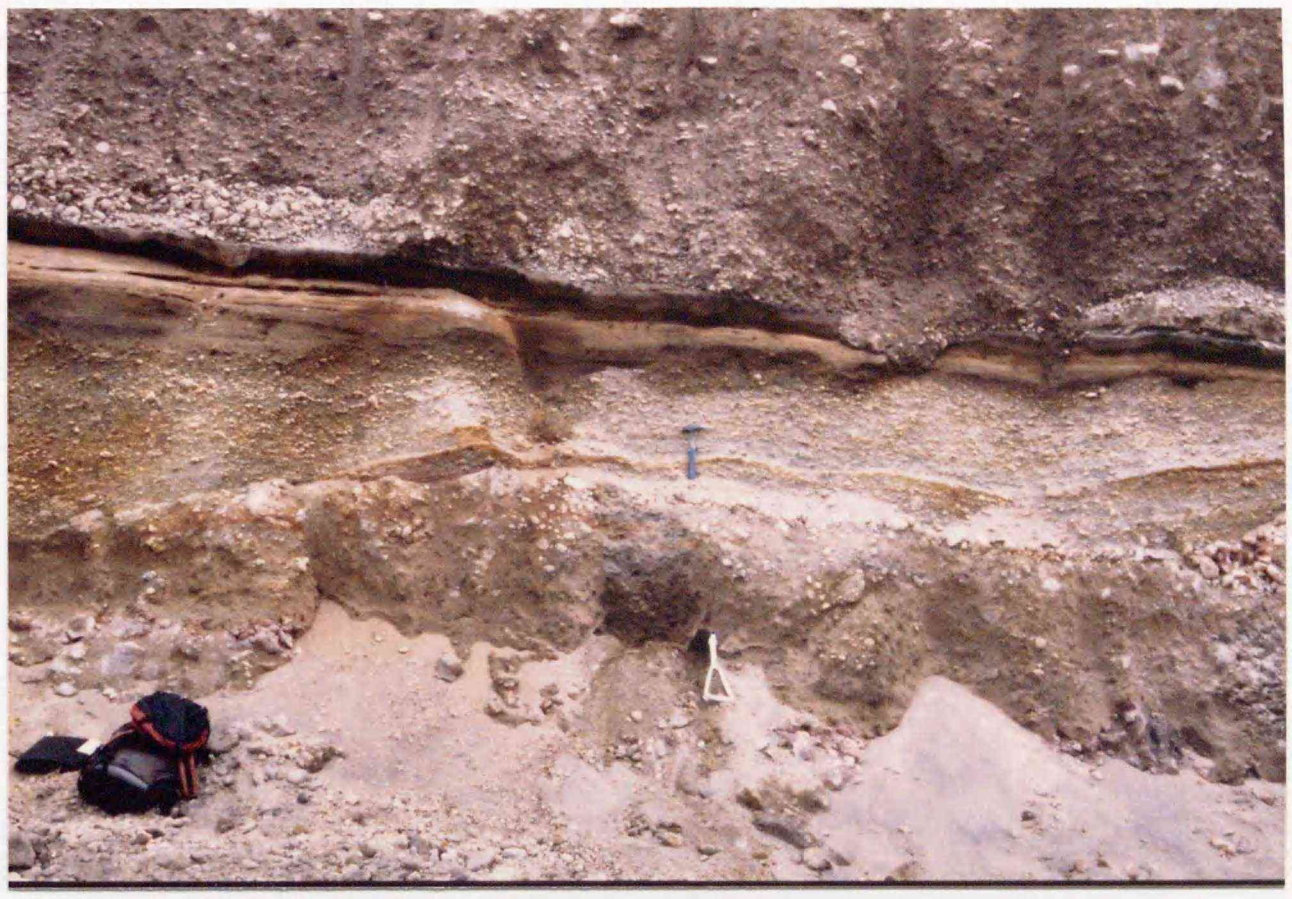

F

Plate 4-3 E. The 1640 K_o-d pyroclastic flow deposit and overlying K_o-d air-fall and the 1929 K_o-a pyroclastic flow deposits. **F.** The 1856 K_o-c_1 pyroclastic flow deposit showing the red color due to the high temperature oxidization.

G

H

Plate 4-3 G. The 1942 explosion breccias scattered on the rim of the amphitheater. Mt. Sumitamori is observed at the upper-left part. Fissures were formed in the 1929 eruption due to the compaction of the thick Ko-a air-fall deposit in the amphitheater. **H.** The 1942 explosion breccia which composed of the welded 1929 air-fall deposit.

4-4. Unzen Volcano

Unzen Volcano, 1452 meters in height, is composed largely of dacite to andesite lava domes and thick lava flows, along with portions of small stratovolcanoes (Plate 4-4a, b). This volcano is located within the Shimabara Graben at the central part of the Shimabara Peninsula (Fig. 4-7). Geology of the Unzen Volcano was previously surveyed by Honma (1936), Kurasawa and Takahashi (1965), Ohta (1984), Sugiyama et al. (1986), Tanaka and Nakada (1988), NEDO (1988), Nakada and Tanaka (1991), and Watanabe et al. (1991)(Fig. 4-7).

Volcanic rocks at this area can be divided into five stages, such as basements, Takadake, Kusenbu, Fugendake Older and Younger Groups (Fig. 4-7; Ohta, 1984; Sugiyama et al. 1986; Tanaka and Nakada, 1988; Nakada and Tanaka, 1991). The basements are composed of hypersthene-hornblende andesite tuff breccia (Toonosaka andesite; 'B_t' in Fig. 4-7). The age of this volcanics are 0.25 and 0.28 Ma by the Fission Track method (Sugiyama et al., 1986). The Takadake Group ('Tt' in Fig. 4-7) is subdivided into Kinugasayama, Takadake, Takaiwayama, and Yatake volcanics, consisting of hornblende andesite and dacite. These volcanics are distributed at the western and southwestern foot of the Unzen Volcano (Fig. 4-7). The age of these volcanics are 0.18-0.26 Ma by Fission Track and K-Ar methods (Sugiyama et al., 1986; NEDO, 1988; Watanabe et al., 1991). The Kusenbu Group is subdivided into Kusenbudake, Azumadake, and Sarubayama volcanics (K_k), and debris avalanche deposits (K_d), consisting of hornblende andesite. These volcanics are distributed at the northwestern part of the Unzen Volcano (Fig. 4-7). The age of these volcanics are 0.13-0.26 Ma by FT and K-Ar methods (Sugiyama et al., 1986; NEDO, 1988; Watanabe et al., 1991). The Fugendake Older Group is composed of Mayuyama (O_m), Fugendake basal (O_b), Nodake (O_n), and Inaoyama (O_i) lavas, and debris avalanche deposits

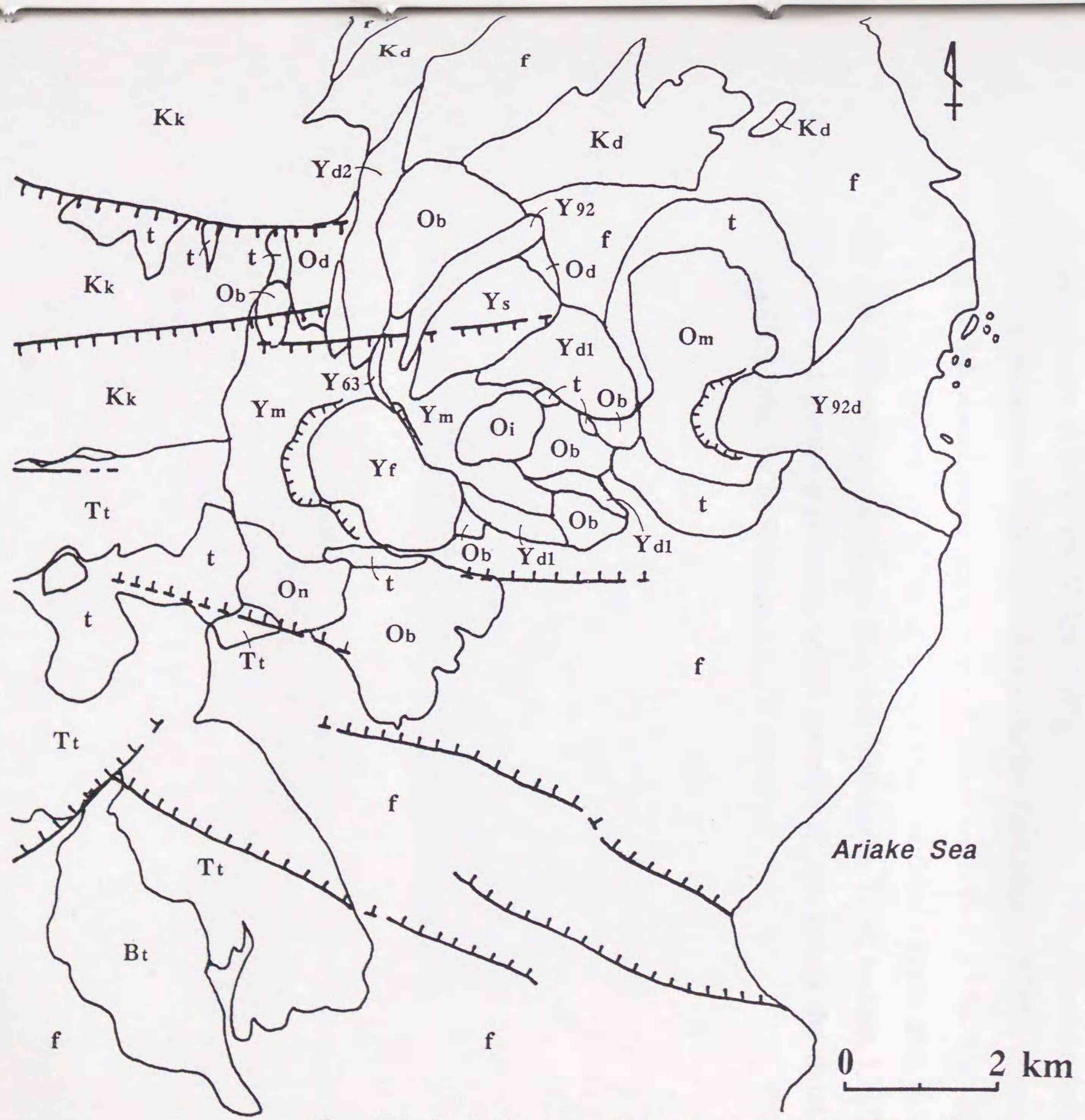

Legend

f	Fan deposits
t	Talus

Fugendake Younger Group

Y_{92d}	1792 debris avalanche deposit
Y_{92}	1792 Shinyake lava flow
Y_{63}	1663 Furuyake lava flow
Y_s	Senbugi lava
Y_{d2}	Debris avalanche / debris flow deposits
Y_f	Fugendake lava
Y_{d1}	Debris avalanche / debris flow deposits
Y_m	Myokendake lavas

Fugendake Older Group

Od	Debris avalanche / debris flow deposits
Oi	Inaoyama lava
On	Nodake lava
Ob	Fugendake basal lava
Om	Mayuyama lava

Kusenbudake Group

Kd	Debris avalanche / debris flow deposits
Kk	Kusenbudake lavas (Kusenbudake, Azumadake and Sarubayama lavas)

Takadake Gruop

Tt	Takadake lavas (Kinugasayama, Takadake, Takaiwayama and Yadake lavas)

Basements

Bt	Toonosaka andesite

Fig. 4-7. Geologic map of the Unzen Volcano (after Tanaka and Nakada, 1988).

(O_d), consisting of hornblende andesite and dacite. These volcanics are distributed around the Volcano (Fig. 4-7). The age of these volcanics are 0.02-0.17 Ma by FT and K-Ar methods (Sugiyama et al., 1986; NEDO, 1988; Watanabe et al., 1991). The Fugendake Younger Group is composed of Myokendake (Y_m), Fugendake (Y_f), and Senbugi (Y_s) lavas; debris avalanche deposits (Y_{d1} and Y_{d2}); historical 1663 Furuyake (Y_{63}) and 1792 Shinyake (Y_{92}) lavas; and 1792 debris avalanche deposit (Y_{92d})(Fig. 4-7). The 1663 Furuyake lava, consisting of olivine-hypersthene-biotite-hornblende andesite (Takahashi, 1989), flowed down 1 km on the northern slope of the Volcano (Fig. 4-7). The 1792 Shinyake lava, consisting of hypersthene-biotite-hornblende dacite (Takahashi, 1989), flowed down 2 km on the northeastern slope of the Volcano from Feb. 27 to Apr. 20. On May 21, 1792, collapse of Mayuyama generated the debris avalanche, 0.34 km^3 in volume, that swept into the sea (Fig. 4-7; Takahashi, 1989; Siebert, 1987). The avalanche and resulting tsunami, which traveled 20 km across the Ariake Sea, caused 14500 fatalities in Shimabara and Kumamoto.

A

B

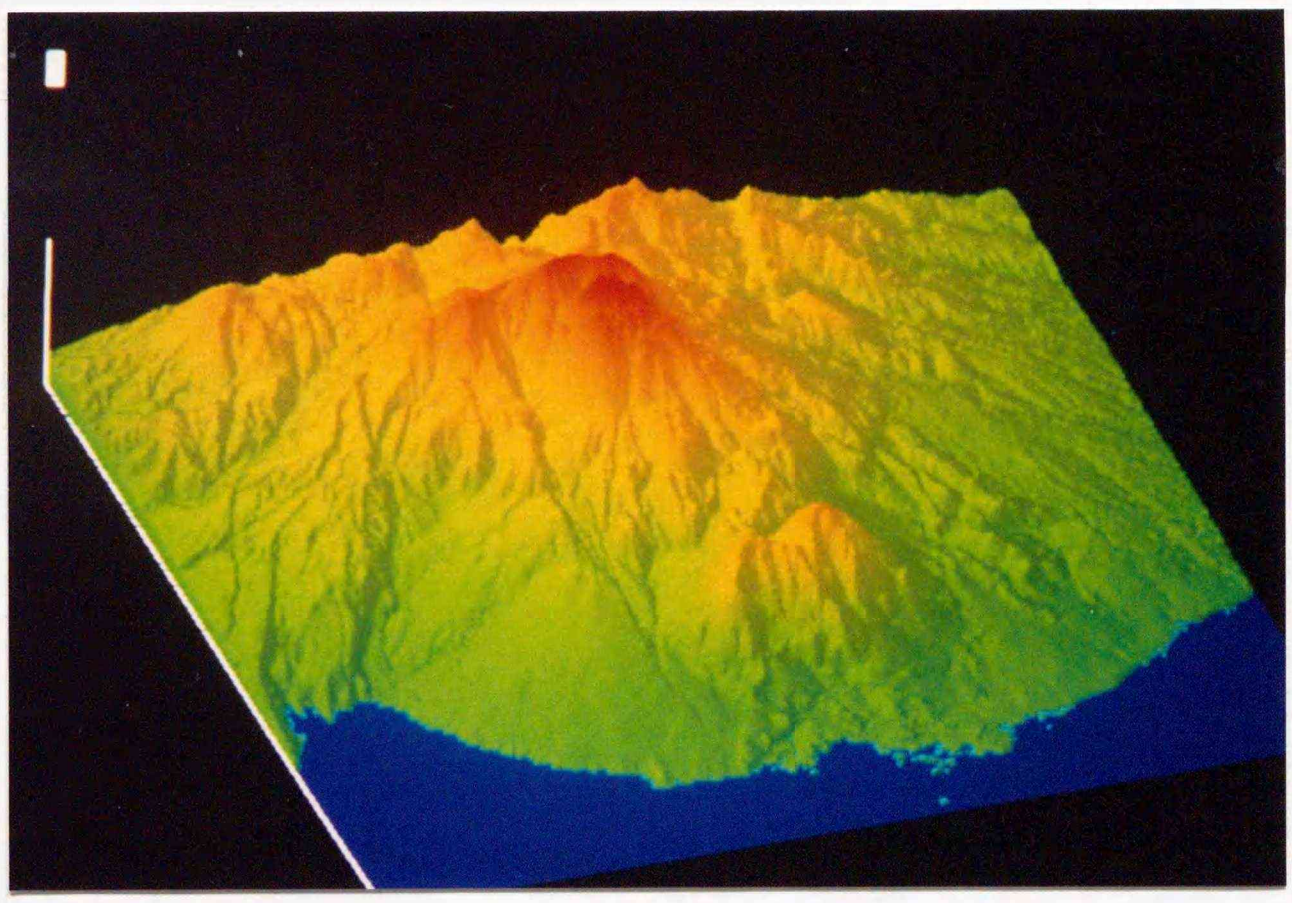

Plate 4-4. A. The Unzen Volcano taken from the eastern foot of the volcano on Jan., 1993. Growing lava dome, the Mizunashi River, and the Akamatsudani valley descending many pyroclastic flows are observed. **B.** Bird-looking view of the Unzen Volcano before the eruption. This computer graphic was made by Nakano, T (GSJ). Unzendake digital elevation data (GSI, 1991: 5. 31) was used to draw this topography.

Chapter 5. Debris avalanche deposits

5-1. Iwasegawa debris avalanche deposit, Tashirodake Volcano

5-1-1. Distribution of the Iwasegawa debris avalanche deposit

The Iwasegawa debris avalanche deposit is distributed along the Iwasegawa River and its tributaries (Fig. 5-1). The lateral runout distance (L) of the deposit is 12.4 km, and the vertical drop (H) is 0.7 km. Therefore, the H/L ratio is 0.06, indicating high mobility of the avalanche, because the range of the H/L ratio of Japanese debris avalanches is from 0.06 to 0.18 (Fig. 2-9). The estimated volume of the deposit is 0.1 km^3. The thickness of the deposit reaches a maximum of 25 meters. Hummocky hills are scattered in the middle region of the deposit. The Iwasegawa debris avalanche deposit is also exposed at the top of a 150 meters-high ridge in the upper stream region at locality I1 (Fig. 5-1). Thus, a part of the flow climbed up this ridge. The Iwasegawa debris avalanche deposit is distributed along the Iwasegawa, Tsunakinosawa, Uchimachizawa, and Hitouchizawa Rivers. Therefore, the main part of the avalanche flowed down along the Iwasegawa River, and another part of the avalanche climbed over the ridge and flowed into the Tsunakinosawa River. Another part of the avalanche flowed upstream of the Uchimachizawa and Hitouchizawa Rivers.

The source amphitheater is located 2.5 km southeast of the summit of the Tashirodake Volcano (Fig. 4-1; Fig. 5-1). The size of the amphitheater is 1.75 km across, and the scarp of the amphitheater is 150 meters high. The bottom of the amphitheater is relatively flat, but streams are eroding inside the amphitheater. Most of the rocks in the amphitheater are altered due to the past fumarolic activity. The Hirataki nuée ardente deposit partly covers this area (Fig. 4-2).

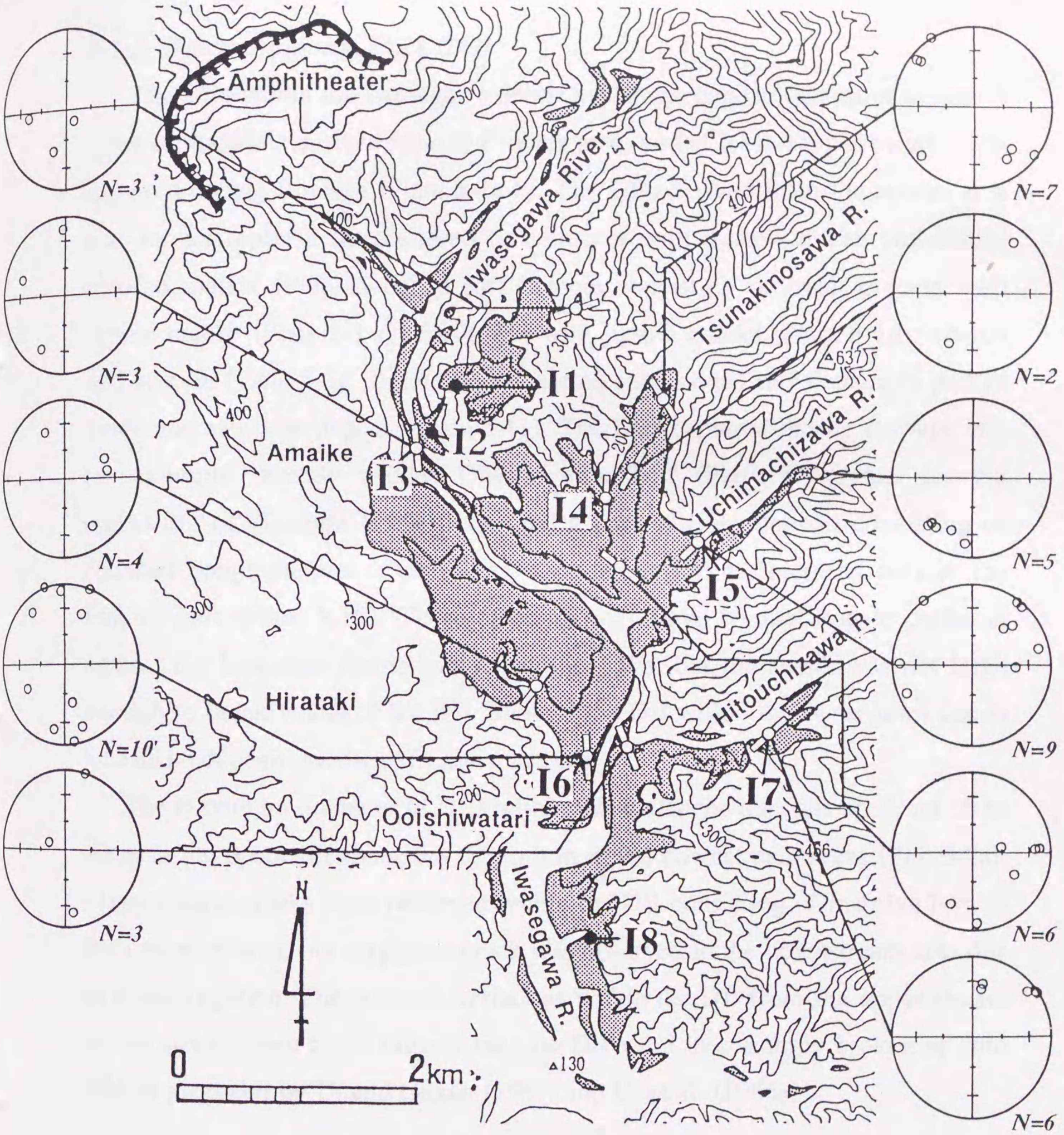

Fig. 5-1. Distribution of the Iwasegawa debris avalanche deposit, and the locality points: I1-I8, and the lineation of wood fragments. Eleven Schmidt nets beside the map show lineations of wood fragments. Schmidt net is projected to the lower hemisphere. "N" indicate total number of samples in each site. Open circle with open rectangle in the map shows the average orientation of the wood fragments at each site. The average orientation of the wood fragments coincide with the assumed local flow directions of the Iwasegawa debris avalanche, which inferred from the distribution of the deposit.

5-1-2. Debris avalanche block (DB)

The DBs within the Iwasegawa debris avalanche deposit consist of at least 8 types of materials derived from the source area, and at least 4 types of materials captured during flowage (Plate 5-1a-k). The DBs derived from the source area are, for example: a little altered tuff breccia with jigsaw cracks and black-colored matrix (Plate 5-1b); a tuff breccia consisting of fresh breccia with jigsaw cracks (Plate 5-1 c); fresh lava with jigsaw cracks (Plate 5-1d); altered tuff breccia (Plate 5-1e, f); and poorly-sorted subrounded tuff breccia (a part of block and ash flow deposit; Plate 5-1g). The DBs captured during flowage are, for example: weakly welded Obirakiyama Tuff (Plate 5-1i); tuff breccia consisting of siltstone (Plate 5-1j); and a part of river deposit consisting of rounded conglomerates (Plate 5-1k). One of the DB is fractured only at the bottom part (Plate 5-1h). These fractures may have formed due to collision against the basement formations or another DBs, but the shock was not large enough to break whole of the DB. Most of the DB within the Iwasegawa debris avalanche deposit consist of fragile materials.

The maximum diameter of DBs within the avalanche deposits are from 10 to 40 m in the upstream areas, but 0.5 to 3 m in the downstream areas (Fig. 5-2a). Many jigsaw cracks were observed within the DB consisting of massive lava in the upstream area, but no jigsaw crack was observed in the downstream area due to disaggregation. These lateral variations within the DB from the upper stream to the downstream areas suggest that the DB were increasingly broken up into DM as proposed by Ui and Gliken (1986) and Ui et al. (1986a).

5-1-3. Debris avalanche matrix (DM)

The DM in the Iwasegawa debris avalanche deposit consists of andesitic clasts derived from the source area, rhyolitic clasts of pumiceous tuff breccia captured during the flowage, conglomerates, and wood fragments (Plate 5-1*l*). The DM

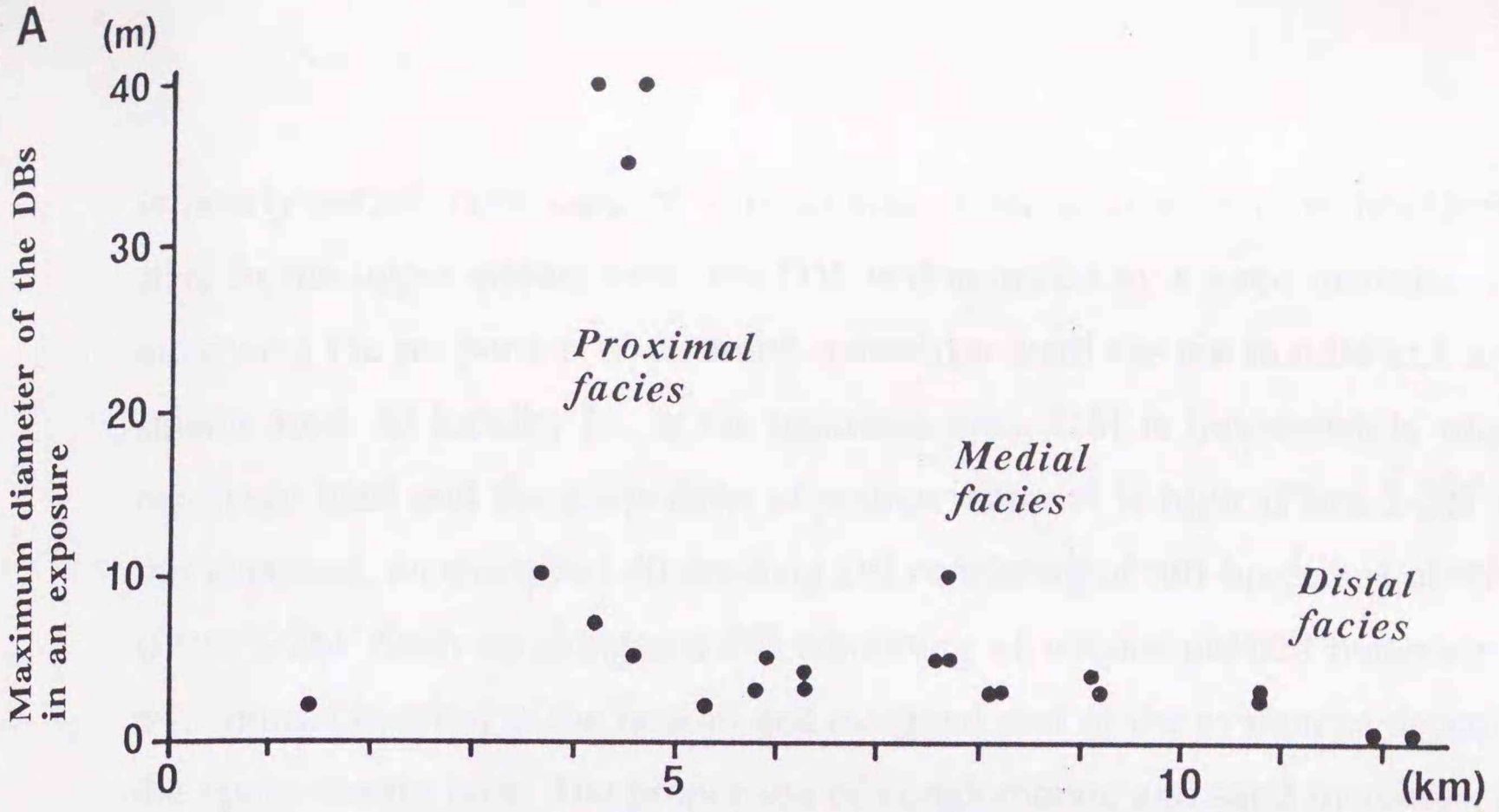

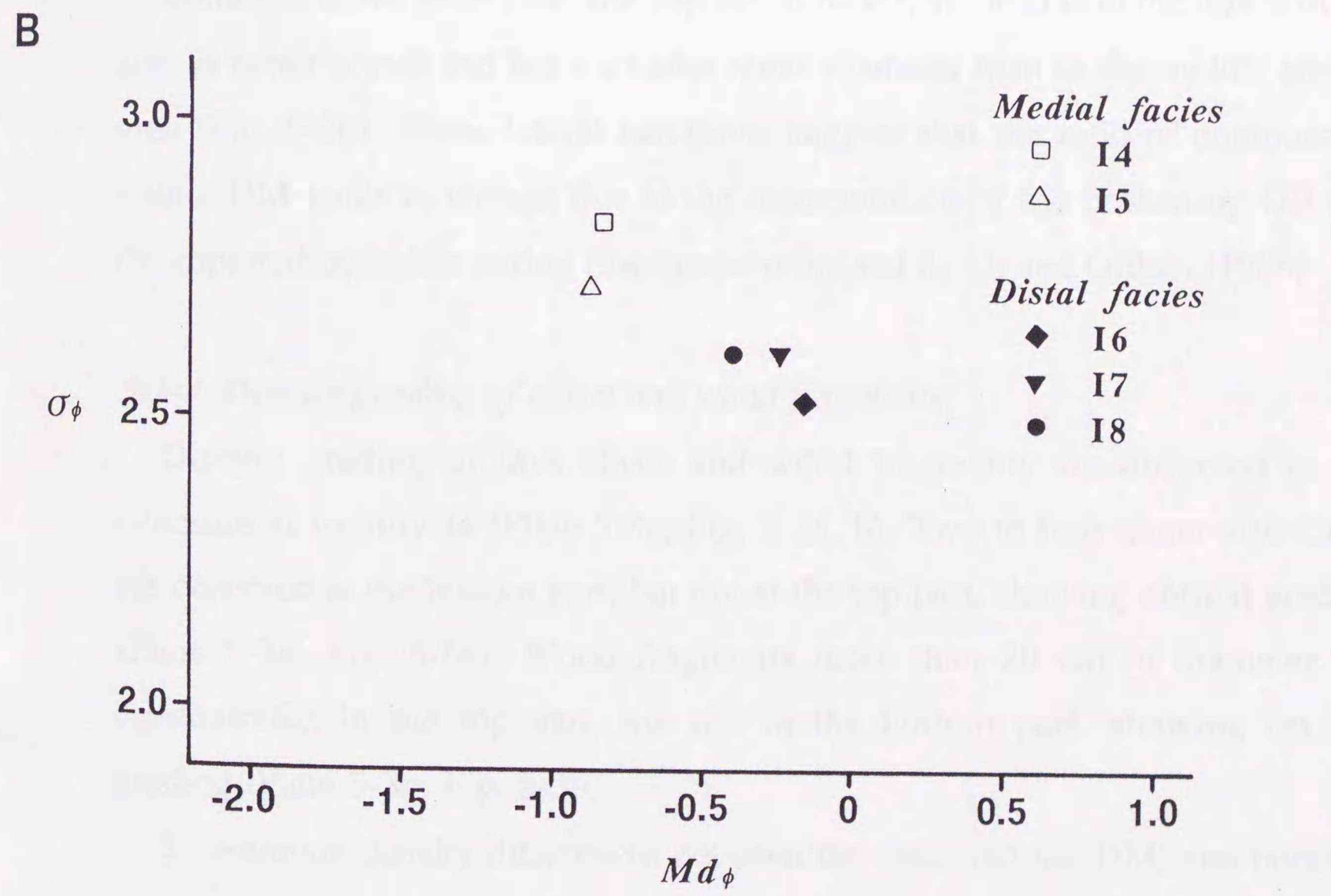

Fig. 5-2A-B. Lateral variation in size distribution of the Iwasegawa debris avalanche deposit. **A.** Maximum diameter of the DBs in an exposure. **B.** Md_ϕ-σ_ϕ diagram of the DM: $Md_\phi=\phi_{50}$, median diameter; $\sigma_\phi=(\phi_{84}-\phi_{16})/2$, sorting, where $\phi=-\log_2 d$, d=grain diameter (after Inman, 1952). Site of sampling points, I4-I8, are shown in Fig. 5-1. The maximum diameter of the DBs decreases toward the distal facies. The median diameter and the sorting of the DM became better in the distal facies than those in the medial facies.

is poorly-sorted, composed of various size of clasts from clay to boulders in size. In the upper stream area, the DM is dominated by source material, with increasing the proportion of captured material toward the the middle and lower stream area. At locality I1, in the upstream area, DM is incompletely mixed, relatively hard and the proportion of source material is high (Plate 5-2a). At this exposure, an elongated 40 cm-long DB consisting of tuff breccia is observed (Plate 5-2b). Such an elongated DB consisting of unconsolidated materials are sometimes observed at the bottom and marginal part of the avalanche deposit in the upper stream area. The proportion of conglomerate and sand increases, and that of clay decreases within the DM towards the lower stream area, due to an increase the proportion of captured river deposits.

Results of sieve analysis of the deposit showed that the DM in the downstream area is better sorted and has a smaller mean diameter than in the middle stream area (Fig. 5-2b). These lateral variations suggest that the ratio of components within DM tends to change due to the incorporation of the broken-up DB and the captured materials during flowage as proposed by Ui and Gliken (1986).

5-1-4. Density grading of clasts and wood fragments

Density grading of lava clasts and wood fragments are observed in the exposure at locality I4 (Plate 5-3a; Fig. 5-3a, b). Two to four meter-size clasts are observed at the bottom part, but not at the top part, showing normal grading (Plate 5-3a; Fig. 5-6a). Wood fragments more than 20 cm in diameter are concentrated in the top part, but not in the bottom part, showing reverse grading (Plate 5-3b; Fig. 5-3b).

To estimate density differences between the clast and the DM, and between the wood fragments and the DM, densities of clast, wood fragment, and DM were measured using the glass bead method (Sasaki and Katsui, 1981). In dry

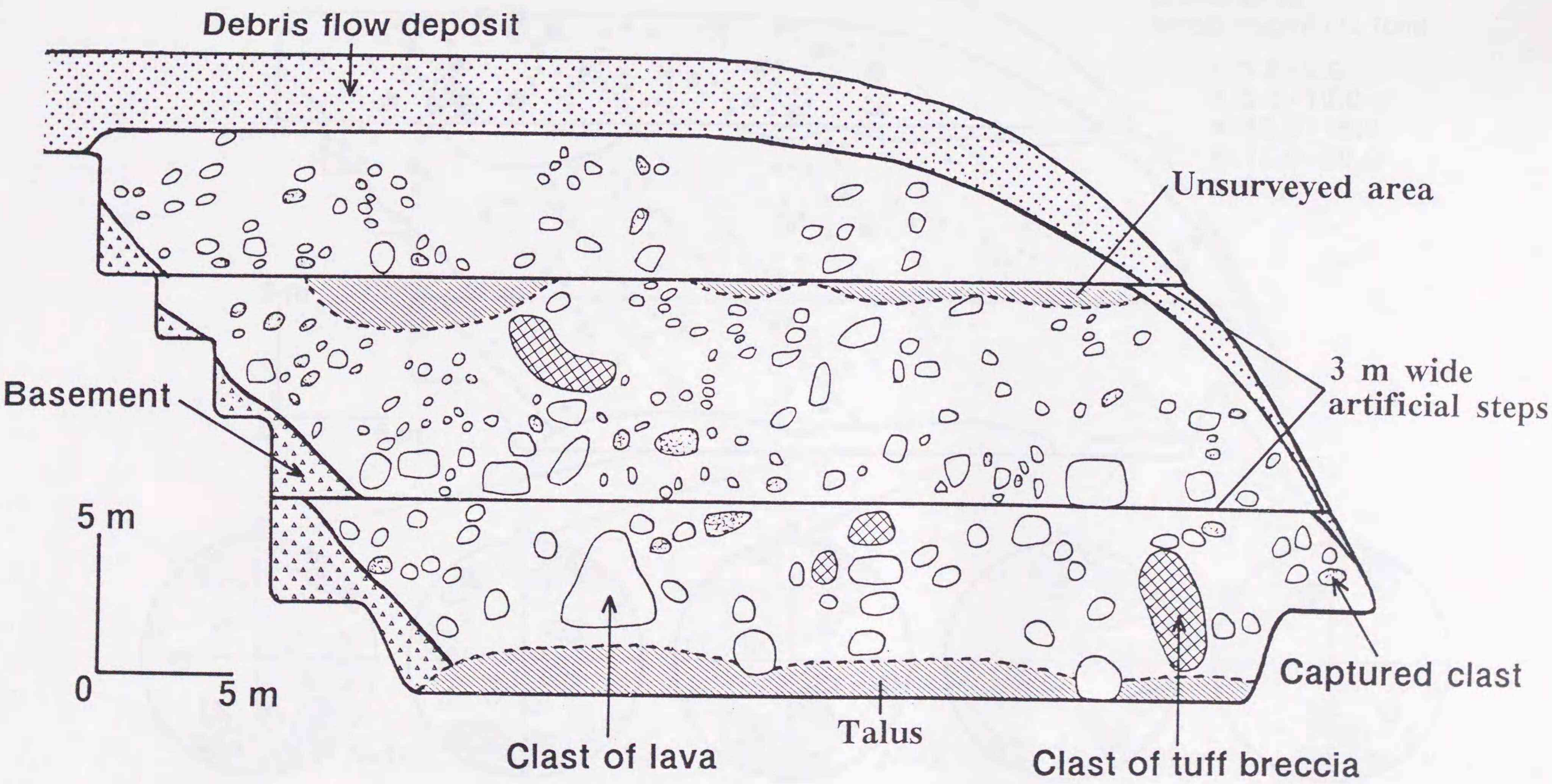

Fig. 5-3A. Schematic diagram of the exposure of the Iwasegawa debris avalanche deposit at the locality I4, a quarry site, showing size and distribution of clasts. Two horizontal lines are 3 m-wide artificial steps made during the construction. The apparent discontinuity of sedimentary structures between horizontal lines is due to these steps. Normal grading of the large clasts are observed.

B

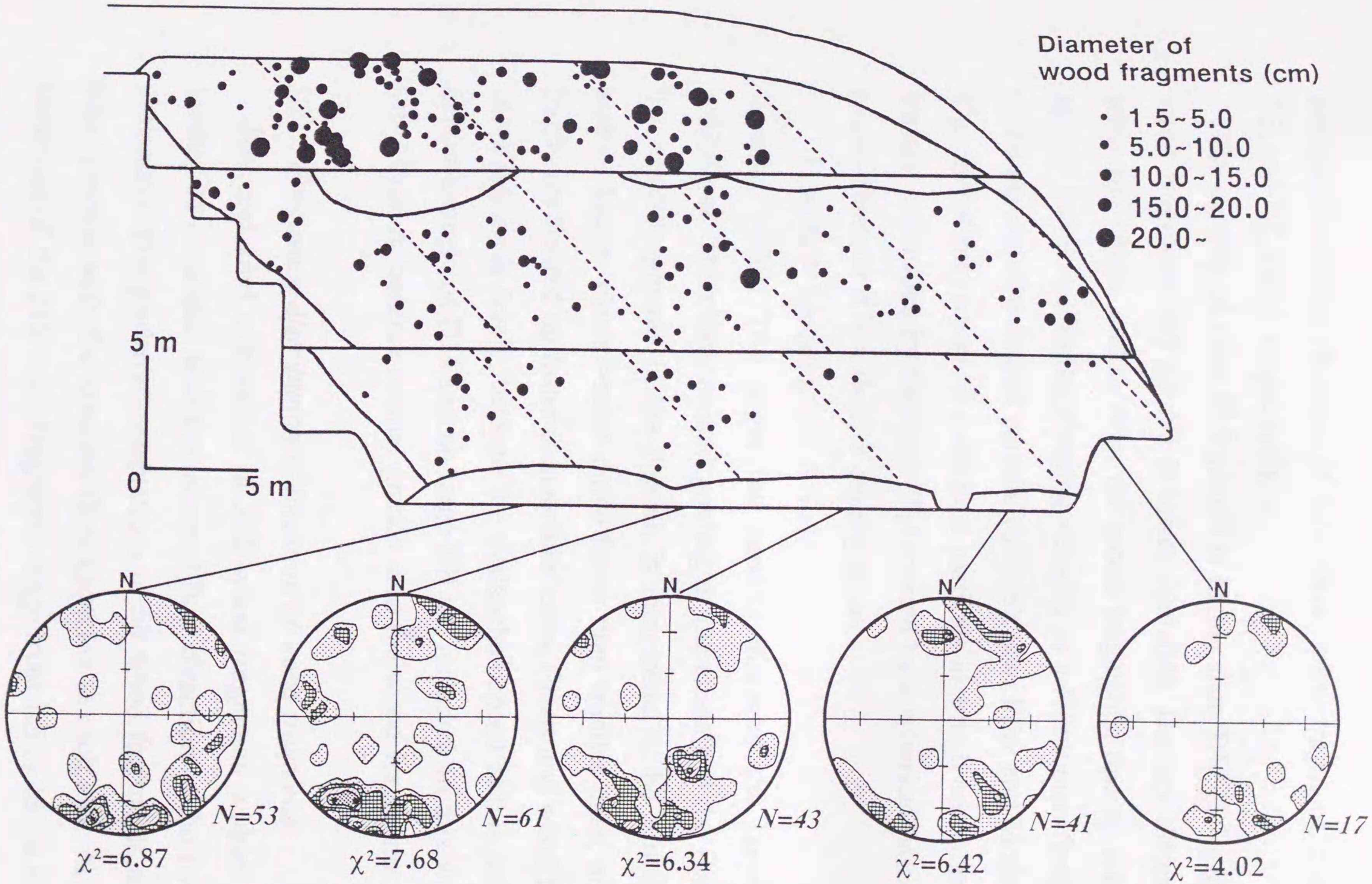

Fig. 5-3B. Schematic diagram of the same exposure, showing size distribution and frequency distributions of lineations of 215 wood fragments. Diameter of the wood fragments are indicated by the size of the solid circles at 5 cm intervals. Reverse grading of the wood fragments are observed. Broken lines in the upper figure indicate the five segments from the left-bottom contact at 5 m intervals. Five Schmidt nets represents the data at each segment. The Schmidt net is projected to the lower hemisphere. "N" indicate the total number of samples in each site. Each contour in the nets indicates 100i/N (i=1-5; N=total number). χ^2 value at each net is after Davis (1973). χ^2 value at 80 % of confidence level is 3.22, 90 % is 4.61, and 95 % is 5.99, respectively. The preferred orientation is approximately N-S direction, regardless of the distance from the contact.

condition, average densities of fresh lava, wood fragment, and DM were 2.5, 0.5, and 1.7 g/cm^3, respectively.

The density of clast (2.5 g/cm^3) is higher than DM (1.7 g/cm^3). Density of wood fragment (0.5 g/cm^3) is lower than DM. Density differences forced to settle the clasts, and to float the wood fragments, due to vibration or shock against the flow. Settling/floating velocity in a Newtonian fluid is proportional to the square of radius of particle (Stokes's law; Fritz and Moore, 1988, p.171). The rate of movement of individual particles in a high concentration dispersion are also controlled by the force (F_g) exerted by a spherical particle with density ϱ_s and diameter d in a fluid of density ϱ_f is:

$$F_g=1/6\ d^3\ (\varrho_s-\varrho_f)\ g$$

(Sparks, 1976). The larger the particle diameter the larger the force to settle/float. Therefore, normal grading of the clasts and the reverse grading of the wood fragments in the deposit is interpreted to be formed as following reason. Larger clasts settled down faster than smaller ones, and bigger wood fragments floated up faster than smaller ones. Clasts and wood fragments could move relatively freely, because the avalanche deposit at this point is composed almost entirely of DM and no large DB are included. In this way, the clasts in this exposure became normal graded, and the wood fragments reverse graded.

5-1-5. Frequency distribution of lineation of wood fragments

The preferred orientation of 215 wood fragments within the DM at the locality I4 coincides with the assumed flow direction of the Iwasegawa debris avalanche. The preferred orientations of 58 wood fragments at 11 other sites also coincide with the assumed flow direction at each site. At locality I4, the lineations of the 215 wood fragments range from 1.5 to 45 cm in diameter were measured using a clinometer (Plate 5-3b). The measured data were plotted using the Schmidt nets (Fig. 5-3b). Each net represents data at 5 m intervals from the

left side bottom contact. Their preferred orientation were approximately in a N-S direction, regardless of the distance from the bottom contact. The χ^2 values at each segment of 0-20 meters from the contact, are larger than 5.99 (Fig. 5-3b). These results shows that preferred orientations exist at these segments more than 95 % confidence level (Davis, 1973). But, the χ^2 value at the segment of 20-25 meters from the contact, are rather small (χ^2=4.02). This result might occur due to the less data (N=17) than the other segments.

The lineation of wood fragments at 11 other sites were also measured (Fig. 5-1). The number of measured wood fragments range from 2 to 10 at each site, and again the results were plotted on the Schmidt nets. Assumed flow lineations for all 12 sites are shown on the distribution map (Fig. 5-1). These results suggest that the avalanche flowed down a steep slope, and surmounted a ridge 150 meters high. The avalanche flowed down the slope roughly from north to south. However, the avalanche flowed upstream in a local tributary at the distal area.

The reason for the coincidence between the preferred orientations of wood fragments and the local flow directions of the avalanche inferred from the distribution can be interpreted as follows. The Iwasegawa debris avalanche deposit is composed of DB and DM, which forms massive structure. It is impossible to form such a structure within a turbulent flow (Fritz and Moore, 1988, p.259). This structure suggest that the Iwasegawa debris avalanche flowed in a laminar condition. When the laminar viscous flow runs down slope, shear stress is produced at the bottom portion, parallel to the flow, due to a velocity gradient. This shear stress dominated portion at the bottom of the flow is called the laminar boundary layer (eg. Allen, 1985, p.13). The form drag (Kubo et al., 1987, p.376, p.818) of wood fragments within the laminar boundary layer were affected by the shear stress. The form drag is at a minimum when the projected area of wood fragment toward the flow direction is smallest. Therefore,

captured wood fragments were rotated and aligned themselves parallel to the flow direction of minimum form drag by shear stress. Thus the preferred orientation of wood fragments coincide with the assumed local flow direction of the avalanche.

5-1-6. Captured clasts at the bottom part of the deposit

The Iwasegawa debris avalanche deposit, seven meters thick, lies on altered white tuff breccia at the locality I2 (Fig. 5-1; Plate 5-4a). The boundary is sharp, but irregular. Many 2 to 10 cm-size fragments of captured white tuff breccia are present in the bottom zone of the avalanche deposit, within 30 cm from the bottom contact. At an outcrop located 120 m northeast of locality I2, the Iwasegawa debris avalanche deposit, 5 meters thick, lies on the altered brown to black colored tuff breccia (Plate 5-4b). Again, the boundary is sharp, but irregular. Many 1 to 3 cm-size fragments of tuff breccia are observed at the bottom of the avalanche deposit.

These textures may have formed due to the cessation of the avalanche, before the captured fragments completely mixed with the DM. During flowage, a strong shear stress and high pressure were concentrated at the bottom part of the avalanche due to the build up of a velocity gradient and the pressure of its own weight. These textures at the bottom of the deposit should have formed by capturing and incorporation of basement formations due to high shear stress and high pressure at the bottom of the flow.

5-1-7. Sedimentary structure of the bottom part of the deposit

A sedimentary structure at the bottom part of the Iwasegawa debris avalanche deposit is observed at the locality I3 (Fig. 5-1; Fig. 5-4; Plate 5-5). At this site, the Iwasegawa debris avalanche deposit, 5 meters thick, lies on the welded Obirakiyama Tuff. The ratio between source and captured materials within the

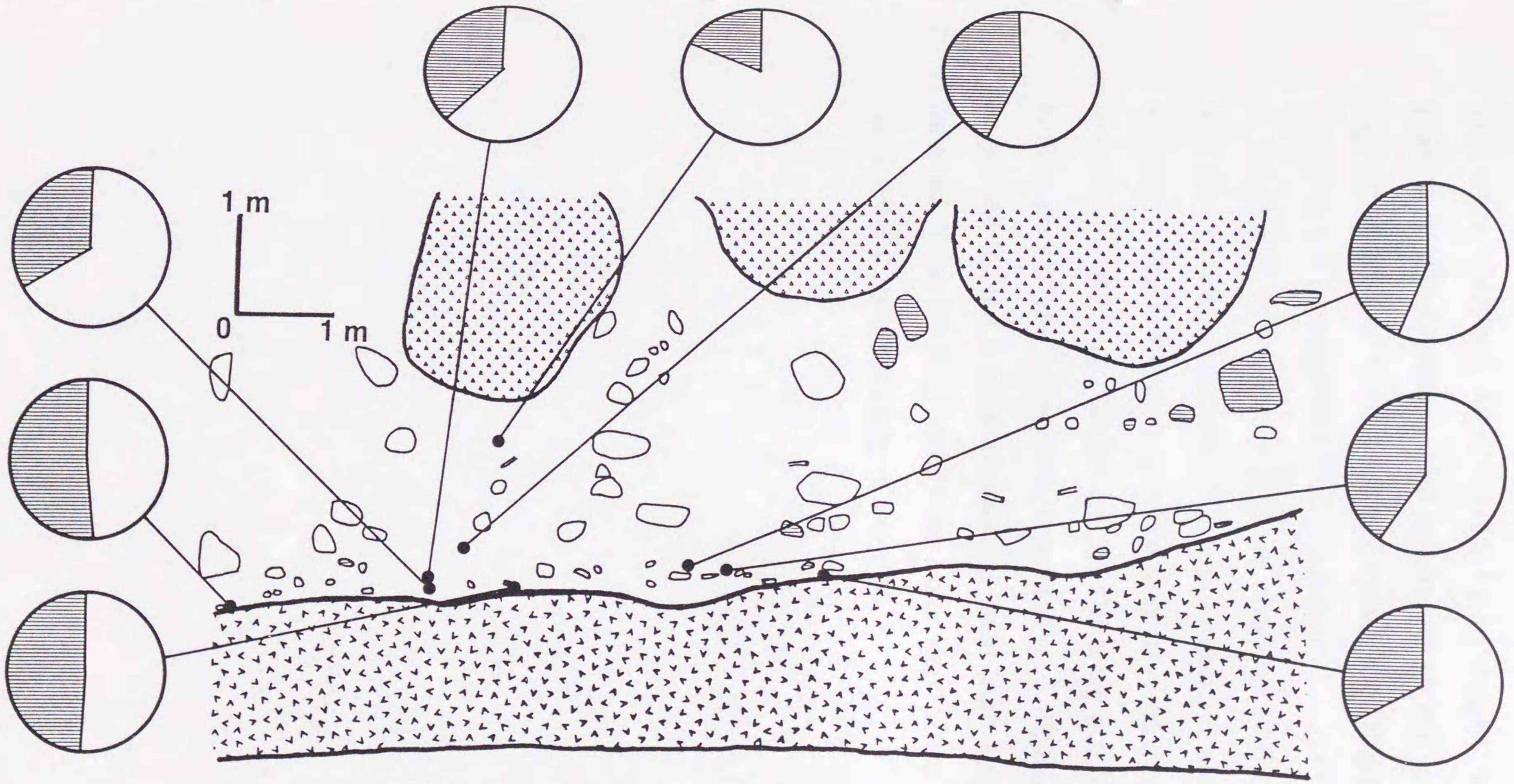

DB made of tuff breccia (from source area)
clast of lava and tuff breccia (from source area)
captured clast : tuff and siltstone (from basement)
wood fragment
Obirakiyama tuff (basement)

Fig. 5-4. Sedimentary structure of the bottom part of the Iwasegawa debris avalanche deposit and the ratio between the source and the captured material within the DM (9 circles). This outcrop is located at I3. The Iwasegawa debris avalanche deposit, 5 m in thickness, overlie on the welded Obirakiyama Tuff. Reverse grading of DBs and clast is observed at the bottom part. The ratio of captured clasts within the DM, shaded part in the circle, tends to be higher at the bottom part than at the upper part.

DM were analyzed. DM, 0.5-1.0 kg in weight, were sampled from different heights in this exposure. The results are shown on the circles in the Fig. 5-4. The proportion of captured clasts within the DM, shaded part in the circle, are higher at the bottom level of this outcrop.

Large DB up to 2 m in size are observed in the upper levels of the deposit. The size of the clasts near the bottom contact are smaller than in that of the upper part. Such a reverse grading may have formed by dispersive pressure, due to collision of clasts. Larger fragile DB were not found at the marginal and the bottom part of the Iwasegawa deposit (Fig. 5-4). Such fragile material cannot be preserved within a flow possessing such high shear stress. Thus, the DB are inferred to be carried within the inner part of the avalanche, due to the high yield strength and viscosity of the DM.

A

B

Plate 5-1. A. Example of the DB composed of altered tuff breccia derived from the source area (black-colored part, 2 m in width), and the captured DB composed of the chloritized brecciated siltstones (green-colored part at the lens-cap, 50 cm in width). Locality point is at I6 (Fig. 5-1). **B.** Example of the DB composed of a little altered breccia with jigsaw cracks and black-colored matrix. Locality point is at the 170 m east from I4 (Fig. 5-1).

C

D

Plate 5-1. C. Example of the DB composed of a tuff breccia made of fresh breccia with jigsaw cracks and black-colored matrix at I3. **D.** Example of the DB made of fresh lava with jigsaw cracks at 170 m NE from I2.

E

F

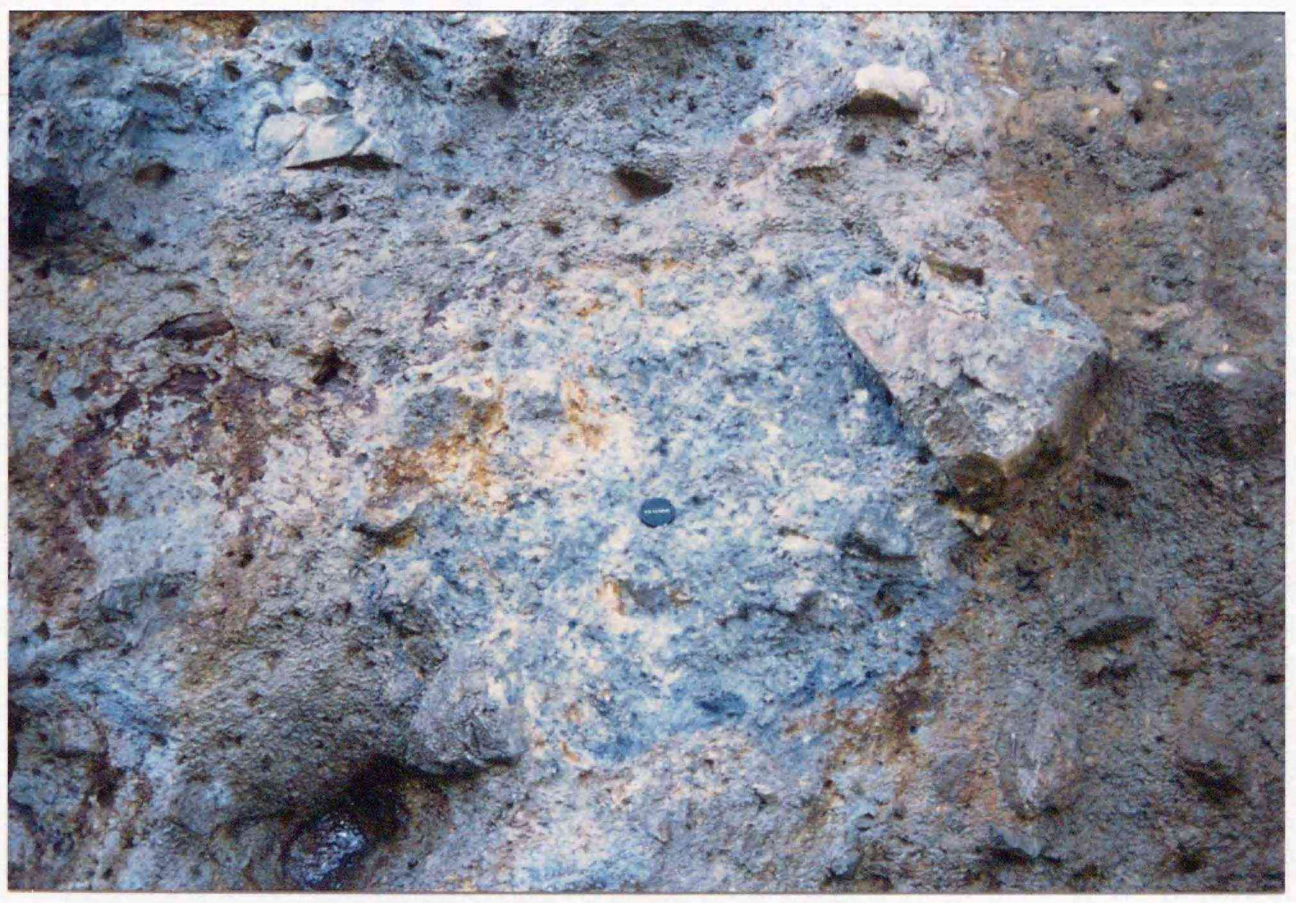

Plate 5-1. E. Example of the DB made of altered tuff breccia at I6. **F.** Example of the DB made of highly altered tuff breccia at I6.

G

H

Plate 5-1. G. Example of the DB composed of poorly-sorted tuff breccia (a part of the block and ash flow deposit). Jigsaw cracks are observed in the breccia. Locality point is at 170 m SW from I1. **H.** Example of the DB which fractured only at the bottom portion. These fractures might have formed due to collision against the basement formations or another DB, but the shock was not large enough to fracture whole of the DB. Locality point is at 750 m NNE from I6.

I

J

Plate 5-1. I. Example of the DB captured during flowage, consisting of weakly welded Obirakiyama Tuff. Locality point is at 600 m WSW from I5. **J.** Example of the DB made of tuff breccia composed of chloritized brecciated siltstones. Locality point is at I6.

K

L

Plate 5-1. K. Example of the DB captured during flowage, composed of a part of the river deposit made of rounded conglomerates. Locality point is at I6. **L.** Example of the DM at locality I4. The DM is composed of andesitic clasts derived from the source area, rhyolitic clasts of pumice tuff breccia captured during the flowage, and wood fragments. The DM is poorly-sorted, consisting of the various kind of materials from clay to boulders in size.

A

B

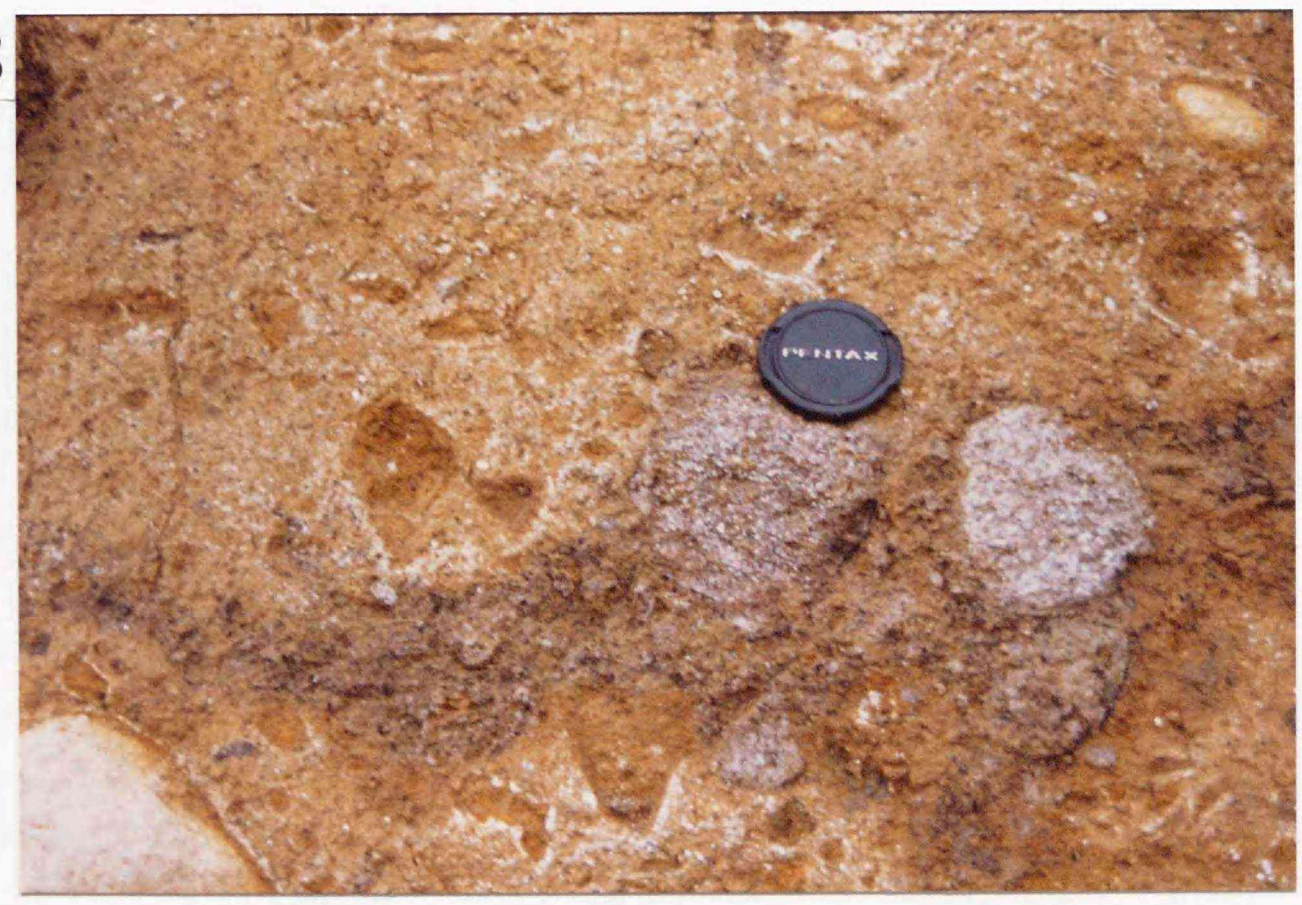

Plate 5-2. A. Example of the DM at the upstream area (I1). The DM is incompletely mixed, relatively hard, and the proportion of the source material is high. **B.** Close-up of the middle part of the Plate 5-2a. An elongated DB, 40 cm-long, made of unconsolidated tuff breccia is observed.

A

B

Plate 5-3. A. The exposure at locality I4. Normal grading of the larger clasts, up to 4 meters in diameter, are observed at this exposure. The size of the exposure is 20 m in height and 40 m in width. Basement formation made of reworked deposit of the Obirakiyama Tuff is exposed at the lower-left part of the exposure. Sketch of the exposure is shown in Fig. 5-3a. **B.** Example of the wood fragment including in the DM in this exposure. The lineations of 215 wood fragments range from 1.5 to 45 cm in diameter were measured using a clinometer (Fig. 5-3b).

A

B

Plate 5-4. A. The texture at the bottom part of the Iwasegawa debris avalanche deposit at I2. The avalanche deposit lies on the altered white tuff breccia. The boundary is sharp, but irregular. Many 2 to 10 cm-size fragments composed of captured white tuff breccia are observed at the bottom part, within the zone of 30 cm in height from the bottom contact. **B.** The texture at the bottom part of the avalanche deposit at 120 m NE from I2. The avalanche deposit lies on the altered brown to black-colored tuff breccia. The boundary is sharp, but irregular. Abundant fragments, 1 to 3 cm in size, made of captured tuff breccia are observed at the bottom of the avalanche deposit. These textures should have formed by capturing and incorporation of basement formations due to the high shear stress and the high pressure at the bottom part of the flow.

Plate 5-5. Sedimentary structure at the bottom part of the avalanche deposit at locality I3. The avalanche deposit, 5 meters thick, lies on the welded Obirakiyama Tuff. The large DBs, up to 2 m in size, are observed in the upper levels of the deposit. The size of the clasts at the bottom level is smaller than in that of the upper level. This reverse grading may have formed by dispersive pressure due to collision of clasts. Sketch of this outcrop is shown in Fig. 5-4.

5-2. Kaida debris avalanche deposit, Ontake Volcano

5-2-1. Distribution of the Kaida debris avalanche deposit

The Kaida debris avalanche deposit is distributed along the Suekawa and the Nishino Rivers at the eastern foot of the Ontake Volcano (Fig. 5-5; Plate 5-6a-i). The maximum thickness of the Kaida debris avalanche deposit is ca. 30 m at locality K1 (Fig. 5-5). The estimated volume of the avalanche deposit in the surveyed area is ca. 0.1 km^3. The total volume of the deposits, which can be traced as far as 46 km from the source (Fig. 4-3), is more than 0.3 km^3. At locality L1, located as far as 30 km from the source, the altered Kaida avalanche deposit, 3 m in thickness, is observed (Fig. 4-3; Plate 5-6j). This outcrop is located at the upstream from the junction of the Nakano and the Kiso Rivers (Fig. 4-3). This distribution of the deposit suggest that a part of the Kaida debris avalanche flowed upstream from the junction of the Rivers. At locality L2, located as far as 29 km from the source, the Kaida debris avalanche deposit, 1.5 m in thickness, is observed (Plate 5-6k). At this outcrop, 80 cm-long elongated DB and small DBs, 10 cm in size, are included. At locality L3, located as far as 46 km from the source, the avalanche deposit is observed (Plate 5-6*l*). At this outcrop, 2 meters-long DB composed of tuff breccia with jigsaw cracks are still remained. Therefore, the Kaida debris avalanche deposits can be traced along the Nishino and the Kiso Rivers as far as at least 46 km from the source (Fig. 4-3). The vertical drop height from the source to this point is 2.5 km. Therefore, the H/L ratio is 0.05, indicating a great mobility of the Kaida avalanche. Because, the data from a catalog of around 200 debris avalanches shows that the H/L ratios are range from 0.05 to 0.18 (Siebert et al., 1987).

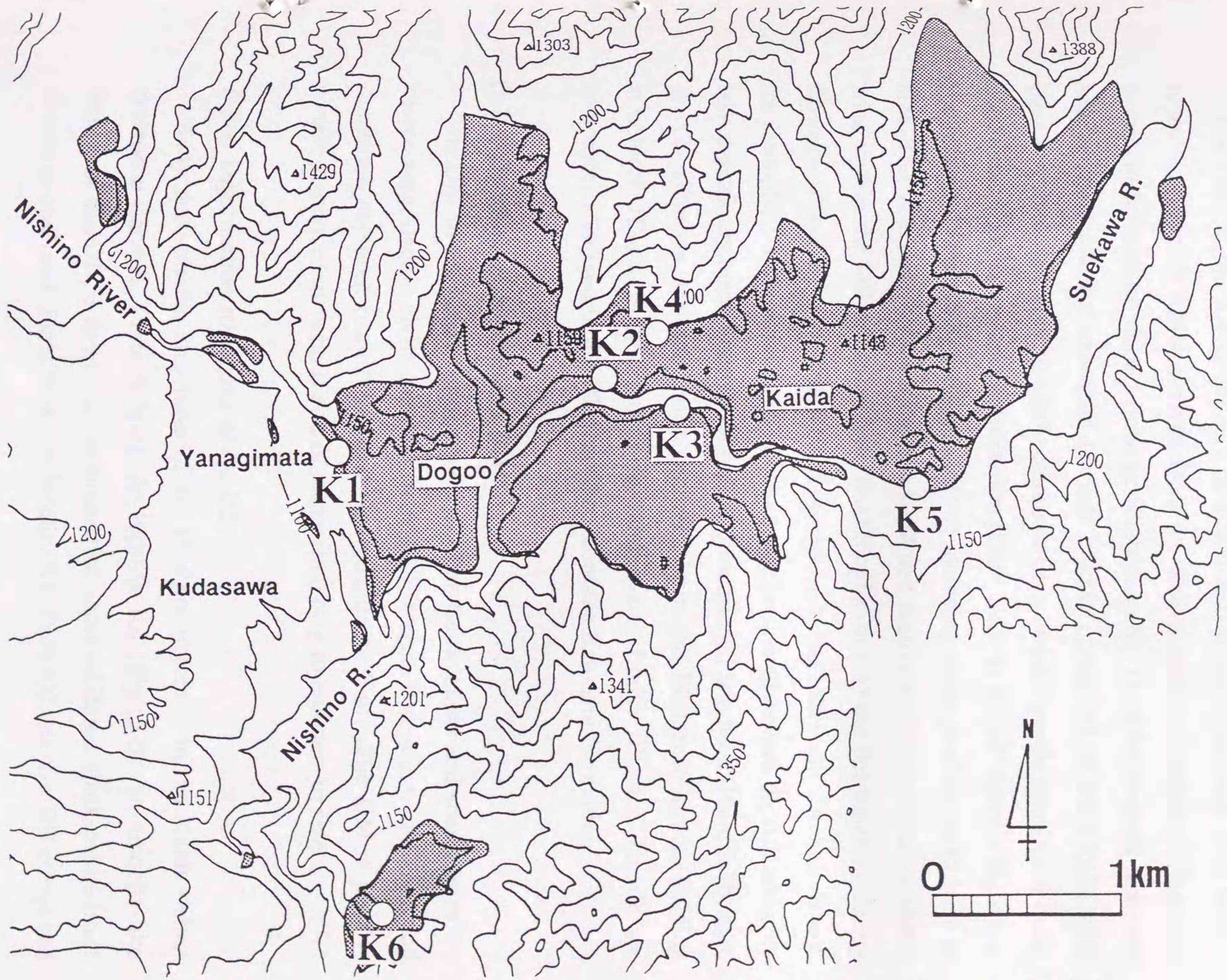

Fig. 5-5. Distribution of the Kaida debris avalanche deposit and the locality points, K1-K6.

5-2-2. Debris avalanche block (DB)

The DBs in the Kaida debris avalanche deposit are composed of at least 5 types of materials which derived from the source area; and captured from the basement formations during flowage (Plate 5-6a-h). The DBs derived from the source areas are, for example: (1) tuff breccia composed of the blocks with jigsaw cracks and gray to black-colored matrix, which partly shows red color due to the high temperature oxidization (Plate 5-6a-f); (2) tuff breccia including some scoriae (Plate 5-6g); (3) tuff breccia including some pumices up to 1 cm in size. The boundary between the black-colored matrix and red-colored oxidized zone within the DB are sometimes intermingled due to the deformation during flowage (Plate 5-6e, f). The DBs captured from the basement formations are, for example: (1) unconsolidated silty to sandy laminated rework deposit and silty lake deposit captured from the Kisodani Formation (Plate 5-6h; Plate 5-7b, c, d, g); (2) siltstone and sandstone captured from the Mesozoic strata. Folding structures (Plate 5-6h; Plate 5-7g) and minor faults (Plate 5-7b, d) are sometimes observed in the DBs captured from the Kisodani Formation.

5-2-3. Debris avalanche matrix (DM)

The DM in the Kaida deposit consists of andesitic clasts and scoria from the source area; dacitic clasts captured from the Kisodani Formation; and chert and sandstone captured from the Mesozoic strata (Plate 5-6i). The DM is poorly-sorted, composed of various size of clasts from clay to boulders in size.

5-2-4. Deformation structures of the DBs

Many deformation structures of the DBs are observed in the Kaida debris avalanche deposit (Plate 5-7a-h). At locality K6 (Fig. 5-5), an amoeba-like texture of the DB, 1 m in size, composed of unconsolidated black-colored tuff breccia is observed (Plate 5-7a). At locality K1, 200x500 cm-size DB composed

of the Kisodani Formation is exposed (Plate 5-7b). This DB is composed of an unconsolidated sandy reworked deposit intercalated with 2 to 10 cm-thick silt layers. The DB is deformed with lateral minor faults. The dislocations are from 1 to 10 cm inferred from the slightly displaced silt layers. At locality K2, an elongated DB composed of unconsolidated sandy to silty Kisodani Formation is exposed (Plate 5-7c). This outcrop is located near the bottom part of the deposit. The size of this DB is 10 to 30 cm wide and 3 m long. The enlargement of the upper part of this DB is shown in Plate 5-7d. Vertical minor faults are detected by the several millimeters to centimeters dislocation of silty layers. At locality K5, conjugate reverse faults within the DB are observed (Plate 5-7e, f). This DB is composed of a few cm-thick, brown to black-colored successive debris flow deposits. The successive layers show almost vertical dip, indicating the rotation during the flowage. The dislocations of each layer are a few centimeters to several ten's of centimeters. At locality K3, a folding structure, one meter-size DB is observed (Plate 5-7g). This DB is composed of a succession of a few centimeter thick silt layers. This outcrop is also located near the bottom part of the deposit. At locality K4, the thin Kaida debris avalanche deposit, 35 cm in thickness, lies on the hill composed of the Mesozoic strata (Plate 5-7h). This outcrop is located at the margin of the deposit. At the bottom of this debris avalanche deposit, a 150 cm-long elongated DB which composed of unconsolidated black-colored tuff breccia is observed.

The amoeba-like texture at the locality K6 (Plate 5-7a; Fig. 5-5) may indicate the processes of breaking up the DB composed of unconsolidated materials. The minor faults within unconsolidated sandy to silty layers at locality K1 and K2 (Plate 5-7b, d) suggest that these DBs reacted as a rigid bodies against the strong force in a short time. These faults may have formed due to the impact when the high velocity Kaida debris avalanche capturing these DBs from the basement. The conjugate faults at locality K5 (Plate 5-7e, f) suggest that this DB also

reacted as a rigid body. These faults may have formed due to the impact when high speed Kaida debris avalanche collided with basement at the curve points of the valleys. The elongated structures at locality K2 (Plate 5-7c) and K4 (Plate 5-7h), and folding structure at locality K3 (Plate 5-7g) suggest that these DBs reacted as plastic bodies. These elongated and folding structures may have formed by the shear stress at the marginal and bottom part of the flow due to a velocity gradient.

5-2-5. Lithic components within the DM

The lithic components within the DM at seven sites in the Kaida debris avalanche deposit were investigated (Fig. 5-6). The DM, 1-2 kg in weight at each site, were sieved. The lithic components, from 4 to 16 mm in size, were analyzed by hand picking. The number of analyzed grains were between 159 to 727 at each site. The lithics were divided into three components: (1) andesitic dense clasts and scoria fragments derived from the source area; (2) dacitic clasts captured from the Kisodani Formation; and (3) chert and sandstone captured from the Mesozoic strata.

The ratios of dacitic clasts within the DM at the sites which is located beside the areas of exposing the dacitic Kisodani Formation (at the sites where the analyzed grain numbers are N=331 and N=339), tend to have higher ratio of the material which was captured from the adjacent basement formations. Therefore, the lithic components within the DM tend to have a higher ratio of the material which was captured from the adjacent basement formations. This result suggests that the Kaida debris avalanche flowed down the slope capturing basement material, and the material immediately mixed with the DM.

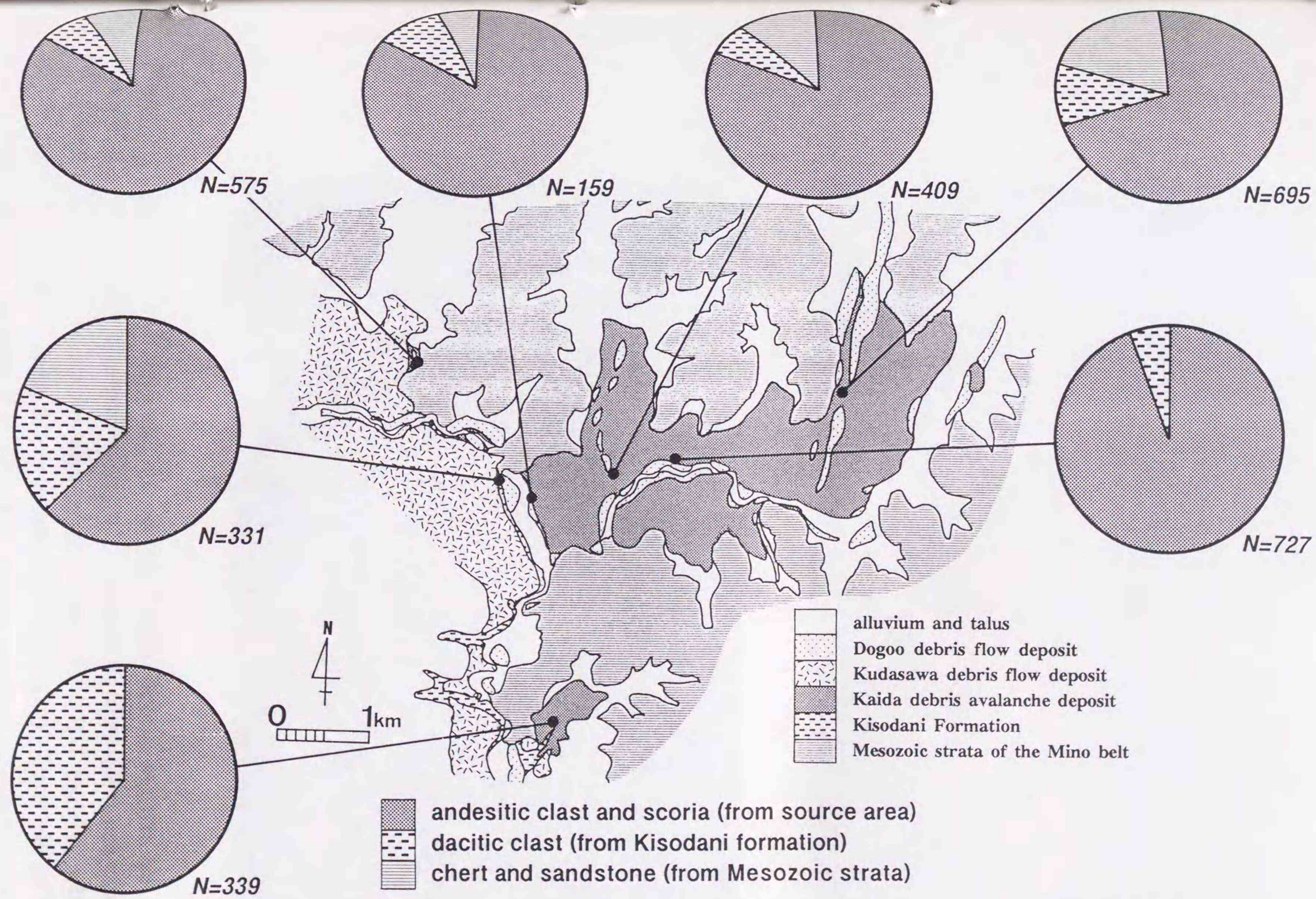

Fig. 5-6. Lithic components within the DM at seven sites in the Kaida debris avalanche deposit. The lithic components of the grains within the DM, from 4 to 16 mm in size, are shown in seven circles. The lithics were divided into three components: (1) dense-andesite clasts and scoria clasts derived from the source area, (2) dacite clasts captured from the Kisodani Formation, and (3) chert and sandstone clasts captured from the Mesozoic strata. The ratio of dacite clasts within the DM at the sites which is located beside areas of exposing the dacitic Kisodani Formation, tend to be higher than the other points. Therefore, the lithic components within the DM tend to have a higher ratio of the material which was captured from the adjacent basement formation.

A

B

Plate 5-6. A. Example of the DB in the Kaida debris avalanche deposit at locality K1 (Fig. 5-5). These DBs, up to 3 meters in diameter, are composed of the breccia with jigsaw cracks and gray to black-colored matrix, which partly shows red color due to high temperature oxidization. **B.** Example of the DB at 210 m SE from the locality K2. This DB is composed of the breccia with jigsaw cracks and gray to black-colored matrix, which partly shows high temperature oxidization.

C

D

Plate 5-6. C. Example of the DB at 150 m from locality K3. **D.** Example of the DB consisting of andesitic breccias with black-colored matrix at locality K1.

E

F

Plate 5-6. E. Example of the DB made of tuff breccia with black and red-colored matrix at 420 m SW from K3. **F.** Close-up of the Plate 5-6e. The boundary between the black-colored matrix and the red-colored oxidization zone within the DB are intermingled due to deformation during flowage.

G

H

Plate 5-6. G. Example of the DB made of tuff breccia including some scoriae (black-colored part) at 900 m NW from locality K2. **H.** Example of the DBs composed of unconsolidated silty lake deposit captured from the Kisodani Formation at 240 m SSE from K2. Deformation of the DBs is observed.

I

J

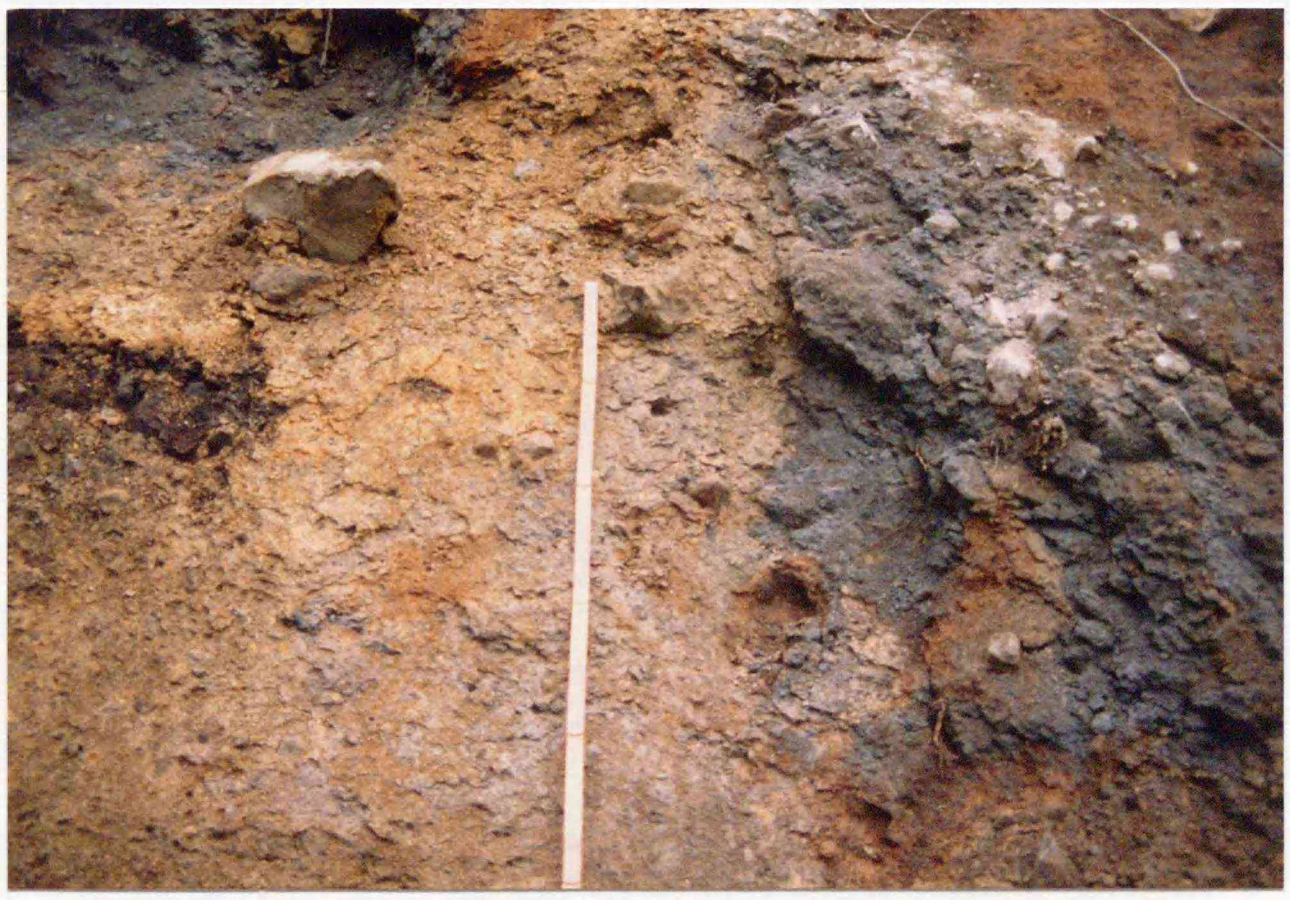

Plate 5-6. I. Example of the DM at the bottom part of the avalanche deposit at 360 m WNW from the locality K1. The DM consists of andesitic clasts from the source area; dacitic clasts captured from the Kisodani Formation; and chert (a clast at the left-bottom part) and sandstone captured from the Mesozoic strata. The DM is poorly-sorted consisting of the various kind of the materials from clay to boulders in size. **J.** The Kaida debris avalanche deposit at the locality L1 (Fig. 4-3) as far as 30 km from the source.

K

L

Plate 5-6. K. The Kaida debris avalanche deposit at the locality L2 as far as 29 km from the source area. The 80 cm-long elongated DB (dark colored DB at the top of the picture) and small 10 cm-size DBs (at the lens-cap) are observed. **L.** The Kaida debris avalanche deposit at the locality L3 as far as 46 km from the source area. The DB, 2 m in length, composed of tuff breccia with jigsaw cracks is observed at the bottom.

A

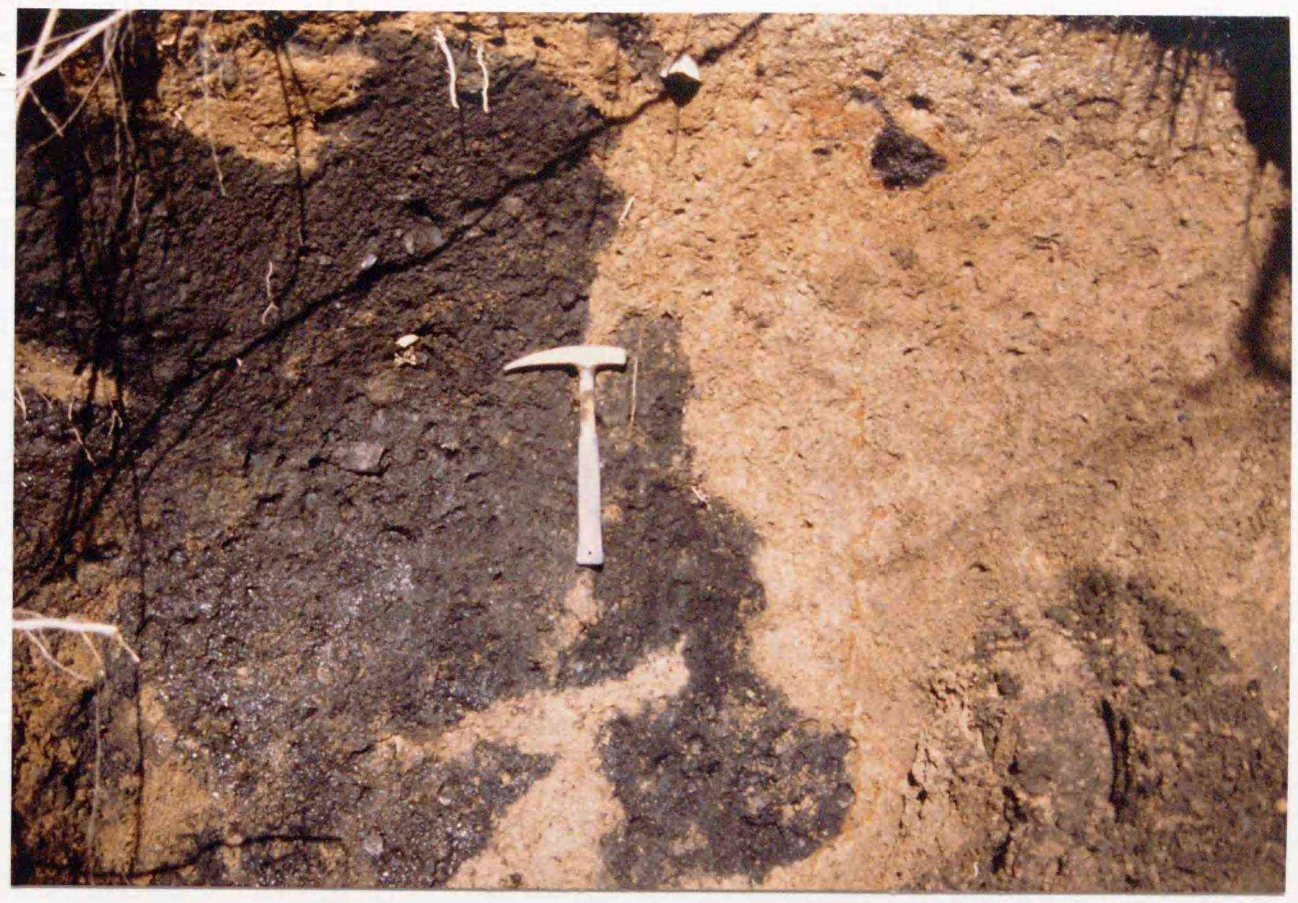

B

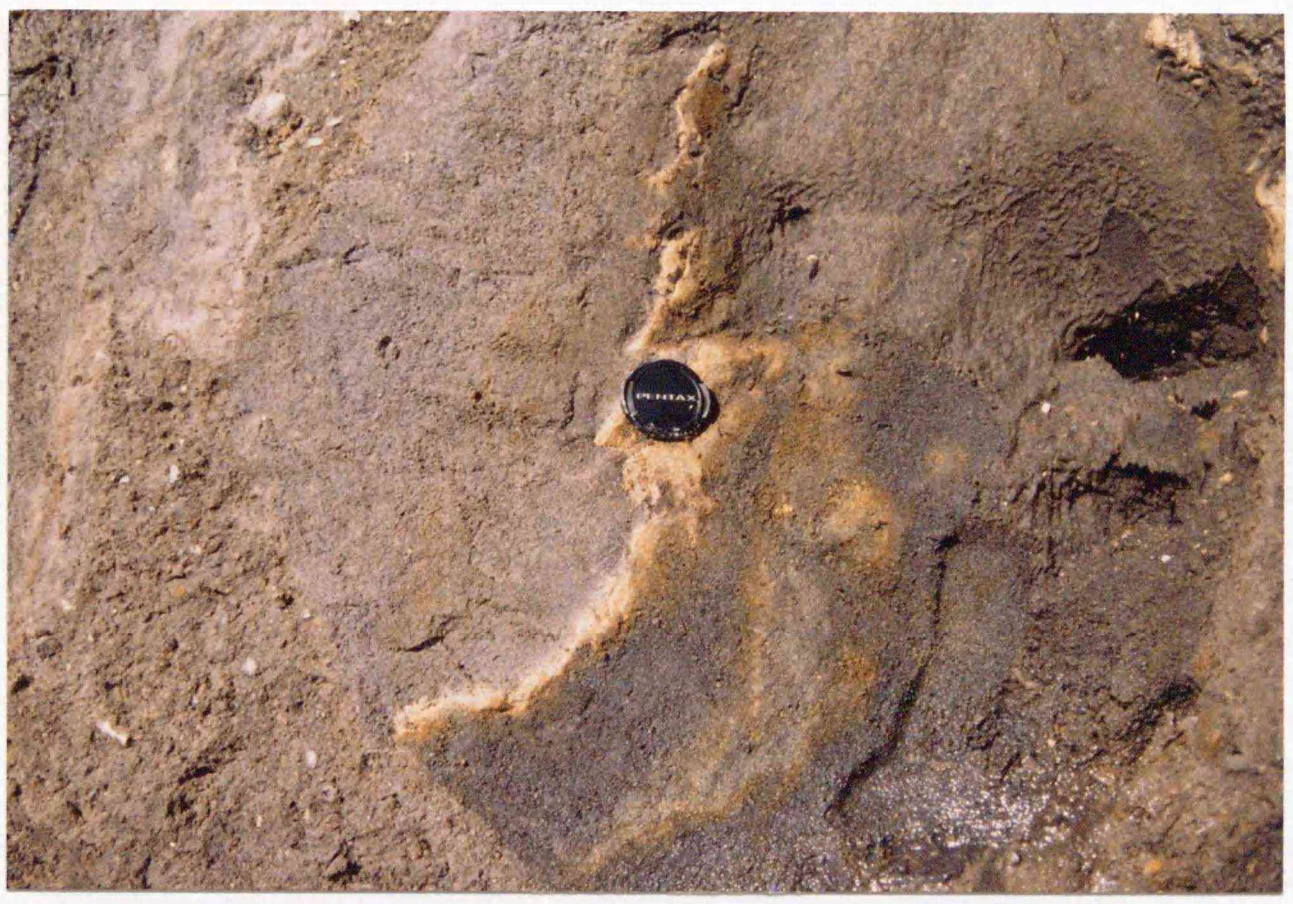

Plate 5-7. A. An ameoba-like texture of the DB, 1 m in size, composed of unconsolidated black-colored tuff breccia at locality K6 (Fig. 5-5). **B.** The DB, 200x500 cm in size, composed of an unconsolidated sandy reworked deposit intercalated with 2 to 10 cm-thick silt layers at locality K1. The DB is deformed with lateral minor faults. The dislocations are from 1 to 10 cm inferred from the slightly displaced silt layers.

C

D

Plate 5-7. C. An elongated DB composed of unconsolidated sandy to silty layers captured from the Kisodani Formation at locality K2. This outcrop is located near the bottom part of the deposit. The size of this DB is 10 to 30 cm wide and 3 m long. **D.** Enlargement of the upper-left part of the DB. Vertical minor faults are detected by the several millimeters to centimeters dislocations of the slit layers. Elongation of the DB are also observed.

E

F

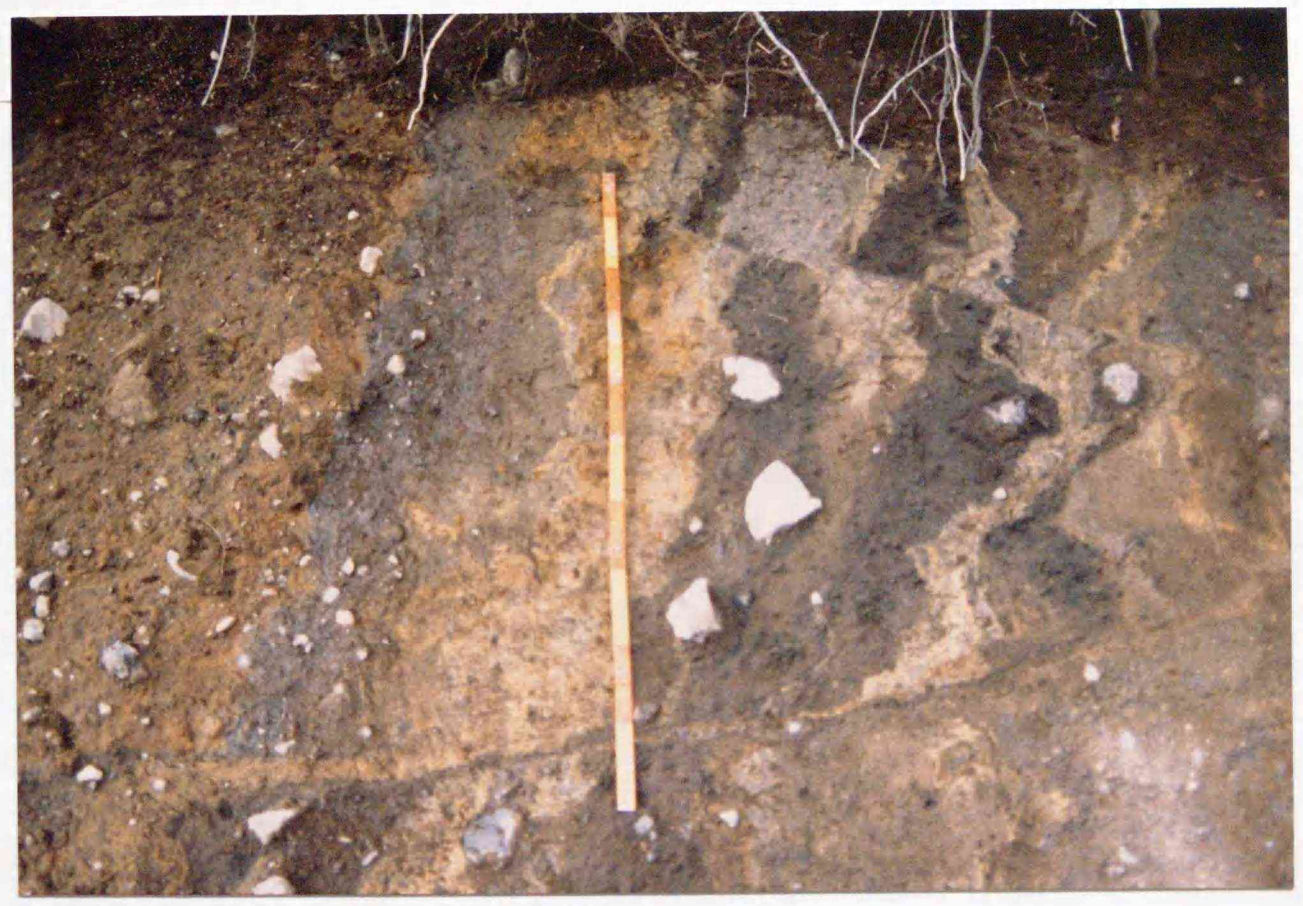

Plate 5-7. E. The conjugate reverse faults within the DB which composed of a few cm-thick, brown to black-colored successive debris flow deposits at the locality K5. The dips of the debris flow layers are nearly vertical due to the rotation during the flowage. **F.** Close-up of this DB. The dislocations of each layer are a few centimeters to several ten's of centimeters.

G

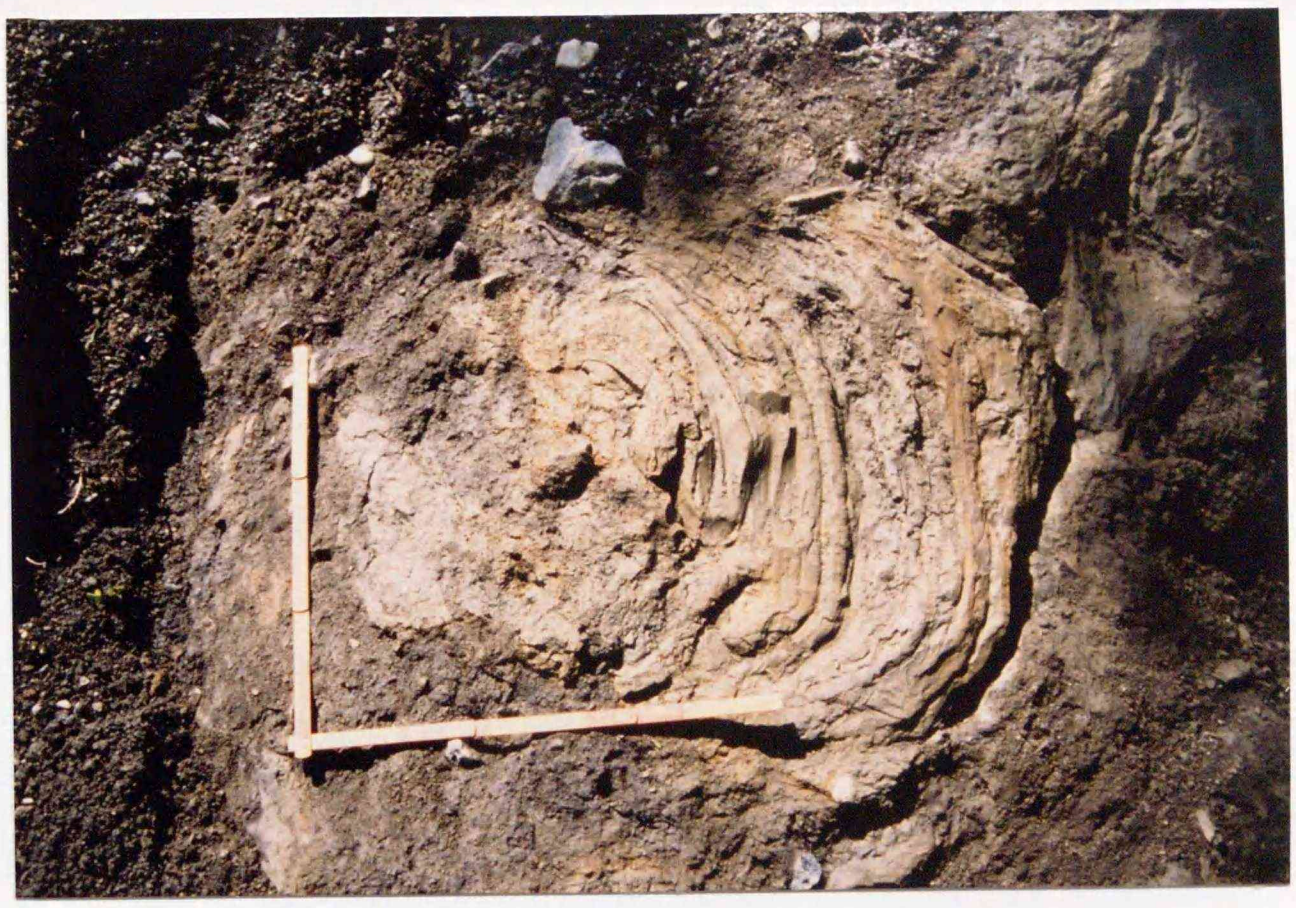

H

Plate 5-7. G. A folding structure of the DB composed of a succession of a few centimeter-thick silt layers at locality K3. This outcrop is located at the bottom part of the deposit. **H.** An elongated 150 cm-long DB, composed of unconsolidated black-colored tuff breccia at the bottom part of the Kaida debris avalanche deposit, 35 cm in thickness, which overlies the hill. This outcrop is located at K4, at the margin of the deposit.

Chapter 6. Pyroclastic flows and deposits

6-1. Komagatake 1929 pyroclastic flow deposits

6-1-1. Outline of the 1929 eruptions

On June 17, 1929, the Komagatake Volcano erupted for a day after the 73 years' dormancy (Plate 6-1a, b; Katsui et al., 1975; Katsui et al., 1986; Katsui et al., 1989). At this eruption, the Ko-a air fall, pyroclastic surges, and pyroclastic flows were distributed around the Volcano. At this eruption, no major precursor phenomenon occurred. On June 15, the Komagatake Volcano was rumbled. On June 16, small insensible two earthquakes occurred. At 0:30 on June 17, small eruptions were started. At 9:53, the mode of the eruptions were changed into the plinian phase. The height of the eruption column reached 13.9 km (Plate 6-1b), and the air fall were distributed toward the SE direction. From 12:30, small pyroclastic flows occurred. At 14:00, the height of the eruption column was 13.1 km. From 14:30, number of fall back pumices into the amphitheater were increased, and many pyroclastic flows were observed (Plate 6-1a). From 20:00, intensity of the air fall was increased again. At 24:00, the intensity of the activity was decreased. At 3:00 on June 18, the eruption was finished. On June 19, secondary mud flows were generated at the NE foot of the Volcano.

The Ko-a air-fall deposit was distributed toward the SE direction from the Volcano. At Shikabe, 12 km NE from the crater, Ko-a air-fall deposit, 1 m in thickness, was buried the village (Plate 6-1c). The pyroclastic flow deposits were distributed around the Volcano (Plate 6-1d, e; Fig. 4-6; Fig. 6-1a). During this eruption, two person were dead, 4 person were injured, and 365 houses were burned or destroyed.

At this eruption, the previous Ansei Crater was buried and a new Showa 4 crater, 230 m in diameter, 50 m in depth, was opened at the southeast part of the previous Ansei crater (Plate 6-1g). Bread crust bombs were projected into the air and scattered around the amphitheater (Plate 6-1f). The thickness of the air-

fall deposit within the amphitheater is more than 100 m. The welded Ko-a air-fall deposit are observed at the walls in the 1942 fissure (Plate 6-1h). At the rim of the amphitheater, several fissures were opened, due to the compaction of the air-fall deposit in the amphitheater (Plate 4-3g). The better-sorted thin pyroclastic surge deposits are distributed around the Volcano (Fig. 4-6; Plate 6-1i, j, k; Moriya, 1983, p.13-15; Moriya, 1984a). The surface of these pyroclastic surge deposits shows the dune structure (Plate 6-1i). The Ko-a air-fall deposit can be subdivided into the five fall units, Ko-a_1-a_5 (Plate 6-1*l*). Most of the pyroclastic flows occurred during the Ko-a_4 stage (Katsui et al., 1986).

6-1-2. Distribution and characteristics

The main 1929 pyroclastic flow deposits were distributed toward the E, N, NW, and SW direction (Fig. 6-1a). The volume of these pyroclastic flow deposits were ca. 0.14 km^3 (Katsui et al., 1986). These pyroclastic flow deposits were previously surveyed by Kuno (1941), Moriya (1983, p.11-13), Moriya (1984b), and Suzuki et al. (1986). Kuno (1941) described the distinctive characters of the pyroclastic flow deposits and those formed by the air-fall pumice deposits. Moriya (1983, 1984b) showed the characteristic surface morphology of the pyroclastic flows at the NW slope, such as pyroclastic levees, lobes, gullies, and hills. Suzuki et al. (1986) analyzed grain size and component variation of the pyroclastic flow and the pyroclastic surge deposits according to the distance from the vent. They showed that the pyroclastic flow (a valley-type pyroclastic flow) was a high-concentration, low-velocity (ca. 14 km/h) flow; and the pyroclastic surge (a ridge-type pyroclastic flow) was a low-concentration, high-velocity (>200 km/h) flow.

The sections of the pyroclastic flow deposits are observed at the walls in the Oshidashisawa Valley at the NW slope of the Volcano (Fig. 6-1b; Plate 6-2a-c). Succession of more than eight pyroclastic flow deposits are exposed at these sections (Plate 6-2a, c). Pumice-concentrated layers (PL) are observed at the top of the each pyroclastic flow deposit at these sections (Plate 6-2a). Some of

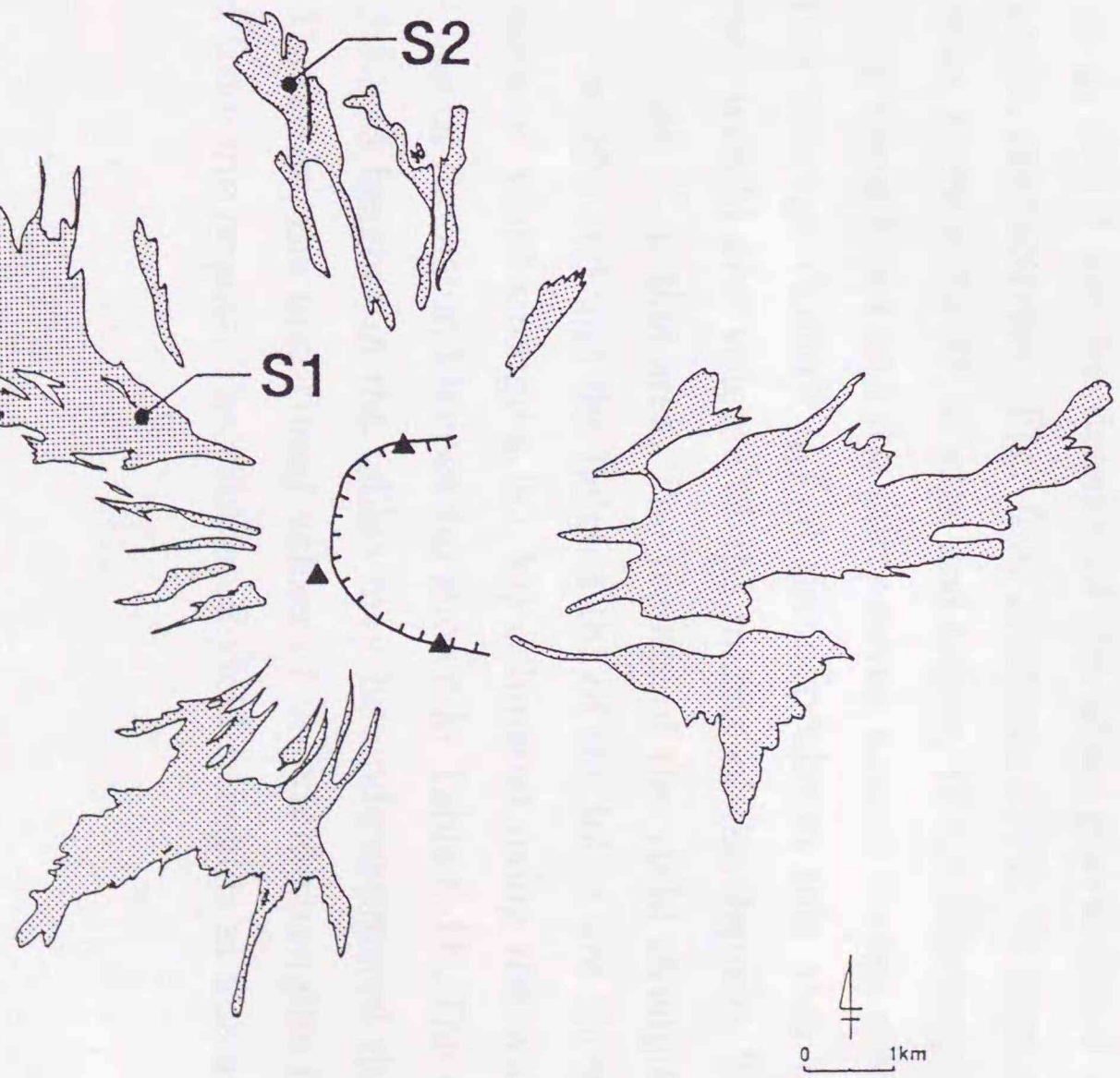

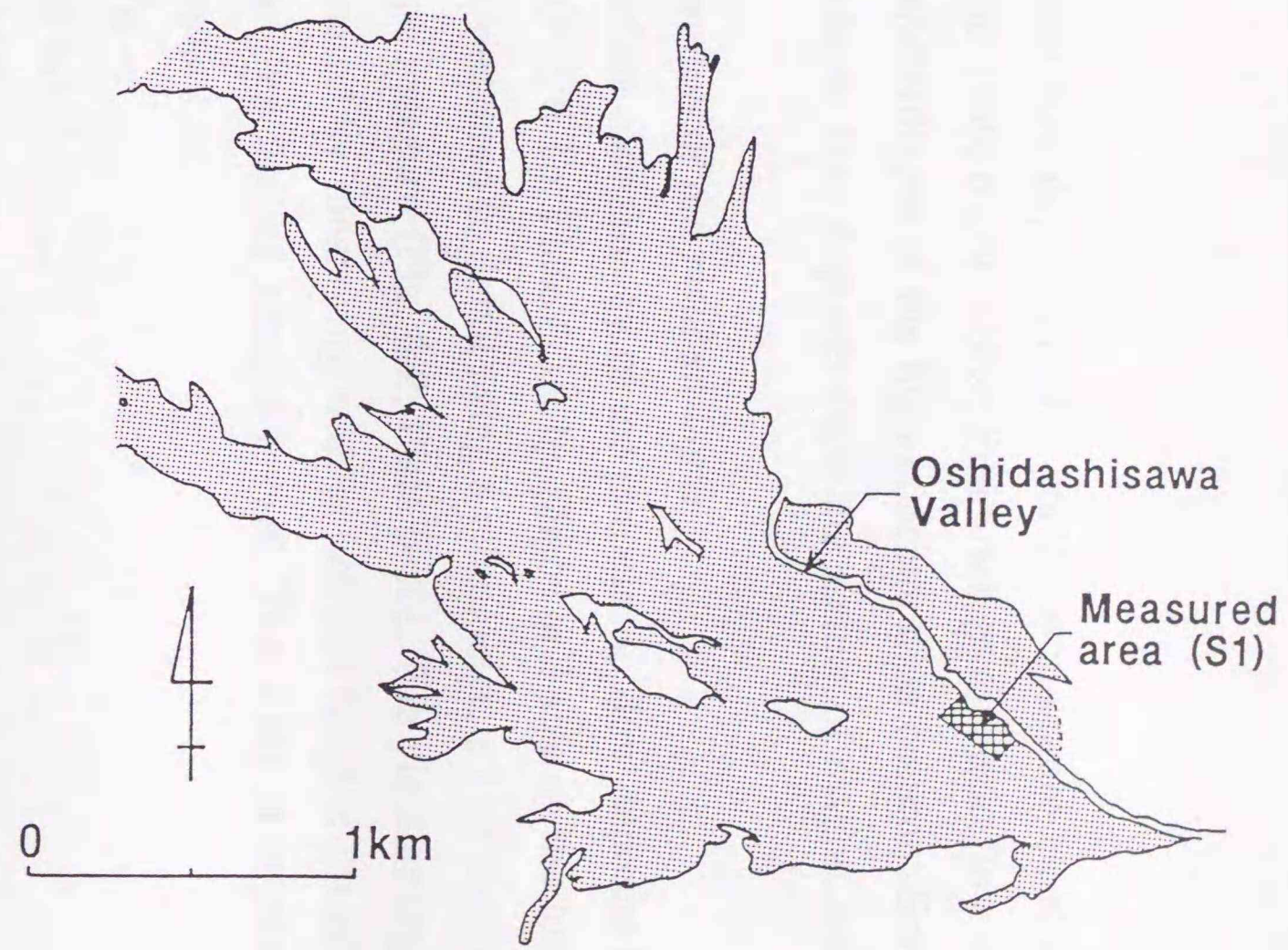

Fig. 6-1A-B. A. Distribution of the 1929 pyroclastic flow deposits at the Komagatake Volcano and locality points (S1 and S2). **B.** Distribution of the 1929 pyroclastic flow deposits at the northeastern foot of the Komagatake Volcano and a measured area at the locality S1.

the pyroclastic flow deposits at this point contain more lithic fragments than the other deposit (Plate 6-2b). These lithic-rich pyroclastic flow deposits may have formed by the collapse of the high-concentration column. Some of the pumices in the pyroclastic flow deposits show the texture of magma mixing (Plate 6-2d).

6-1-3. Estimation of the yield strength

Detail surface morphology of the pyroclastic flow deposits is preserved at the locality S1 (Fig. 6-1b; Plate 6-3a, b). Shape and size of the lobes and the natural levees were measured in detail using a clinometer, a 1 m-long scale, and a 30 m-long reel-type measure (Fig. 6-2; Plate 6-3b). The yield strengths of these lobes can be estimated by measuring widths (w) and heights (h) of lobes and widths (w_b) and heights (h_s) of natural levees. The yield strengths are obtained by three-type equations:

$k_1=\varrho g h^2/w$

$k_2=\varrho g \sin\theta\ h_s$

$k_3=\varrho g \sin^2\theta\ 2w_b$

where ϱ, g, and θ are the density of the lobe, gravitational acceleration, and slope angle, respectively (Fig. 6-3; Johnson, 1970; Wilson and Head, 1981; Cattermole, 1989, p.72-93; Wadge and Lopes, 1991). The heights and the widths of the fifty-three lobes and the thirty-seven natural levees were measured (Fig. 6-2). The average density (ϱ) of the deposits at this area is 1300 kg/m^3 by measuring weight and volume of the matrix of the deposit. The average slope angle (θ) was 6° at this area. The results of the yield strengths (k_1) estimated using the widths (w) and the heights (h) of the lobes are shown in Table 6-1a. The results of yield strengths (k_2, k_3) estimated using the widths (w_b) and the heights (h_s) of the natural levees are shown in Table 6-1b. The underlined values of widths and heights in the tables may be underestimated due to overlapping lobes. Therefore, the underlined values of the yield strengths in the tables were omitted from the results. The estimated yield strengths at this area are:

Fig. 6-2. Morphological features of lobes and natural levees at the locality S1. Shaded parts indicate the natural levees. Small italic number indicates the height of its point. Eastern edge of this area faces to the Oshigadani Valley. Each number at the lobes and the levees corresponds to that in Table 6-1.

$k_1 = \varrho g h^2 / w$

$k_2 = \varrho g \sin\theta \; h_s$

$k_3 = \varrho g \sin^2\theta \; 2w_b$

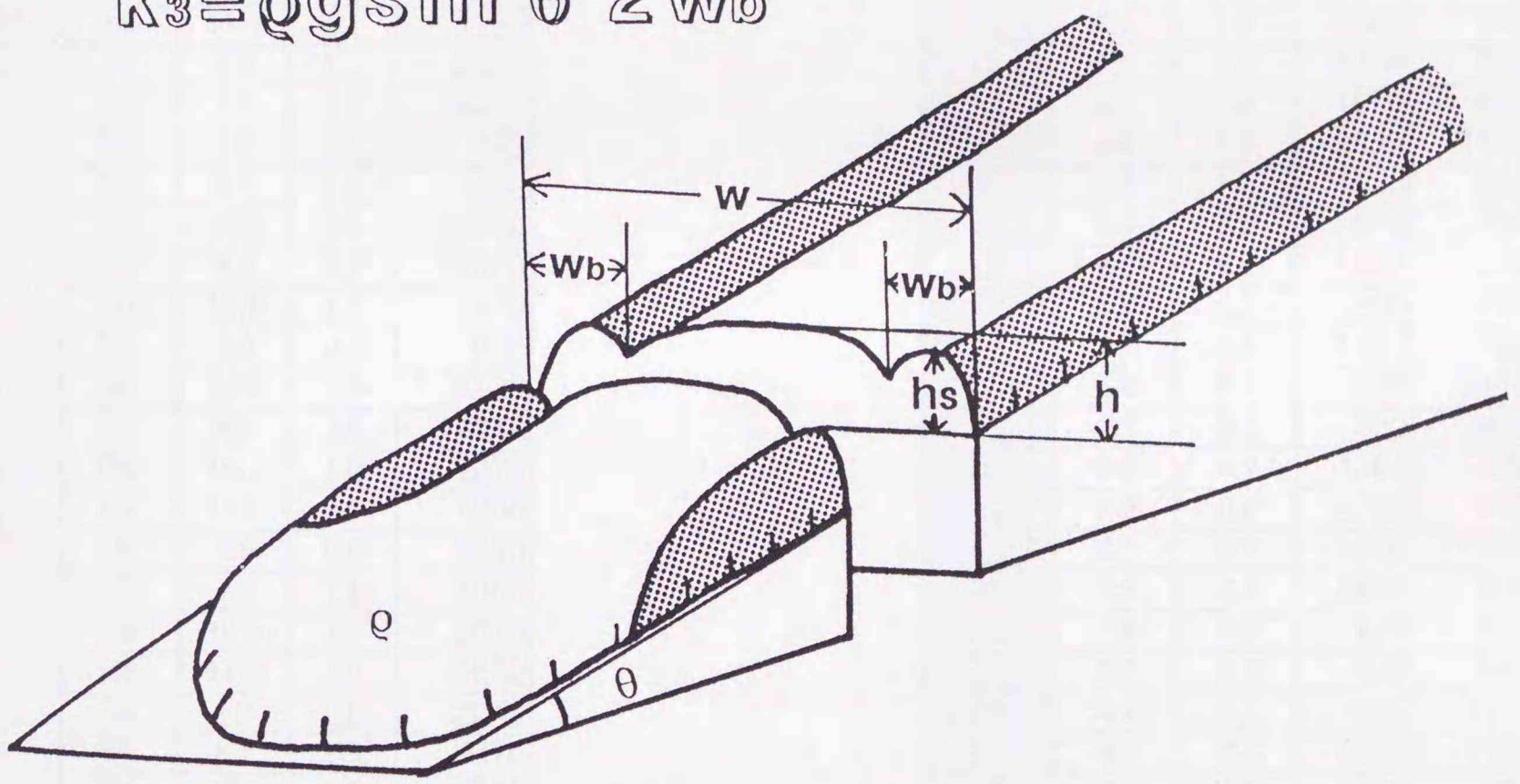

Fig. 6-3. Three-type equations to estimate the yield strengths (after Moore et al., 1978, and Wadge and Lopes, 1991). ϱ, density; g, gravitational acceleration; θ, slope angle; w, width of lobe; h, height of lobe; w_b, width of natural levee; h_s, height of natural levee.

Table 6-1 A. Results of the yield strength estimation (k_1), using the widths (w) and the heights (h) of the lobes.

Number	w(m)	h(m)	k1(Pa)
1	12.0	3.0	9560
2	2.0	0.8	4080
3	4.5	0.5	710
4	5.0	0.8	1630
5	5.0	1.0	2550
6	6.5	1.7	5660
7	5.0	0.7	1250
8	3.5	0.9	2950
9	8.0	0.5	400
10	8.0	1.5	3580
11	5.5	1.5	5210
12	5.5	0.6	830
13	13.0	1.1	1190
14	8.0	1.2	2290
15	7.0	3.0	16380
16	7.0	0.5	460
17	7.0	0.9	1470
18	10.0	3.5	15610
19	9.5	3.0	12070
20	10.0	1.2	1830
21	5.0	0.6	920
22	13.0	2.5	6130
23	8.0	3.0	14330
24	10.0	1.0	1270
25	10.0	2.5	7960
26	4.0	0.9	2580
27	4.0	1.1	3850
28	10.0	1.5	2870
29	11.0	2.0	4630
30	4.0	0.8	2040
31	8.5	2.5	9370
32	10.0	2.5	7960
33	5.5	0.5	580
34	10.5	2.0	4850
35	5.0	0.5	640
36	10.0	1.5	2870
37	9.5	2.0	5360
38	5.0	1.0	2550
39	10.5	2.0	4850
40	10.0	3.0	11470
41	9.5	3.0	12070
42	3.5	1.1	4400
43	4.0	0.5	800
44	5.0	1.2	3670
45	6.0	1.0	2120
46	5.0	1.5	5730
47	10.0	3.0	11470
48	7.5	1.0	1700
49	10.0	1.5	2870
50	4.0	1.0	3190
51	3.5	0.9	2950
52	3.5	1.0	3640
53	2.0	1.1	7710

Table 6-1 B. Results of the yield strength estimation (k_2 and k_3), using the widths (w_b) and the heights (h_s) of the natural levees.

Number	wb(m)	hs(m)	k2(Pa)	k3(Pa)
1	1.5	0.6	800	420
2	3.0	1.1	1460	840
2	2.0	0.7	930	560
3	3.5	1.0	1330	970
4	3.0	1.1	1460	840
5	3.0	1.1	1460	840
6	3.5	1.5	2000	970
6	4.0	1.5	2000	1110
7	3.5	1.3	1730	970
8	1.0	1.1	1460	280
9	2.5	0.5	670	700
10	3.0	1.4	1860	840
11	0.5	3.0	4000	140
12	3.5	1.0	1330	970
13	1.5	0.8	1070	420
14	4.0	2.0	2660	1110
15	2.0	1.2	1600	560
16	2.5	0.5	670	700
17	3.5	0.9	1200	970
18	1.5	0.6	800	420
19	2.5	1.1	1460	700
20	4.0	0.7	930	1110
21	1.5	0.6	800	420
22	3.0	0.9	1200	840
23	2.0	0.8	1070	560
24	2.5	0.9	1200	700
25	3.5	2.0	2660	970
26	2.0	0.7	930	560
27	2.0	0.6	800	560
28	4.0	0.3	400	1110
29	4.0	2.0	2660	1110
30	3.5	1.7	2260	970
31	4.0	2.0	2660	1110
32	4.5	1.1	1460	1250
33	4.0	1.5	2000	1110
34	4.0	1.3	1730	1110
35	3.5	0.5	670	970
36	2.0	1.0	1330	560
37	2.5	0.5	670	700

*The underlined values of the widths and the heights in the tables may have the possibility of underestimation, due to the overlap of the lobes, as showing the lower figures. Therefore, the underlined values of the yield strengths may also be underestimated.

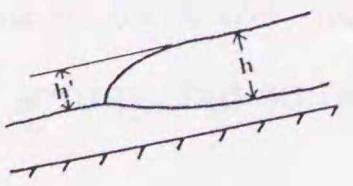

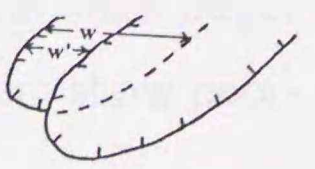

k_1= 4850 - 15610 Pa

k_2= 670 - 4000 Pa

k_3= 280 - 1250 Pa.

It is concluded that the yield strengths of the pyroclastic flow deposits in this area are 10^2 - 10^4 Pa. The yield strengths estimated using the natural levees tend to be smaller values than those using the lobes. This result suggest that the Komagatake 1929 pyroclastic flows had the enough yield strength to support the large grains up to a meter.

6-1-4. Sedimentary structures

Section of the pyroclastic flow deposits, which consist of the succession of a few meters-thick lobes, are exposed at locality S2 (Fig. 6-1a; Plate 6-4a-d; Fig. 6-4). The pumice-concentrated layer (PL), which consists of the clast-supported pumices up to 35 cm in size, are also observed at the top of the each lobe in this exposure (Plate 6-4c, d; Fig. 6-4). Oblique sections of individual lobes; and erosional contact of lobes due to erosion by the upper lobe are observed in this exposure (Fig. 6-4). Many lobes show the typical poorly-sorted texture of pyroclastic flow deposits (Plate 6-5a; Fig. 2-19). Although, some lobes are further subdivided into a fines-depleted layer (DL) and a fines-rich layer (FL)(Plate 6-5b-h). The FL is observed just beneath the PL (Plate 6-5c, f, h). Idealized sequence of the one unit of lobe, which consists of the DL, the FL, and the PL, are shown in Fig. 6-5. Grain size distributions (Fig. 6-6a, b; Fisher and Schminke, 1984, p.118-122) and F1-F2 diagram (Fig. 6-6d; Walker, 1983) indicate that much fine components are contained in the FLs than in the DLs. These results suggest that fine components segregated from the DLs were concentrated into the FLs. Mean-size (M_z)-sorting (σ_I) diagram (Fig. 6-6c; Folk and Ward, 1957) indicate that the DLs tend to have the mean grain sizes larger than the FLs. Some of the FLs show better sorting, but some of them show poor-

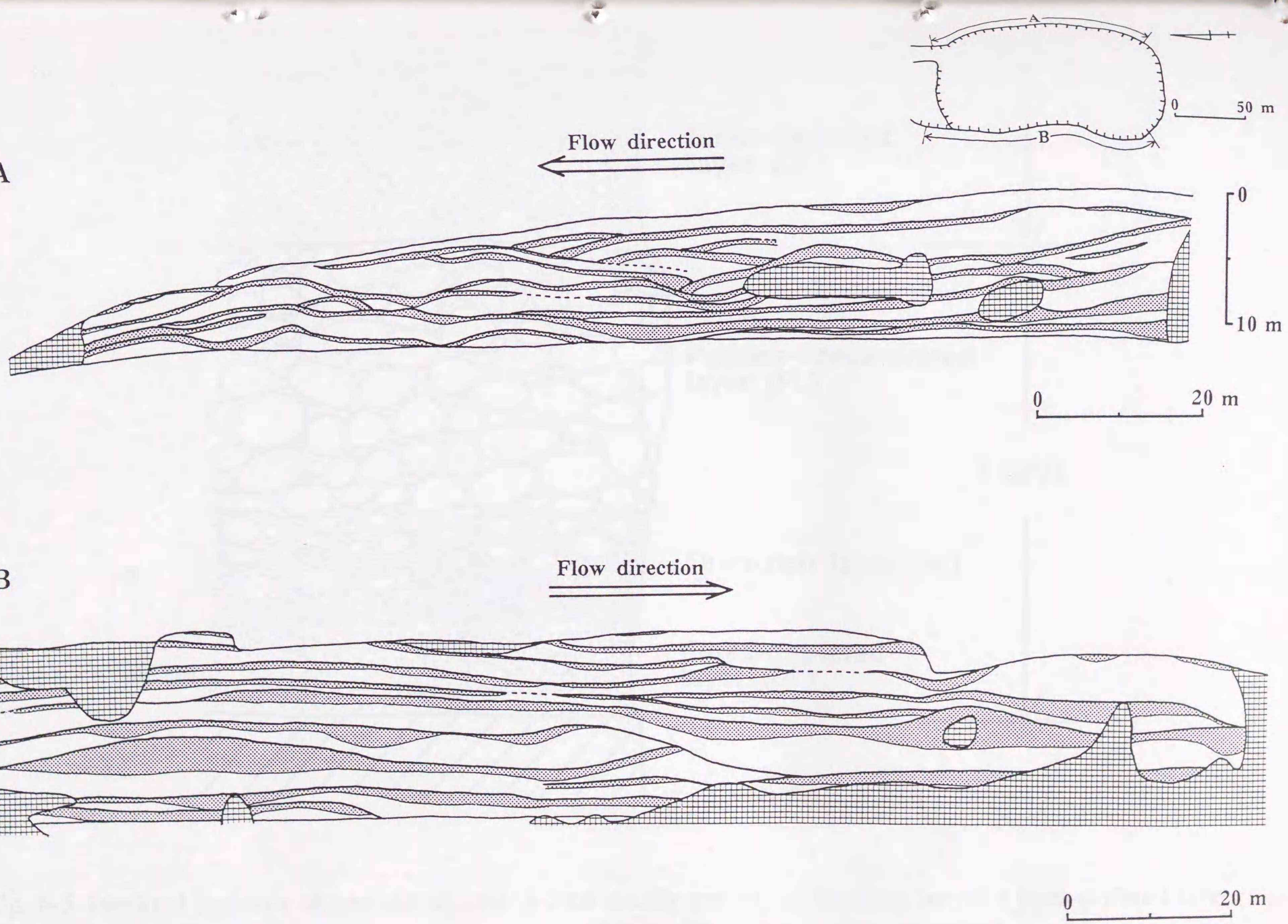

Fig. 6-4. Sketch of the succession of lobes of the 1929 pyroclastic flow deposits at the locality S2. Shaded parts indicate pumice-concentrated layers at the upper part of lobes.

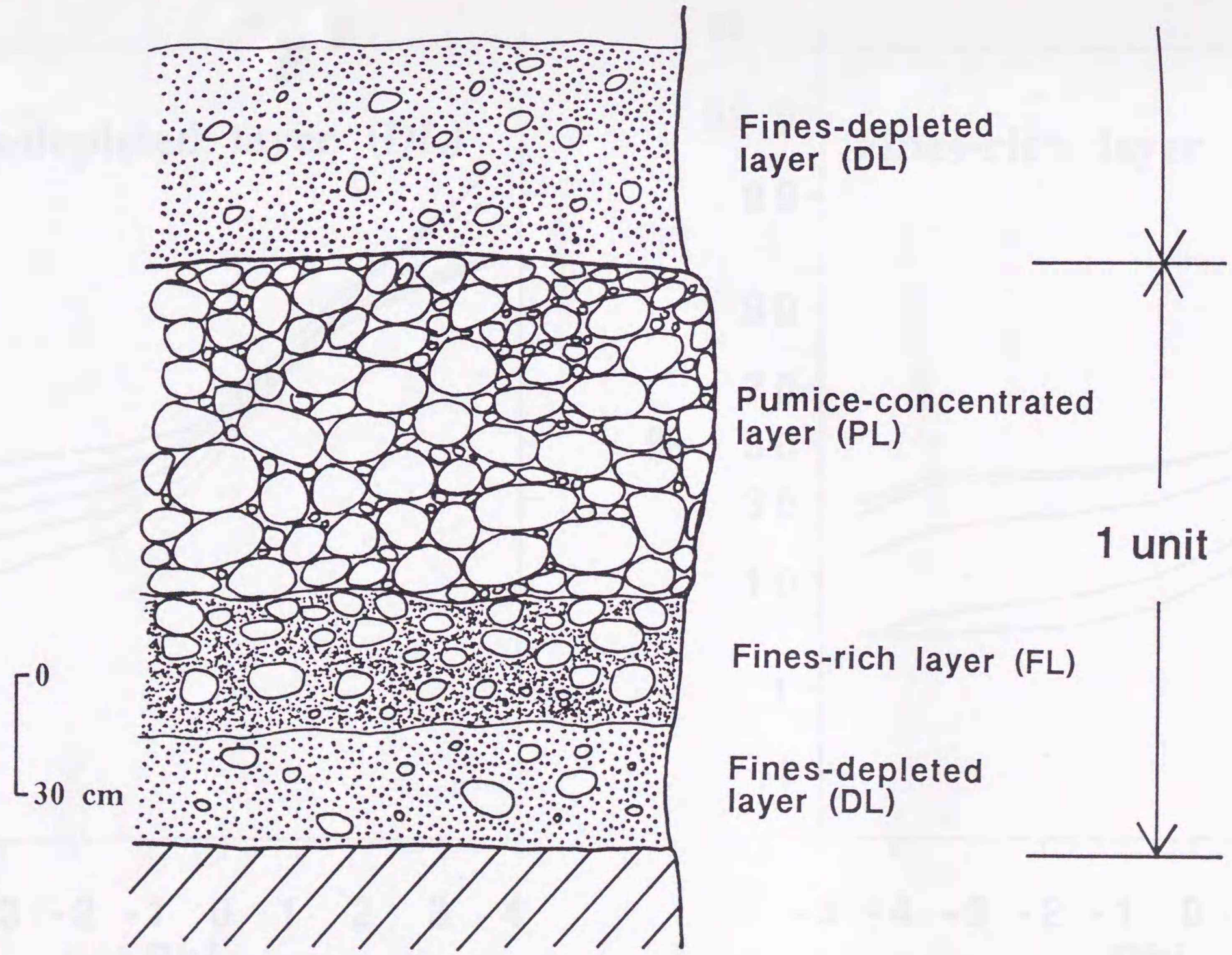

Fig. 6-5. Idealized sequence of one unit of lobe. A lobe usually consists of the three layers: a fines-depleted layer (DL); a fines-rich layer (FL); and a pumice-concentrated layer (PL), where many carbonized wood fragments are incorporated in the lobe.

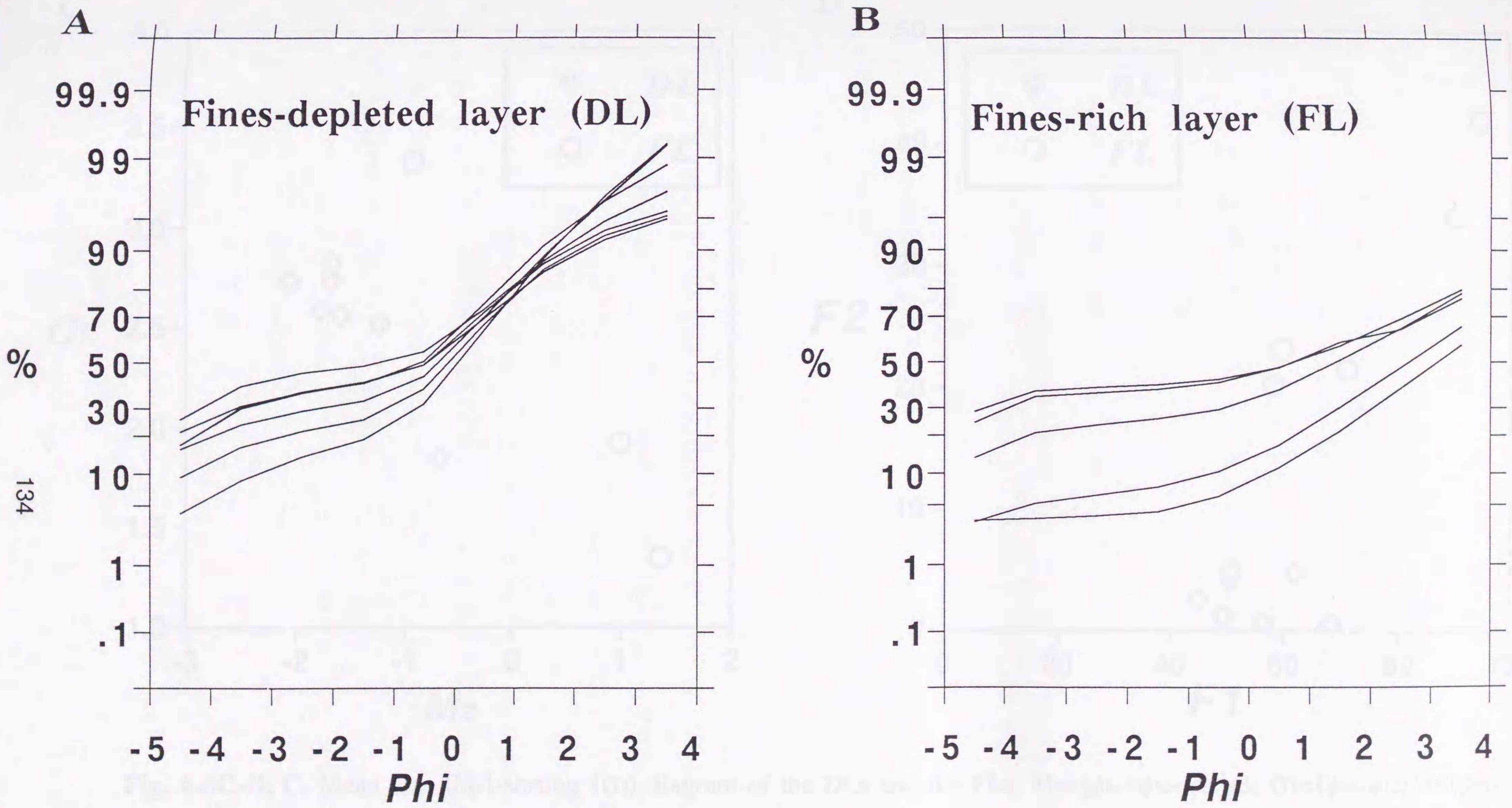

Fig. 6-6A-B. Grain size distributions of the fines-depleted layer, DL (**A**) and the fines-rich layer, FL (**B**). Sieved results are plotted on the cumulative weight percentage (normal probability plot) versus grain size diagrams, where phi, ϕ=-log$_2$d; d, grain size in millimeter. The samples were taken from the bottom and the second lobes. Much fine components are contained in the FLs than the DLs.

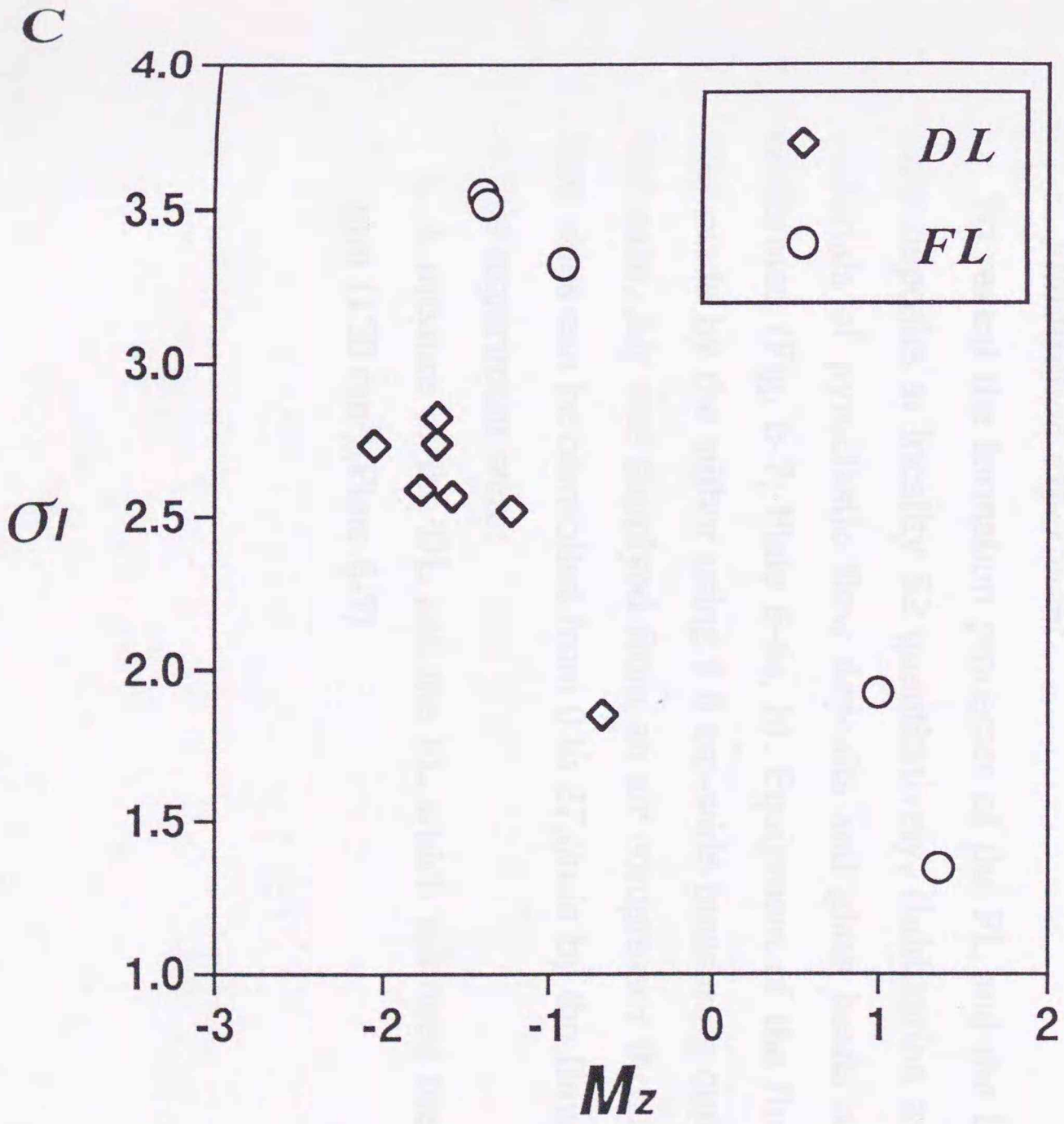

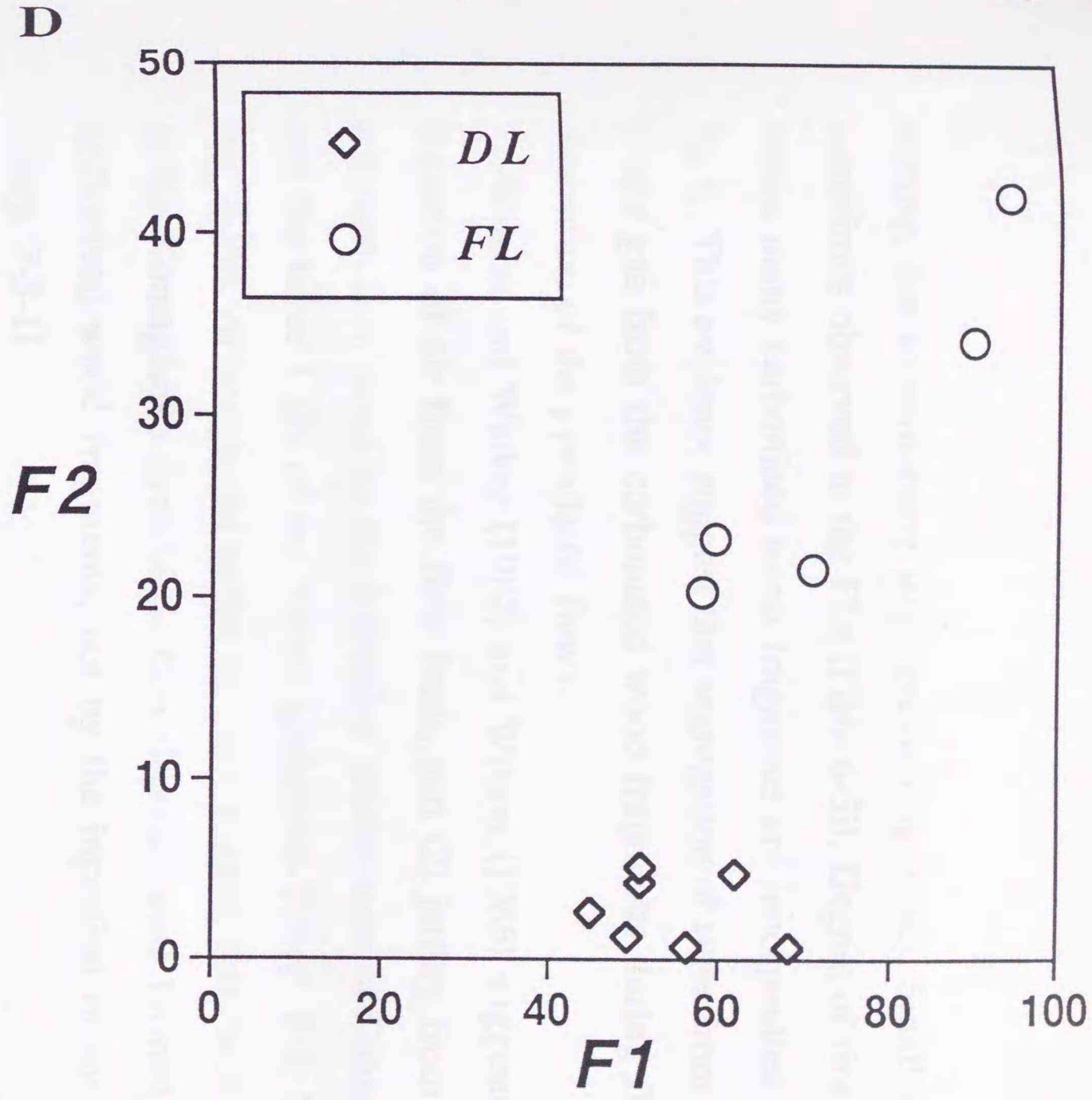

Fig. 6-6C-D. C. Mean size (M_Z)-sorting (σ_I) diagram of the DLs and the FLs. $M_Z=(\phi_{16}+\phi_{50}+\phi_{84})/3$; $\sigma_I=(\phi_{84}-\phi_{16})/4+(\phi_{95}-\phi_5)/6.6$ (after Folk and Ward, 1957). The DLs tend to have larger mean grain size than the FLs. The upper three samples of the FLs in the figure show poor-sorting, because of possession of large grains. **D.** Plots of the weight percentage finer than 1/16 mm (F2) versus weight percentage finer than 1 mm (F1) of the DLs and the FLs. (after Walker, 1983). Much fine-grains are contained in the FLs than the DLs.

sorting, due to containing large grains (Fig. 6-6c). Small segregation pipes are sometimes observed in the FLs (Plate 6-5i). Degree of fines depletion was high where many carbonized wood fragments are incorporated in the lobe (Plate 6-5g, j). This evidence suggest that segregation of fines from the DL occurred due to the gas from the carbonized wood fragments during flowage and after the deposition of the pyroclastic flows.

Wilson and Walker (1982) and Wilson (1985) suggested the models of (1) ingestion of air from the flow front; and (2) jetting from the highly-fluidized turbulent flow head for the formation mechanisms of fines-depletion of the FDI and the layer 1 (P) of the Taupo ignimbrite (Chap. 2-2; Fig. 2-25; Fig. 2-26; Fig. 2-29). Although, the author strongly suggest that fines-depletion of the DLs in the Komagatake pyroclastic flow deposits were formed by the gas from the carbonized wood fragments, not by the ingestion or the jetting mechanisms (Chap. 7-3-1).

6-1-5. Fluidization experiment

To reveal the formation processes of the FL and the DL in the pyroclastic flow deposits at locality S2 quantitatively, fluidization experiments using the materials of pyroclastic flow deposits and glass beads of various sizes were performed (Fig. 6-7; Plate 6-6a, b). Equipment of the fluidization experiment was made by the author using a 8 cm-wide measuring cup, gauze, and a tennis ball case. Air was supplyed from an air compressor through a flowmeter. The flow rates can be controlled from 0 to 27 *l*/min by the flowmeter. Used samples in this experiment were:

1. A mixture of the DL and the FL which removed the grains larger than 4 mm (150 cm^3)(Plate 6-7).

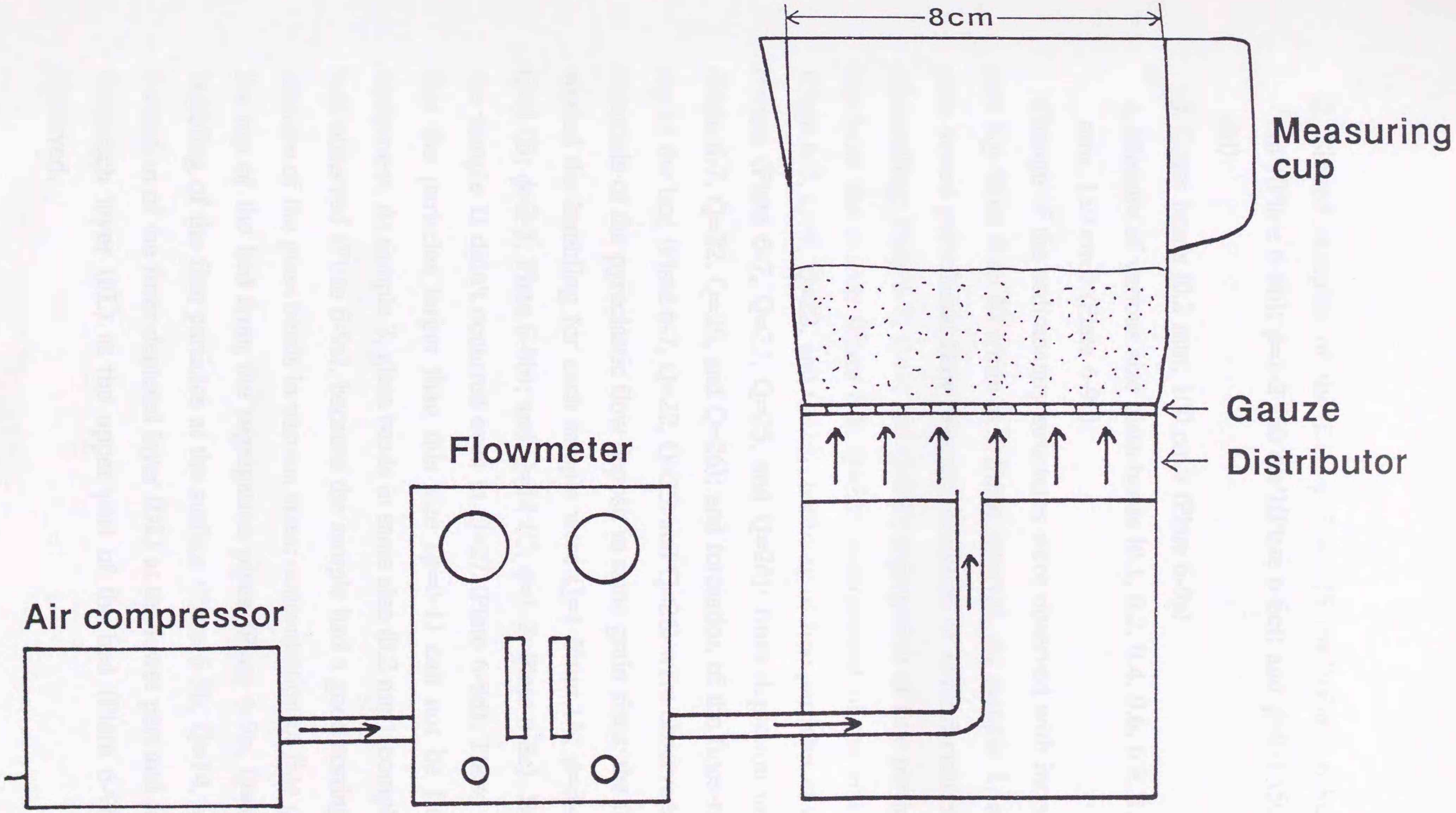

Fig. 6-7. Schematic diagram of the equipment of fluidization experiment.

2. Sieved samples of the DL. ϕ=3-4 (25 cm^3)(Plate 6-8a); ϕ=2-3 (50 cm^3)(Plate 6-8b); ϕ=1-2 (50 cm^3)(Plate 6-8c); and ϕ=0-1 (50 cm^3)(Plate 6-8d).
3. Grass beads (0.2 mm; 100 cm^3) (Plate 6-9a).
4. Mixture of various size glass beads (0.1, 0.2, 0.4, 0.6, 0.8, 1.0, 2.0, and 4.0 mm; 150 cm^3) (Plate 6-9b).

Change of the sedimentary structures were observed with increasing the flow rate (Q) from 0 to 27 *l*/min at 1 *l*/min interval. At sample 1, material of the poor-sorted pyroclastic flow deposit: formation of several craters at the surface (channeling; Plate 6-7, Q=9, and Q=22); segregation of fine particles toward the top from the craters (Plate 6-7, Q=22); enlargement of the size of the craters (Plate 6-7, Q=9, Q=22, and Q=26); bubbling of fine particles at the floor of the craters (Plate 6-7, Q=22, Q=25, and Q=26); fines-depletion under the crater (Plate 6-7, Q=22, Q=25, and Q=26); and formation of the fines-rich layer at the top of the bed (Plate 6-7, Q=22, Q=25, and Q=26) were observed. At samples 2, materials of the pyroclastic flow deposit in same grain sizes: the flow rates when started the bubbling for each sample were Q=1 *l*/min (A; ϕ=3-4; Plate 6-8a); Q=4 (B; ϕ=2-3; Plate 6-8b); and Q=14 (C; ϕ=1-2; Plate 6-8c). But, bubbling of the sample D didn't occurred even at Q=27 (Plate 6-8d). These results suggest that the particles larger than this size (ϕ=0-1) can not be fluidized in this equipment. At sample 3, glass beads in same size (0.2 mm): complete fluidization was observed (Plate 6-9a), because the sample had a good sorting. At sample 4, mixture of the glass beads in various sizes: concentration of fine particles toward the top of the bed from the segregation pipes (Plate 6-9b, Q=14, and Q=25); bubbling of the fine particles at the surface (Plate 6-9b, Q=14, and Q=25); and formation of the fines-depleted layer (DL) at the lower part and formation of the fines-rich layer (FL) at the upper part of the bed (Plate 6-9b, Q=25) were observed.

The result of the experiment strongly suggest that the FLs and the DLs in the Komagatake pyroclastic flow deposit should have been formed by the concentration of fine-particles toward the top of the layer due to the upward flow such as the gas from the carbonized wood fragments. Most of the fine particles of the FLs were remained beneath the PLs (Fig. 6-5). This evidence suggest that upward flow velocity was not enough to elutriate the fines from the lobe (the upward flow velocity was smaller than the settling velocity of the particles; Fig. 7-5). At this experiment, the fine particles were concentrated at the upper part, but the particles larger than ca. 1 mm weren't affected by the upward flow at all (Plate 6-9b). This result suggest that large grains up to a meter in the pyroclastic flow can not be fluidized by the upward flow (Chap. 7-3-1).

A

B

Plate 6-1. A. A pyroclastic flow descending toward the SW of the Volcano at 18:20 on June 17, 1929 (after Kozu et al., 1932). **B.** An eruption column from the NW of the Volcano at 11:20 on June 17, 1929 (after Kozu et al., 1932).

C

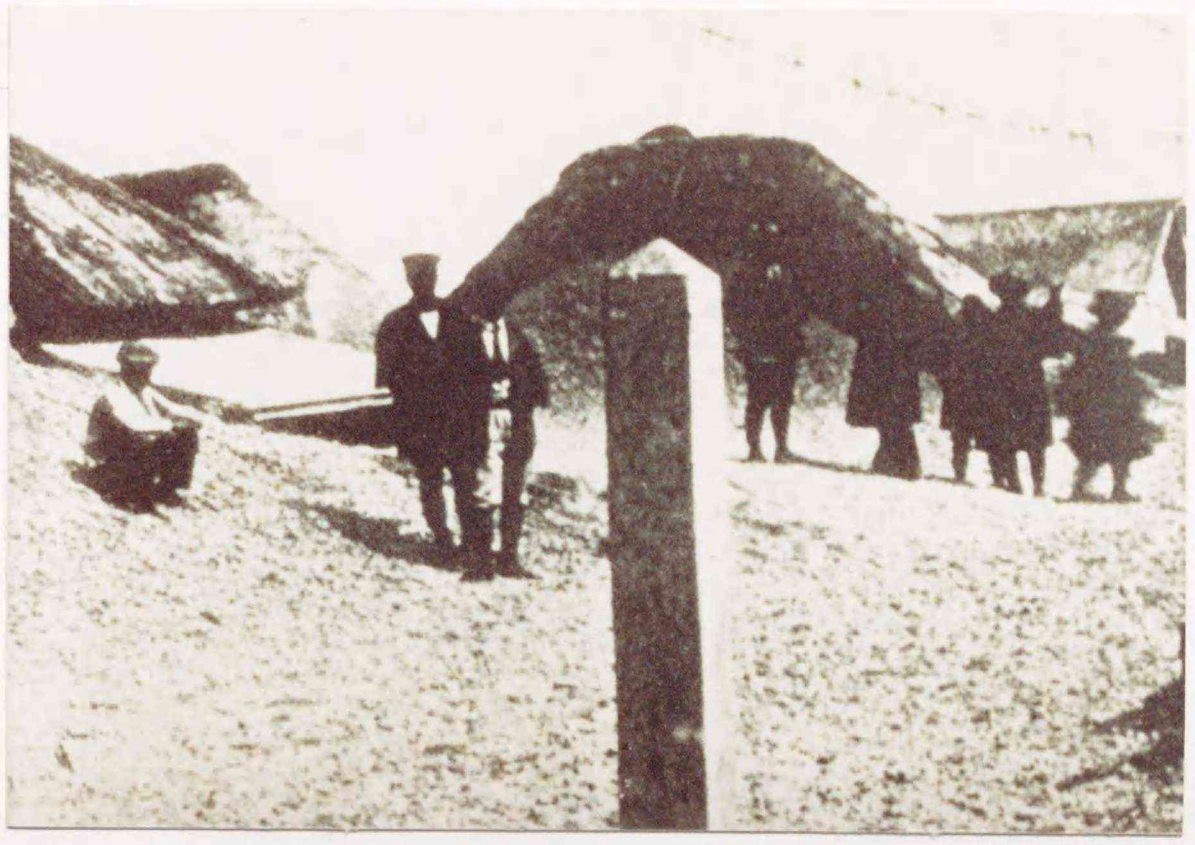

D

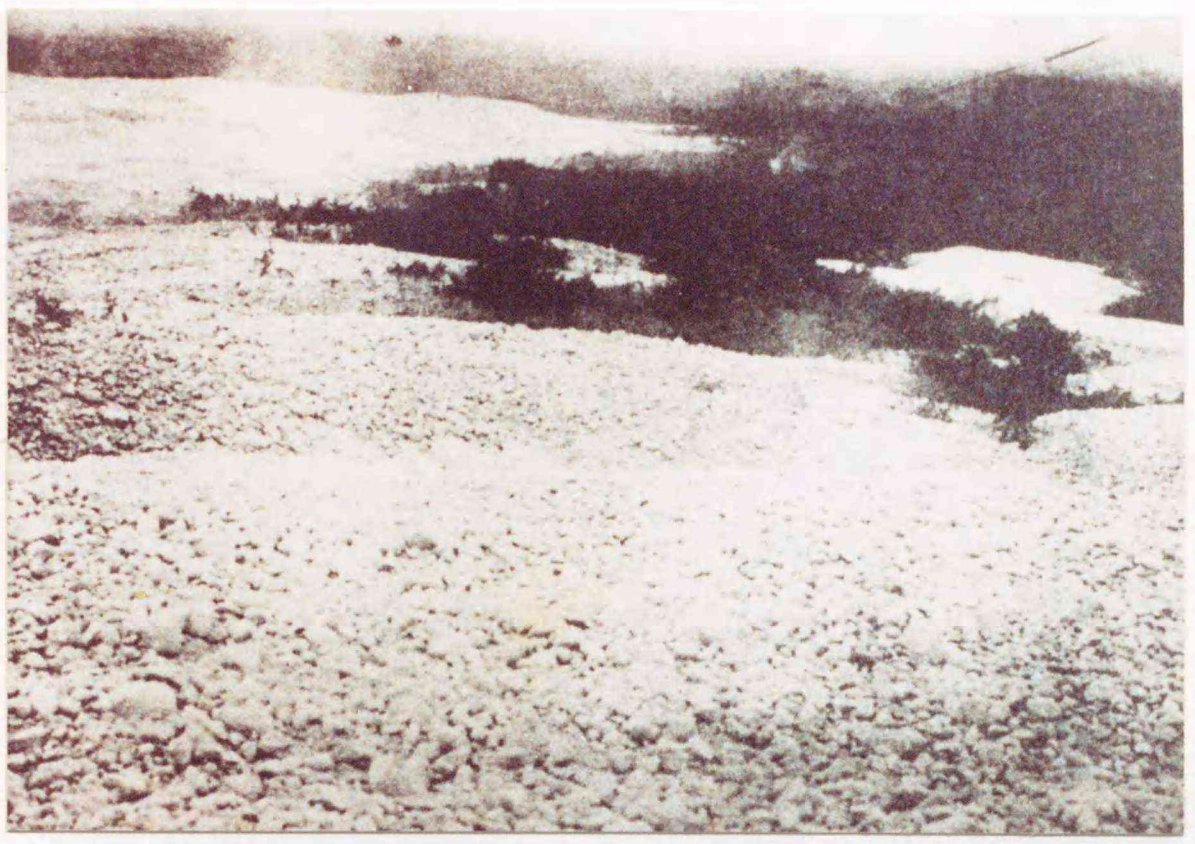

Plate 6-1. C. One-meter thick Ko-a air-fall deposit which buried the Shikabe Village, 12 km away from the source crater (after Kozu et al., 1932). **D.** The 1929 Ko-a pyroclastic flow deposit which distributed at the SW slope of the Volcano (after Kozu et al., 1932).

E

F

Plate 6-1. E. The 1929 K_O-a pyroclastic flow deposit which distributed at the NW slope of the Volcano (after Kozu et al., 1932). **F.** A bread crust bomb at the upper part of the S slope of the Volcano. This picture was taken on July 8, 1929 (after Kozu et al., 1932).

G

H

Plate 6-1. G. The Showa 4 Crater, 230 m in diameter, 50 m in depth, which is located at the center of the amphitheater. This crater was formed in the 1929 eruption. **H.** The welded 1929 air-fall deposit observed at the wall of the 1942 fissure in the amphitheater.

I

J

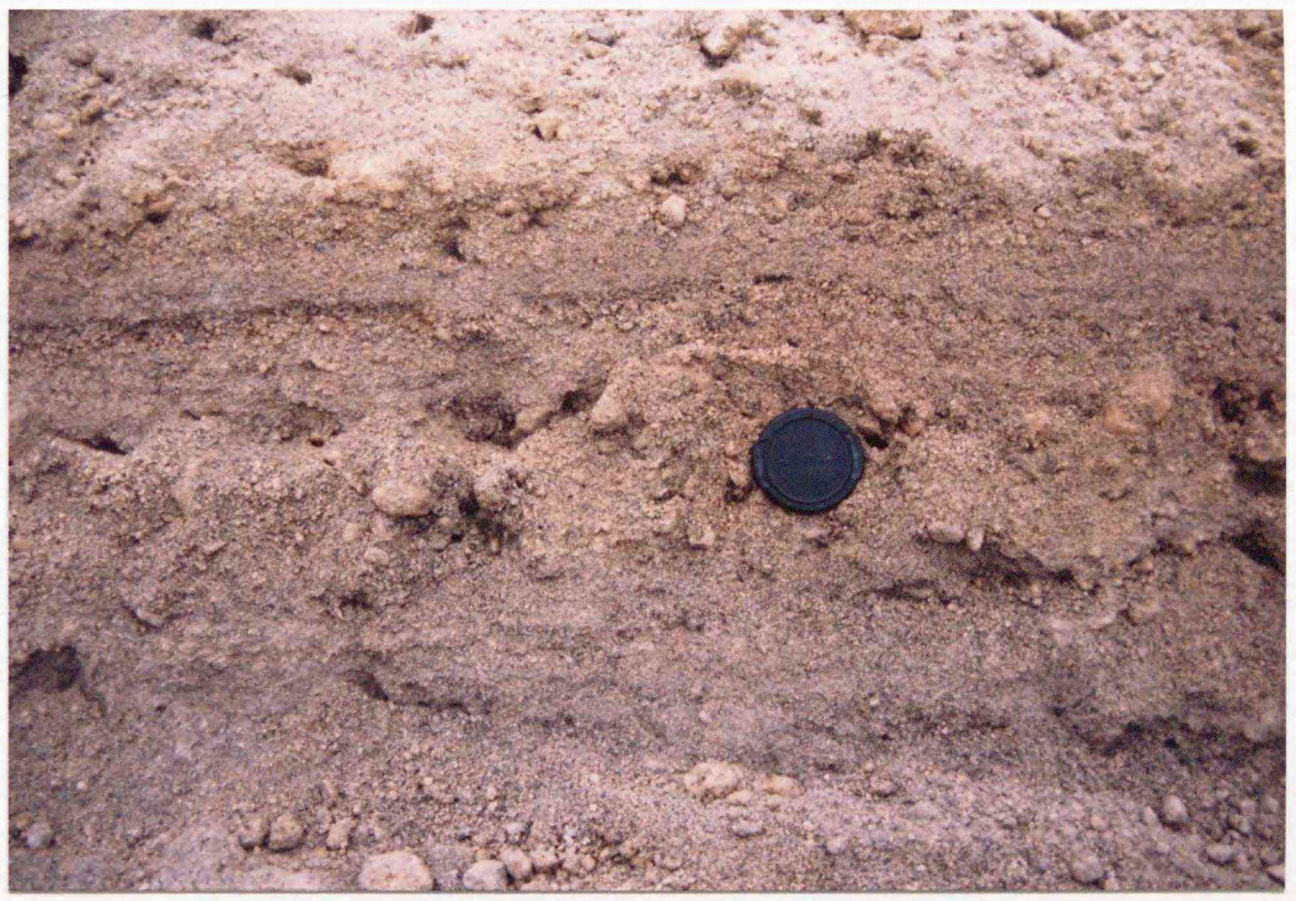

Plate 6-1. I. Dune structures of the 1929 pyroclastic surge deposit at the 2.15 km SSW from the source crater. **J.** Close-up of the pyroclastic flow deposit at the 2.15 km SSW from the source crater. This deposit is composed of fines-depleted, better-sorted pumices, volcanic sand, and ash.

K

L

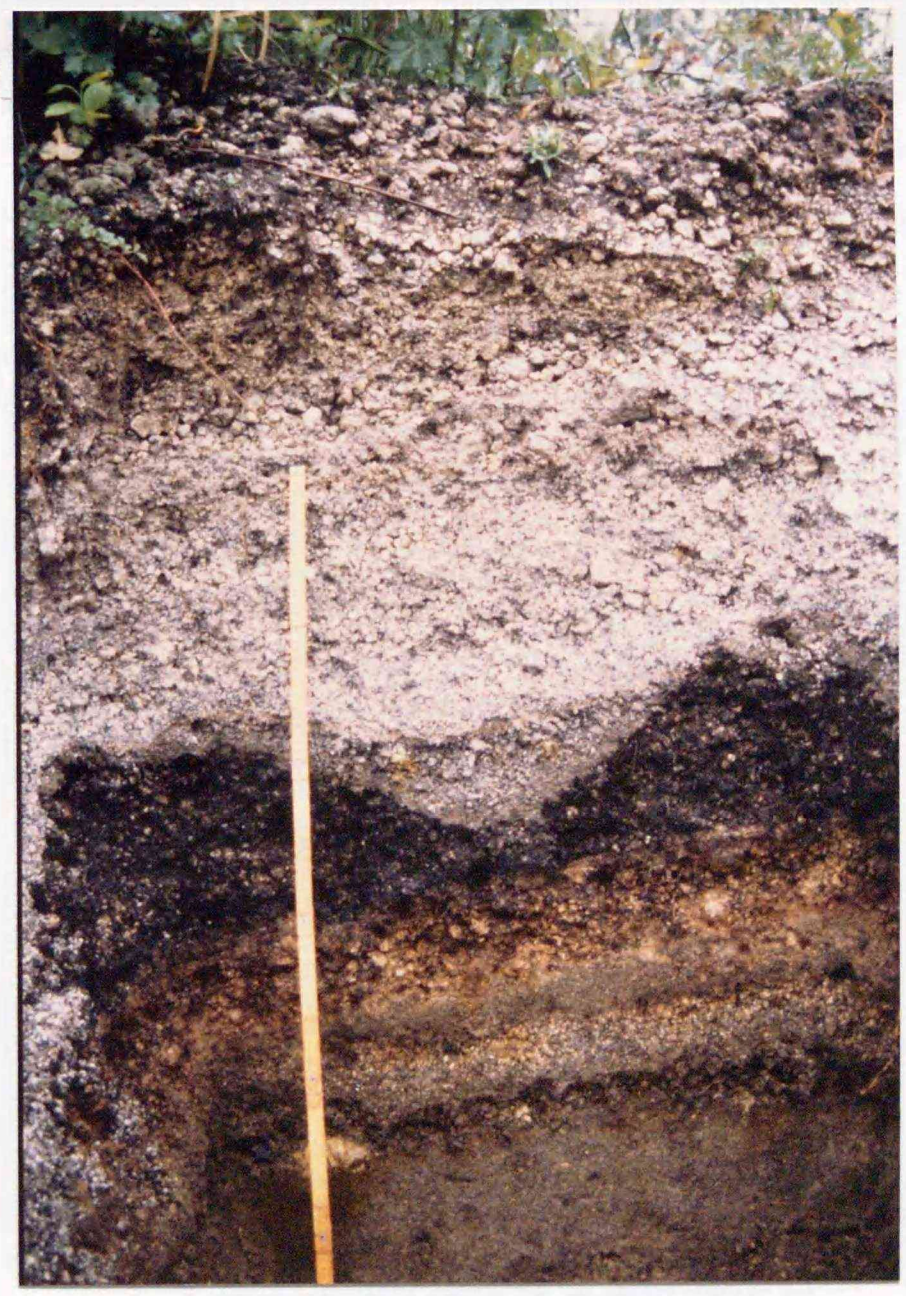

Plate 6-1. K. The 1929 K_o-a pyroclastic surge deposit, representing the cross bedding structure at the 2.45 km SSE from the source crater. **L.** K_o-d (dark-colored part at the bottom), K_o-c_2, K_o-c_1, and K_o-a_1-a_5 (light colored part) air-fall deposits, in ascending order. This outcrop is located at the 9.5 km ESE from the source crater. Thick soil (black-colored part) is observed between the K_o-a_1 and K_o-c_1 air-fall deposits.

A

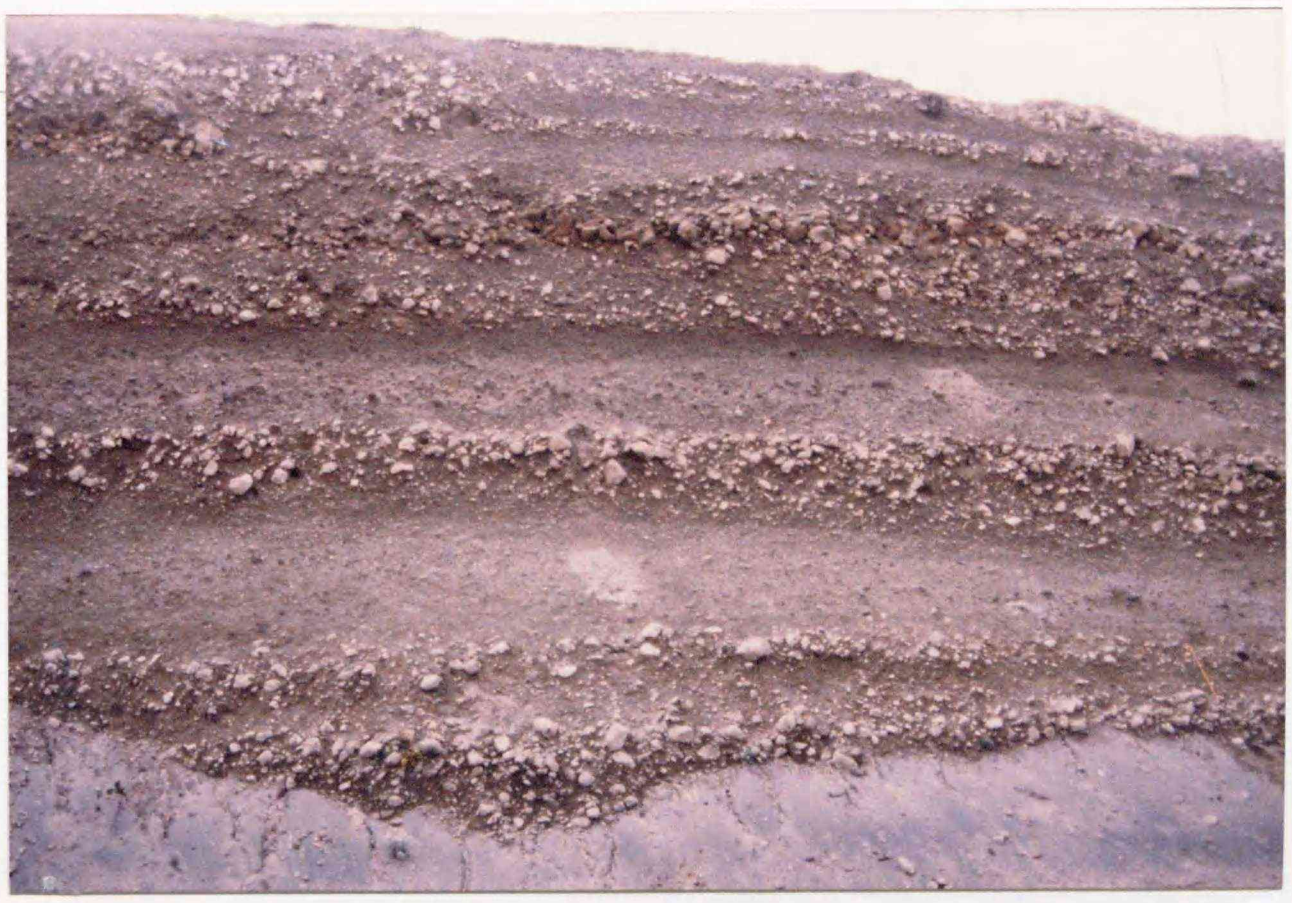

B

Plate 6-2. A. Succession of the 1929 pyroclastic flow deposits at the side of the measured area (S1 in Fig. 6-1b) along the Oshidashisawa Valley. The pumice-concentrated layers are observed at the top of the each flow unit of the pyroclastic flow deposit. A 1 m-long scale is seen at the bottom-right part. **B.** Close-up of the Plate 6-1a. Some of the pyroclastic flow deposits at this point contains more lithic fragments than the other deposits. These lithic-rich pyroclastic flow deposits may have formed by the collapse of the higher-concentrated column.

C

D

Plate 6-2. C. Succession of the 1929 pyroclastic flow deposits at the other side of the measured area (S1 in Fig. 6-1b) along the Oshidashisawa Valley. Oblique sections of more than eight lobes are observed. **D.** Pumices showing the intermingled texture between light-colored part and black-colored part. This texture may have formed by magma mixing.

A

B

Plate 6-3. A. Lobes in the measured area at locality S1. The No. 3 (in front) and No. 23 lobes are observed (Fig. 6-2). This picture was taken from the site of No. 32 lobe. **B.** Scenery of the measuring lobe (at No. 13 lobe in Fig. 6-2). A natural levee is observed at the 1 m-long scale.

A

B

Plate 6-4. A. A quarry site of the 1929 pyroclastic flow deposit at locality S2 (Fig. 6-1a). The northern view of the Mt. Sahara, northern peak of the Komagatake Volcano, is seen behind the exposure. **B.** Succession of the 1929 pyroclastic flow deposits at locality S2. The debris flow deposits and K_O-d air-fall deposit is exposed beneath the 1929 pyroclastic flow deposit at this exposure. The sketch of this exposure is shown in Fig. 6-4.

C

D

Plate 6-4. C. Succession of the 1929 pyroclastic flow deposits, and the debris flow deposits at the bottom. The pumice-concentrated layers (PL), which composed of the clast-supported pumices, up to 35 cm in size, are also observed at the top of the each lobe. **D.** Succession of the 1929 pyroclastic flow deposits. Oblique sections of the individual lobe, and erosional surface of the lobes due to upper lobe are observed. This picture is correspond to the middle part of the sketch of the Fig. 6-4a.

A

B

Plate 6-5. A. Close-up of the section of the 2nd lobe from the bottom. The typical poorly-sorted texture of the pyroclastic flow deposit is observed. **B.** The section of the 1st lobe from the bottom. This lobe is subdivided into fines-depleted layer (DL), fines-rich layer (FL), and pumice-concentrated layer (PL), in ascending order (Fig. 6-5).

C

D

Plate 6-5. C. Close-up of the Plate 6-5b. The FL is concentrated just beneath the PL. **D.** Close-up of the Plate 6-5b. Finer grains were depleted from the DL. Thin precursor air-fall ash layer is observed between the DL and the previous debris flow deposit.

E

F

Plate 6-5. E. Example of the PL, the FL, and the DL at the 1st lobe from the bottom. **F.** Close-up of the FL and the DL.

G

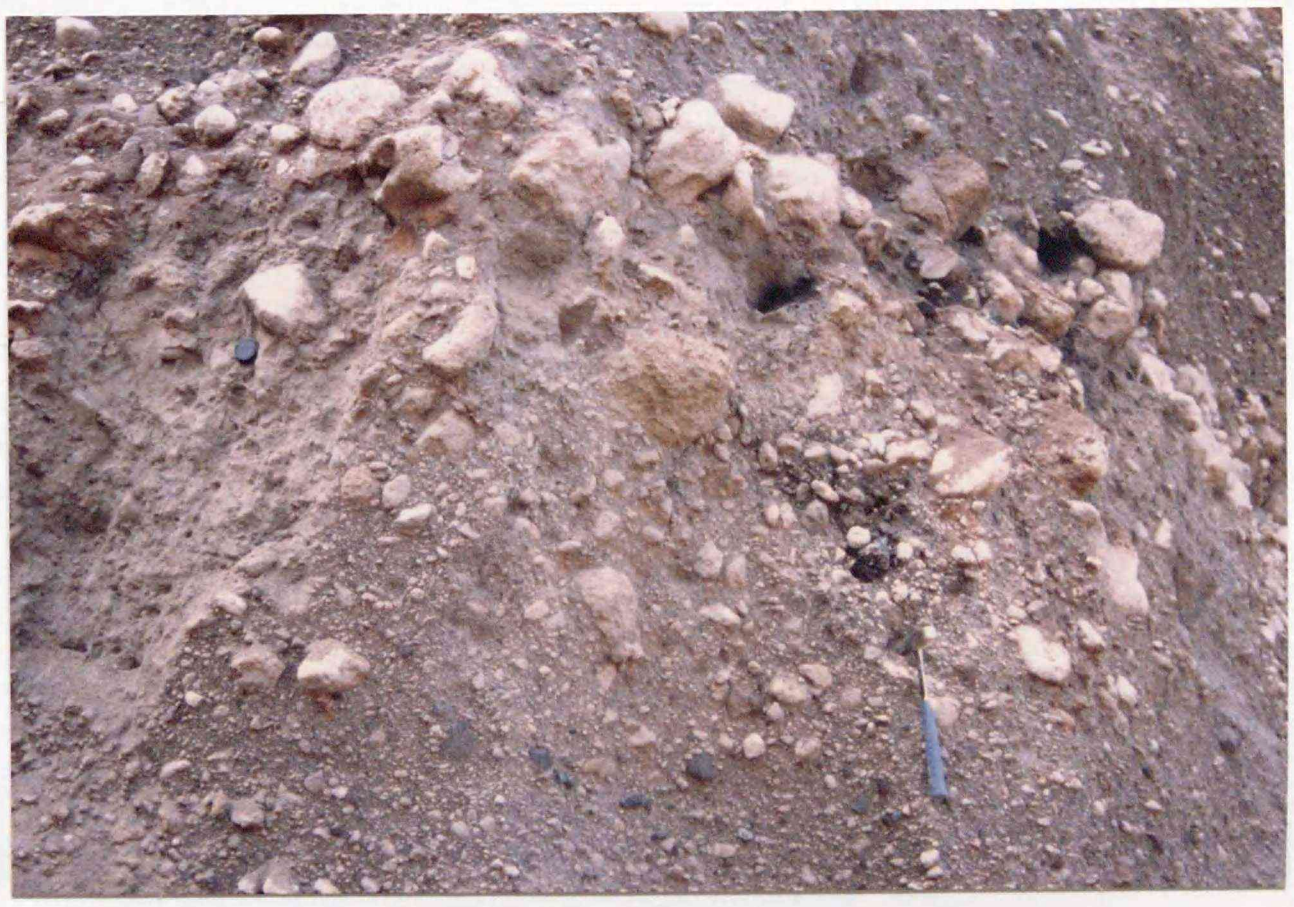

H

Plate 6-5. G. Example of the PL, the FL, and the DL at the forth lobe from the bottom. This site is located at the left-side part of the Fig. 6-4b. Some carbonized wood fragments are included in this lobe. **H.** Close-up of the Plate 6-5g. The FL and the DL are observed.

I

J

Plate 6-5. I. Small segregation pipes within the FL. **J.** Carbonized wood fragments included within the DL. The degree of fines-depletion is high when many carbonized wood fragments are included within the DL.

A

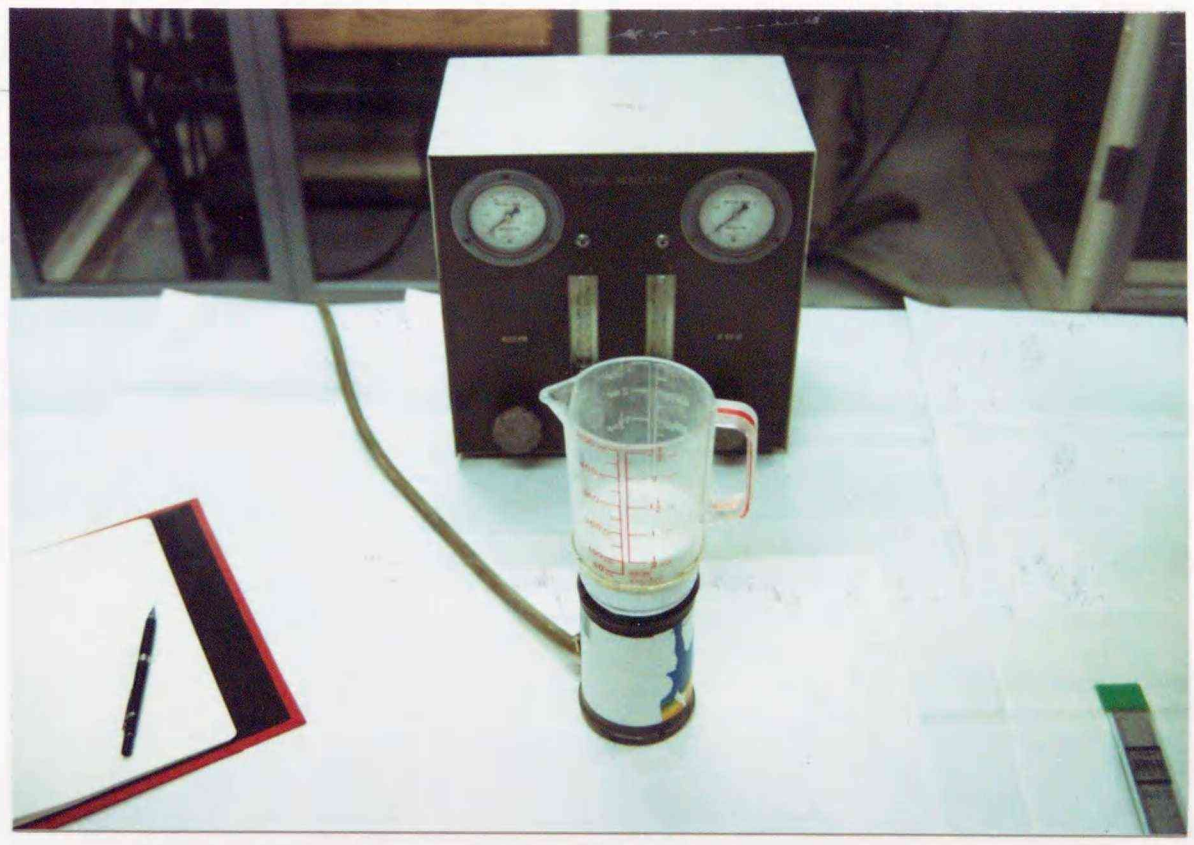

B

Plate 6-6. A. The fluidization equipment, which made of a 8 cm-wide measuring cup, distributor, and flowmeter (Fig. 6-7). **B.** An air compressor and an air tank to supply the air to the fluidization equipment (Fig. 6-7).

Q=0
(*l*/min)

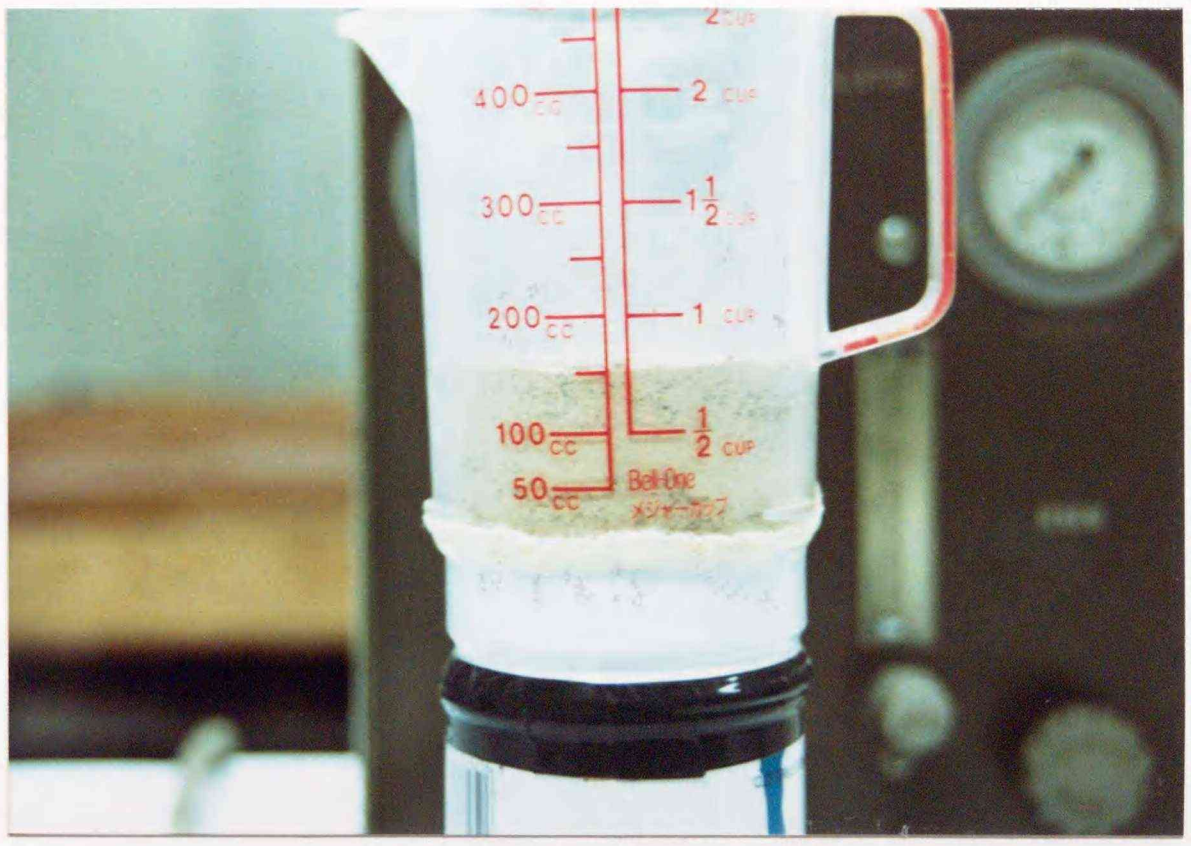

Plate 6-7. The result of the fluidization experiment using the mixture of the DL and the FL (ratio=1:1), which removed grains larger than 4 mm (150 cm^3). Q= flow rate (*l*/min). Before the experiment (Q=0).

Q=9

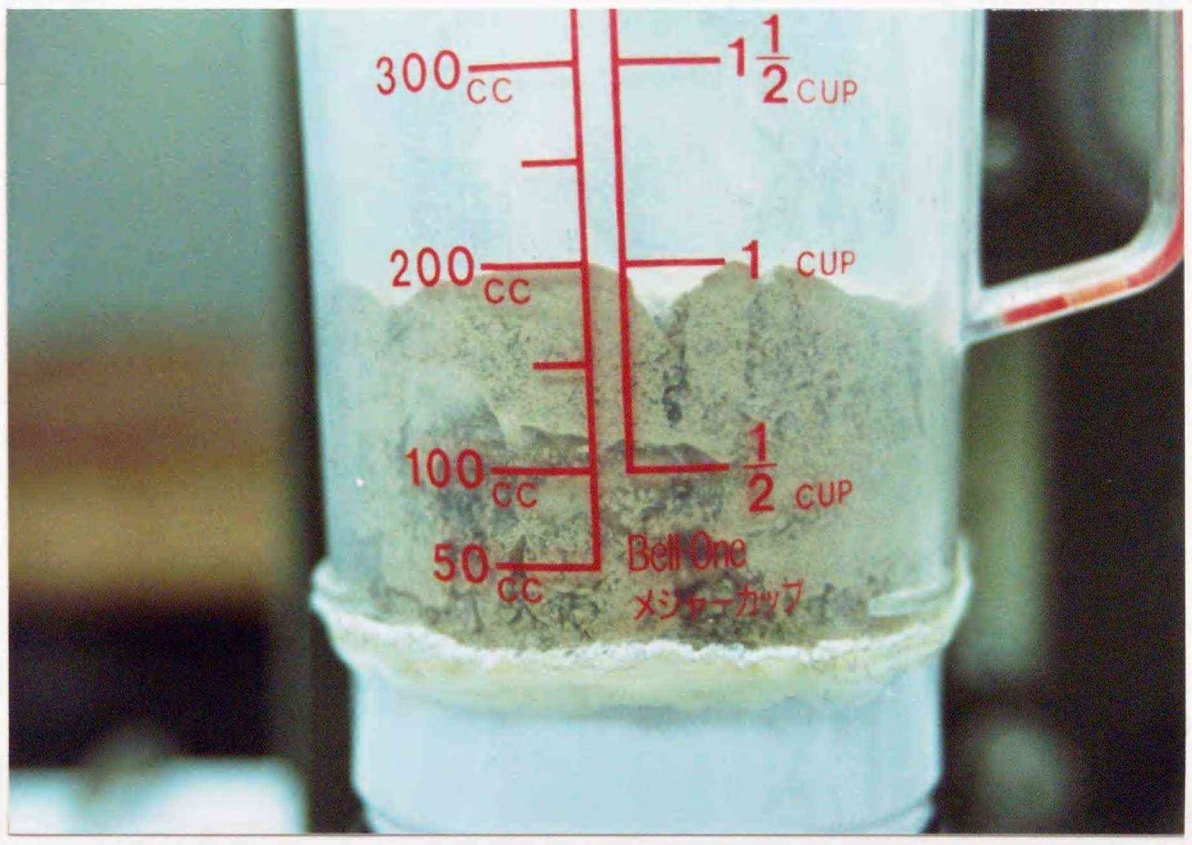

Plate 6-7. Q=9 (*l*/min). Formation of the several craters at the surface (channeling); segregation of the finer particles toward the top from the craters; and formation of the segregation pipes beneath the each crater are observed.

Q=22

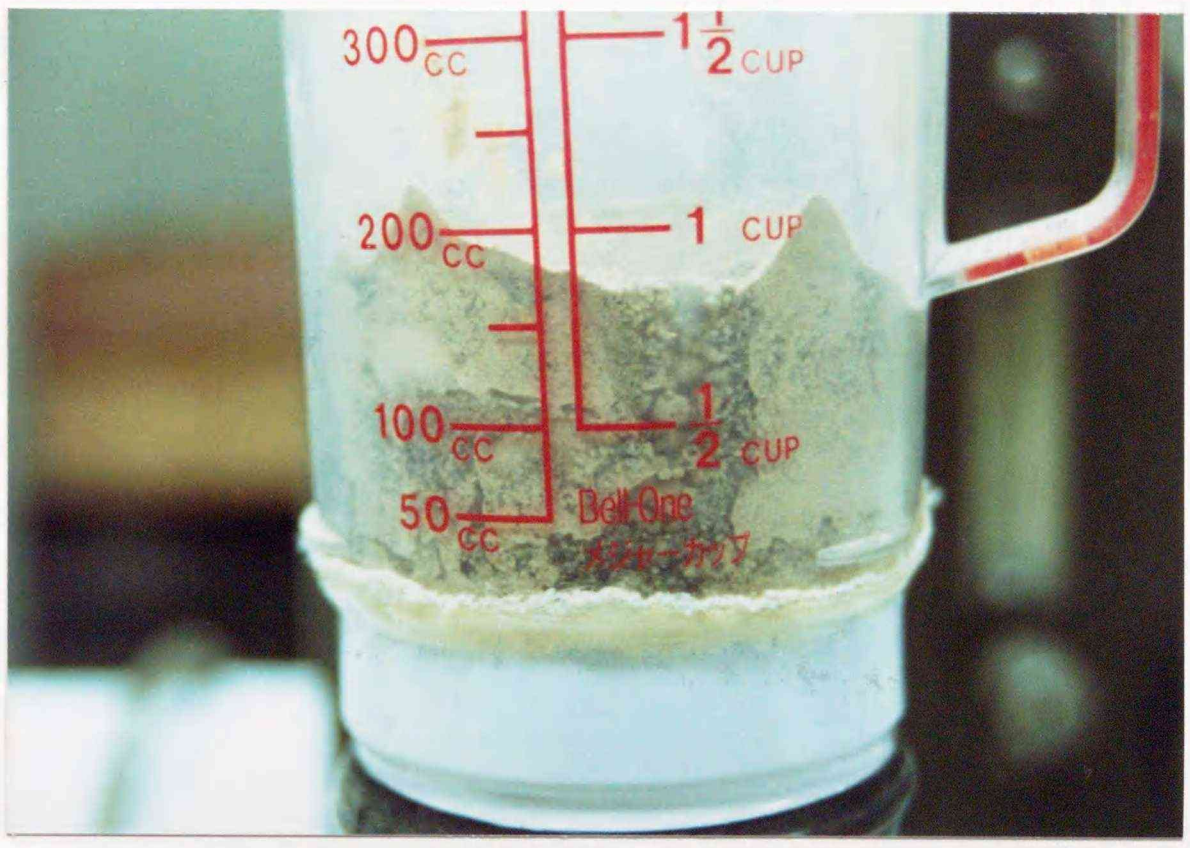

Plate 6-7. Q=22 (*l*/min). Enlargement of the crater size; bubbling of the finer particles at the surface of the craters; and formation of the fines-rich layer at the surface of the bed are observed.

Q=25

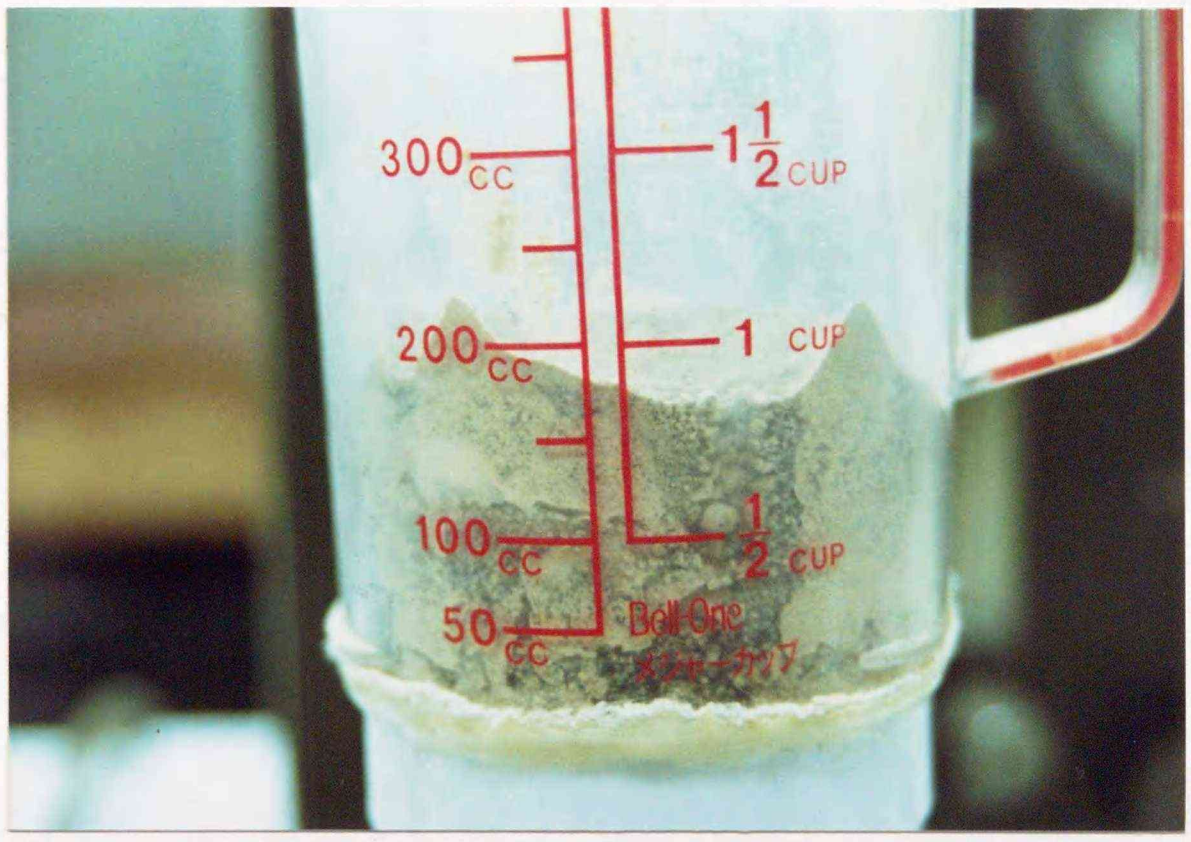

Plate 6-7. Q=25 (*l*/min). Segregation beneath the craters; and bubbling at the surface of the craters segregating finer particles toward the top are observed.

Q=26

Plate 6-7. Q=26 (*l*/min). Enlargement of the size of the craters; bubbling at the surface of the craters; formation of the fines-depleted layer (DL) under the crater; and formation of the fines-rich layer (FL) at the top of the bed are observed. In this experiment, grains larger than ca. 1 mm were not affected by the upward flow at all.

A
Q=1
(ϕ=3-4)

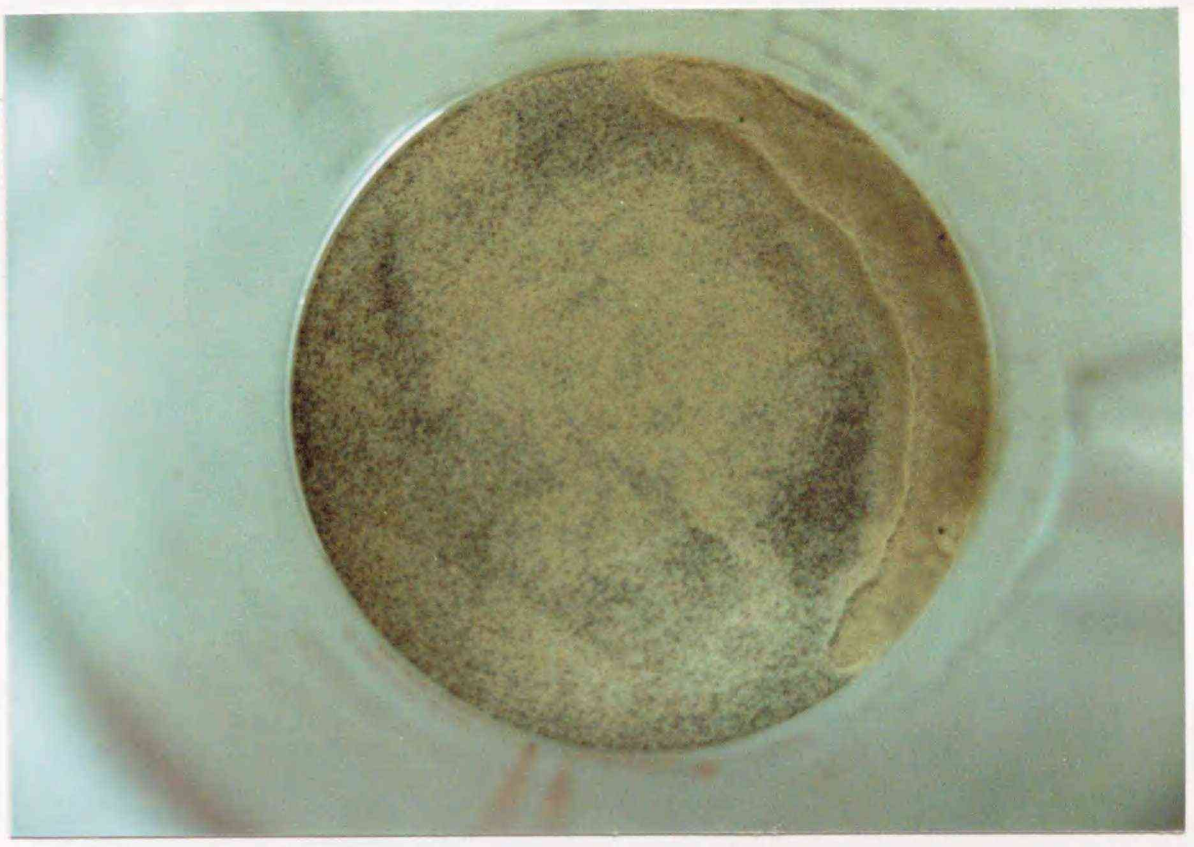

B
Q=4
(ϕ=2-3)

Plate 6-8. The results of the fluidization experiments using the sieved samples of the DL. **A.** ϕ=3-4 (1/16-1/8 mm; 25 cm^3). **B.** ϕ=2-3 (1/8-1/4 mm; 50 cm^3). **C.** ϕ=1-2 (1/4-1/2 mm; 50 cm^3). **D.** ϕ=0-1 (1/2-1 mm; 50 cm^3). Flow rates when started the bubbling for each sample were Q=1 (A), Q=4 (B), and Q=14 (C). The bubbling of the sample D didn't occurred even at 27 *l*/min. These results indicate that larger particles than this size (ca. 1 mm) can not be fluidized in this equipment.

C
Q=14
(ϕ=1-2)

D
Q=27
(ϕ=0-1)

Plate 6-8. Continued.

Q=25
0.2 mm
glass beads

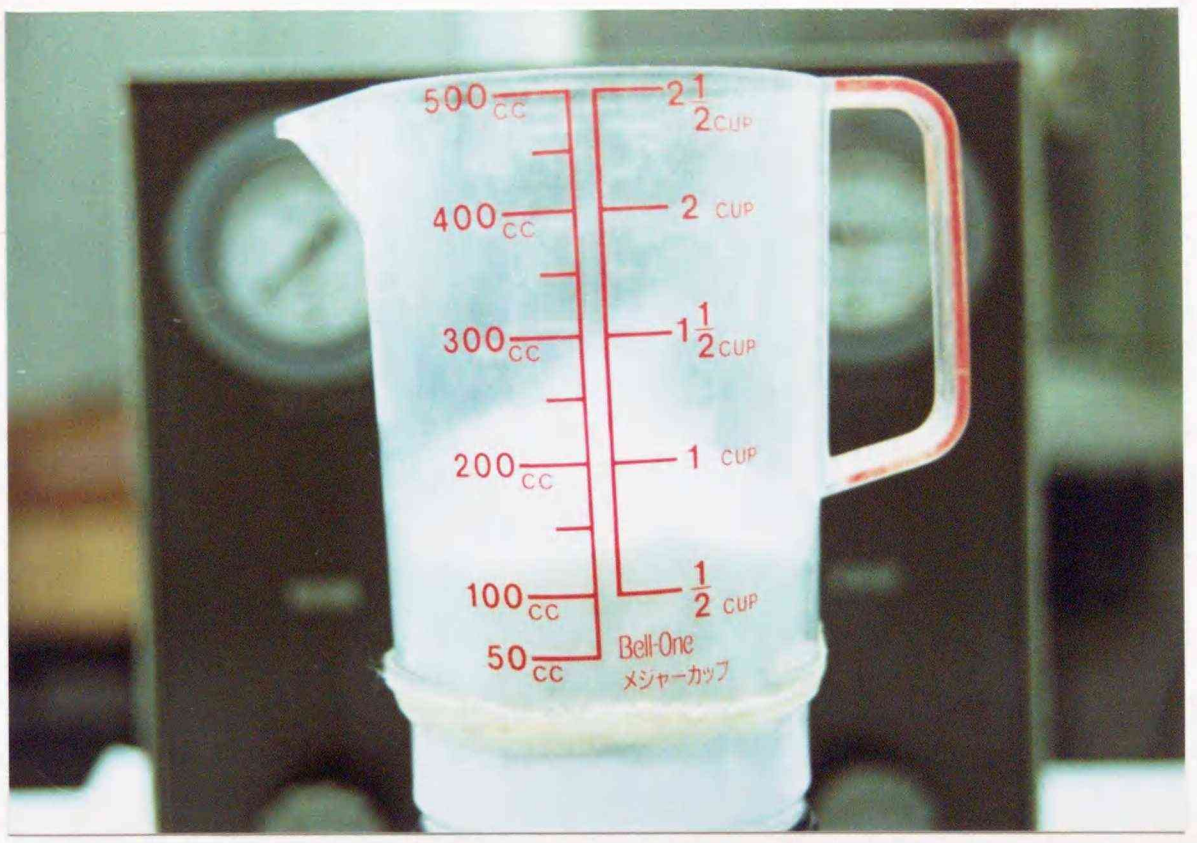

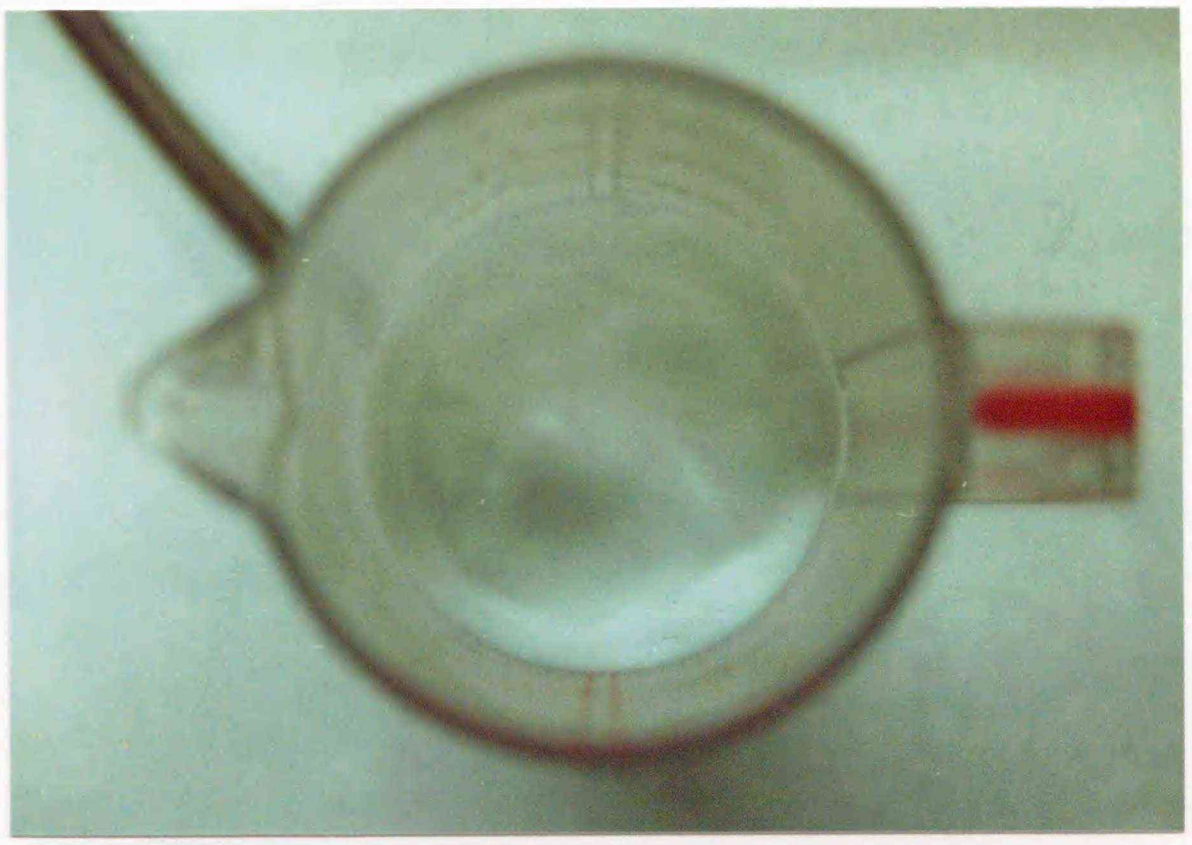

Plate 6-9A. Result of fluidization experiment using glass beads (100 cm^3). The size of the glass beads is 0.2 mm. Complete fluidization is observed due to good-sorting of the sample.

Q=14

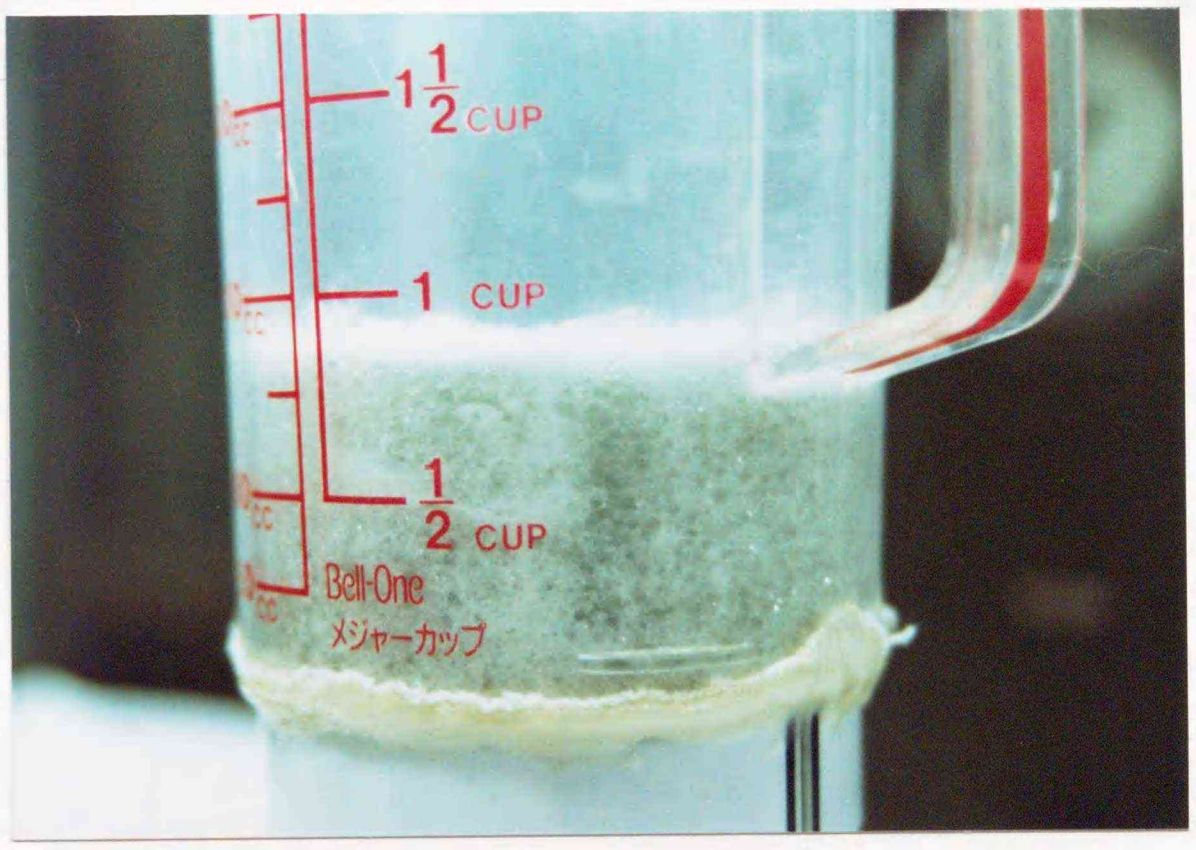

Plate 6-9B. The result of fluidization experiment using the mixture of glass beads in various sizes (150 cm^3). Size of the glass beads is 0.1, 0.2, 0.4, 0.6, 0.8, 1.0, 2.0, and 4.0 mm. Q=14 (*l*/min). Concentration of the finer particles toward the top of the bed from the segregation pipes; and bubbling of the finer particles at the surface are observed.

Q=25

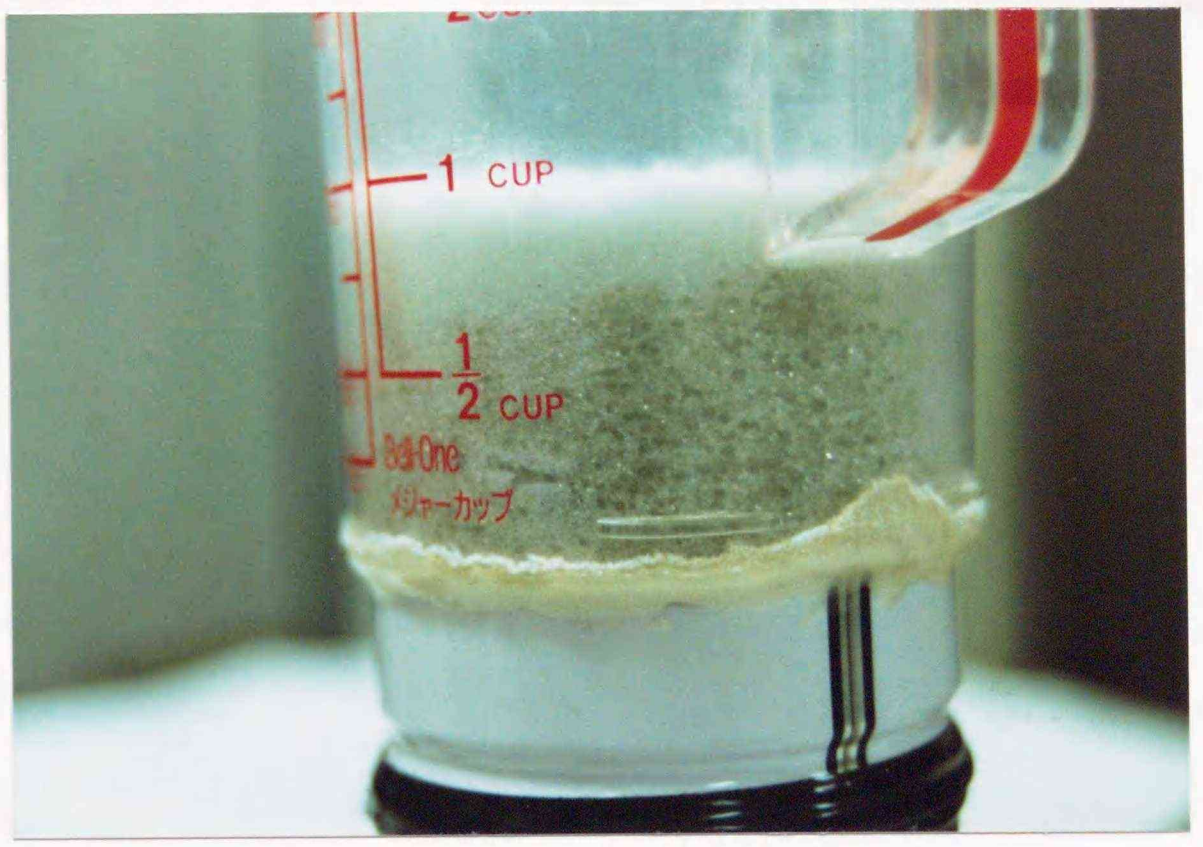

Plate 6-9B. Q=25 (*l*/min). Formation of the fines-depleted layer (DL) at the lower part; and formation of the fines-rich layer (FL) at the upper part of the bed are observed. In this experiment, particles larger than ca. 1.0 mm were not affected by the upward flow at all.

6-2. Unzen 1991-93 pyroclastic flows and deposits

6-2-1. Outline of the 1991-93 eruption

Outline of the 1991-93 eruption of the Unzen Volcano is summarized based mainly on the description of Ohta (1993), Komiya (1993), and Nakada (1993) (Table 6-2).

Earthquake swarms occurred in the Tsubaki Bay, west of the Unzen Volcano on Nov. 21-22, 1989. The hypocenters of the earthquakes migrated toward the east. The hypocenters reached the Unzen Volcano at the early July, 1990. First volcanic tremors were recorded on July 4 and 5, 1990. The earthquakes beneath the Volcano (M=3.9) occurred on July 7. Emissions of steam including volcanic ash occurred at the Jigokuato and the Tsukumojima craters on Nov. 17 (Fig. 6-8). New Byobuiwa craters were opened and the steams with volcanic ash were emitted on Feb. 12, 1991. Three craters: Jigokuato, Tsukumojima, and Byobuiwa craters, started the eruptions on Mar. 29. Larger phreatomagmatic eruptions occurred on Apr. 9. The eruption sites were concentrated on the Jigokuato crater. Shallow earthquake swarms occurred beneath the Jigokuato crater on May 12. The inflation at the summit area was detected by the Electric Distance Measurement (EDM) during this period (Saito et al., 1991). A graben structure was observed around the Jigokuato crater on May 18. A new lava dome (dome 1), 30 m in height, 30 m in width, was extruded at the site of the Jigokuato crater on May 20 (Plate 6-10a).

A first pyroclastic flow occurred due to collapse of the lava dome at 8:07 on May 24, flowing down along the Mizunashi River up to 1 km from the source (Fig. 6-8; Plate 6-10c, d). A pyroclastic flow injured one person in the Mizunashi River at 2.4 km from the source at 11:25 on May 26. A large pyroclastic flow occurred due to landslide of the lava dome at 16:08 on June 3 (Chap. 6-2-3), reaching the Kitakamikoba area, 3.6 km away from the source

Table 6-2. Outline of the 1991-93 eruption of the Unzen Volcano.

1991	Apr. 9:	Phreatic explosions occurred at the Jigokuato vent.
	May 12:	Shallow earthquakes were increased at the summit area.
	May 20:	A lava dome, dome 1, appeared at the Jigokuato vent.
	May 24:	The first pyroclastic flow occurred by the collapse of the lava dome, flowing down along the Mizunashi River. The runout distance (L) was 1.0 km from the source.
	June 3:	The large pyroclastic flow, L=3.6 km, occurred, causing 43 fatalities at the Kitakamikoba area.
	June 8:	The large pyroclastic flow, L=5.6 km, occurred, causing the explosions.
	June 11:	The explosion occurred at the lava dome. Pumices and lithic fragments were ejected toward the northeastern area.
	June 30:	The large debris flow occurred, reaching the Ariake Bay.
	Sep. 15:	The large pyroclastic flow, L=6.5 km, occurred, flowing down along the Oshigadani Valley.
1992	May 1:	The large debris flow, L=8.0 km, occurred, flowing down along the Mizunashi River.
	Mid-Aug.:	Debris flows occurred frequently.
	Late-Aug.:	Pyroclastic flows, L=3-4 km, occurred frequently.
	Sep. 27:	The large pyroclastic flows, L=3-4 km, occurred along the Mizunashi and the Akamatsudani Rivers.
	Oct. 3:	The large pyroclastic flow, L=4 km, occurred.
	Oct. 10:	The large pyroclastic flow, L=4 km, occurred.
	Dec. 20:	The large pyroclastic flow, L=4 km, occurred along the Mizunashi River.
1993	Apr. 28:	The large debris flow occurred along the Mizunashi River.
	May 2:	The large debris flow occurred along the Mizunashi River.
	June 23:	The large pyroclastic flow, L=4.0 km, occurred, reaching the Senbongi area, causing a fatality.
	June 26:	The largest pyroclastic flow, L=6.7 km, occurred, flowing down along the Mizunashi River.

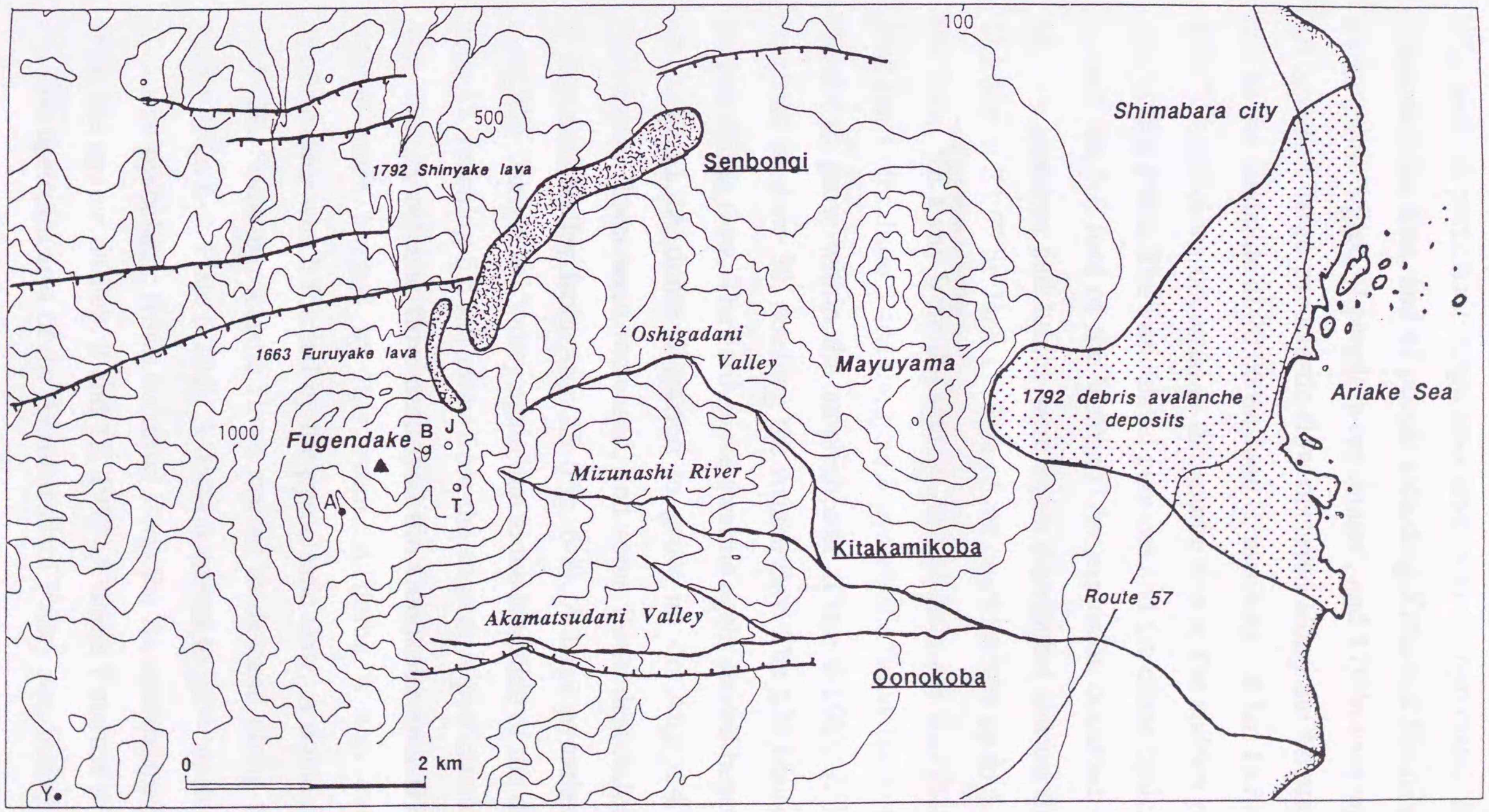

Fig. 6-8. Topographic map of the Unzen Volcano before the eruption (after, Yamamoto et al., 1993). Pyroclastic flows are flowing down along the Mizunashi River, the Akamatsudani and the Oshigadani Valleys. Recently, pyroclastic flows also descend the slope toward northeastern area, Senbongi. J, Jigoku-ato crater; T, Tsukumojima crater; B, Byobuiwa crater. A and Y indicate the site of seismograph at Azamidani and Yadake, respectively. Contour interval is 100 m.

(Fig. 6-8). A pyroclastic surge associated with the pyroclastic flow destroyed the Kitakamikoba area, and 43 people including Katia and Maulice Kraft and Harry Gliken were killed, 9 people were injured, and 179 houses were burned (Plate 6-10g, h). A large pyroclastic flow occurred along the Mizunashi River again due to the landslide at 20:06 on June 8, reaching 5.6 km from the source (Plate 6-10f). Explosions occurred at the source due to the sudden pressure reduction during this event. The vesiculated pumices and the dense lithics were distributed toward the NE foot of the Volcano. An explosion occurred at the lava dome, and the pumices and lithics were again distributed toward the NE foot of the Volcano at 23:59 on June 11. Size of the pumices was up to 5 cm in diameter at the 7 km NE away from the source. An amphitheater was formed at the source area due to the June 3 and the June 8 pyroclastic flows (Plate 6-10b). A dome 2 started to grow within the amphitheater (Plate 6-10b). A large debris flow occurred on June 30, reaching the Ariake Bay. The 137 houses were destroyed by this debris flow. The earthquake swarms again started beneath the lava dome on Aug. 11. A dome 3 started to grow up on Aug. 14. The number of pyroclastic flows were increased, and some flows descended down along the Oshigadani Valley from Aug. 25 (Fig. 6-8). A large pyroclastic flow occurred along the Oshigadani Valley again due to the landslide of the dome 3 at 18:54 on Sep. 15, reaching 5.6 km away from the source. A pyroclastic surge associated with this pyroclastic flow destroyed the Oonokoba area (Fig. 6-8). The 218 houses were burned by this event. A dome 4 was extruded from the amphitheater which formed by the pyroclastic flow. A dome 5 was extruded on Nov. 24. Some pyroclastic flows started to descend along the Akamatsudani Valley (Fig. 6-8; Plate 6-10d). A dome 6 started to grow up on Dec. 3.

Large pyroclastic flows occurred along the Akamatsudani Valley up to 3 km from the source on Feb. 2 and 12, 1992. A dome 7 started to grow up on Mar. 25. The upstream area of the Akamatsudani Valley was buried by the pyroclastic

flow deposits. Pyroclastic flows occurred due to the collapse of the most of the dome 7 on Aug. 8. These pyroclastic flows reached near the Oonokoba area and the associated pyroclastic surge burned 17 houses. A dome 8 started to grow up on Aug. 11. Many debris flows occurred along the Mizunashi River at the middle of August. The 240 houses, road, and railway were buried by these debris flows. Large pyroclastic flows occurred along the Akamatsudani Valley and the Mizunashi River at 9:18 on Sep. 27, reaching 4 and 3 km from the source, respectively. A pyroclastic flow reached the Kitakamikoba area on Oct. 3. A pyroclastic flow reached 4 km from the source along the Akamatsudani Valley on Oct. 10. The frequency of the pyroclastic flows was decreased from the Nov. 13. A dome 9 was extruded on Dec. 3.

Many pyroclastic flows occurred on Jan 15, 1993. A dome 10 was extruded on Feb. 2. Large pyroclastic flows occurred on Mar. 9, 12, and 16, reaching 3.5-4.0 km from the source. A dome 11 started to grow up on Mar. 17. Some pyroclastic flows started to descend down toward the Senbongi area, NE foot of the Volcano (Fig. 6-8). Large debris flows occurred on Apr. 28, 29, and May 2, burying 500 houses, two main roads, and railway. A large pyroclastic flow descended toward the NE direction on June 23, reaching the Senbongi area. One person was killed by this pyroclastic flow. A large pyroclastic flow occurred along the Mizunashi River on June 26, reaching 6.7 km from the source. Numerous pyroclastic flows have been continued to occur for more than 2 years and a half (Fig. 6-13). The number of the total pyroclastic flows from May 24, 1991, to Nov. 30, 1993, was more than 8600 based on the seismic records at the Unzendake Weather Station, JMA.

6-2-2. Volume estimation

Volume estimation of the erupted materials is important to evaluate the condition of the volcanic activity and to detect the change of magma supply rate.

Detail techniques of the volume estimation are described in Takarada et al. (1993a).

The volumes of the lava domes from May 20 to July 14, 1991, were measured using the video images and the aerial photos. The lava dome on July 8, 1991, is shown in Fig. 6-9. The amphitheater which was formed by the June 3 and the June 8 pyroclastic flows are visible in the figure (Fig. 6-9; Plate 6-10b). The estimated lost volume of the basement materials at these event was ca. 1.5×10^6 m^3. The volumes of the lava domes were measured by the following method: (1) making topographic cross sections at 100 m intervals using the video images and the aerial photos; (2) measuring the area of the each cross sections; (3) calculating the volumes of each segment; and (4) integrating the volumes of the segments. The measured volumes of the lava domes from May 20 to July 14, 1991, are shown in Table 6-3. It is apparent that major amount of the lava domes were lost on the June 3 and the June 8, 1991.

The volumes of the pyroclastic flow deposits on June 7 and June 16, 1991, were measured using the video images and the aerial photos (Fig. 6-10). The volumes were measured by the same method of lava domes. The volumes of the total pyroclastic flow deposits at June 7 was $2.3 \times 10^6 m^3$ in DRE (Dense Rock Equivalent; Walker, 1980) and those at June 16 was $4.3 \times 10^6 m^3$ in DRE.

Only from the image data, it is difficult to estimate the continuous volume variations of the erupted materials, which change the situation day by day due to the condition of climate and ash cloud. On the other hand, the indirectly method using the tremor records is useful, because it is possible to estimate: (1) the continuous volume variations of the erupted materials; and (2) the volumes of each pyroclastic flow in real-time. The tremors due to pyroclastic flows were recorded on the seismographs of the Unzendake Weather Station, JMA (Yamasato et al., 1993). The tremor records at the Yadake station ('Y' in Fig. 6-8) when the over-amplitudes were recorded for more than 30 seconds at the

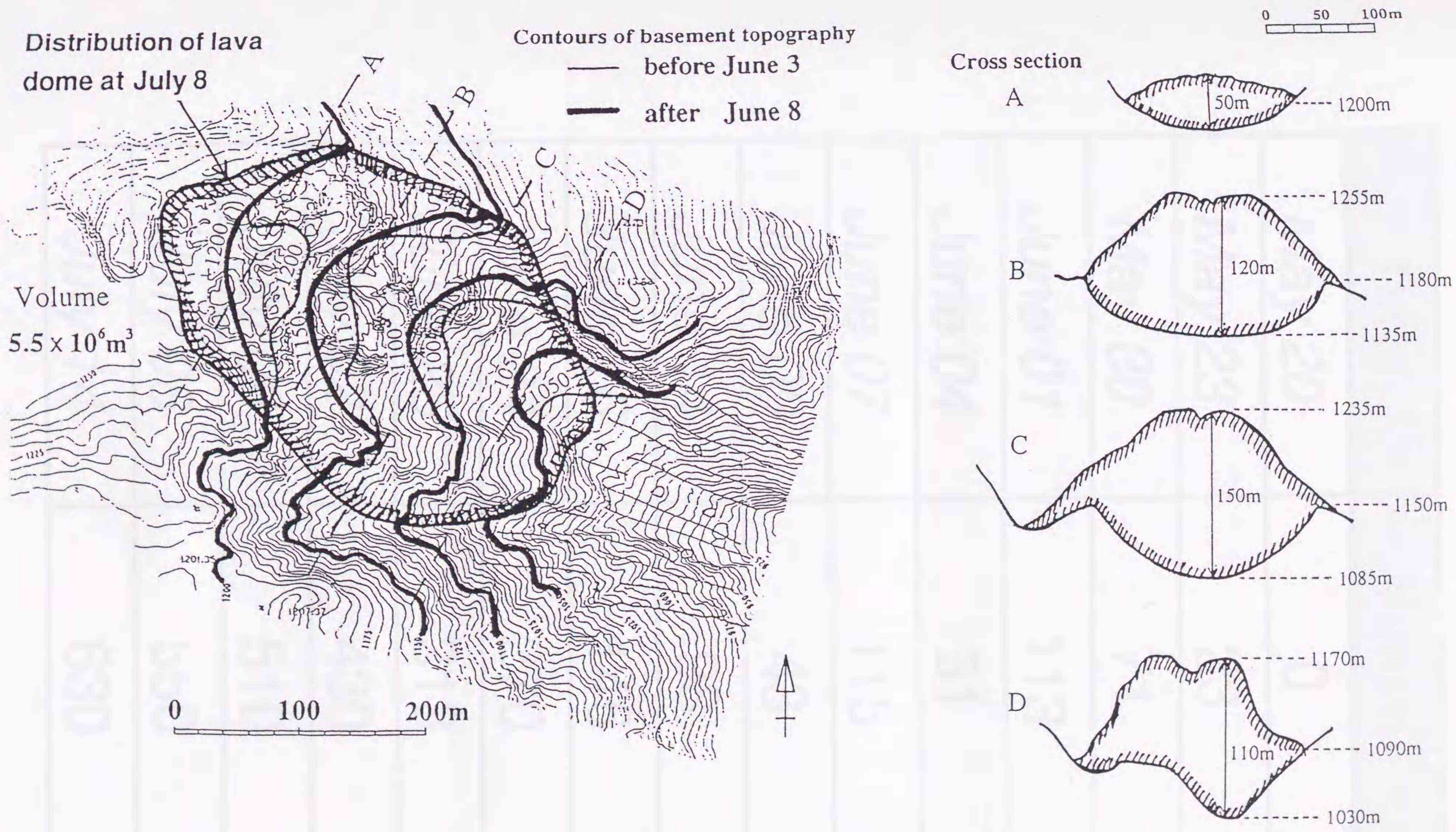

Fig. 6-9. Plan view and cross sections of the lava dome on July 8, 1991. Narrow contour lines indicate the basement topography beneath the dome just before the event on June 3, 1991. Broad contour lines indicate the basement topography just after the event on June 8, 1991. The basement erosion were occurred, forming an eastward facing horseshoe crater, at the time of the pyroclastic flows on June 3 and June 8, 1991. The estimated volume of the lava dome on July 8, 1991, was 5.5×10^6 m^3. The volume was estimated by the method: (1) measuring the areas of the cross sections; (2) calculating the volumes between the sections; (3) integrating them.

Table 6-3. List of the measured volumes ($x10^4$ m^3) of the lava domes from May 20 to July 14, 1991.

Date	Volume
May 20	0
May 23	23
May 30	71
June 01	113
June 04	31
June 07	115
June 09	43
June 14	98
June 16	146
June 24	270
June 26	313
July 02	430
July 06	510
July 08	550
July 14	630

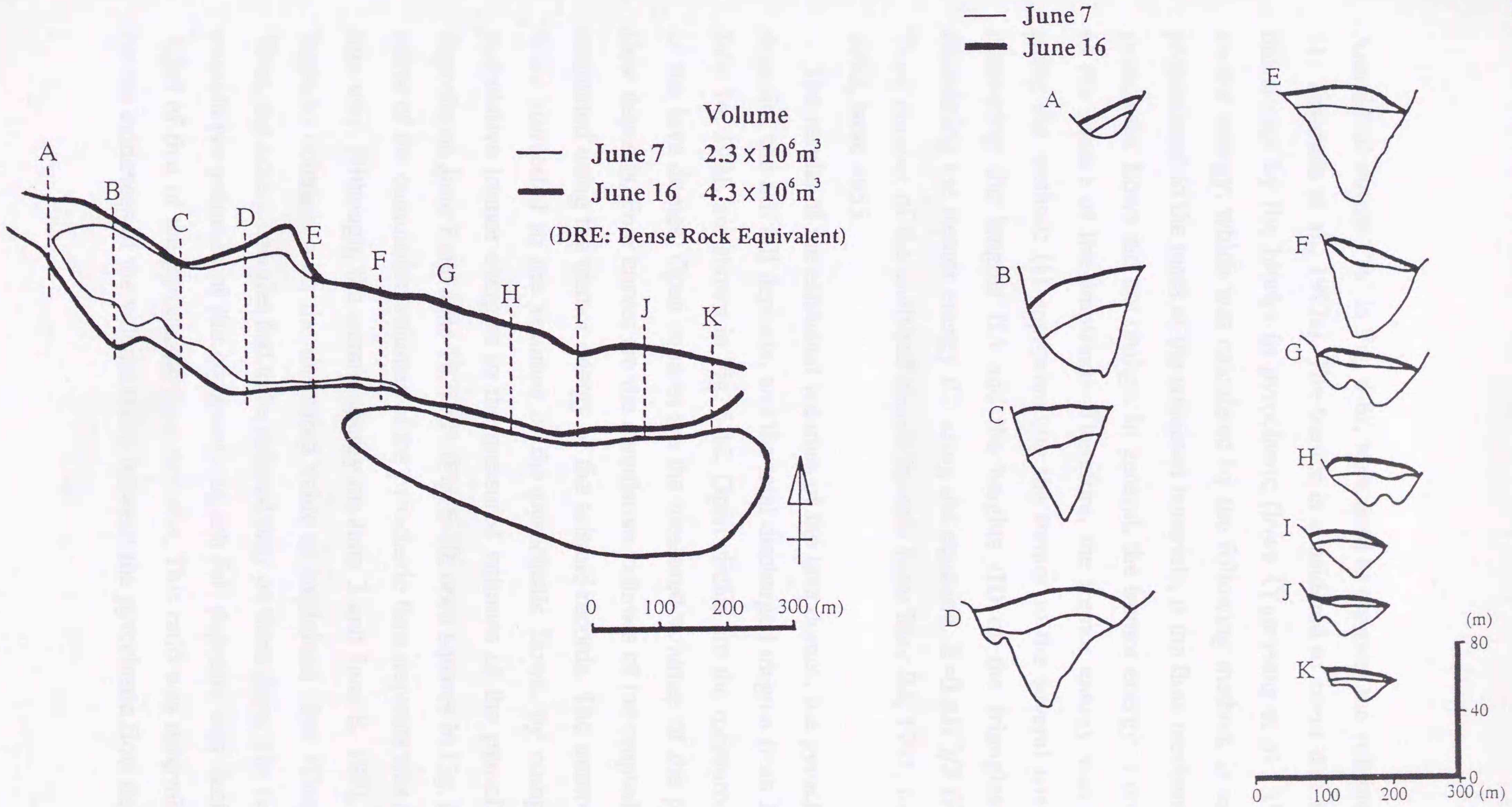

Fig. 6-10. Plan view and cross sections of the pyroclastic flow deposits at the upper stream area of the Mizunashi River on June 7 and June 16, 1991. The estimated volumes of these pyroclastic flow deposits were 2.3×10^6 m^3 and 4.3×10^6 m^3 in DRE, respectively. DRE, dense rock equivalent (Walker, 1980).

Azamidani station ('A' in Fig. 6-8), were used to estimate the volumes (Fig. 6-11; Takarada et al., 1993a). The tremor is considered to occur due to striking the slopes by the blocks in pyroclastic flows (Yamasato et al., 1993). The tremor energy, which was calculated by the following method, is assumed to proportional to the mass of the collapsed materials, if the flow mechanism of the pyroclastic flows did not change. In general, the tremor energy is proportional to the square of the amplitude. Therefore, the tremor energy was estimated using the method: (1) approximating the tremor to the several triangles; (2) measuring the lengths (L) and the heights (H) of the triangles; and (3) calculating the tremor energy (E) using the equation, $E=(L \times H^2)/3$ (Fig. 6-11). Total number of the analyzed tremor records from May 24, 1991, to Nov. 30, 1993, were 4955.

The results of the estimated volumes of the lava domes, the pyroclastic flow deposits, the ash fall deposits, and the total discharged magma from May 23 to July 14, 1991, are shown in Fig. 6-12. Open circles are the measured volumes of the lava domes. Open squares are the measured volumes of the pyroclastic flow deposits. Four curves are the cumulative volumes of the erupted materials estimated using the tremor energy of the seismic records. The tremor energies were converted to the volumes of the pyroclastic flows, by comparing the cumulative tremor energies to the measured volumes of the pyroclastic flow deposits on June 7 and June 16, 1991 (Fig. 6-10; open squares in Fig. 6-12). The curve of the cumulative volumes of the pyroclastic flow deposits was decided in this way. Although, the tremor energy on June 3 and June 8, 1991, were too large to coincide with the measured value as explained later (Chap. 6-2-3). Thus, the excess energies had to be reduced only on these days. The curve of the cumulative volumes of the co-ignimbrite ash fall deposits was decided to be 1/3rd of that of the pyroclastic flow deposits. This ratio was determined based on the evidences of the volume ratios between the pyroclastic flow deposits and

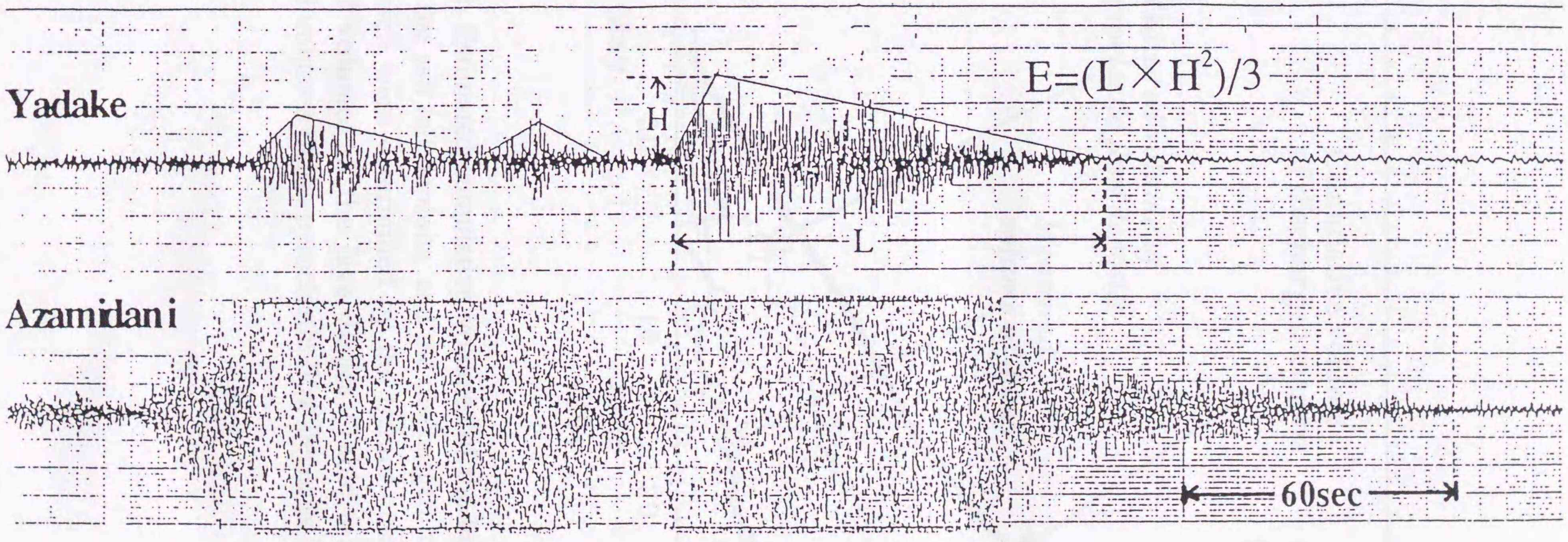

Fig. 6-11. An example of the seismic wave produced by the pyroclastic flows recorded at 14:03 on May 27, 1991. The tremor energy was determined by the method: (1) approximating the tremor record to several triangles; (2) measuring the heights, H, and lengths, L, of the triangles; (3) calculating the energy, E, using an equation: $E=(L \times H^2)/3$. The sites of seismographs, Yadake and Azamidani, are shown in Fig. 6-8.

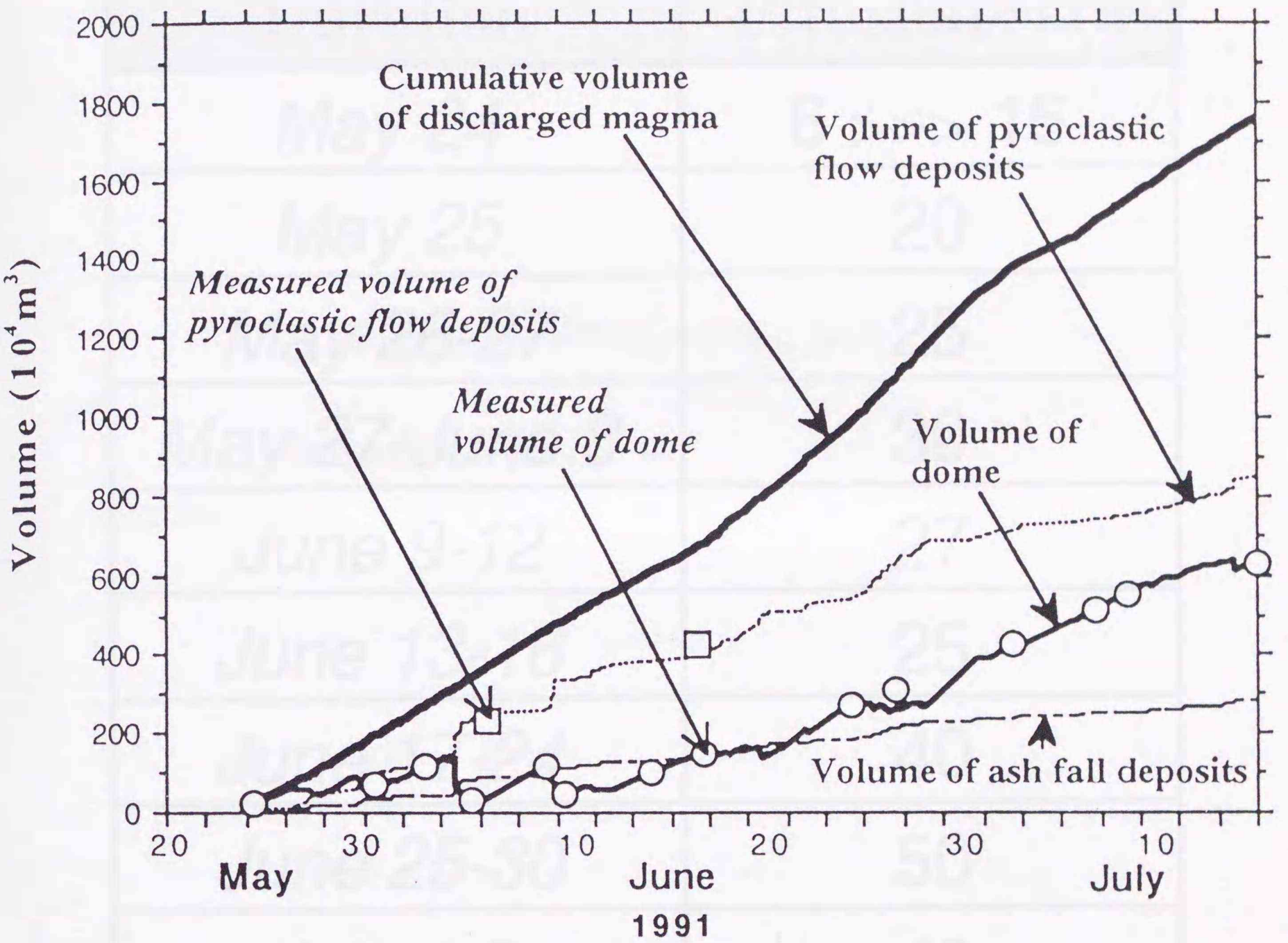

Fig. 6-12. Estimated cumulative volumes of the lava domes, the pyroclastic flow deposits, the ash fall deposits, and the discharged magma from May 23 to July 14, 1991, which were determined by the tremor energy. Open circles indicate the measured volumes of the lava domes (Table 6-3). Open squares indicate the measured volumes of the pyroclastic flow deposits (Fig. 6-10).

Table 6-4. List of the estimated effusion rates ($x10^4$ m^3/day) of magma from May 24 to July 14, 1991.

Duration	Effusion rate
May 24	6 >>> 15
May 25	20
May 26-27	25
May 27-June 8	30
June 9-12	27
June 13-16	25
June 17-24	40
June 25-30	50
July 1-2	40
July 3-5	25
July 6-8	35
July 9-14	32

the associated ash fall deposits on May 29, June 3, and June 8, 1991 (Watanabe et al., 1991). The effusion rates of magma (Table 6-4) were decided based on the measured volumes of the domes (Table 6-3). The effusion rates of magma were low at the first stage. But, relatively constant at a rate of 0.34×10^6 m^3/day in average during this period. The curve of the cumulative volumes of the discharged magma was decided using the Table 6-4. The curve of the cumulative volumes of lava domes was decided by taking the cumulative volumes of the pyroclastic flow deposits and the ash fall deposits from the cumulative volumes of discharged magma (Fig. 6-12). On July 14, 1991, the estimated volumes of the lava dome, the pyroclastic flow deposits, the ash fall deposits, and the total discharged magma were 6.4, 8.5, 2.8, and 18×10^6 m^3 in DRE, respectively.

The curve of the cumulate volumes of the pyroclastic flow deposits from May 24, 1991, to Nov. 30, 1993, are shown in the Fig. 6-13a. The estimated total volumes of the pyroclastic flow deposits until Nov. 30, 1993, was 1.36×10^8 m^3 in DRE. This curve agreed to the values from Dec. 15, 1991, to Aug. 7, 1992, measured by Geographical Survey Institute and Public Works Research Institute (open squares in the middle of Fig. 6-13a). But, the measured values on Nov. 17, 1992, and on Mar. 5 and Oct. 13, 1993, are rather small than the curve. These differences may have occurred due to compaction and erosion of the pyroclastic flow deposits. The dates of the appearances of new lava domes are also shown in Fig. 6-13a (small black circles). It seems that the appearance of new domes changed the frequency of occurrence of the pyroclastic flows. Histograms of monthly average volumes of the pyroclastic flow deposits per day during this period are shown in Fig. 6-13b. High rate of the occurrence of pyroclastic flows were recorded on Sep., 1991 (39.8×10^4 m^3/day) and June, 1993 (43.8×10^4 m^3/day). Low rate of the occurrence of pyroclastic flows were recorded on Jan., 1993 (1.1×10^4 m^3/day) and Nov., 1993 (0.9×10^4 m^3/day).

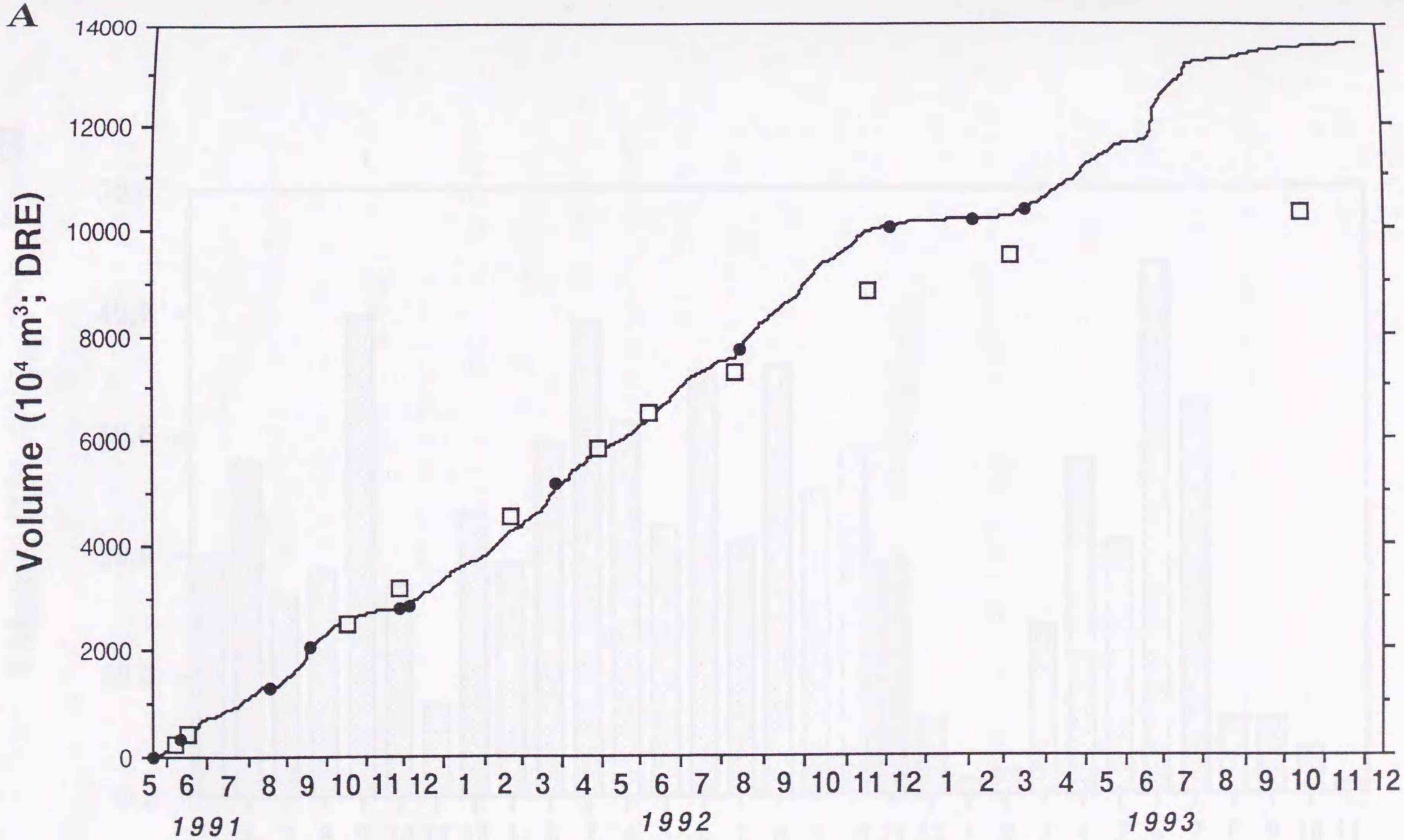

Fig. 6-13A. Cumulative volume of the pyroclastic flow deposits from May 24, 1991 to Nov. 30, 1993. The cumulative volume was determined by the records of tremor associated with pyroclastic flows (Takarada et al., 1993a). Small closed circles indicate the dates of appearance of new lava domes, dome 1 to dome 11. Appearance of new dome seems to change the frequency of occurrence of pyroclastic flows. Open squares indicate the measured cumulative volumes of the pyroclastic flow deposits. GSJ measured the data on June 7 and June 16, 1991. GSI and PWRI measured the other data on Oct. 15 and Nov. 25, 1991, Feb. 19, Apr. 25, June 3, Aug. 7, and Nov. 17, 1992, and Mar. 5 and Oct. 13, 1993. The recent differences between the cumulative curve and the measured data were probably occurred due to compaction and erosion of the deposits.

B

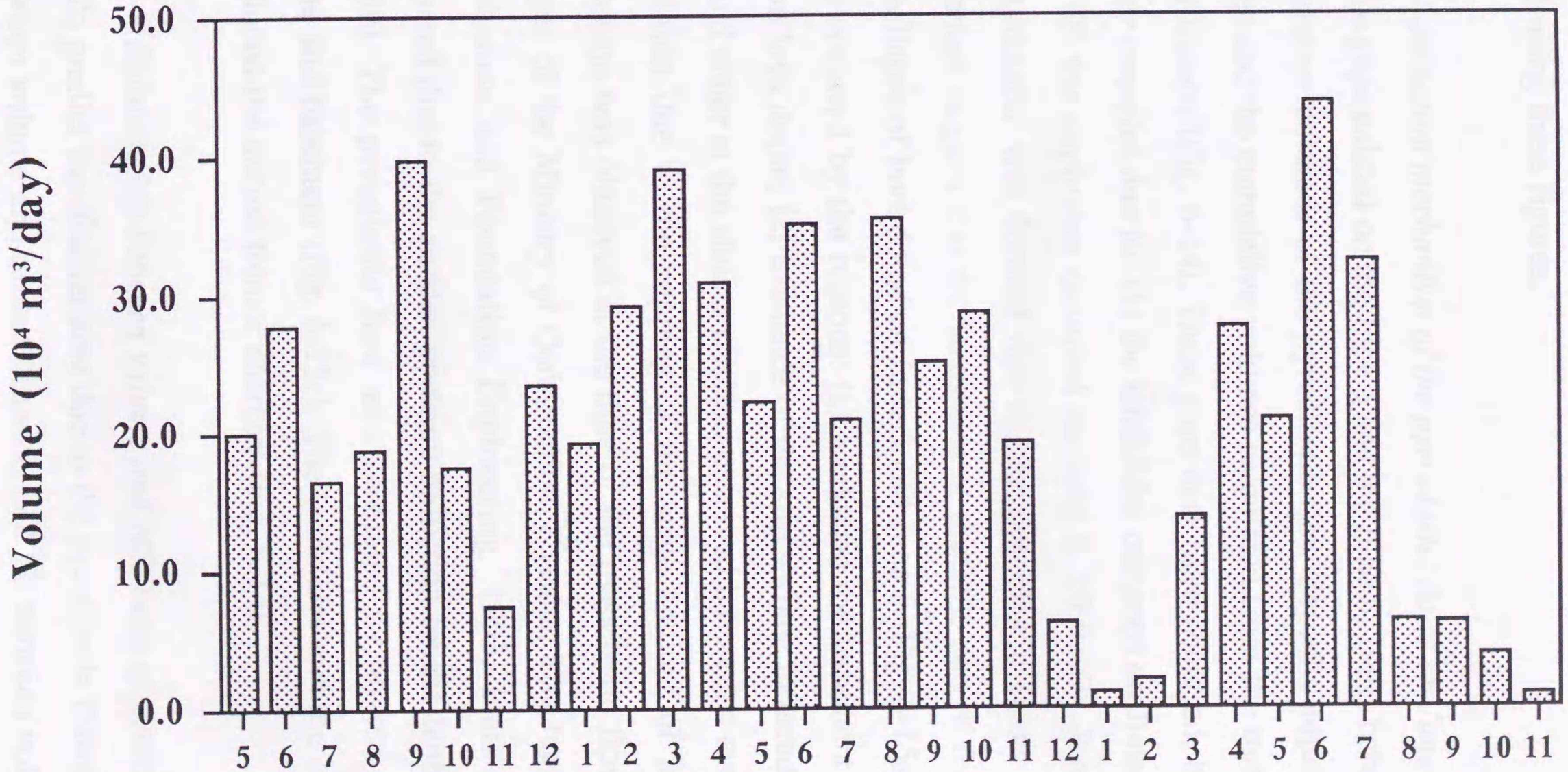

Fig. 6-13B. Histogram of monthly average volumes of the pyroclastic flow deposits per day from May, 1991 to Nov., 1993. High rate of the occurrence of pyroclastic flows were recorded on Sep., 1991, 39.8x10^4 m^3/day, and June, 1993, 43.8x10^4 m^3/day. Low rate of the occurrence were recorded on Jan., 1993, 1.1x10^4 m^3/day, and Nov., 1993, 0.9x10^4 m^3/day.

Changes of frequency of the pyroclastic flows can be evaluated continuously in detail using these figures.

6-2-3. Initiation mechanism of the pyroclastic flows on June 3 and June 8, 1991

The gaps existed on the June 3 and the June 8, 1991, between the curve of the cumulative volumes of the pyroclastic flow deposits adjusted to the measured values and the cumulative volumes calculated from the tremor energies without modification (Fig. 6-14). These gaps may have occurred, because of the excess tremor energies due to: (1) the landslides occurred on June 3 and June 8, 1991; and (2) the explosion occurred on June 8, 1991. On June 3 and June 8, the amphitheater was formed due to the pyroclastic flows (Plate 6-10b). This evidences suggest that the landslides of unstable part of the basement triggered the collapse of lava dome on June 3 and June 8 (Fig. 6-15a). The landslide may have occurred by the reasons: (1) weakened the basement by high temperature of the lava dome; (2) existence of the slip surface inferred from the seepage of ground water at the sliding position observed before the events; and (3) unstable condition due to the capping of the large amount of lava. On June 8, the explosion was observed at the time of the pyroclastic flow (the infrared video images of the Ministry of Construction, Kyushu; The Japanese Society of Soil Mechanics and Foundation Engineering, 1993, Plate 39). The explosion occurred due to the sudden pressure reduction by the landslide on June 8 (Fig. 6-15b). The pyroclastic flow was generated by broken up materials of lava dome and basement (Fig. 6-15c). The landslides and the explosion should have produced the excess tremor energies (Fig. 6-14).

6-2-4. Relationship between volume and H/L ratio of pyroclastic flows

To predict the disaster area due to the pyroclastic flows, the relationships (1) between volume and runout distance, and (2) between volume and H/L ratio of pyroclastic flows from May 25 to June 8, 1991, were analyzed (Fig. 6-16).

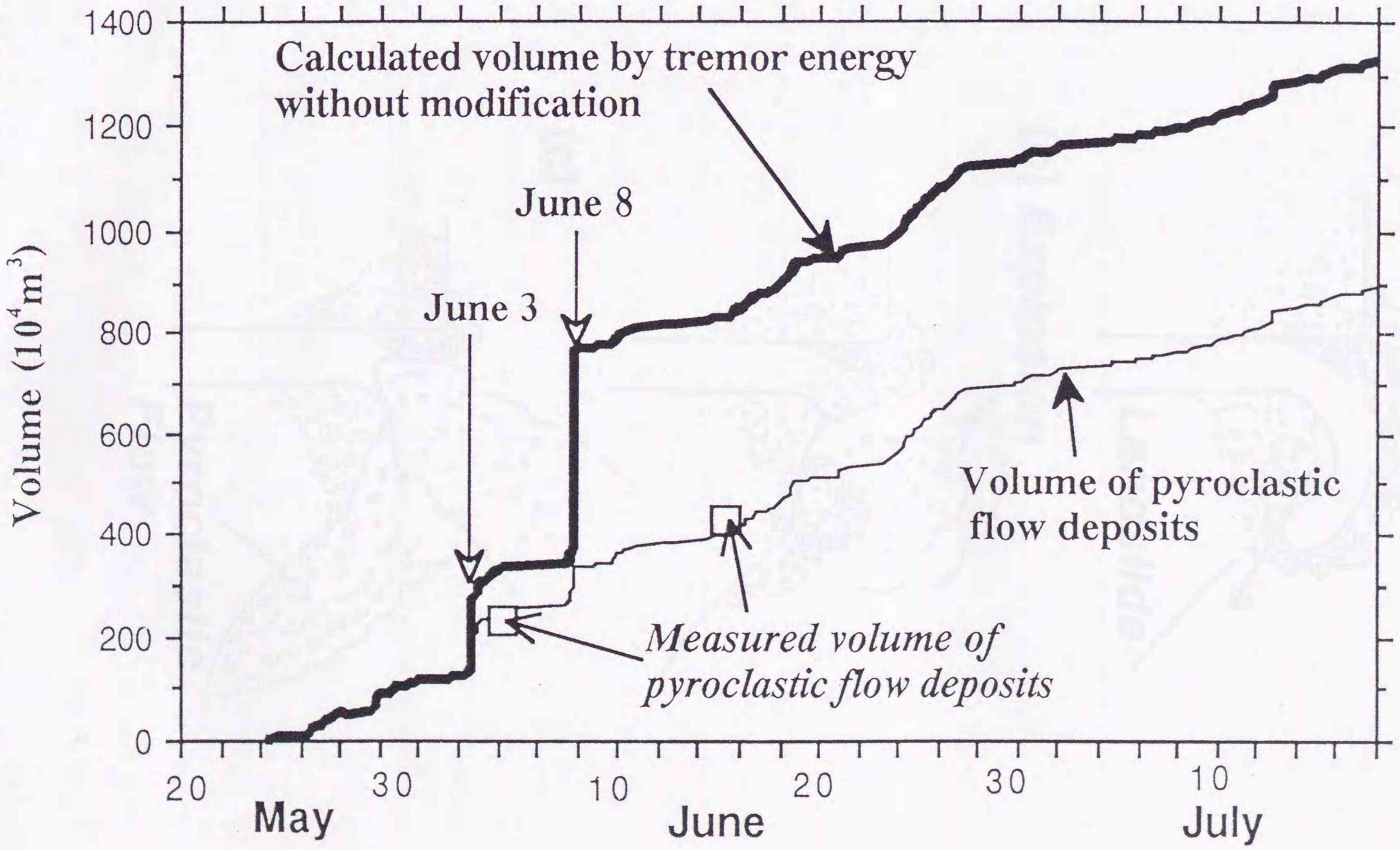

Fig. 6-14. The gaps on June 3 and June 8, 1991, between the cumulative volume of pyroclastic flow deposits adjusted to the measured values (narrow curve), and that calculated from the tremor energy without modification (bold curve). The gaps may have been occurred, because of the excess tremor energies due to: (1) the landslide on June 3 and June 8, 1991, and (2) the explosion on June 8, 1991.

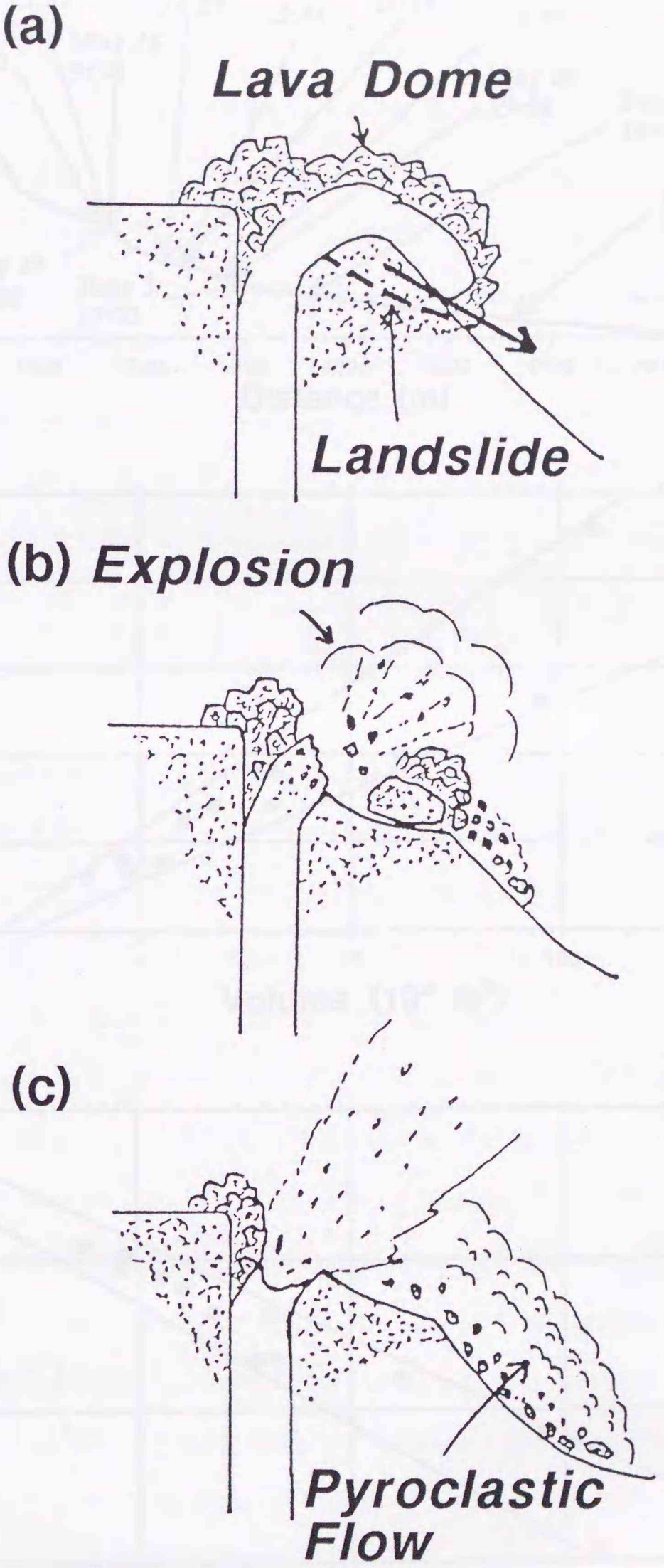

Fig. 6-15. A model of the initiation mechanism of the pyroclastic flow on June 8, 1991. (a) The landslide triggered the collapse of lava dome; (b) the sudden pressure reduction caused the explosion; (c) the pyroclastic flow was generated by the broken up materials of the lava dome and the basement.

A

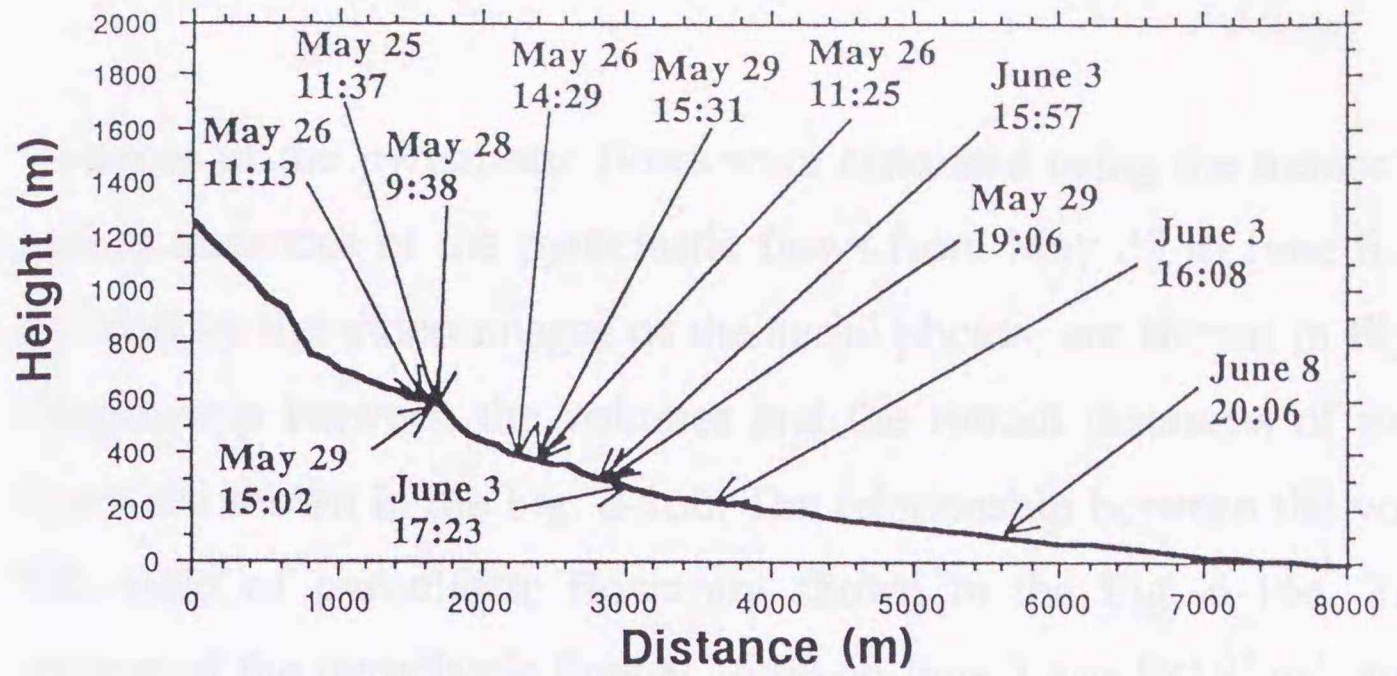

B

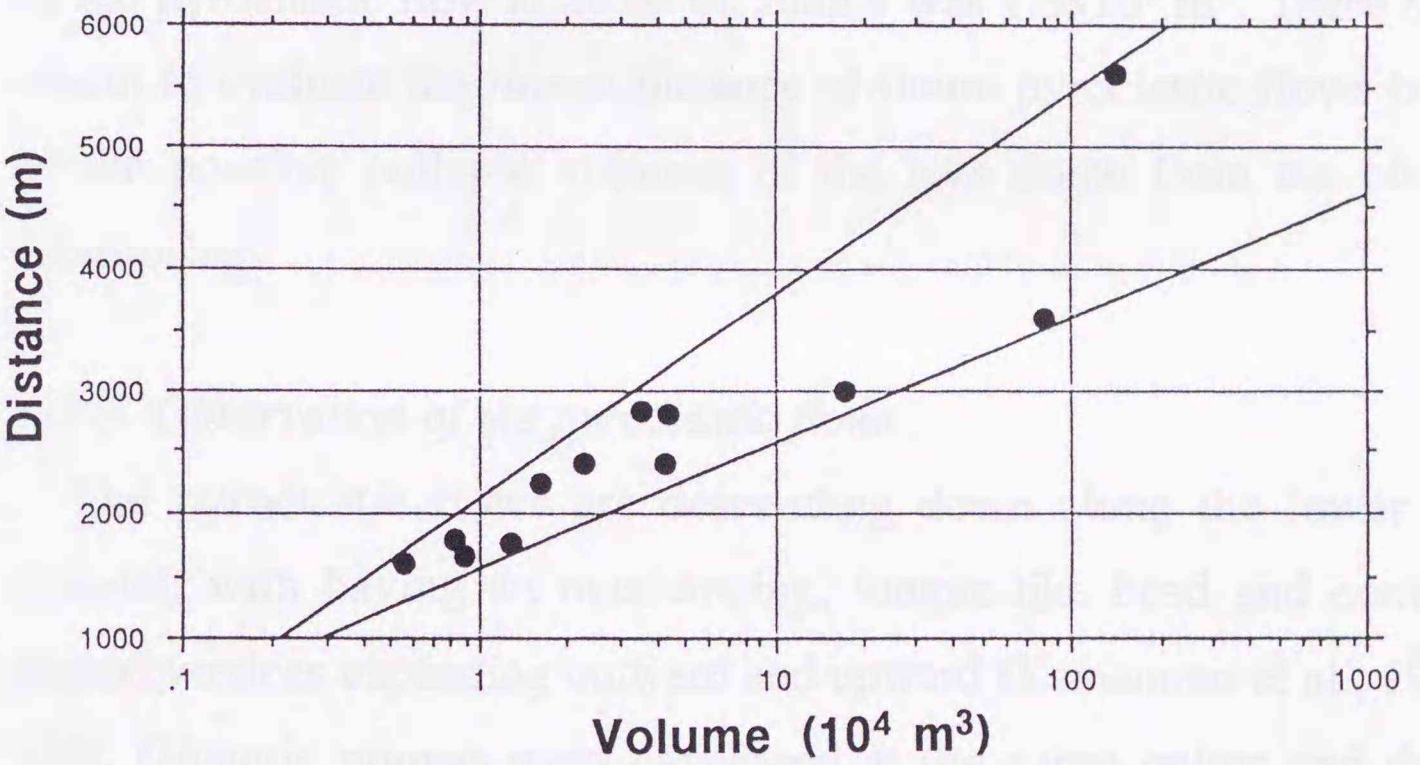

C

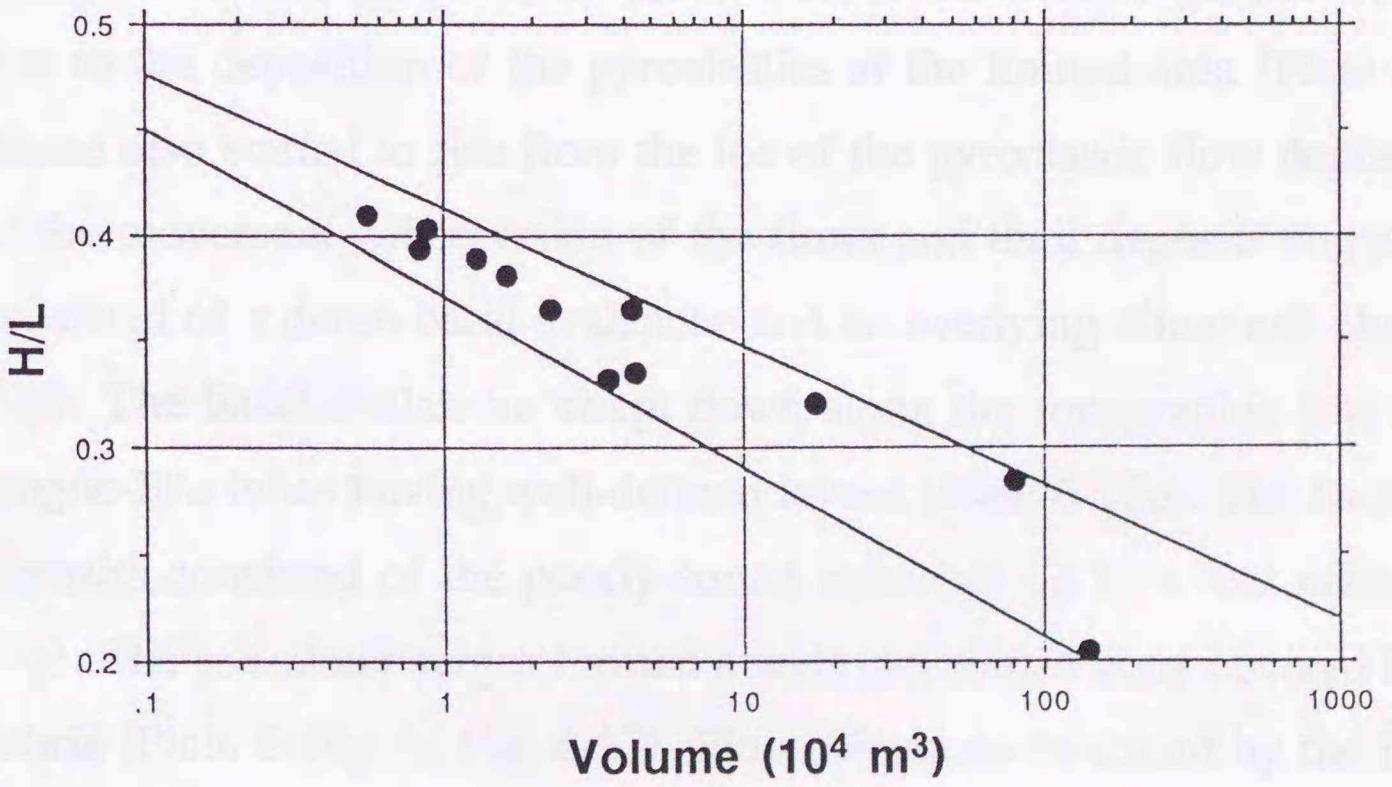

Fig. 6-16A-C. A. Runout distances of the pyroclastic flows from May 25 to June 8, 1991, which were determined using the image data. **B.** Relationship between the volume and the runout distance of pyroclastic flows. **C.** Relationship between the volume and the H/L ratio of pyroclastic flows. H/L, height versus runout distance.

Volumes of the pyroclastic flows were estimated using the tremor energy. The runout distances of the pyroclastic flows from May 25 to June 8, 1991, which decided by the video images or the aerial photos, are shown in Fig. 6-16a. The relationship between the volumes and the runout distances of the pyroclastic flows are shown in the Fig. 6-16b. The relationship between the volume and the H/L ratio of pyroclastic flows are shown in the Fig. 6-16c. The estimated volume of the pyroclastic flow at 16:08 on June 3 was 8×10^5 m^3, and the volume of the pyroclastic flow at 20:06 on June 8 was 1.5×10^6 m^3. These diagrams are useful to evaluate the runout distance of future pyroclastic flows by estimation of the possible collapse volumes of the lava dome from the observation or monitoring.

6-2-5. Observation of the pyroclastic flows

The pyroclastic flows are descending down along the lower part of the channel, with having an overhanging, tongue-like head and cone- or roller-shaped vortices expanding outward and upward (Yamamoto et al., 1993; Plate 6-10d). Gigantic plumes were developed at the curve points and the flat areas along the rivers, where the concentration of the heat of the materials occurred due to the deposition of the pyroclastics at the limited area (Plate 6-10c). The plume also started to rise from the toe of the pyroclastic flow deposit after stop of the movement. Observation of the flows and their deposits suggest that they consisted of a dense basal avalanche and an overlying dilute ash cloud (Plate 6-10d). The basal avalanche swept down along the topographic low and formed tongue-like lobes having well-defined levees (Plate 6-10e). The basal avalanche deposits consisted of the poorly-sorted materials up to a few meters (Plate 6-10g). The ash-cloud surges formed a wide devastated zone covered by very thin debris (Plate 6-10g, h; Fig. 6-17). Flow directions indicated by the blown-down trees within the pyroclastic surge deposits on June 3, 1991, suggest that the

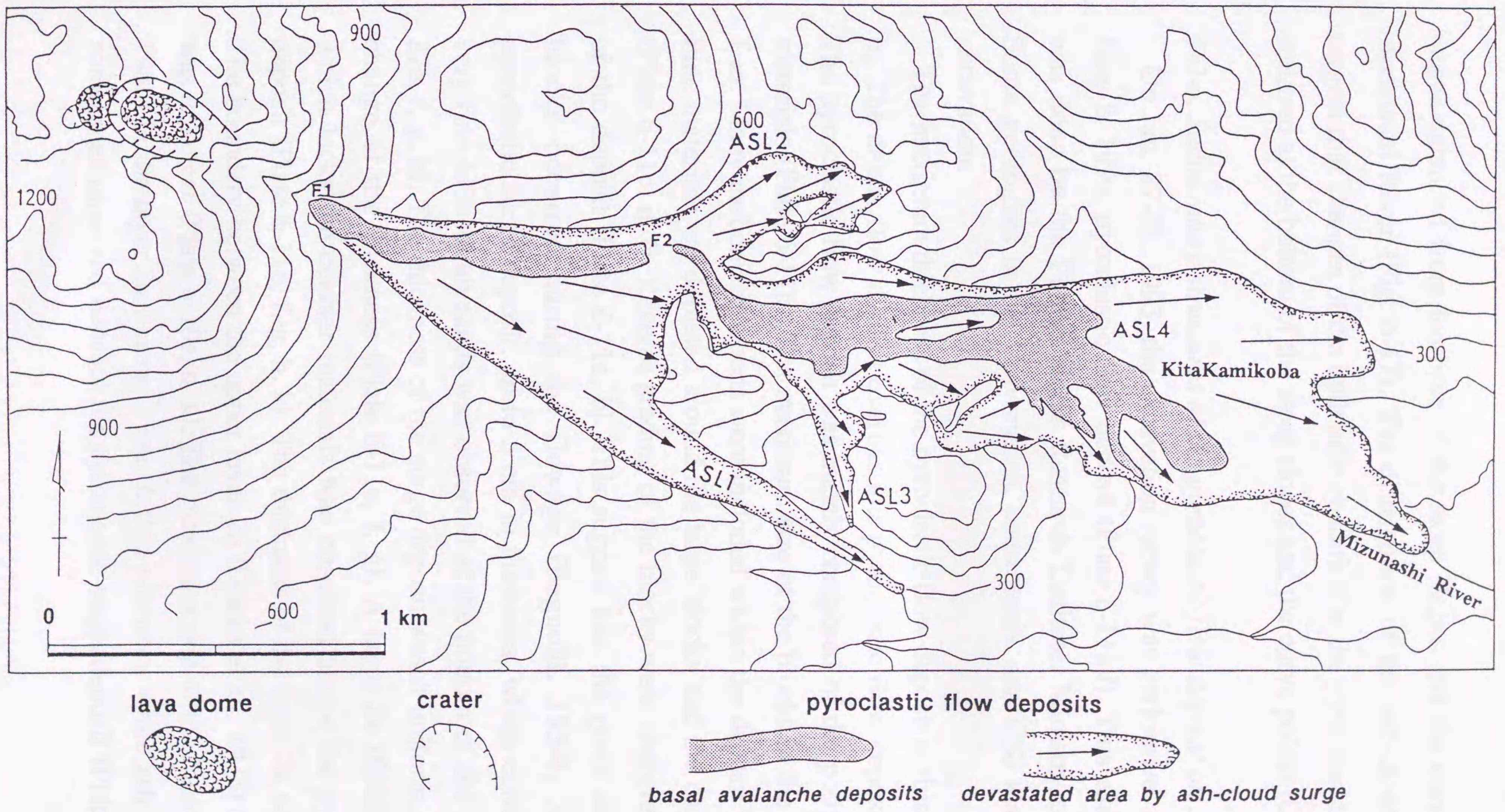

Fig. 6-17. Distribution of the June 3, 1991, pyroclastic flow deposits (after Yamamoto et al., 1993). Contour interval is 50 m. Dark areas along the Mizunashi River are the distribution of the basal avalanche deposits. Hatched area is the distribution of devastated area by the ash-cloud surge. Arrows are the flow directions indicated by downed trees. F1, 1st fall; F2, 2nd fall; ASL, ash-cloud surge lobe.

surges extended from the base of the steep slopes and the curve points of the Mizunashi River (Fig. 6-17). The distribution of the ash-cloud surge deposit suggest that changes of the hydraulic condition in the pyroclastic flow may have occurred at the bottom of the steep slopes and the curve points (Chap. 7-3-2).

6-2-6. Sedimentary structures of the pyroclastic flow deposit on June 8, 1991

On Jan. 27-29, 1993, the excavation survey was performed at the toe of the June 8, 1991, pyroclastic flow deposit (Plate 6-11a-*l*). This excavation project was done by the Public Works Research Institute, Ministry of Construction. Some geologists in the Universities, consultants, and GSJ also attended this excavation.

The maximum thickness of the pyroclastic flow deposit at this point was ca. 4 m. The debris flow deposit overlies this pyroclastic flow deposit (Plate 6-11a). The pyroclastic flow deposit was mainly composed of the poorly-sorted dense materials (Plate 6-11b). The maximum size of the blocks in the deposit was ca. 1 m. Many carbonized woods were included within the deposit (Plate 6-11f, h). Fine materials are depleted around the large blocks and the carbonized woods (Plate 6-11c, d, f). Reverse grading of the blocks were observed at the bottom of the deposit (Plate 6-11a, b). This suggest that the grain interaction of the blocks occurred during the flowage (Bagnold, 1954). A better-sorted pyroclastic surge deposit, up to 5 cm in thickness, which consisted mainly of very-fine to medium sands was observed at the bottom of the deposit (Fig. 6-27e, f, g, h). The thickness of the surge deposit wasn't uniform, showing lateral change of the thickness (Plate 6-11e, f, g). A layer 2a (Sparks et al., 1973) which lacks the coarser materials was observed above the pyroclastic surge deposit (Plate 6-11e, f, g, h, k). The thickness of the layer 2a was up to 15 cm. The boundary between the upper layer 2b (Sparks et al., 1973) and the layer 2a was not clear (Plate 6-10e, h, k). The maximum size of the lithics (ML; Walker, 1980) in the layer 2a was ca. 1 cm. A thin precursor white ash fall deposit was sometimes observed beneath the pyroclastic surge deposit (Plate 6-11h, i). The

segregation pipes were observed at the top of the pyroclastic flow deposit (Plate 6-11i, j, *l*). The top of the pyroclastic flow deposit showed red color due to the high-temperature oxidization. The top of the pyroclastic flow deposit contained much fine materials than the middle level. A trunk remained to stand even in the pyroclastic flow deposit (Plate 6-11k, *l*).

The fines-depletion was also observed in this pyroclastic flow deposit. This evidence suggest that the fines were depleted due to the gas from the carbonized wood fragments and the heated large blocks as proposed at the Komagatake 1929 pyroclastic flow deposit (Chap. 6-1-4). Many segregation pipes and much fine materials at the top of the deposit also support this model. The thin pyroclastic surge deposit at the bottom of the deposit may have formed by an ash-cloud surge which was detached from the basal avalanche at the bottom of the steep slope (Fig. 6-17) and proceeded ahead of the basal avalanche (Chap. 7-3-2).

6-2-7. Velocity measurement

Only a few attempts have ever been tried to measure the velocity of pyroclastic flows in detail due to the rare observation and the dangers to approach (ex. Hobblit, 1986). Although, many excellent video images of the pyroclastic flows were taken by the TV crews and by ourselves at the first stages of the Unzen activities. The author and the colleagues succeeded in measuring the velocities of the pyroclastic flows in detail.

The average velocities of the five pyroclastic flows at the first stages of the activities, which could be obtained excellent video images, were measured (Table 6-5). Pyroclastic flows occurred at 8:07 on May 24 (lateral runout distance, L=1000 m), at 11:13 on May 26 (L=1575 m), at 14:28 on May 26 (L=2250 m), at 15:02 on May 29 (L=1650 m), and at 15:31 on May 29 (L=2400 m) were measured (Table 6-5). Steep slopes existed at the points along the Mizunashi River 800 m and 1800 m from the source (Fig. 6-19a). Gentle slope existed between the two steep slopes (L=800-1800m). Average velocities of each

Table 6-5. Measured average velocities of pyroclastic flows, with showing date; total lateral runout distance; lateral distance, actual length, and times at each measured span. The measured average velocities at each span were calculated, with dividing the actual measured length by the measured time. These data were obtained from the images: (a) TV Nagasaki; (b) TBS; (c)(d) Fuji TV; and (d) 8 mm video image by GSJ.

Pyroclastic flow (Date Time)	Lateral runout distance (m)	Measured lateral distance (m)	Measured length (m)	Measured time (s)	Measured average velocity (m/s)
(a) 5/24 8:07	1000	0 ~ 600	682	33	21
		600 ~ 1000	472	27	18
(b) 5/26 11:13	1575	500 ~ 800	374	14	27
		800 ~ 1150	361	23	16
		1150 ~ 1350	203	13	16
		1350 ~ 1550	203	25	8
		1550 ~ 1575	26	11	2
(c) 5/26 14:28	2250	800 ~ 1800	1034	31	33
(d) 5/29 15:02	1650	650 ~ 800	208	6	35
		800 ~ 1600	818	34	24
		1600 ~ 1650	50	18	3
(e) 5/29 15:31	2400	500 ~ 800	374	9	42
		800 ~ 1750	970	32	30
		1750 ~ 1825	81	6	14
		1825 ~ 1900	90	22	4

measured span were calculated by measuring of the time to pass the tip of pyroclastic flow during the span (Table 6-5). The maximum average velocity was 42 m/s at the first steep slope (L=500-800 m) of the pyroclastic flow at 15:31 on May 29. The pyroclastic flows which traveled longer distances (=larger volume; Fig. 6-16b) tended to flow faster (Table 6-5 c, d, e). The flow velocities were high on the steep slope (L= 0-800 m), but rather low on the gentle slope (L=800-1800 m)(Table 6-5b, d, e). The flow velocity decreased gradually from a few hundred meters behind the stop points (Table 6-5b, d, e). The velocity change between the steep slope (L= -800 m) and the gentle slope (L=800- m) suggest that the change of the hydraulic condition of the pyroclastic flows (Chap. 7-3-2).

6-2-8. Computer simulations

Numerical simulations of the 1991-93 pyroclastic flows were performed to evaluate the runout distances, disaster areas, flow velocities, and arrival times. Three gravity current models were used for the simulations: the energy cone, the energy line, and the Bingham flow models. Detail techniques of these simulations are described in Takarada et al. (1993b).

In general, the equation of motion of gravity flows are expressed as:

$$dv/dt=g\sin\theta-\tau/\varrho D$$

where v, t, g, θ, τ, ϱ, and D are the velocity of the flow, time, gravity of acceleration, slope angle, flow resistance, flow density, and flow depth, respectively. τ is expressed as:

$$\tau=a_0+a_1v+a_2v^2$$

where a_0, a_1, and a_2 are the parameters of the effect of the friction or cohesion, viscosity, and turbulence, respectively (Voight et al., 1983). For the energy cone/line models, the resistance is expressed as:

$$\tau=\mu Mg\cos\theta$$

where M is the mass, μ is the apparent coefficient of friction (μ=H/L). At the energy line model, the total energy (potential and motion) was decreased by the friction, and the flows stop at the point where the total energy became to zero

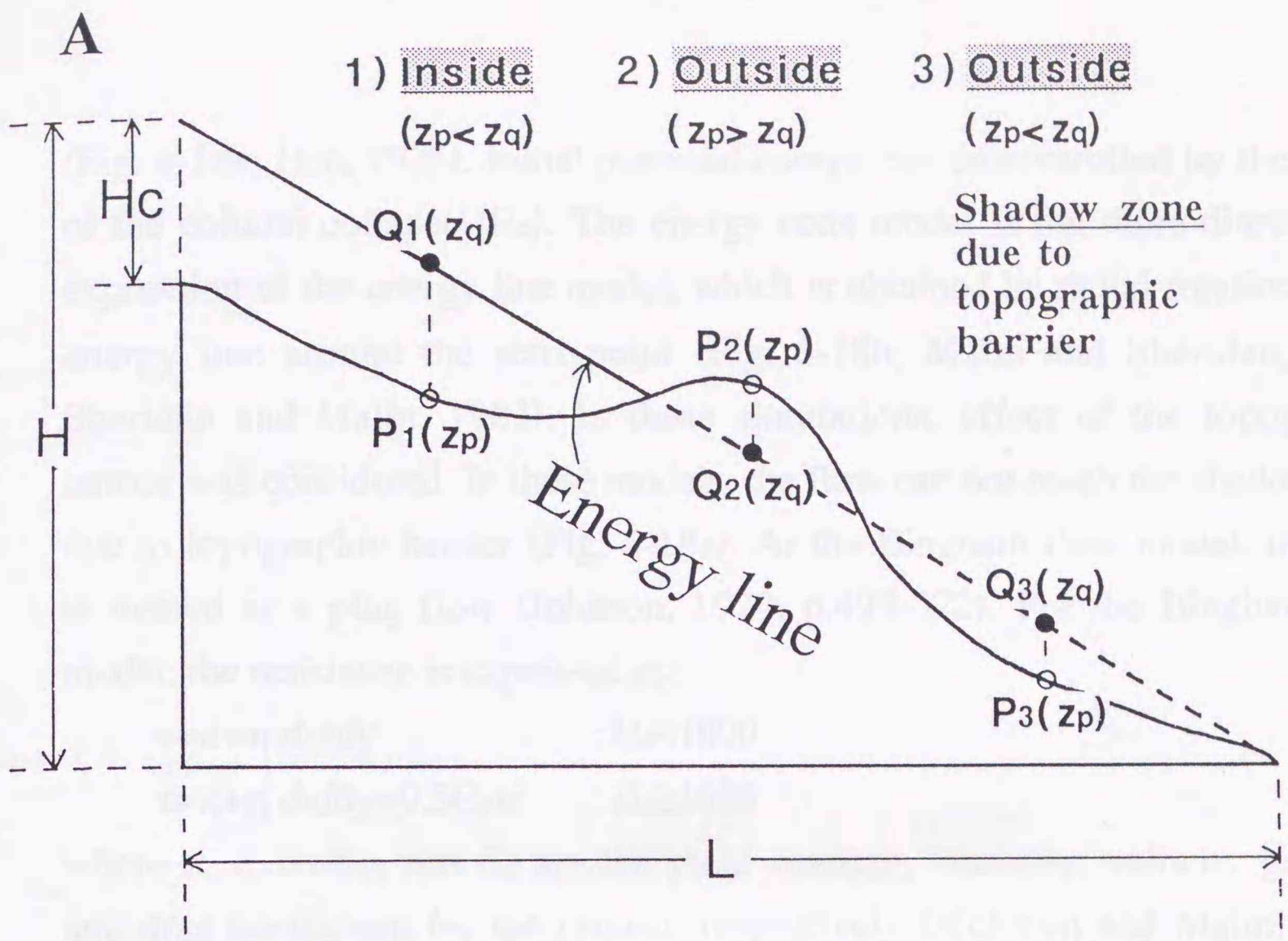

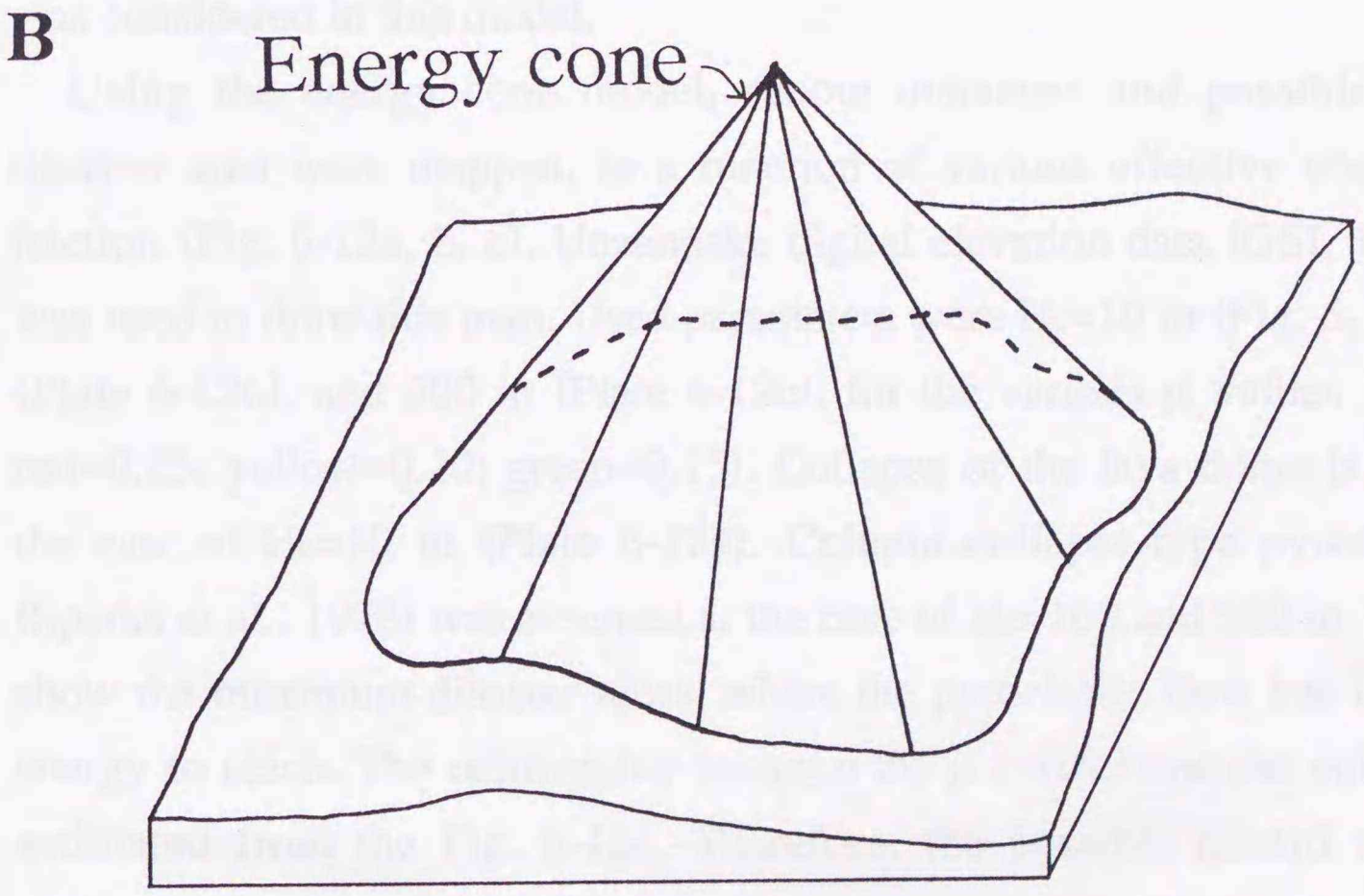

Fig. 6-18A-B. **A.** Concept of the energy line. H, relative height; L, lateral runout distance; Hc, Column collapse height; $P(z_p)$, height of topography; $Q(z_q)$, height of energy line. The point P_1 is located within the disaster area ($z_p<z_q$). The point P_2 is located out of the disaster area ($z_p>z_q$). The point P_3 is also located out of the disaster area, due to topographic barrier (shadow zone). **B.** Concept of the energy cone. The energy cone is obtained by radial rotation of the energy line around the start point.

(Fig. 6-18a; Hsü, 1975). Initial potential energy can be controlled by the height of the column collapse (H_c). The energy cone model is the three dimensional expression of the energy line model, which is obtained by radial rotation of the energy line around the start point (Fig. 6-18b; Malin and Sheridan, 1982; Sheridan and Malin, 1983). In these simulations, effect of the topographic barrier was considered. In these models, the flow can not reach the shadow zone due to topographic barrier (Fig. 6-18a). At the Bingham flow model, the flow is treated as a plug flow (Johnson, 1970, p.495-572). For the Bingham flow model, the resistance is expressed as:

$$\tau=\varkappa+\eta\ dv/dy \qquad ; H_a<1000$$

$$\tau=\varkappa+\eta\ dv/dy+0.5C_gv^2 \qquad ; H_a\geq1000$$

where $\varkappa$, η, dv/dy, and C_g are the yield strength, viscosity, velocity gradient, and drag coefficient for the ground, respectively (McEwen and Malin, 1989). H_a is the Hampton number ($=\varrho v^2/\varkappa$). When the H_a exceeds 1000, the flow become to be turbulence (Hampton, 1972). The effect of the turbulent resistance was considered in this model.

Using the energy cone model, runout distances and possible maximum disaster area were mapped, as a function of various effective coefficients of friction (Fig. 6-12a, b, c). Unzendake digital elevation data (GSI, 1991: 5. 31) was used to draw this map. Used parameters were H_c=10 m (Fig. 6-18a), 100 m (Plate 6-12b), and 500 m (Plate 6-12c), for the various μ values (pink=0.30; red=0.25; yellow=0.20; green=0.15). Collapse of the lava dome is assumed at the case of H_c=10 m (Plate 6-12a). Column collapse-type pyroclastic flow (Sparks et al., 1978) was assumed at the case of H_c=100 and 500 m. These areas show the maximum disaster areas where the pyroclastic flow has the potential energy to reach. The relationship between the μ (=H/L) and the volume can be estimated from the Fig. 6-16c. Therefore, the possible hazard area can be evaluated for the pyroclastic flows in various volumes. All of the pyroclastic flows at the first stage were restricted within the area which shown in Plate 6-12a. But, recently, initial potential energy has been increased due to the dome

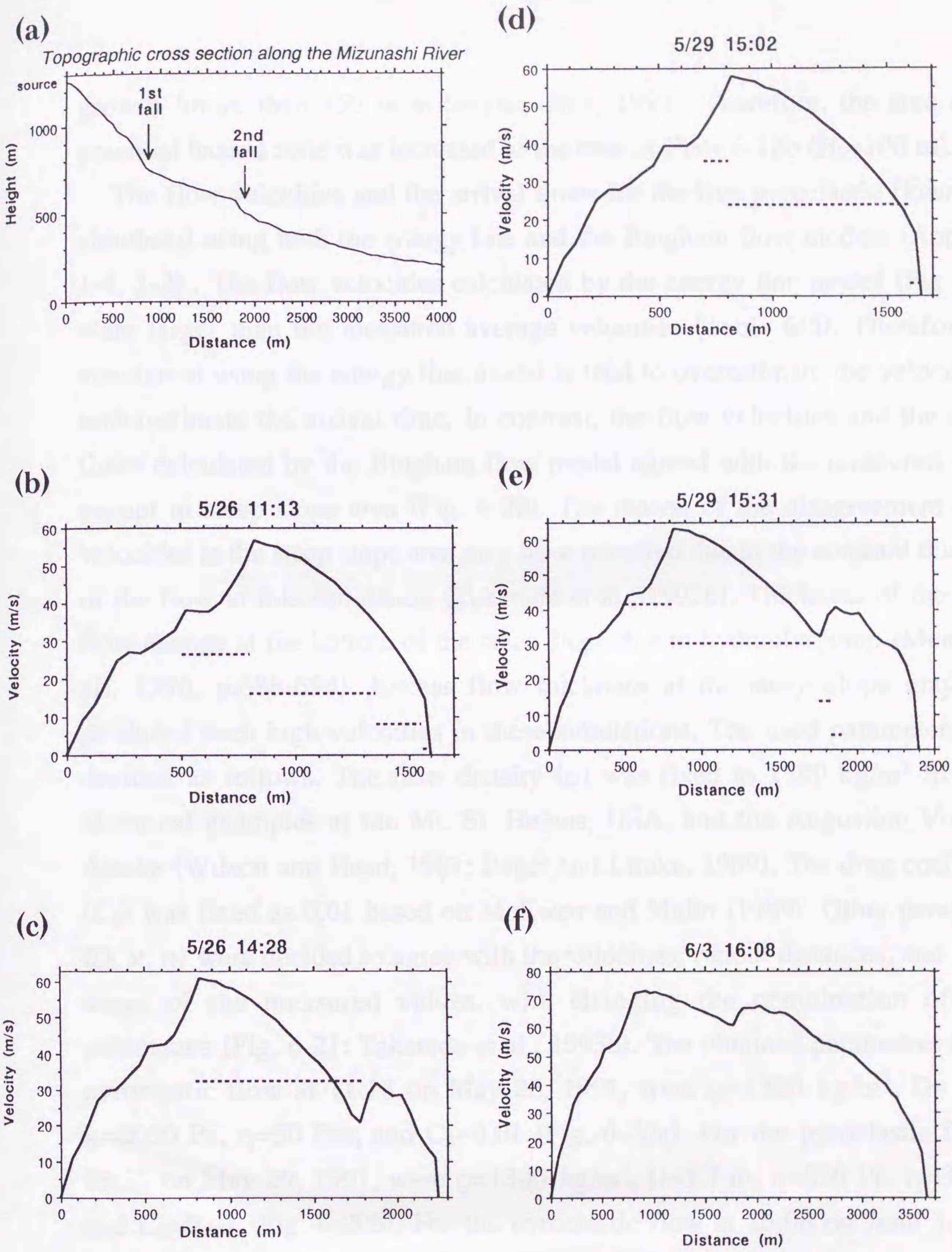

Fig. 6-19. Topographic cross section along the Mizunashi River and the results of the velocity simulation by the energy line model, comparing with the measured average velocities (Table 6-5). (a) Sectional topography along the Mizunashi River. A first steep slope (1st fall) is located at 800 m from the source in lateral distance. A second steep slope (2nd fall) is located at 1800 m from the source. A gentle slope is existed between the two steep slopes. (b) Result of the simulation of the pyroclastic flow at 11:13 on May 26, 1991, using the energy line model, with coefficient of friction, μ=0.41; (c) at 14:28 on May 26, 1991, with μ=0.38; (d) at 15:02 on May 29, 1991, with μ=0.40; (e) at 15:31 on May 29, 1991, with μ=0.36; (f) at 16:08 on June 8, 1991, with μ=0.28.

growth (more than 150 m in height; Ohta, 1993). Therefore, the area of the potential hazard zone was increased to the case of Plate 6-12b (H_c=100 m).

The flow velocities and the arrival times for the five pyroclastic flows were simulated using both the energy line and the Bingham flow models (Appendix 1-1, 1-2) . The flow velocities calculated by the energy line model (Fig. 6-19) were larger than the measured average velocities (Table 6-5). Therefore, the simulation using the energy line model is tend to overestimate the velocity and underestimate the arrival time. In contrast, the flow velocities and the arrival times calculated by the Bingham flow model agreed with the measured values except in steep slope area (Fig. 6-20). The reason of the disagreement of the velocities at the steep slope area may have occurred due to the constant thickness of the flow in this simulation (Takarada et al., 1993b). Thickness of the actual flow change at the bottom of the steep slope due to hydraulic jump (Munson et al., 1990, p.688-694). Excess flow thickness at the steep slope may have produced such high velocities in these simulations. The used parameters were decided as follows. The flow density (ϱ) was fixed as 1300 kg/m^3 from the historical examples at the Mt. St. Helens, USA, and the Augustine Volcano, Alaska (Wilson and Head, 1981; Beget and Limke, 1989). The drag coefficient (C_g) was fixed as 0.01 based on McEwen and Malin (1989). Other parameters (D, $\varkappa$, η) were decided to agree with the velocities, runout distances, and arrival times of the measured values, with changing the combination of these parameters (Fig. 6-21: Takarada et al., 1993b). The obtained parameters for the pyroclastic flow at 11:13 on May 26, 1991, were ϱ=1300 kg/m^3, D=1.5 m, $\varkappa$=2000 Pa, η=50 Pas, and C_g=0.01 (Fig. 6-20a). For the pyroclastic flow at 15:31 on May 29, 1991, were ϱ=1300 kg/m^3, D=1.7 m, $\varkappa$=850 Pa, η=90 Pas, and C_g=0.01 (Fig. 6-20b). For the pyroclastic flow at 16:08 on June 3, 1991, were ϱ=1300 kg/m^3, D=2.5 m, $\varkappa$=850 Pa, η=90 Pas, and C_g=0.01 (Fig. 6-20c). The obtained values of the yield strengths, 850 and 2000 Pa, of these pyroclastic flows agreed with the estimated values of the Komagatake pyroclastic flow deposits (10^2-10^4 Pa; Chap. 6-1-3). The velocities when the flow condition

(A)

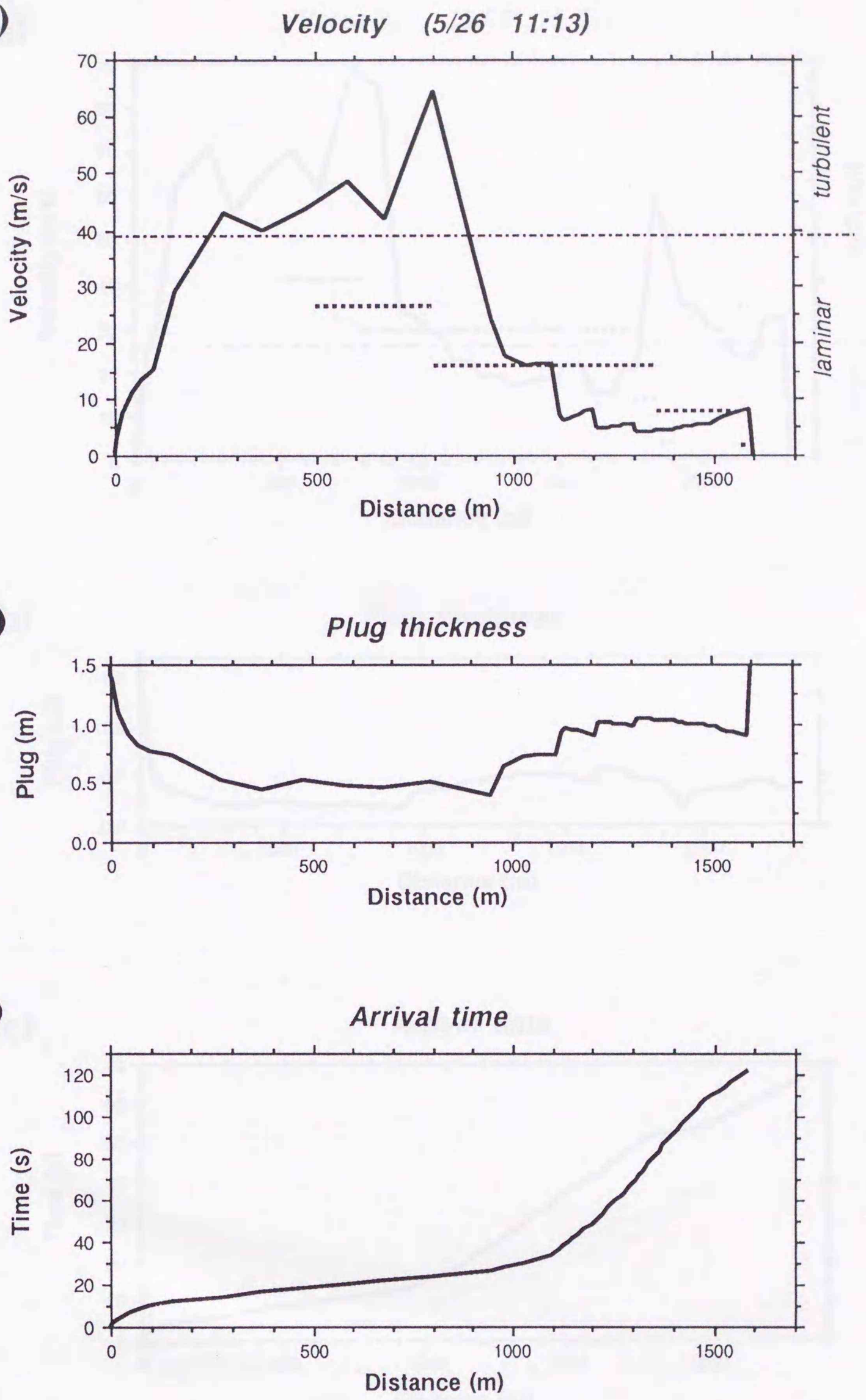

Fig. 6-20A. Result of the velocity simulation of the pyroclastic flow at 11:13 on May 26, 1991, using the Bingham flow model. Used parameters were ϱ=1300 kg/m^3, D=1.5 m, $\varkappa$=2000 Pa, η=50 Pas, and C_g=0.01. (a) Change of the flow velocity (solid line), the measured average velocities (dotted line), and the critical velocity between the laminar and the turbulent flows (39 m/s); (b) change of the plug thickness; (c) arrival time.

(B)

(a)

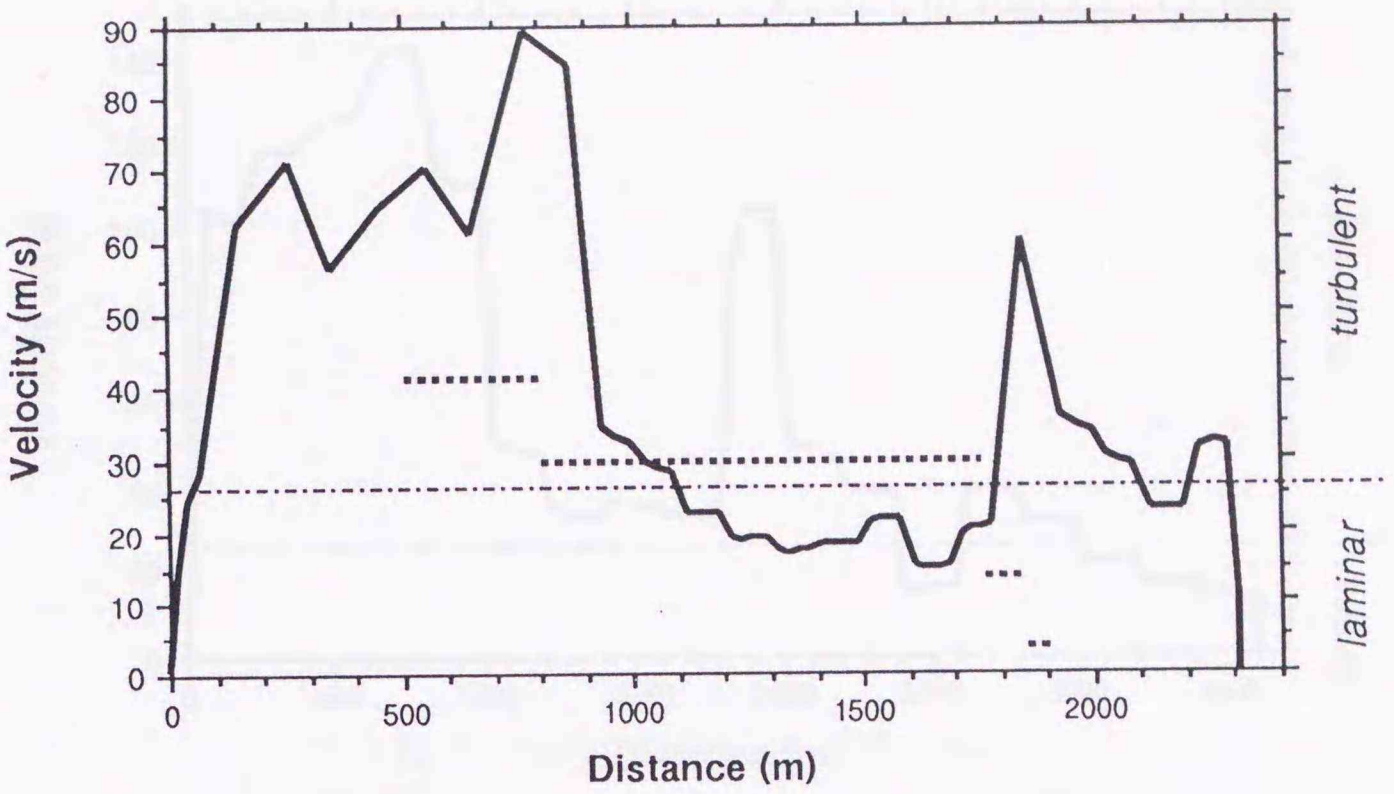

(b)

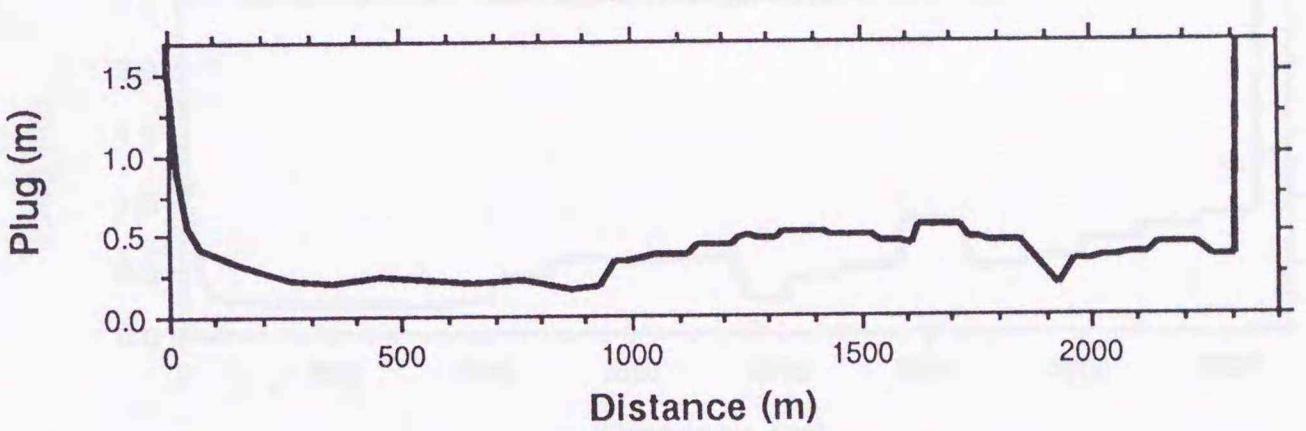

(c)

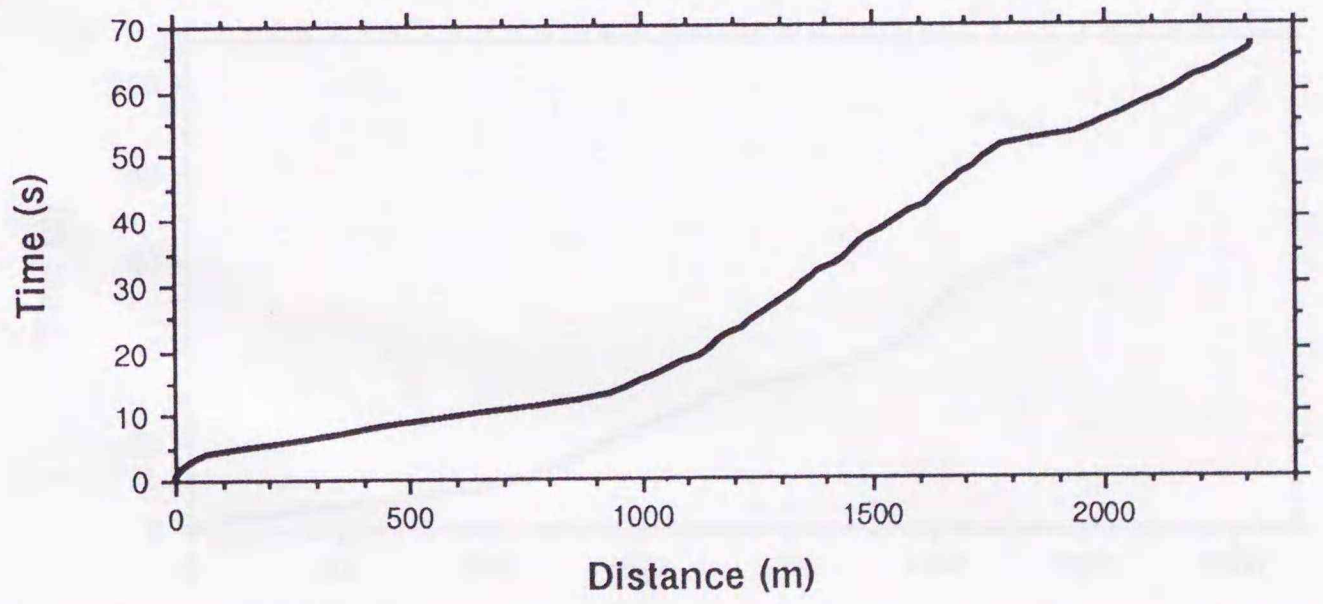

Fig. 6-20B. Result of the velocity simulation of the pyroclastic flow at 15:31 on May 29, 1991, using the Bingham flow model. Used parameters were ϱ=1300 kg/m^3, D=1.7 m, $\varkappa$=850 Pa, η=70 Pas, and Cg=0.01. (a) Change of the flow velocity (solid line), the measured average velocities (dotted line), and the critical velocity between the laminar and the turbulent flows (26 m/s); (b) change of the plug thickness; (c) arrival time.

(C)

(a)

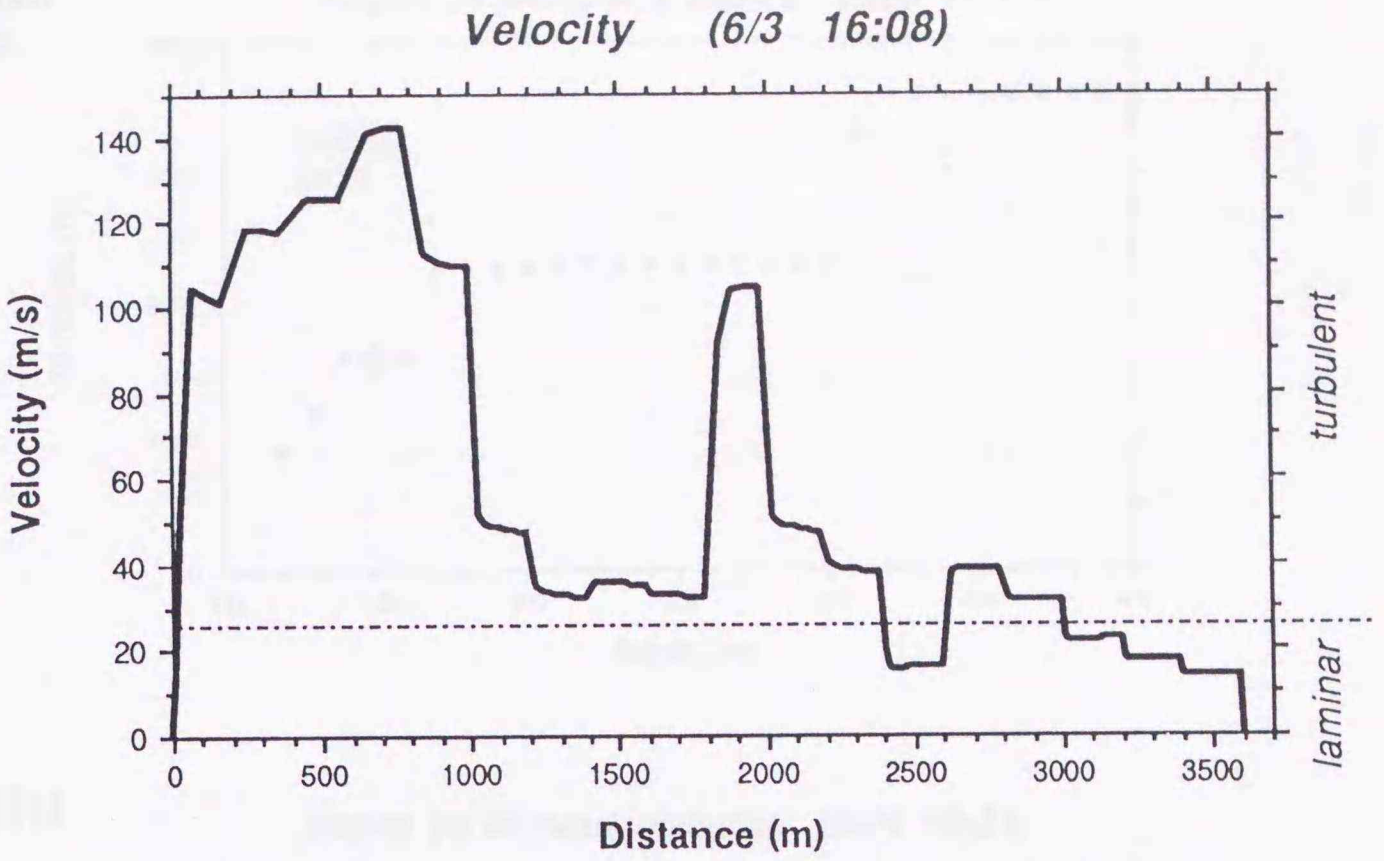

(b)

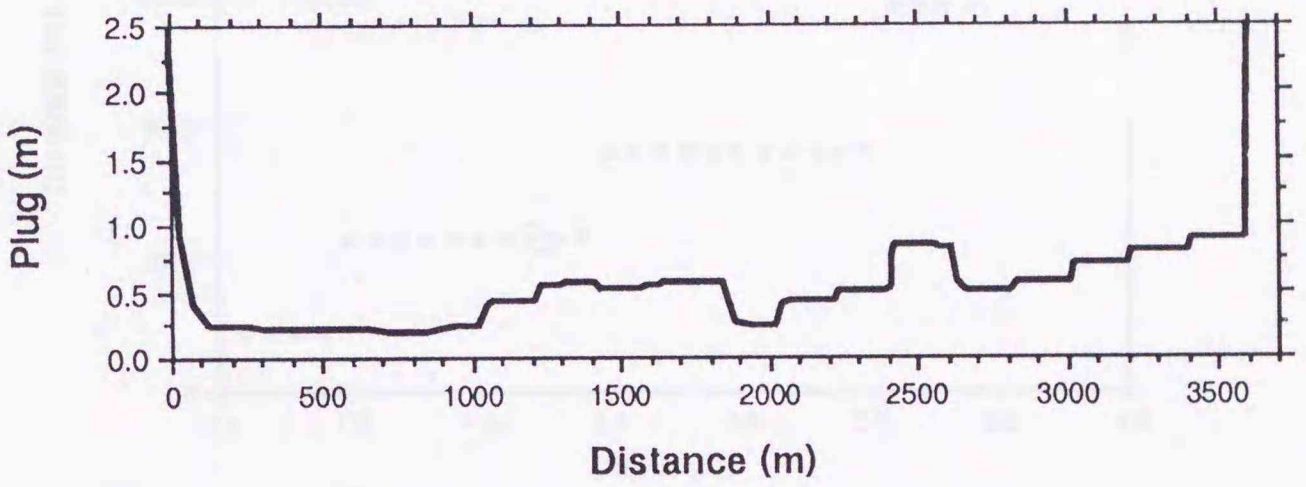

(c)

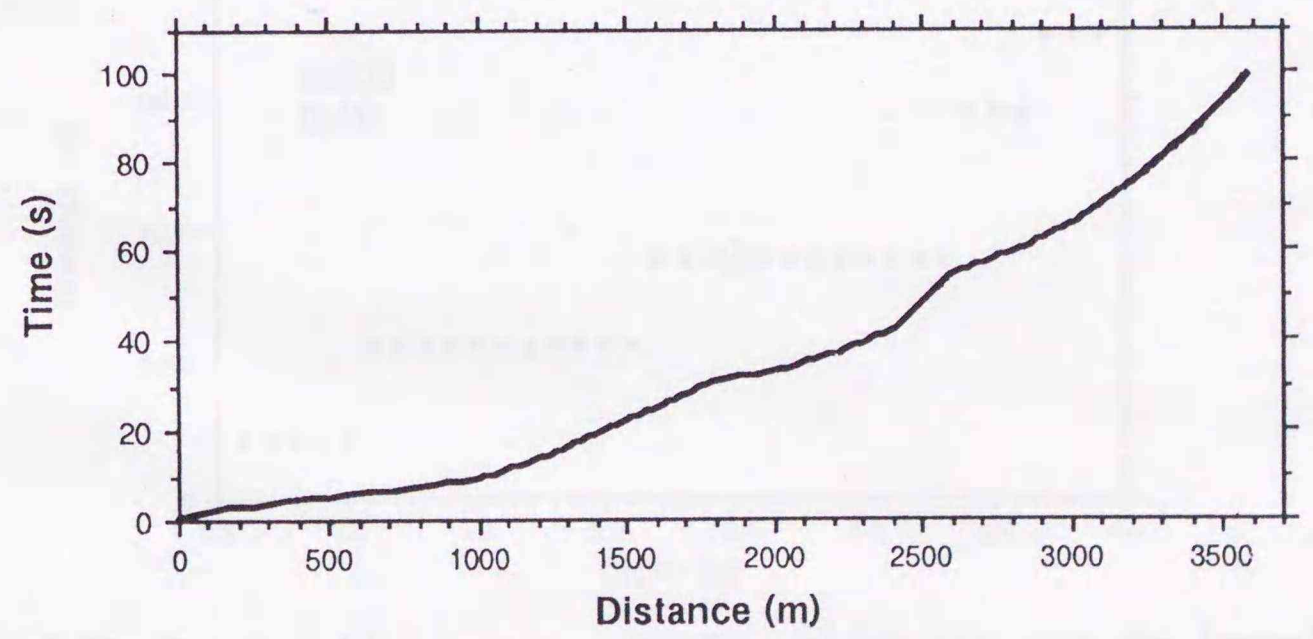

Fig. 6-20C. Result of the velocity simulation of the pyroclastic flow at 16:08 on June 3, 1991, using the Bingham flow model. Used parameters were ϱ=1300 kg/m^3, D=2.5 m, $\varkappa$=850 Pa, η=90 Pas, and C_g=0.01. (a) Change of the flow velocity (solid line) and the critical velocity between the laminar and the turbulent flows (26 m/s); (b) change of the plug thickness; (c) arrival time.

(a)

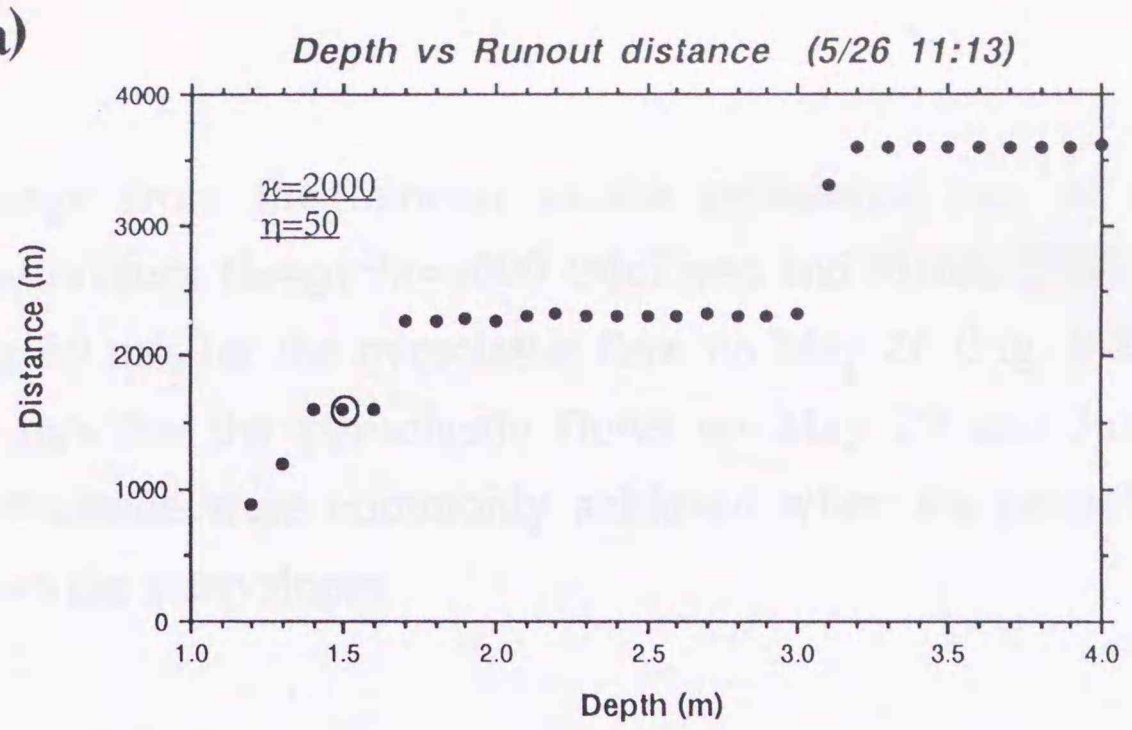

(b)

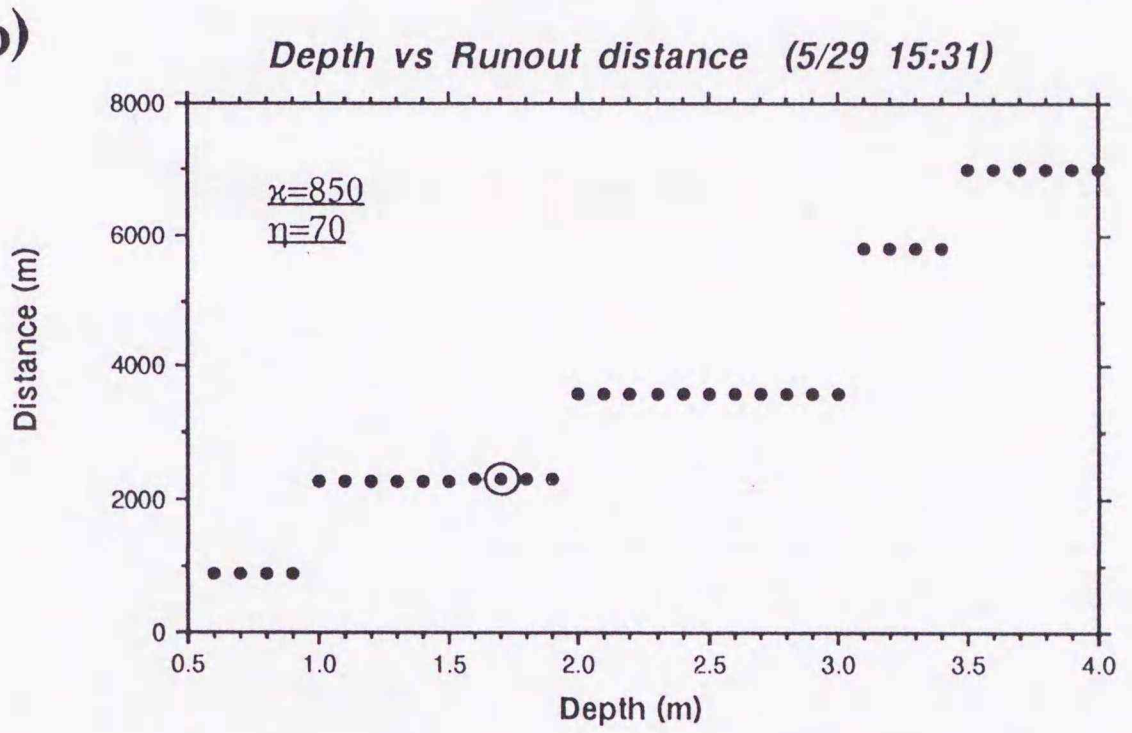

(c)

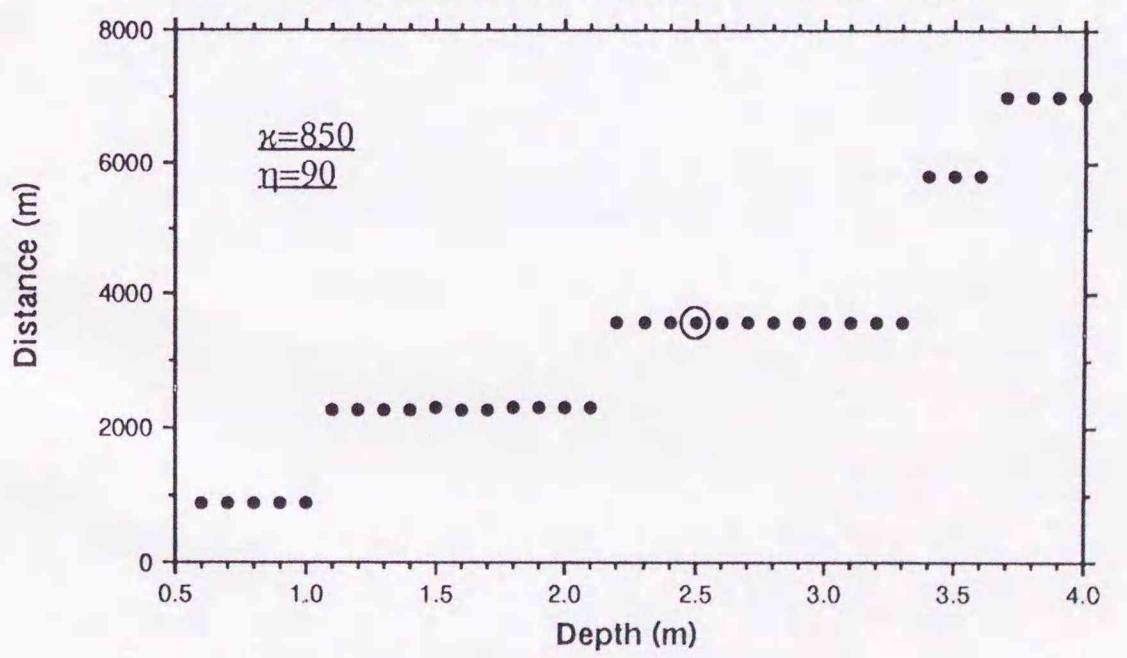

Fig. 6-21. Relationships between the flow depth (D) and the lateral runout distance, which were used to determined the best-fit values of the yield strengths, κ, and viscosities, η (after Takarada et al., 1993). (a) The relationship between the depth and runout distance of the pyroclastic flow at 11:13 on May 26, 1991, where κ=2000 Pa and η=50 Pas; (b) at 15:31 on May 29, 1991, where κ=850 Pa and η=70 Pas; (c) at 16:08 on June 3, 1991, where κ=850 Pa and η=90 Pas.

change from the laminar to the turbulence can be calculated using the relationship: $H_a=\varrho v^2/\varkappa=1000$ (McEwen and Malin, 1988). The critical velocity was 39 m/s for the pyroclastic flow on May 26 (Fig. 6-20a). The velocity was 26 m/s for the pyroclastic flows on May 29 and June 3 (Fig. 6-20b, c). Turbulence were commonly achieved when the pyroclastic flow descended down the steep slopes.

A

B

Plate 6-10. A. The lava dome (dome 1) which extruded at the Jigokuato crater (after Ohta, 1992). This picture was taken on May 21, 1991. The size of this dome is 60 m in across and 40 m in height. **B.** A new lava dome extruded within the amphitheater which formed at the June 3 pyroclastic flow (after Ohta, 1992). This picture was taken in the morning on June 8, 1991. A large pyroclastic flow occurred at 20:06 in this day due to the landslide of the basement and this new dome.

C

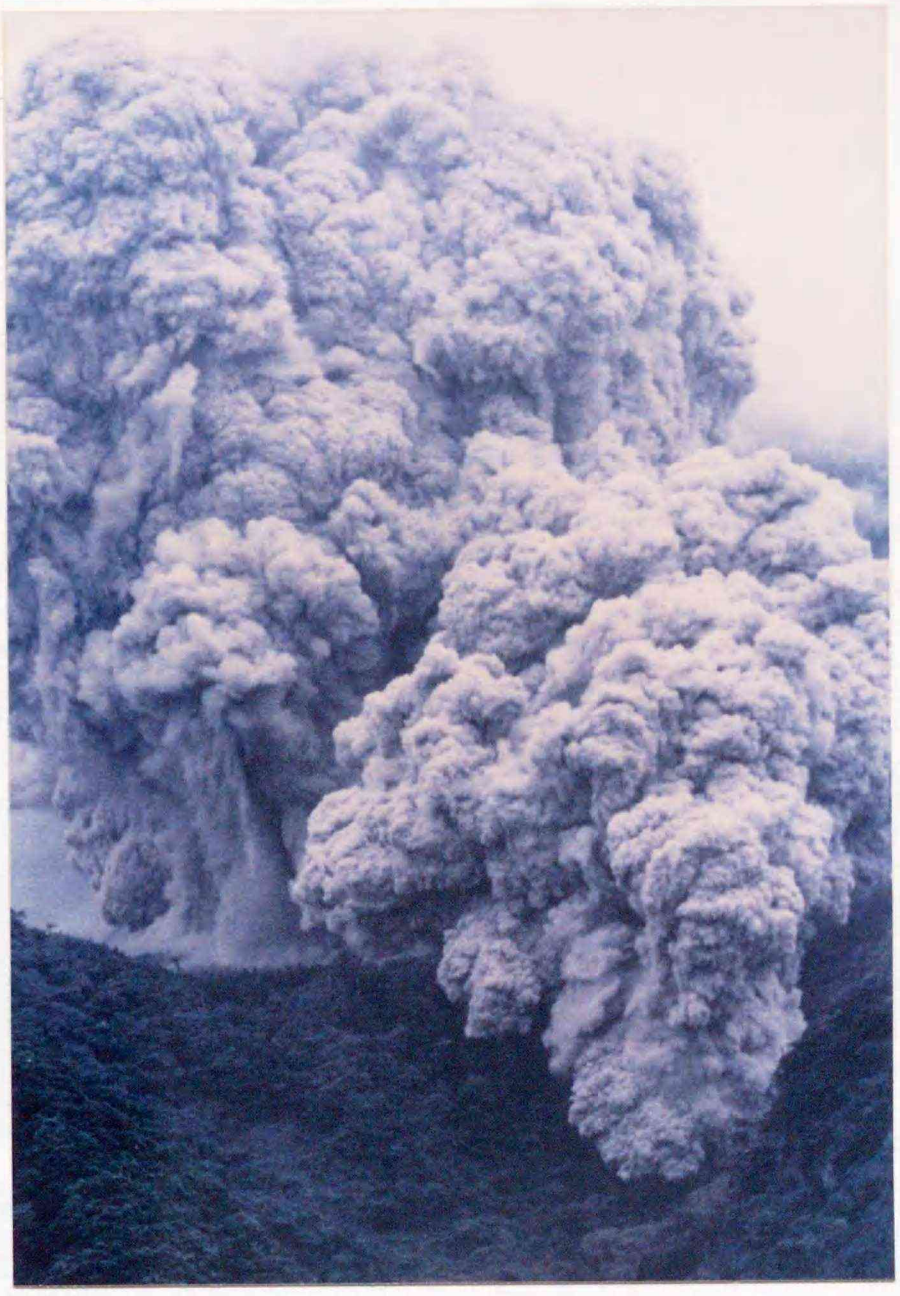

D

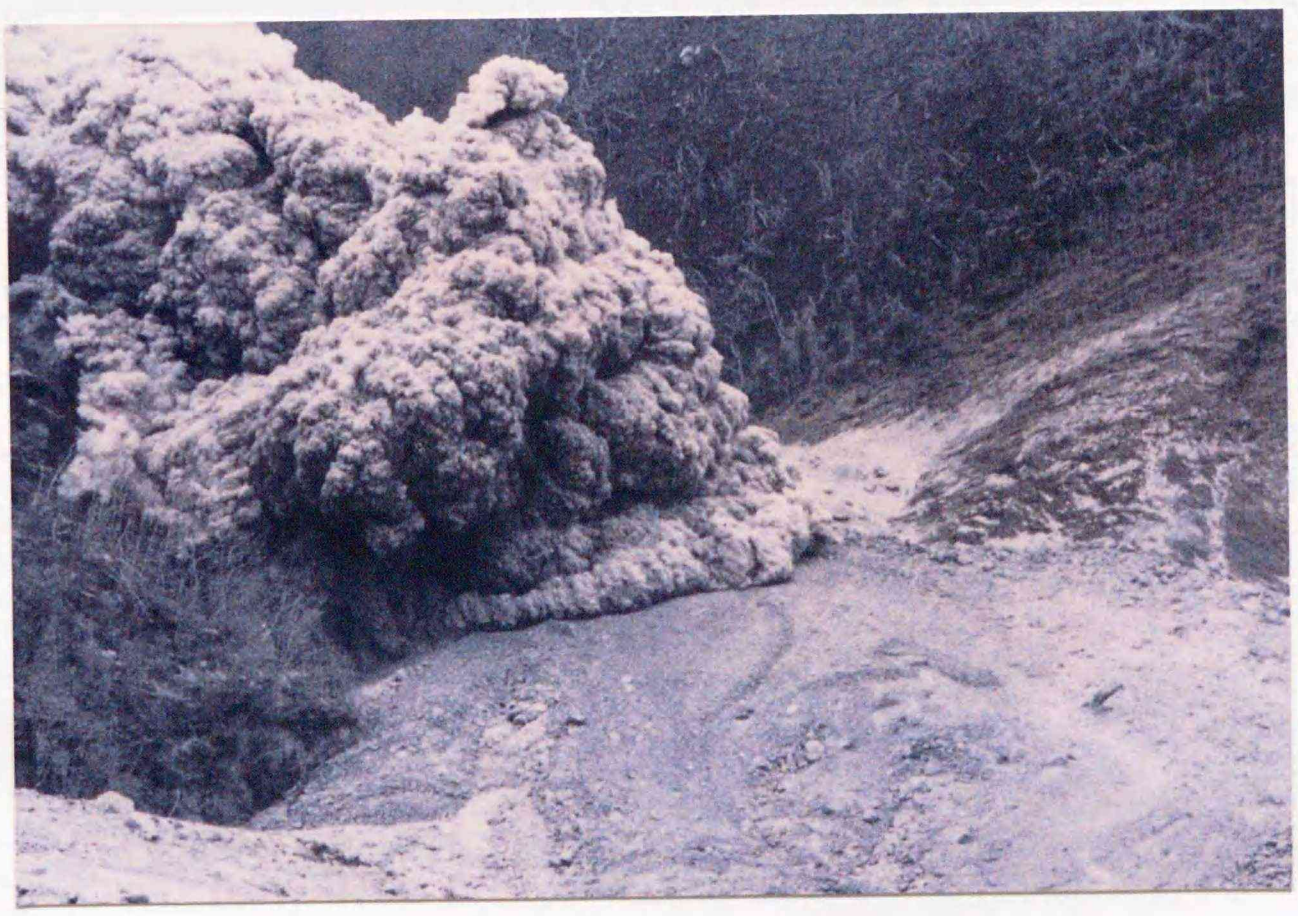

Plate 6-10 C. Giant plumes developing from the pyroclastic flow at 15:31 on May 29, 1991 (after The Nishinippon, 1992). Such plumes were formed at the curve points and flat areas along the rivers, where concentration of the heat of essential blocks occurred due to deposition from the pyroclastic flow in a limited area. **D.** A pyroclastic flow descending toward the Akamatsudani Valley on May 19, 1992 (after Nakada, 1992). The pyroclastic flow is descending along the lower part of the channel, with having an overhanging, tongue-like head and cone-or roller shaped vortices expanding outward and upward.

E

F

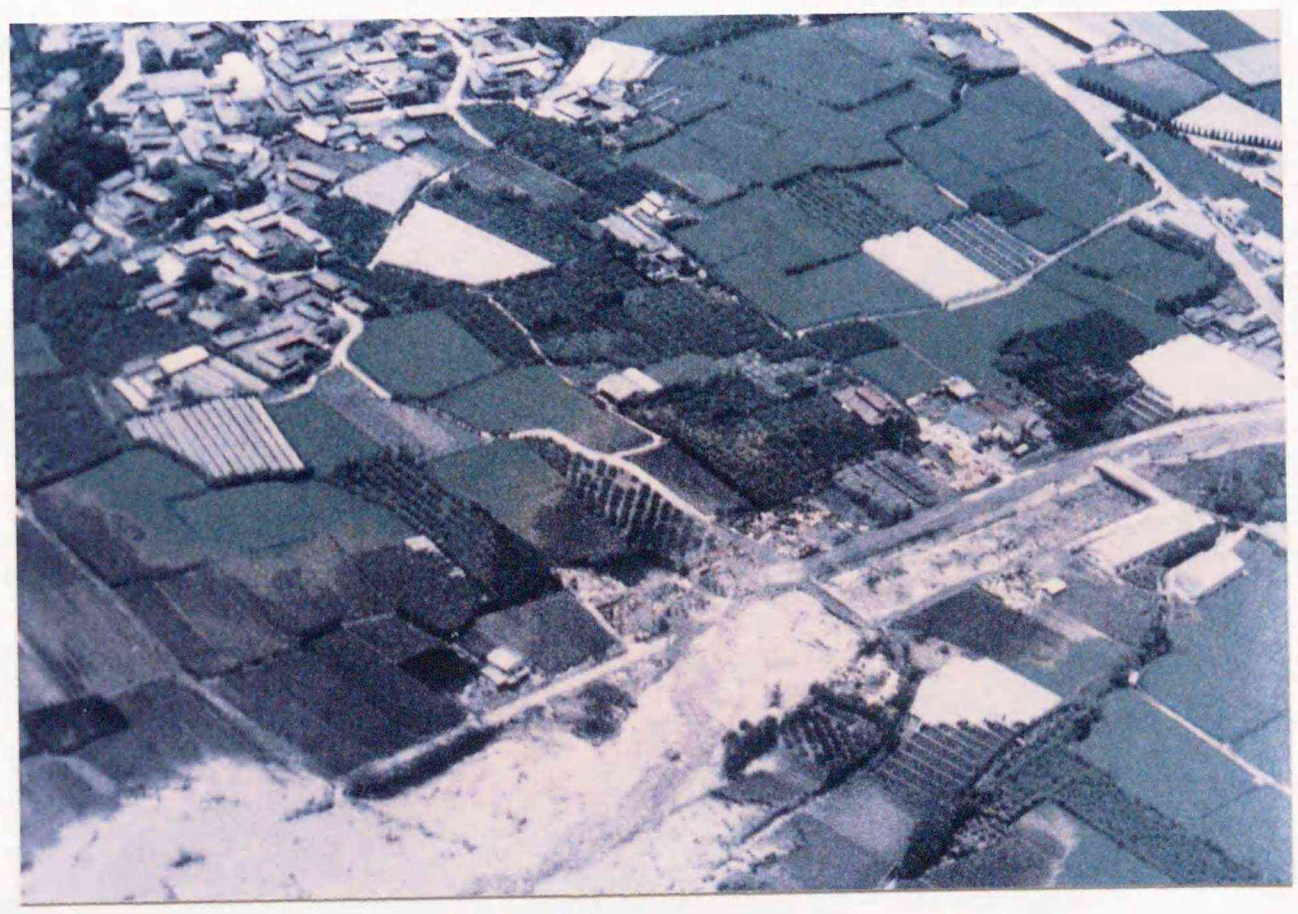

Plate 6-10. E. Pyroclastic flow deposits at the Akamatsudani Valley, showing well-defined levees. This picture was taken on Jan. 16, 1993. **F.** The pyroclastic flow deposit occurred on June 8, 1991 (after Ohta, 1992). The deposit is filling in the Mizunashi River. The excurvation survey (Chap. 6-2-6; Plate 6-11a-*l*) were made at this area. The Route 57 is seen at the upper-right part of the picture.

G

H

Plate 6-10. G. The pyroclastic flow deposit at the Kitakamikoba area occurred on Sep. 15, 1991 (after Nakada, 1992). The deposit is subdivided into the basal avalanche deposit consisting of poorly-sorted materials up to a few meters within the valley (behind the people), and the ash-cloud surge deposit consisting of the thin, fine-grained, better-sorted materials (in front of the people). **H.** The devastation due to the ash-cloud surge which detached from the parental basal avalanche of the pyroclastic flow at 16:08 on June 3, 1991 (after Ohta, 1992).

A

B

Plate 6-11. A. The Unzen June 8, 1991, pyroclastic flow deposit (gray-colored part), filling in the Mizunashi River, at the excavation survey by the PWRI on Jan. 27-29, 1993. A debris flow (brown-colored part) eroded the top of the pyroclastic flow deposit. **B.** The pyroclastic flow deposit which composed of poorly-sorted dense rocks. The maximum size of the blocks in this deposit is ca. 1 m.

C

D

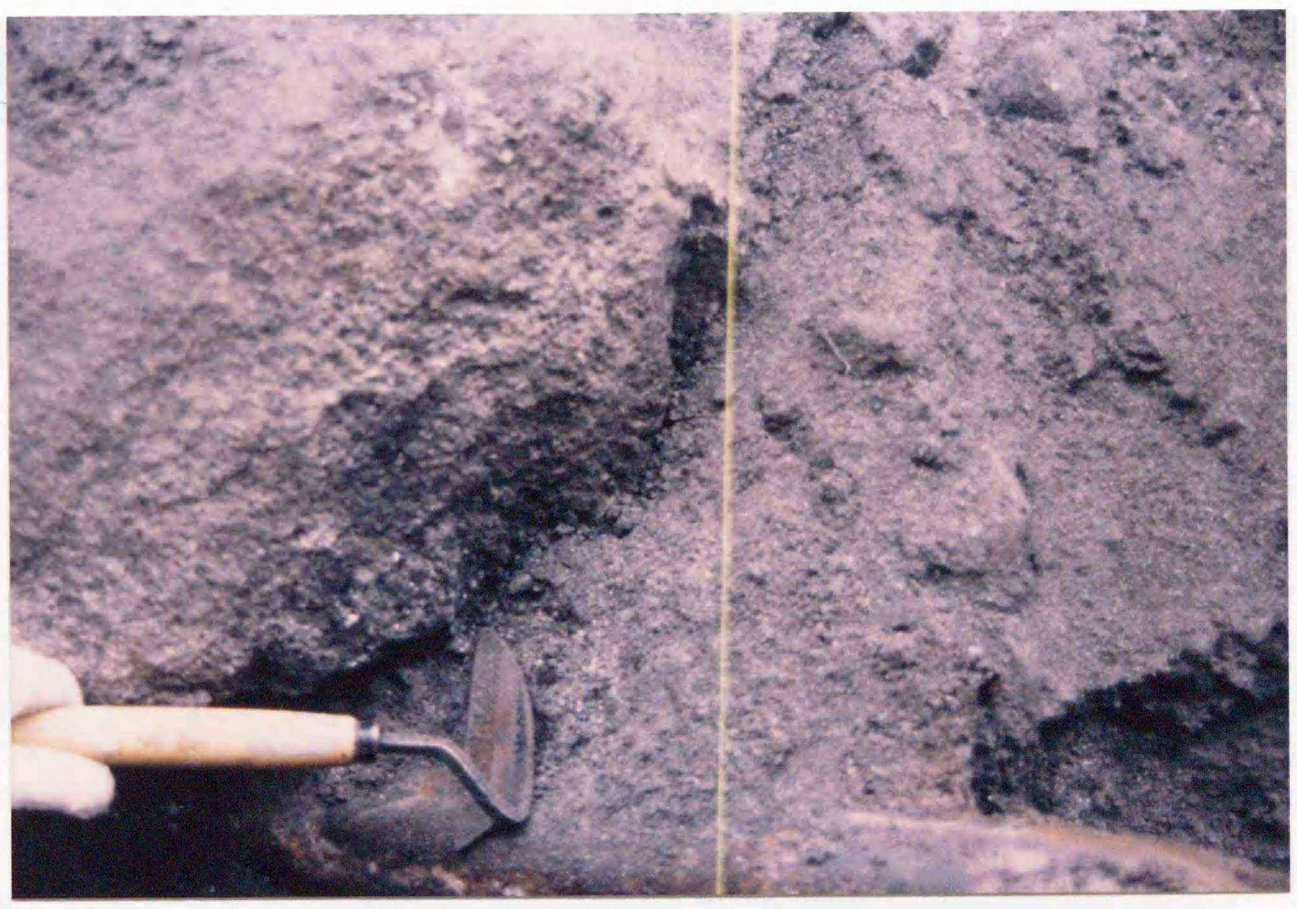

Plate 6-11. C. Depletion of fine materials beneath the large block. This depletion may have occurred due to the gas from the carbonized wood fragments and the large essential block. Note the tiny charcoals. **D.** Fines-depletion around the large block.

E

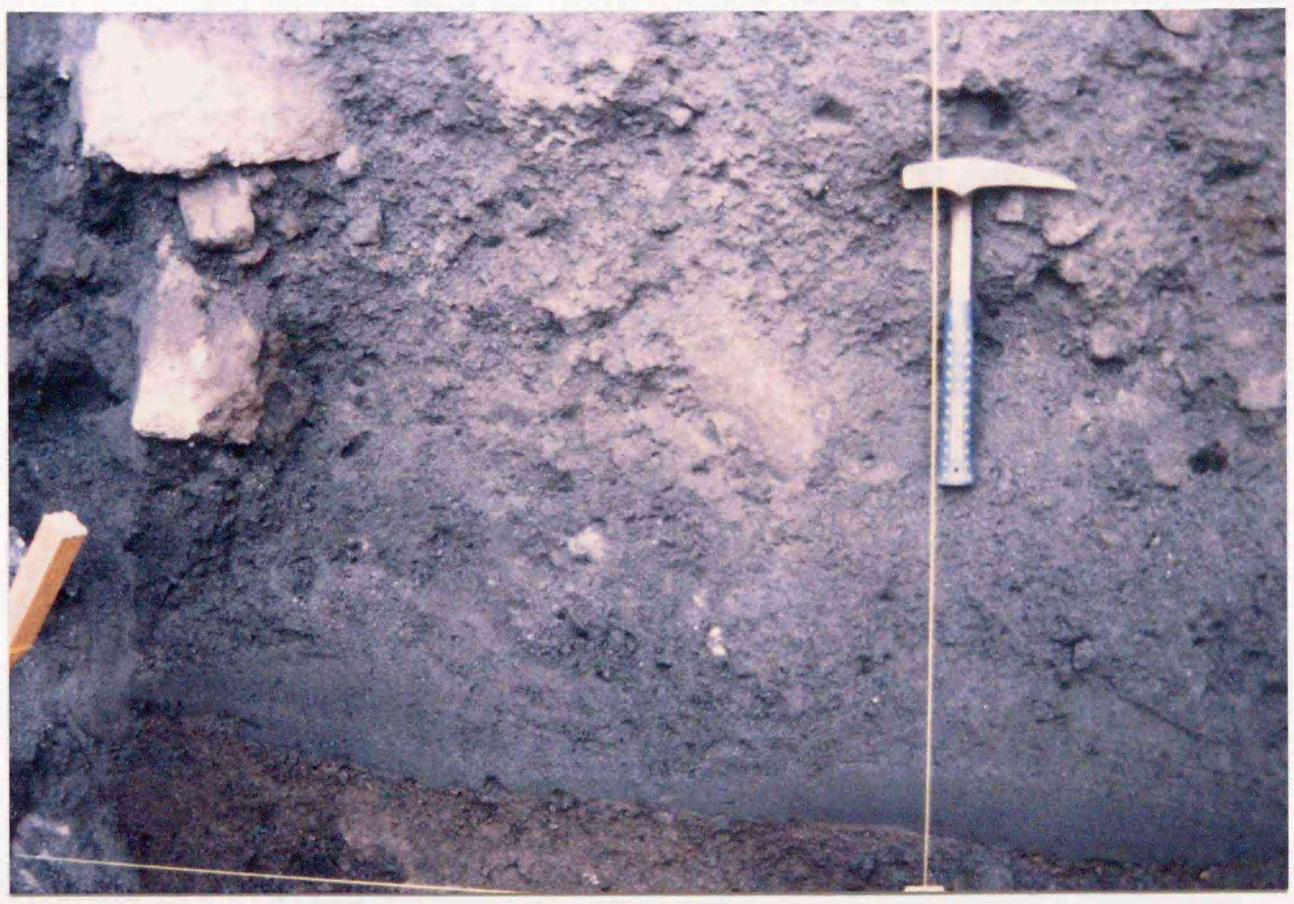

F

Plate 6-11. E. A pyroclastic surge deposit (layer 1) and a layer 2a (Sparks et al, 1973) at the bottom of the deposit. The pyroclastic surge deposit is better-sorted, up to 5 cm in thickness, consisting mainly of the medium to very fine sands (at the dark-gray colored part). The thickness of this surge deposit is not uniform. The layer 2a, up to 15 cm in thickness, lacked the coarser materials than ca. 1 cm (above the pyroclastic surge deposit). The boundary between the upper layer 2b (Sparks et al., 1973) and the layer 2a is not clear. **F.** The pyroclastic surge deposit, the layer 2a, and carbonized wood. Around the carbonized wood shows the white color due to the ash from the carbonized wood.

G

H

Plate 6-11. G. The pyroclastic surge deposit showing the lateral change of the thickness, and the layer 2a. **H.** The pyroclastic surge deposit, layer 2a, and the carbonized wood fragment, which filling between the long mounds at the Tabaco field. A thin precursor ash-fall deposit is observed beneath the pyroclastic surge deposit.

I

J

Plate 6-11.I. The June 8 pyroclastic flow deposit which spilled over from the Mizunashi River to the flat area. The precursor ash-fall deposit, the pyroclastic surge deposit, the layer 2a, layer 2b, and segregation pipes are observed. Thin debris flow deposit covers the pyroclastic flow deposit. **J.** The segregation pipes at the top of the pyroclastic flow deposit. Thin debris flow deposit covers the pyroclastic flow deposit. The top of the pyroclastic flow deposit shows red color due to high temperature oxidization.

K

L

Plate 6-11. K. A trunk remains to stand up even in the pyroclastic flow deposit. The layer 2a is observed at the bottom of the deposit. **L.** Thin June 8 pyroclastic flow deposit which spilled over from the river to the flat area. Thin debris flow deposit covers the pyroclastic flow deposit. Segregation pipes are observed at the upper part of the pyroclastic flow deposit.

A

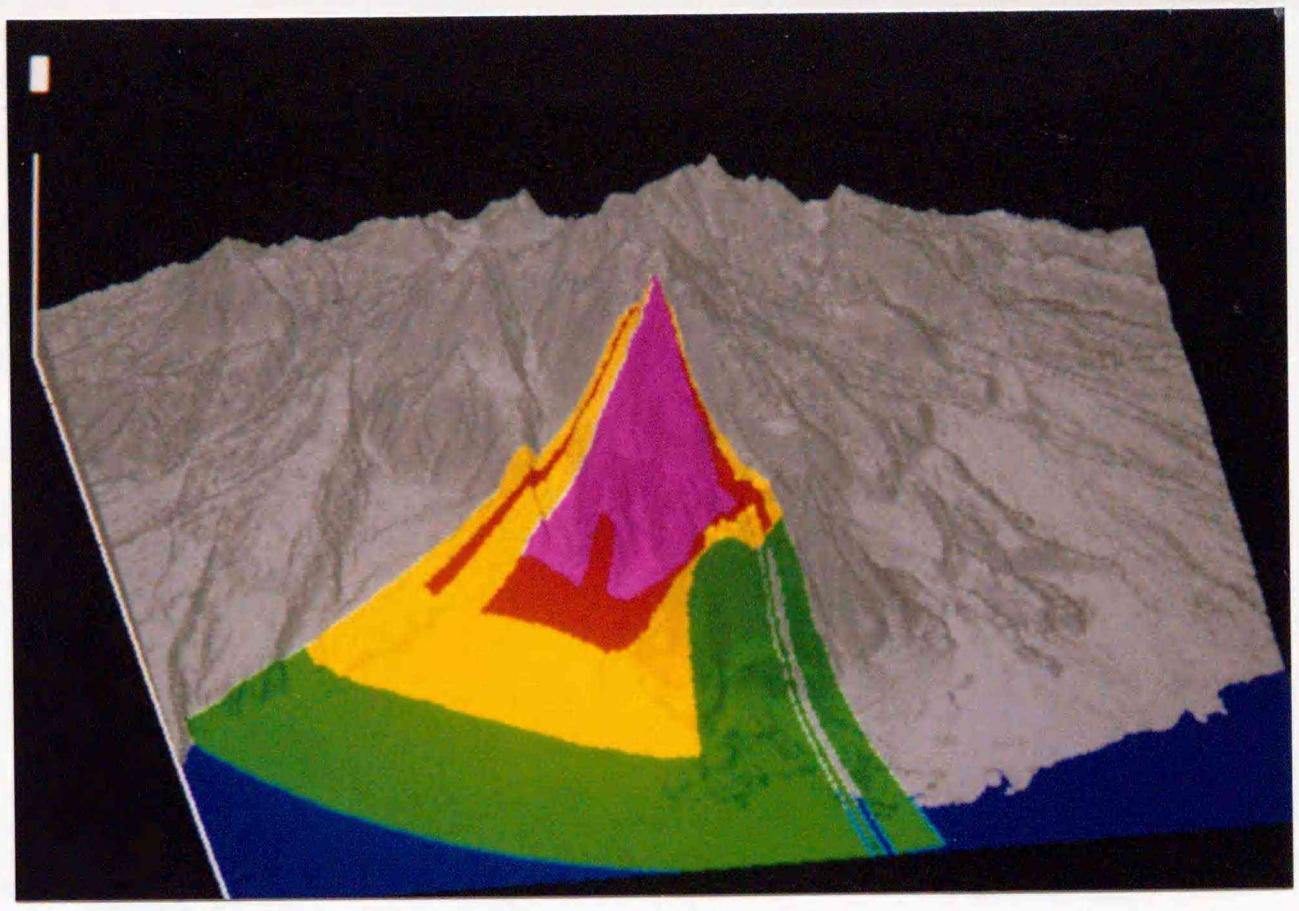

B

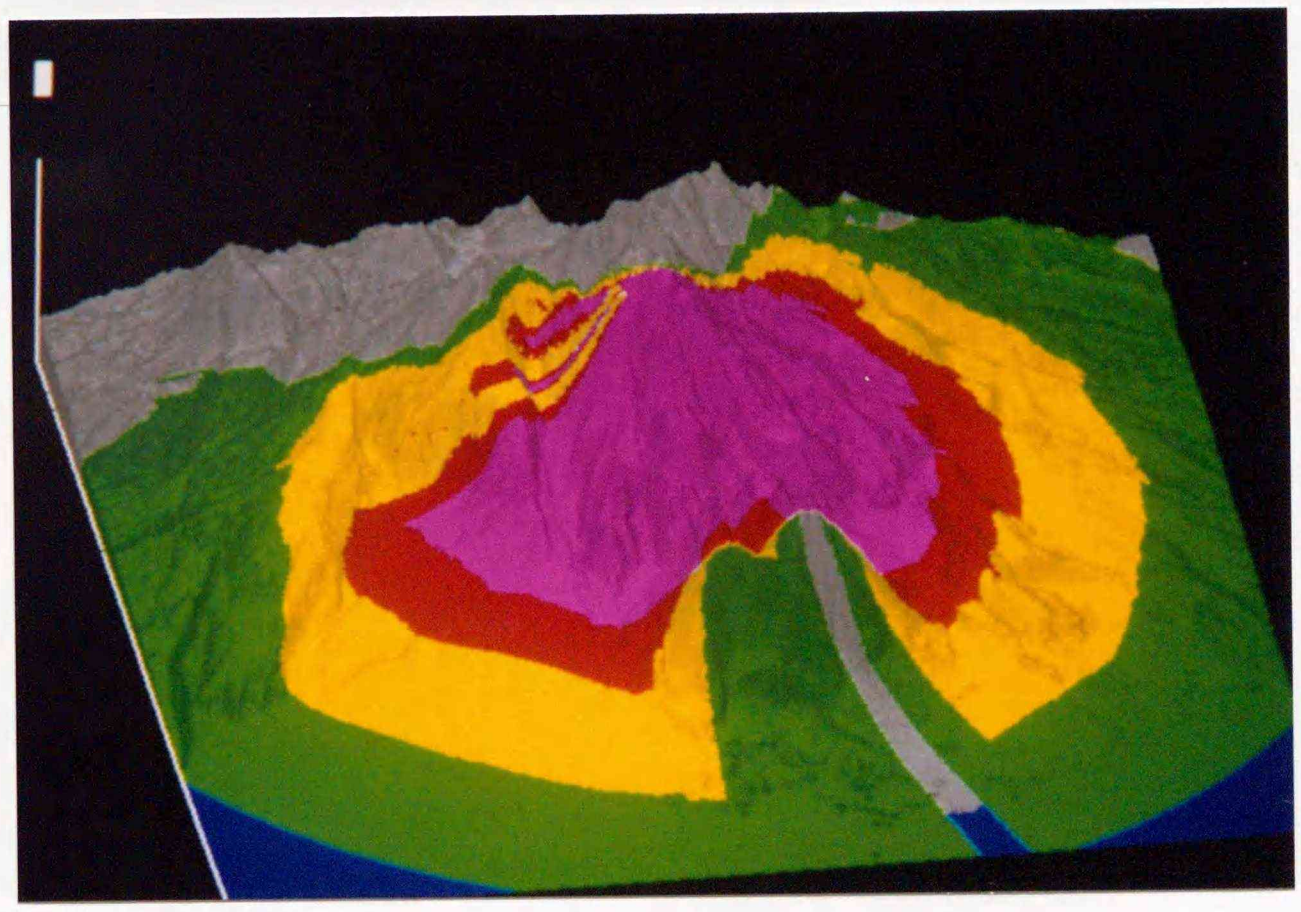

Plate 6-12. A. The result of the computer simulation using the energy cone model. Used parameter is H_c=10 m (Fig. 6-18a) for the various μ values (pink=0.30; red=0.25; yellow=0.20; green=0.15). Lava dome collapse-type pyroclastic flows are assumed in this simulation. The program and the graphics were made by Nakano, T. (GSJ). **B.** The result of the computer simulation using the energy cone model. Used parameter is H_c=100 m (Fig. 6-18a) for the various μ values (pink=0.30; red=0.25; yellow=0.20; green=0.15). Column collapse-type pyroclastic flows are assumed in this simulation.

C

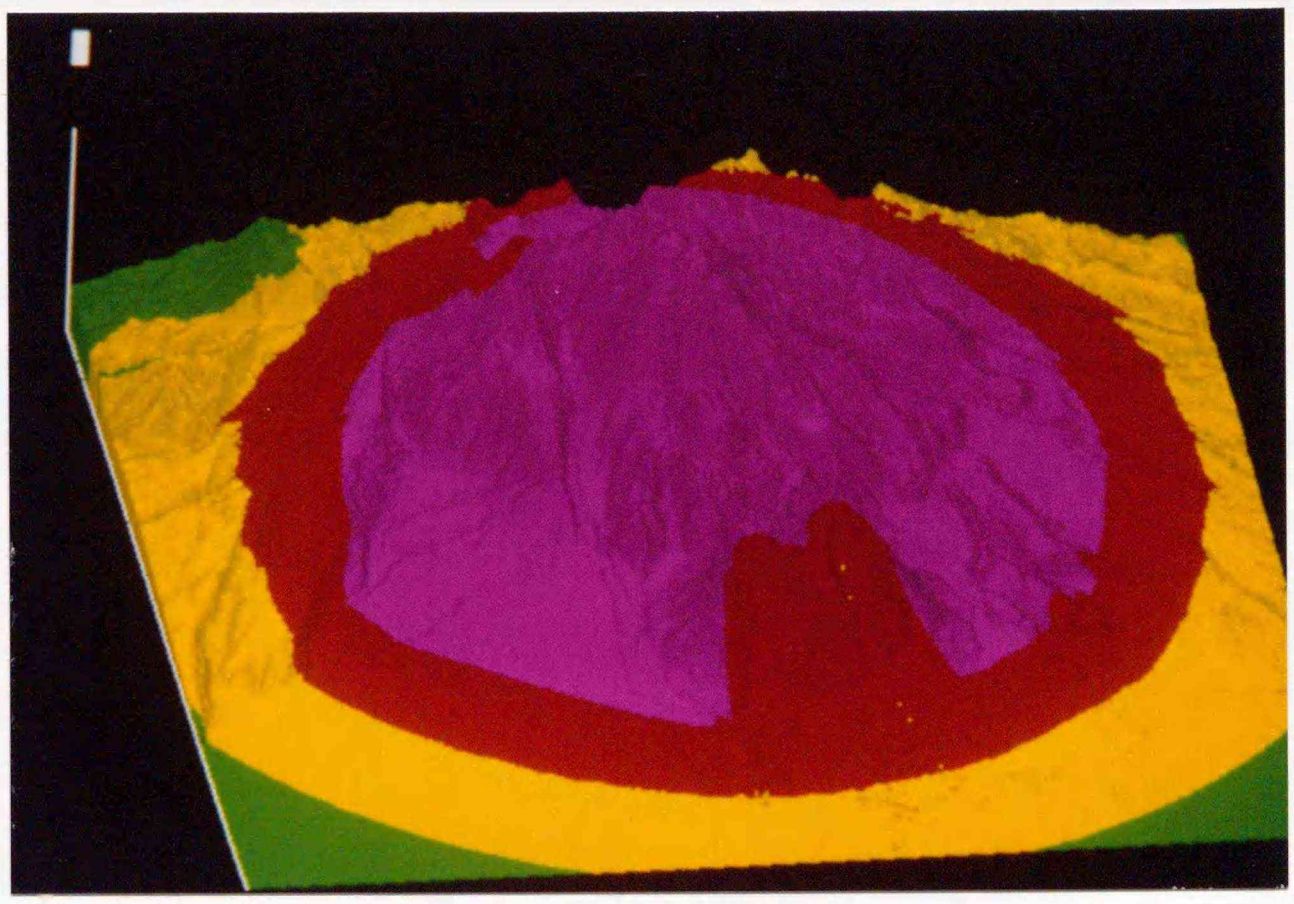

Plate 6-12. C. The result of the computer simulation using the energy cone model. Used parameter is H_c=500 m (Fig. 6-18a) for the various μ values (pink=0.30; red=0.25; yellow=0.20; green=0.15). Column collapse-type pyroclastic flows are assumed in this simulation.

Chapter 7. Discussions

7-1. Fundamental clast support mechanisms

Concepts of the four fundamental clast support mechanisms of gravity flows: turbulence, fluidization, grain interaction, and matrix strength, are important to explain the flow and deposition mechanisms of the debris avalanches and the pyroclastic flows (Fig. 7-1; Middleton and Hampton, 1976; Lowe, 1982). "Turbulence" support the clasts by upward component of fluid eddies (Allen, 1985, p.103-137). "Fluidization" support the clasts by upward flow of fluid escaping from between the clasts (Chap. 6-1-5; Sparks, 1976; Wilson, 1980; Wilson, 1984). "Grain interaction" support the clasts by dispersive force due to collision or friction of clasts (Bagnold, 1954; Fig. 2-12). "Matrix strength" support the clasts by yield strength and viscosity of the mixture of interstitial fluid and fine materials (Hampton, 1975; Hampton, 1979). These mechanisms are the end components to support the clasts in the gravity flows. Therefore, (1) combination of these mechanisms (Lowe, 1982), and (2) transformation of the main support mechanism sometimes occur (ex. turbulence to laminar; Fisher, 1983).

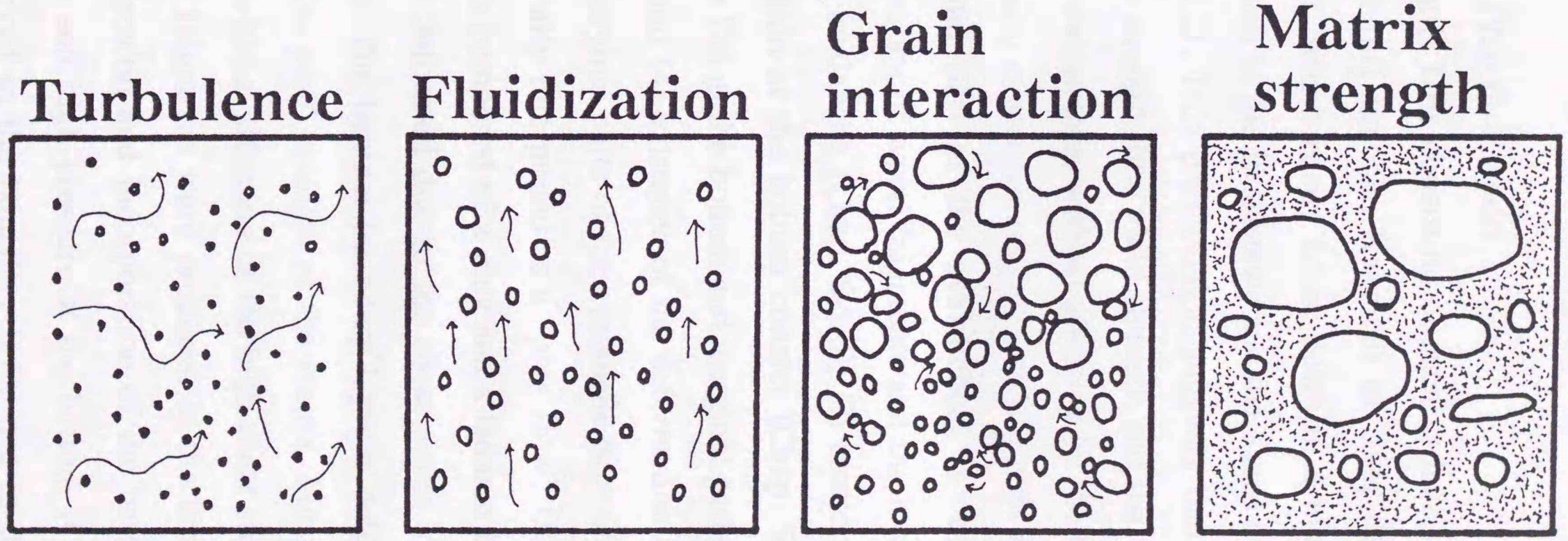

Fig. 7-1. Four fundamental clast support mechanisms of gravity flows (after Middleton and Hampton, 1976). The turbulence support the clasts by the upward component of fluid eddies. The fluidization support the clasts by the upward flow of fluid escaping from between the clasts. The grain interaction support the clasts by the dispersive force produced by collision and/or friction between the clasts. The matrix strength support the clasts by the yield strength and the viscosity of the mixture of interstitial fluid and/or fine materials.

7-2. Flow and deposition mechanism of the debris avalanches

7-2-1. Plug flow model

Fragile DBs consisting of such as lava fragment with jigsaw cracks, highly altered tuff breccia, fragment of river deposit, and unconsolidated rework deposit, which easily break down in a moment due to high shear stress, are preserved in the Iwasegawa and the Kaida debris avalanche deposits (Chap. 5-1-2, 5-2-2). This preservation suggests that the DBs were transported by the matrix strength (the yield strength and the viscosity of the DM) in a inner part of the avalanches, without affecting by the high shear stress. On the other hand, following evidences suggest that the high shear stress affected the bottom and marginal part of the avalanches: (1) coincidence between the preferred orientations of wood fragments and the local flow directions of the Iwasegawa debris avalanche (Chap. 5-1-5); (2) erosion and incorporation of the basement formation at the bottom contact (Chap. 5-1-6); (3) no preservation of large fragile DB at the bottom and marginal parts of the avalanche deposits (Chap. 5-1-7), and (4) existence of the deformation structures of soft DBs at the bottom and marginal parts of the avalanche deposits (Chap. 5-2-4). This kind of flow is physically interpreted as a “plug flow” (Johnson, 1970, p.495-570). The plug flow is composed of a plug and a laminar boundary layer (Fig. 2-18). The plug is not deformed due to the shear stress lower than the yield strength of the matrix. The laminar boundary layer is deformed due to the shear stress higher than the yield strength of the matrix. Most of fragile DBs were carried in the plug without affection of the high shear stress. The preferred orientation of the wood fragments were produced in the laminar boundary layer (Chap. 5-1-5). The erosion and incorporation of the basement occurred by the strong shear stress and high pressure at the bottom (Chap. 5-1-6). Fragile DBs could not preserved in the boundary layer due to the strong shear stress. Deformation

structures of the unconsolidated DBs were produced in the boundary layer due to the shear stress (Chap. 5-2-4).

Another flow mechanisms, such as the air cushion (Fig. 2-11; Shreve, 1968; Johnson, 1978), the dilatant flow (Fig. 2-14; Takahashi, 1982, 1986; Egashira et al., 1989), and the acoustic fulidization (Fig. 2-16; Melosh, 1979) models can not explain the sedimentary structures and characteristics of the Iwasegawa and the Kaida debris avalanche deposits.

In the air cushion model, shear stress does not be produced at the bottom part of the flow. Therefore, this model can not explain the coincidence of preferentially orientated wood fragments defining the flow direction, and the incorporation of the basement materials from the bottom contact of the flows.

The Dilatant flow model explains the transportation of large clasts by dispersive pressure due to collision of clasts (Takahashi, 1986). Dispersive pressure is proportional to the square of the shear stress and that of the grain size (Bagnold, 1954). Therefore, larger clasts tend to move to upper levels of the deposit due to dispersive pressure, resulting in reverse grading (Fritz and Moore, 1988, p.267). But, large clasts in the Iwasegawa debris avalanche deposit are normally graded (Fig. 5-3a). In this model, clasts continue to be transported by dispersive force resulting from severe collision between clasts. But, the DBs in the two debris avalanche deposits are composed of fragile materials. Such kinds of fragile DBs can't produce enough dispersive pressure to continue to be transported.

In the acoustic fluidization model, sufficiently strong acoustic waves in the debris avalanche can momentary relieve the static overburden pressure in the bottom regions of the avalanche, allowing sliding to occur in the unloaded region (Melosh, 1979; Fig. 2-16). Irreversible sliding occurs in a debris avalanche under a static overburden pressure $P=\varrho gh$ (where ϱ is density, g is acceleration of gravity, and h is the overburden thickness) for an applied shear

stress τ, when the net pressure P-s drops below τ/μ (where s is the pressure deviation and μ is the coefficient of friction of the debris avalanche). The critical value of pressure deviation is

$$s_c=P-\tau/\mu=\varrho gh-\tau/\mu$$

These parameters for the Iwasegawa and the Kaida debris avalanches were estimated quantitatively. For $\varrho=1.7\times10^3$ kg/m^3, g=9.8 m/s^2, and h=10-50 m, the overburden pressure at the bottom of the avalanche is

$$P=\varrho gh=10^5\text{-}10^6 \text{ Pa}$$

For a maximum flow velocity of v=100 m/s, and h=10-50 m, the pressure due to an applied shear stress is

$$\tau/\mu=\mu xv/hx1/\mu=v/h=2\text{-}10 \text{ Pa}$$

Then, the estimated critical value of pressure deviation is

$$s_c=P-\tau/\mu=10^5\text{-}10^6 \text{ Pa}$$

Thus, sliding occurs when the overburden pressure at the bottom of the avalanche, $P=10^5$-10^6 Pa, reduces under the τ/μ=2-10 Pa by the pressure deviation exceed a critical value, $s_c=10^5$-10^6 Pa. Actually, such a large pressure deviation can not be expected within these avalanches. Therefore, the acoustic fluidization model is not a suitable flow mechanism for these debris avalanches.

The sedimentary structures observed in these two debris avalanche deposits can be explained using the plug flow model. But, the avalanche did not flow from initial stage. The maximum size of the DBs gradually decrease, and the proportion of DM within the deposit increases toward the distal area (Chap. 5-1-2, 5-1-3). These evidences suggest that the DM was produced as a result of shearing and impact between the DBs, and DBs and basement formation. It is, therefore, interpreted that the debris avalanches did not contain enough DM at the initial stage of the avalanche. Thus, the DBs and basement formation were in direct contact, and the contact was slipped during this stage. No laminar boundary layer existed at the contact between the DBs and the basement

formation during this stage. Such kind of flow is interpreted as "slide" (Johnson, 1978). Sliding of a debris avalanche at the initial stage was observed at the 1980 debris avalanche of Mt. St. Helens, USA (Voight, et al., 1983).

7-2-2. Flow and deposition model of the debris avalanches

Based on the sedimentary structures in the Iwasegawa and the Kaida debris avalanche deposits (Chap. 5-1, 5-2), the flow and deposition mechanism of these debris avalanches are discussed using the plug flow model. The following discussion is divided into three stages: initial, flow, and deposition.

Initial stage (Fig. 7-2a): The unstable part of the volcanos such as the altered part by fumarolic activities, started to slide at the source area due to phreatic explosion or tectonic earthquake. Relatively small size DBs were ripped-off by the shear stress and the DM was produced by friction at the contact between the DBs and DBs and basement formation during this stage. The production of DM was minimal during this stage. The contact between DBs and the basement was slipped. Therefore, the transport mechanism during this stage was "slide".

Flow stage (Fig. 7-2b): The avalanche flowed down a steep slope at high speed. Collision between the DBs and basement formation at high speed resulted in fracturing. Larger shock due to the collision of the DBs and basement, breaking up the DBs. DBs which bumped against the basement, received a momentum and moved within a plug and a laminar boundary layer. At that time, DM was produced due to the shear stress and the friction at the contact between the DBs. A large amount of DM was also produced at the bottom contact between the DBs and the basement by strong shear stress due to a high pressure of its own weight. Larger DBs became supported by increasing in the yield strength and the viscosity of the DM during this stage. Basement materials were eroded and incorporated into the flow due to a strong shear stress. Also, the wood fragments captured along the flow head, were rotated and aligned

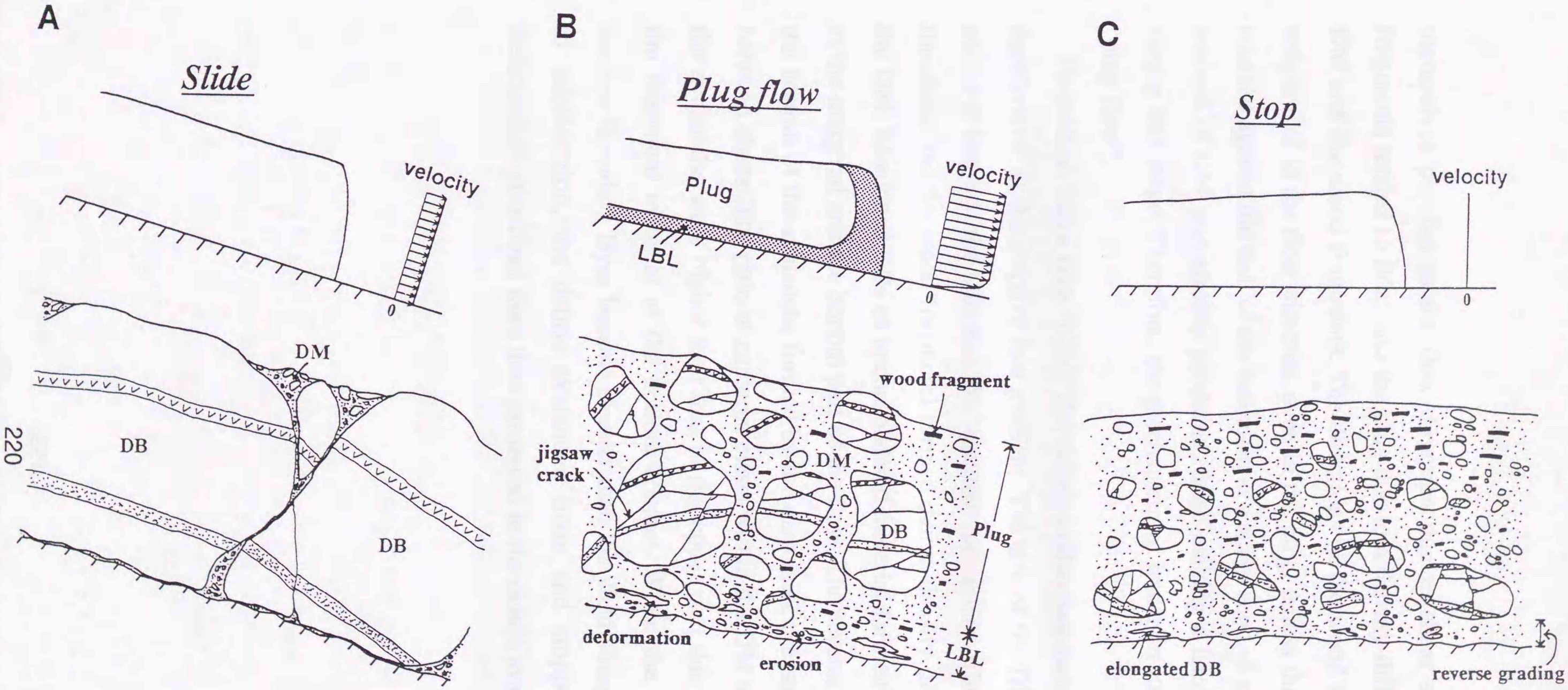

Fig. 7-2A-C. Flow and deposition mechanisms of the Iwasegawa and the Kaida debris avalanches. **A.** initial stage; **B.** flow stage; **C.** deposition stage. Lower figures show the cross sections of the avalanches. Upper figures show physical models with velocity profiles. LBL indicates the laminar boundary layer. See text for details.

themselves parallel to the flow direction due to shear stress. These wood fragments tended to float into the plug due to a density difference between the DM and the wood fragments. The directions of the wood fragments were still subparallel to the flow direction even in the plug, unless the avalanche became crushed against the wall of the basement at a sharp bend of a valley. A sufficient amount of DM was already produced, these making a laminar boundary layer during this stage. Therefore, the mechanism of transport during this stage was "plug flow".

Deposition stage (Fig. 7-2c): The debris avalanches started to recede due to deceleration at the slope of low gradient. The size of the DBs decreased due to collision between the DBs and the basement formations. The density grading of the clasts and the wood fragments formed due to density differences relative to the DM. Elongated DBs of unconsolidated material formed by the shear stress, at the marginal and the bottom part of the flow. The reverse grading of clasts at the bottom of the avalanche formed by the dispersive pressure through collision between clasts. The ratio of captured clasts within the DM at the bottom part of the avalanche were higher than that in the upper part due to incorporation of the basement material at the bottom contact. When the shear stress in the laminar boundary layer became smaller than the yield strength of the flow due to deceleration, the debris avalanche froze and stopped thixotropically. Sedimentary structures were then preserved in the debris avalanche deposits.

7-3. Flow and deposition mechanism of the pyroclastic flows

7-3-1. Density-modified grain flow model

The flow and deposition mechanism of pyroclastic flows are discussed, based on the characteristics of the deposits, yield strength estimation, fluidization experiment, observation of flows, and velocity measurement of the Komagatake 1929 and the Unzen 1991-93 pyroclastic flows, using the concept of four fundamental clast support mechanisms of gravity flows.

At first, the maximum grain size within the turbulent ash-cloud surge is evaluated using theoretical consideration and the measured velocities of the Unzen pyroclastic flows (Table 6-5). The relationship between the flow velocity (u) and Rouse number (Rs), according to the grain size (d) and solid concentration of the flow (C) is shown in Fig. 7-3b, based on the relations in Fig. 7-3a and following equations:

$$R_s = \omega_i / \varkappa u^*$$

$$u = u^*/\varkappa \ \ln(30y/k_s)$$

where ω_i, settling velocity; u^*, shear velocity; $\varkappa$, Von Kármán's constant (=0.4); y, thickness of boundary layer; and k_s, height of roughness elements (Valentine et al., 1987). Grain can suspend, when Rs is smaller than 2.5. For the ash-cloud surge, y and ks are ca. 5 m and 1 m, respectively. The solid concentration (C) of the ash-cloud surge is ca. 0.3-0.45, when the temperature of the surge was 400-600 ˚C (Huppert et al., 1986; Fig. 7-7). Measured average velocities of the five Unzen pyroclastic flows were up to 42 m/s (Table 6-5). Then, the maximum velocities of all Unzen pyroclastic flows should be lower than 100 m/s. Therefore, the maximum grain size can be suspended by turbulence, where the Rs is smaller than 2.5, was at most 0.1 to 1.0 cm (Fig. 7-3b). The grains finer than this size were suspended, producing a density stratified turbulent mixing layer (ash cloud), and the grains larger than this size up to a few meters,

A

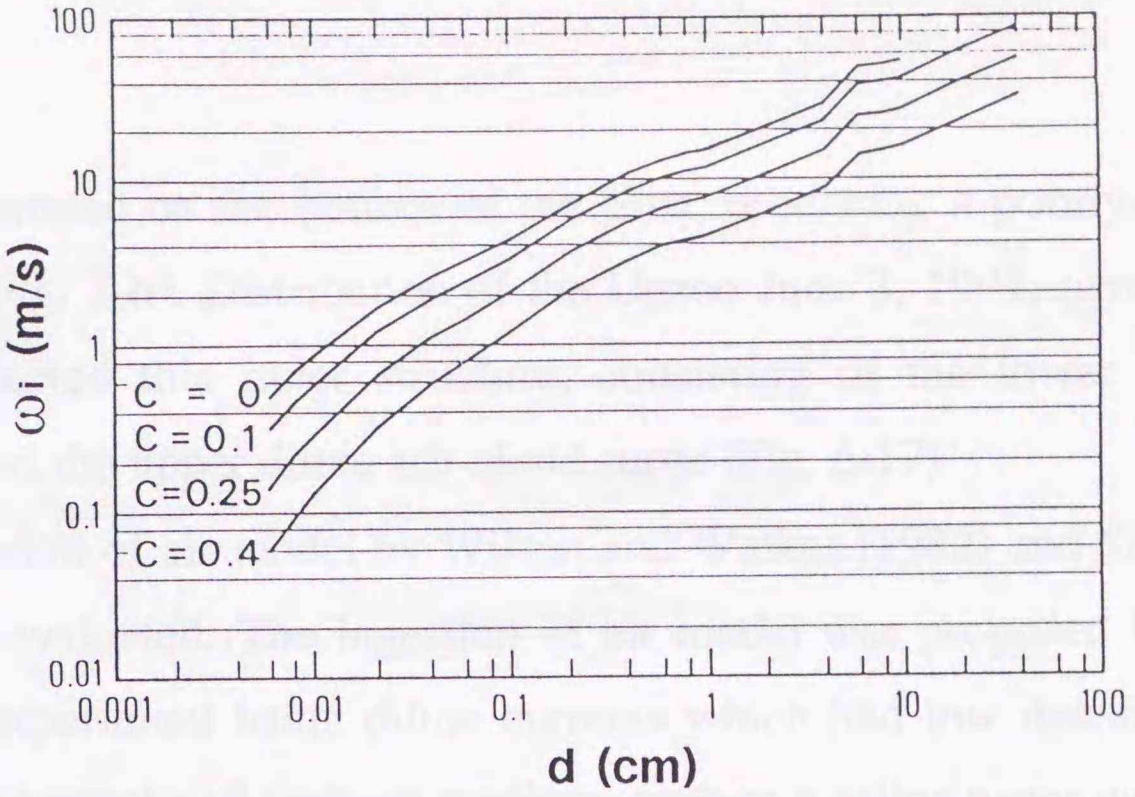

B

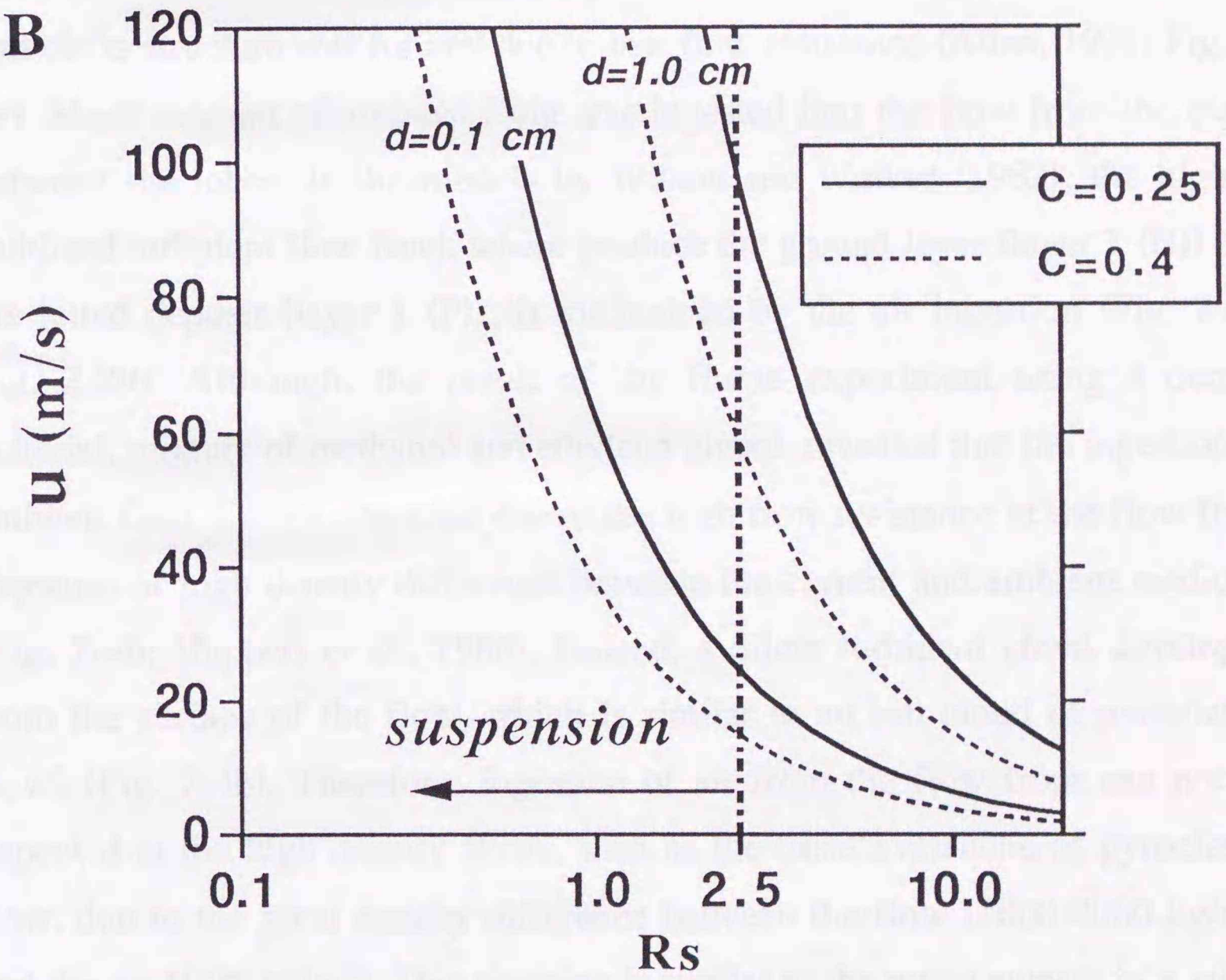

Fig. 7-3A-B. A. The terminal settling velocity (ω_i) as a function of grain diameter (d) and of varying solid concentration (C) (after Brissette and Lajoie, 1990). Assumed solid concentration of the ash-cloud surges was approximately C=0.25-0.4. **B.** The relation between the flow velocity (u) and Rouse number (Rs), according to the grain size (d) and fluid concentration (C), determined by the two equations in chapter 7-3-1 and the upper figure. Grains can suspend when Rs is smaller than 2.5. Maximum grain size can be suspended by turbulence within the ash-cloud surge is at most 0.1 to 1 cm in diameter at the measured average velocities of the Unzen pyroclastic flows (<42 m/s; Table 6-5).

were concentrated on the bottom of the flow, producing a poorly-sorted basal avalanche (Fig. 7-6). Distribution of the Unzen June 3, 1991, pyroclastic flow deposit reflected this inner structure, consisting of the lower dense basal avalanche and the upper dilute ash-cloud surge (Fig. 6-17).

The ingestion of air model by Wilson and Walker (1982) and Wilson (1985) is critically evaluated. The ingestion of air model was proposed based on the laboratory experiment using dilute currents which had low density difference between the current and ambient medium, such as a saline water current in pure water (Allen, 1971; Simpson, 1987, p.141-159). In this experiment, the lobes and clefts structure was formed due to low flow resistance (Allen, 1971; Fig. 7-4a). Much amount of ambient fluid was ingested into the flow from the clefts between the lobes. In the models by Wilson and Walker (1982), the highly-fluidized turbulent flow head, where produce the ground layer (layer 1 (H)) and the jetted deposit (layer 1 (P)), is maintained by the air ingestion (Fig. 7-4a; Fig. 2-29). Although, the result of the flume experiment using a denser material, mixture of methanol and ethylene glycol, revealed that the ingestion of ambient fluid did not observed due to the high flow resistance at the flow front (because of high density difference between the current and ambient medium) (Fig. 7-4b; Huppert et al., 1986). Instead, a dilute turbulent cloud developed from the surface of the flow, which is similar to an ash cloud of pyroclastic flows (Fig. 7-4b). Therefore, ingestion of air from the flow front can not be expected at the high density flows, such as the basal avalanche of pyroclastic flow, due to the great density difference between the flow (1000-2000 kg/m^3) and the air (1.25 kg/m^3). This situation is similar to the water current in a gully, which never ingest the ambient air from the flow front due to great density difference. In this case, the basal avalanche can not maintain the high pressure to continue the fluidization during flowage.

A

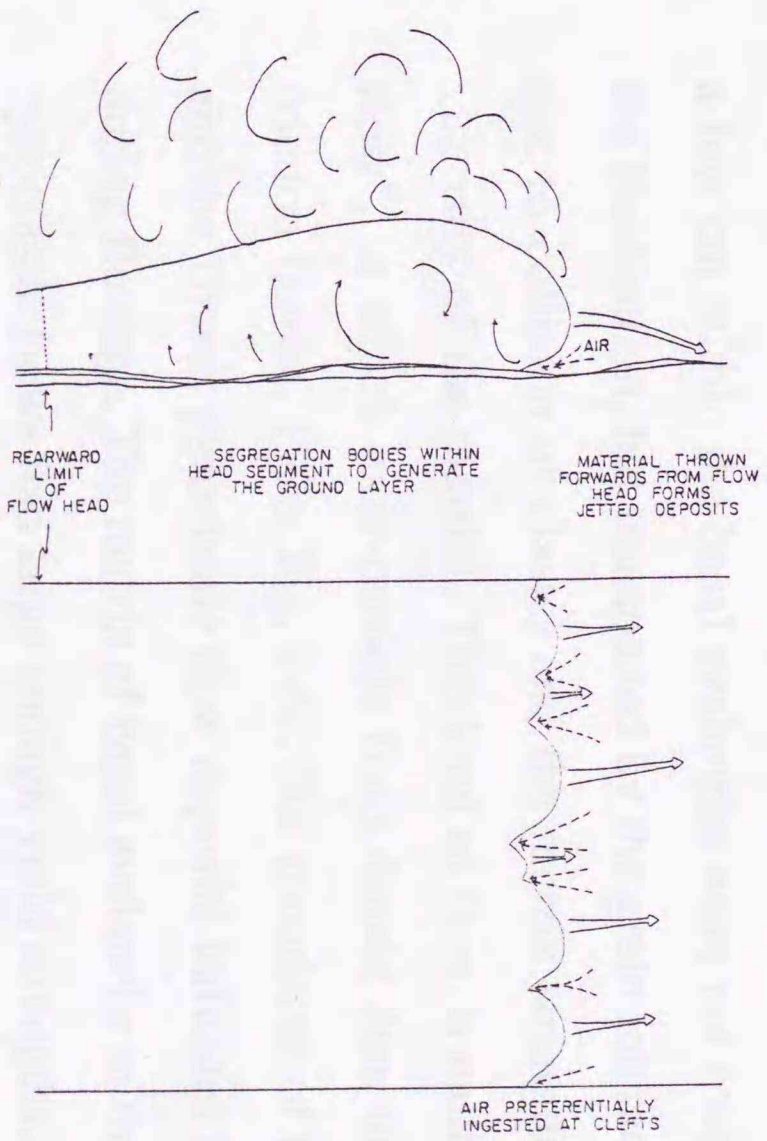

(after Wilson and Walker, 1982)

B

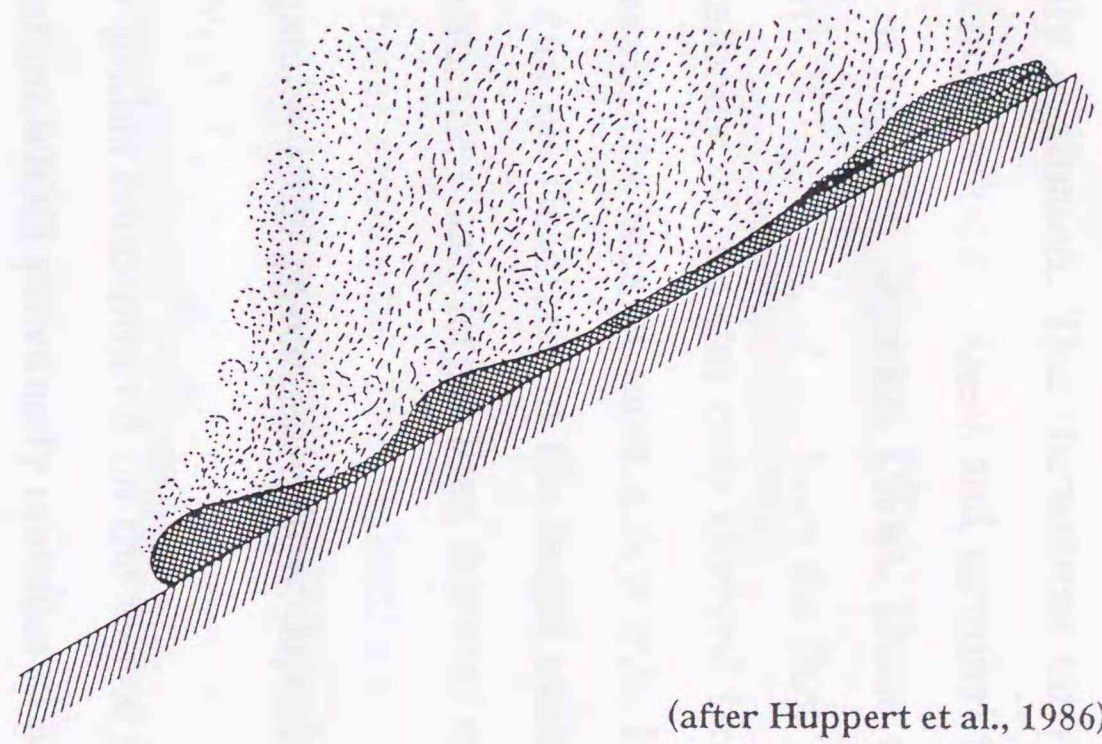

(after Huppert et al., 1986)

Fig. 7-4A-B. A. A model of ingestion of air from the clefts between the lobes for the Taupo ignimbrite, which proposed by Wilson and Walker (1982). In the experiment, the lobes and clefts structure, as proposed by Allen (1971) and Simpson (1987, p. 149), was only observed at the dilute currents, which had low density difference between the current and the ambient medium, such as a saline-water current in pure water. **B.** Result of the flume experiment using the dense current, mixture of methanol and ethylene glycol, by Huppert et al. (1986). Ingestion of ambient fluid from the flow front did not observed at the dense current, due to the high flow resistance at the flow front. Dilute turbulent cloud was developed from the surface of the flow. Therefore, ingestion of air from the flow front can not be expected at the high density flow, such as the basal avalanche of pyroclastic flow, due to the great density difference between the flow and the air.

Possibility of the fluidization as the main clast transport mechanism is critically evaluated. The theoretical curves of the relationship of minimum fluidization velocity (U_{mf}) and terminal fall velocity (U_t), and grain size are shown in Fig. 7-5 (Sparks, 1976). These curves are for the spheres of density 1.0 g/m^3. If ingestion of air from the flow front did not occur, expected upward flow velocity of the gas only derived from the juvenile materials within the basal avalanche was at most a few m/s. In this case, the maximum grain size which can be fluidized in the basal avalanche was at most 1 cm (Fig. 7-5). Therefore, the clasts larger than this size up to a few meter can not be fluidized in the basal avalanche. The fluidization experiment using the material of the Komagatake 1929 pyroclastic flow deposit and the glass beads in various sizes also revealed that larger grains weren't affected by the upward flow at all, even if finer grains concentrated on the top of the bed (Chap. 6-1-5). Therefore, the fluidization which previously considered as main transport mechanism (Wilson, 1980; Wilson, 1984) is not the main clast support mechanism of the basal avalanche.

These theoretical and experimental results revealed that the clasts larger than a few cm within the basal avalanche were not transported by the turbulence or the fluidization, but transported by the grain interaction (the dispersive pressure due to collision of clasts) and the matrix strength (the yield strength and the viscosity of the matrix). This kind of flow is called a “density-modified grain flow”, in which inter-particle fluid denser than the ambient fluid reduces the friction (Lowe, 1976; Fig. 7-6). The roundness of the clasts in the Komagatake and the Unzen pyroclastic flow deposits indicates the severe collision of grains during flowage. The matrix of basal avalanche in the Komagatake and the Unzen pyroclastic flows had large enough yield strengths, 10^2-10^4 Pa and 850-2000 Pa respectively, to support large clasts as estimated from the detail morphology (Chap. 6-1-3) and the parameters of computer simulations (Chap. 6-2-8).

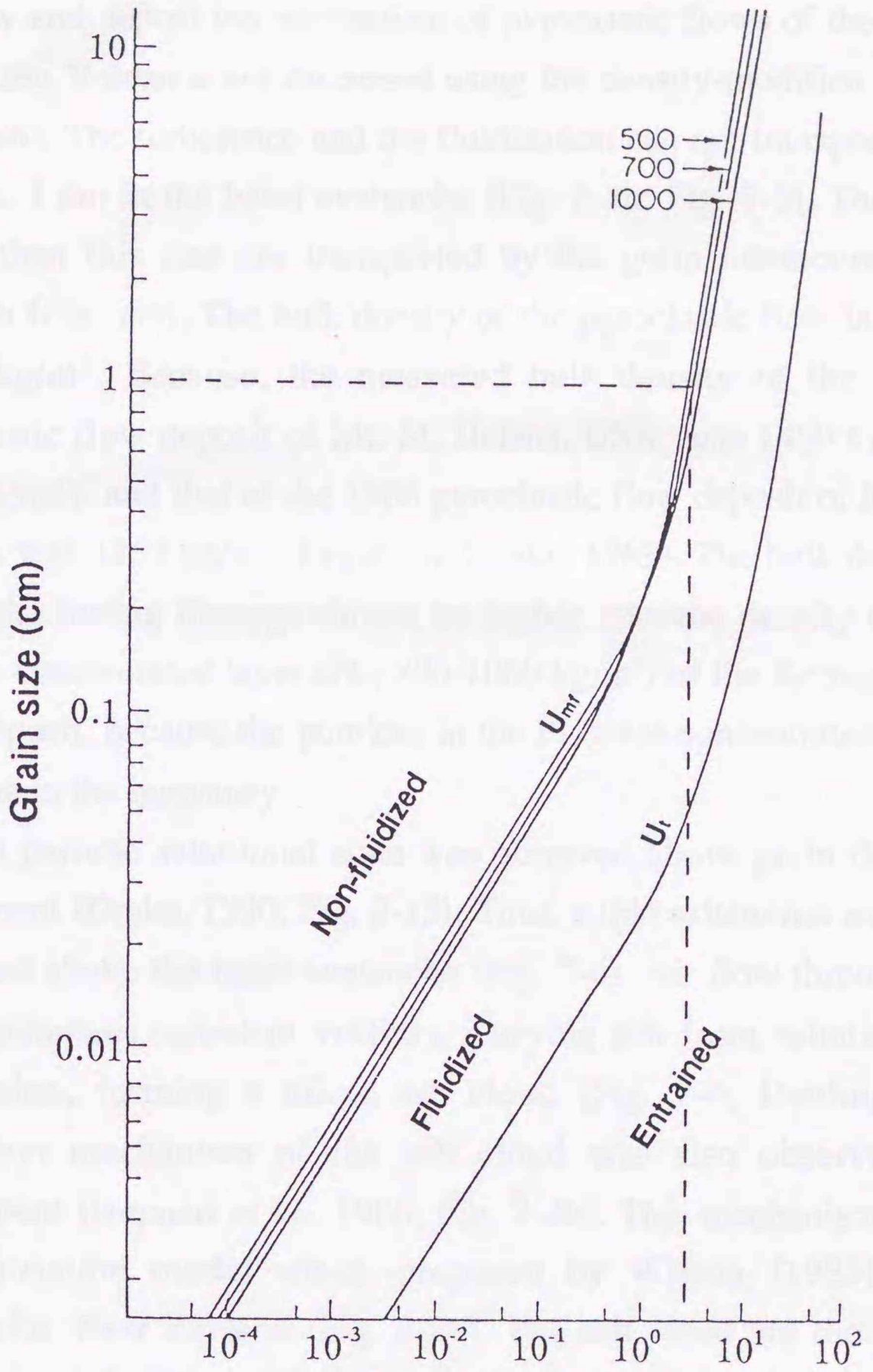

(after Sparks, 1976)

Fig. 7-5. Theoretical curves of the relationship of minimum fluidization velocity (U_{mf}) and terminal fall velocity (U_t) and grain size by Sparks (1976). These curves are for the spheres of density 1.0 g/m^3. The expected velocities of the upward flow degassed from the juvenile materials are at most a few m/s, for the pyroclastic flows at the Unzen and the Komagatake Volcanos, when no ingestion of air from the flow front were occurred. In this case, the maximum grain size which can be fluidized in the basal avalanche was at most 1 cm.

7-3-2. Flow and deposition model of the pyroclastic flows

Flow and deposition mechanism of pyroclastic flows of the Komagatake and the Unzen Volcanos are discussed using the density-modified grain flow model (Fig. 7-6). The turbulence and the fluidization can not transport the clasts larger than ca. 1 cm in the basal avalanche (Fig. 7-3b; Fig. 7-5). Therefore, the clasts larger than this size are transported by the grain interaction and the matrix strength (Fig. 7-6). The bulk density of the pyroclastic flow is as large as 1000-2000 kg/m^3. Because, the measured bulk density of the pumiceous 1980 pyroclastic flow deposit of Mt. St. Helens, USA, was 1450 kg/m^3 (Wilson and Head, 1981); and that of the 1986 pyroclastic flow deposit of Mt. St. Augustine, Alaska, was 1360 kg/m^3 (Beget and Limke, 1989). The bulk density of the basal avalanche during flowage should be higher than the density of pumices in the pumice concentrated layer (PL; 800-1000 kg/m^3) of the Komagatake pyroclastic flow deposit, because the pumices in the PL were concentrated on the top of the lobe due to the buoyancy.

Thin particle saltational zone was observed above grain flows in the flume experiment (Drake, 1990; Fig. 2-15). Thus, a thin saltational zone should also be produced above the basal avalanche (Fig. 7-6). Air flow through the saltational zone, generates turbulent vortices, carrying ash from saltation into turbulent suspension, forming a dilute ash cloud (Fig. 7-6; Denlinger, 1987). This formation mechanism of the ash cloud was also observed in the flume experiment (Huppert et al., 1986; Fig. 7-4b). This mechanism is disagree with the elutriation model which proposed by Wilson (1985) for the Taupo ignimbrite, New Zealand (Fig. 2-29). The ash cloud are the density stratified turbulent mixing layer. The buoyant portions of the ash cloud lighter than the ambient air (<1.25 kg/m^3) produce an ash fall. But, the dense portions heavier than the air (>1.25 kg/m^3) may produce a ash-cloud surge which easily separated from the parental avalanche (Fig. 7-6; Fig. 6-17). This boundary condition between the ash fall and the ash-cloud surge is important. The relationship between the density of mixtures of hot ash and cold air, and the

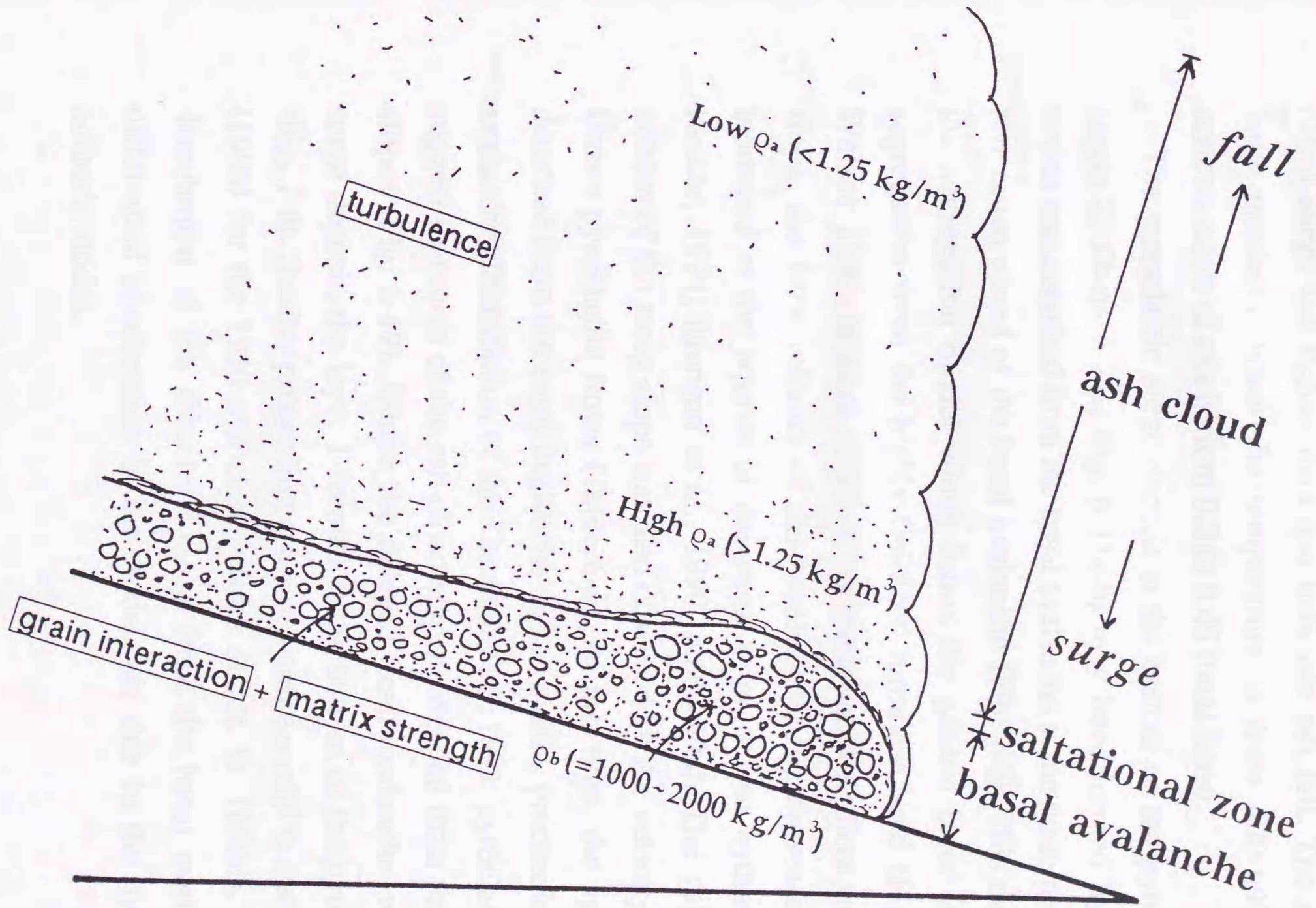

Fig. 7-6. Flow and deposition mechanism of pyroclastic flows of the Unzen and the Komagatake Volcanos, using the density-modified grain flow model. Large clasts within the basal avalanche can not be transported by the fluidization, but transported by the grain interaction: dispersive pressure due to collision of the clasts, and by the matrix strength: the yield strength and the viscosity of the matrix. A thin particle saltational zone was formed above the basal avalanche, according to the experimental data of grain flows (Drake, 1990). Ash cloud was the density-stratified turbulent mixing layer. The buoyant portions of the ash cloud lighter than the ambient air, 1.25 kg/m^3, produced an ash fall. But, the dense portions heavier than the air produced an ash-cloud surge, by the separation from the parental basal avalanche.

solid concentration of ash in the mixture by Huppert et al. (1986) is shown in Fig. 7-7. Heavier than the density of the ambient air (1.25 kg/m^3) indicates ash-cloud surge and lighter than that indicates ash fall. The ash-cloud surge may have produced when the temperature is from 400-600 ˚C and the solid concentration of ash is from 0.3 to 0.45 (bold lines).

The pyroclastic surge deposit at the bottom of the pyroclastic flow deposit (layer 1; Chap. 6-2-6; Fig. 6-11e-h) may have formed by an ash-cloud surge which was detached from the basal avalanche at the bottom of the steep slope and proceeded ahead of the basal avalanche (Fig. 7-8). This model is disagree with the segregation model which forms the ground layer (layer 1 (H)) due to segregation from the highly-fluidized turbulent head (Fig. 2-29; Wilson and Walker, 1982; Wilson, 1985). After the pyroclastic flow rushed down the steep slope, the flow velocity of the basal avalanche decreased and the thickness increased at the bottom of the steep slope due to hydraulic jump (Fig. 7-8; Komar, 1971; Munson et al., 1990, p.688-694). The velocity change at the bottom of the steep slope was also observed by the velocity measurement of the Unzen pyroclastic flows (Table 6-5). At this time, the upper ash-cloud surge detached from the basal avalanche due to inertia, proceeding ahead of the basal avalanche. Distribution of the Unzen June 3, 1991, pyroclastic flow deposit also suggest that most of the ash-cloud surges extended from the bottom of the steep slopes (Fig. 6-17). Where the delayed basal avalanche overlay the ash cloud surge deposit, the layer 1 formed at the bottom of the pyroclastic flow deposit (Fig. 7-8). Similar proceeding ash-cloud surge model is also proposed by Hoblitt (1986) for the 1980 pyroclastic flows of Mt. St. Helens, USA. Although, the detachment of the ash-cloud surge from the basal avalanche occur due to differential acceleration in his model, not due to the hydraulic jump in the author's model.

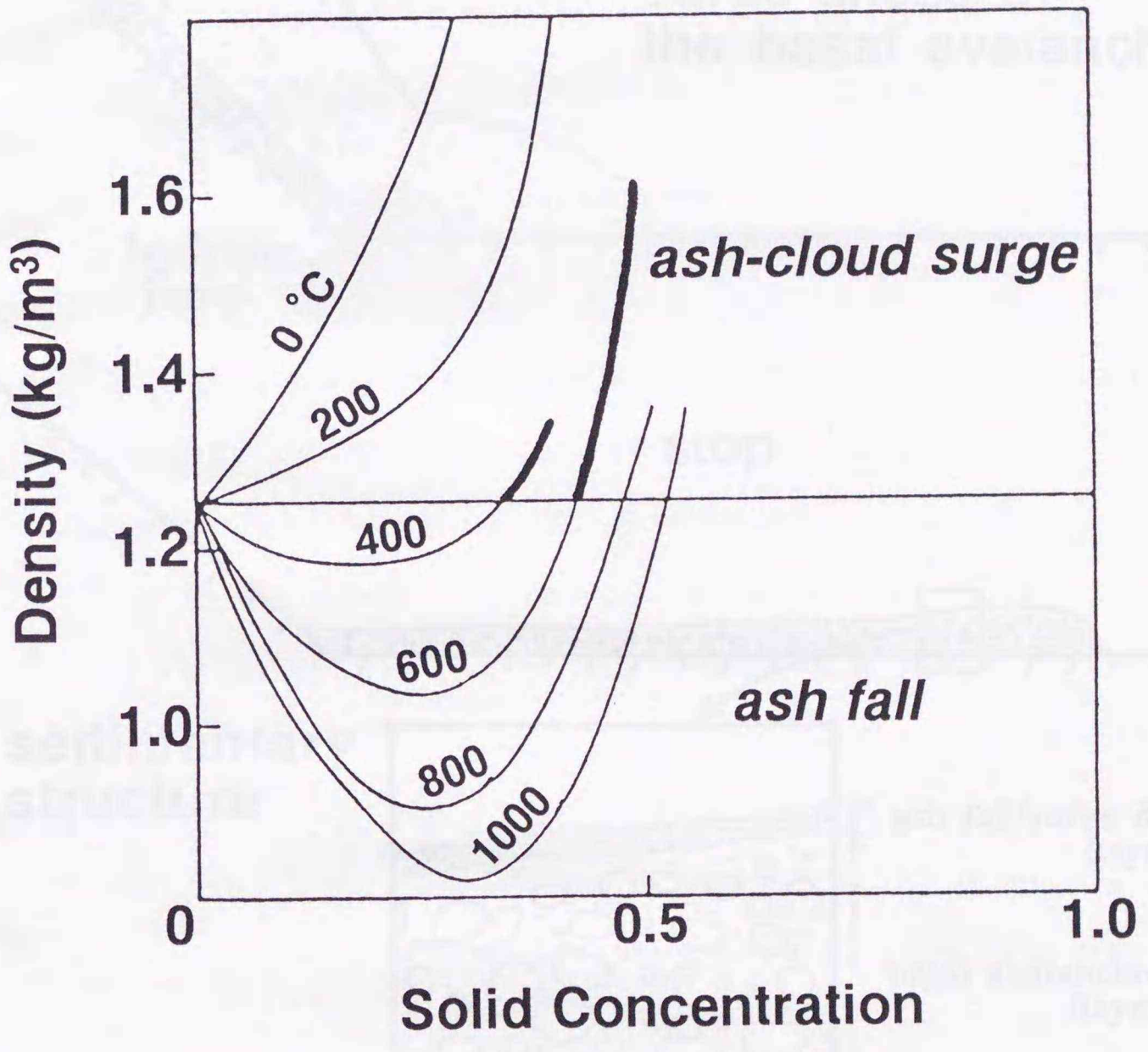

Fig. 7-7. Relationship between the density of mixture of hot ash and cold air, and the proportion of ash in the mixture by Huppert et al. (1986). Temperatures of hot ash are shown on each curve. Density of air at 0 °C is 1.25 g/m^3. The ash-cloud surge may have been produced when the temparature was from 400 to 600 °C, and the solid concentration was from 0.3 to 0.45 (two bold lines).

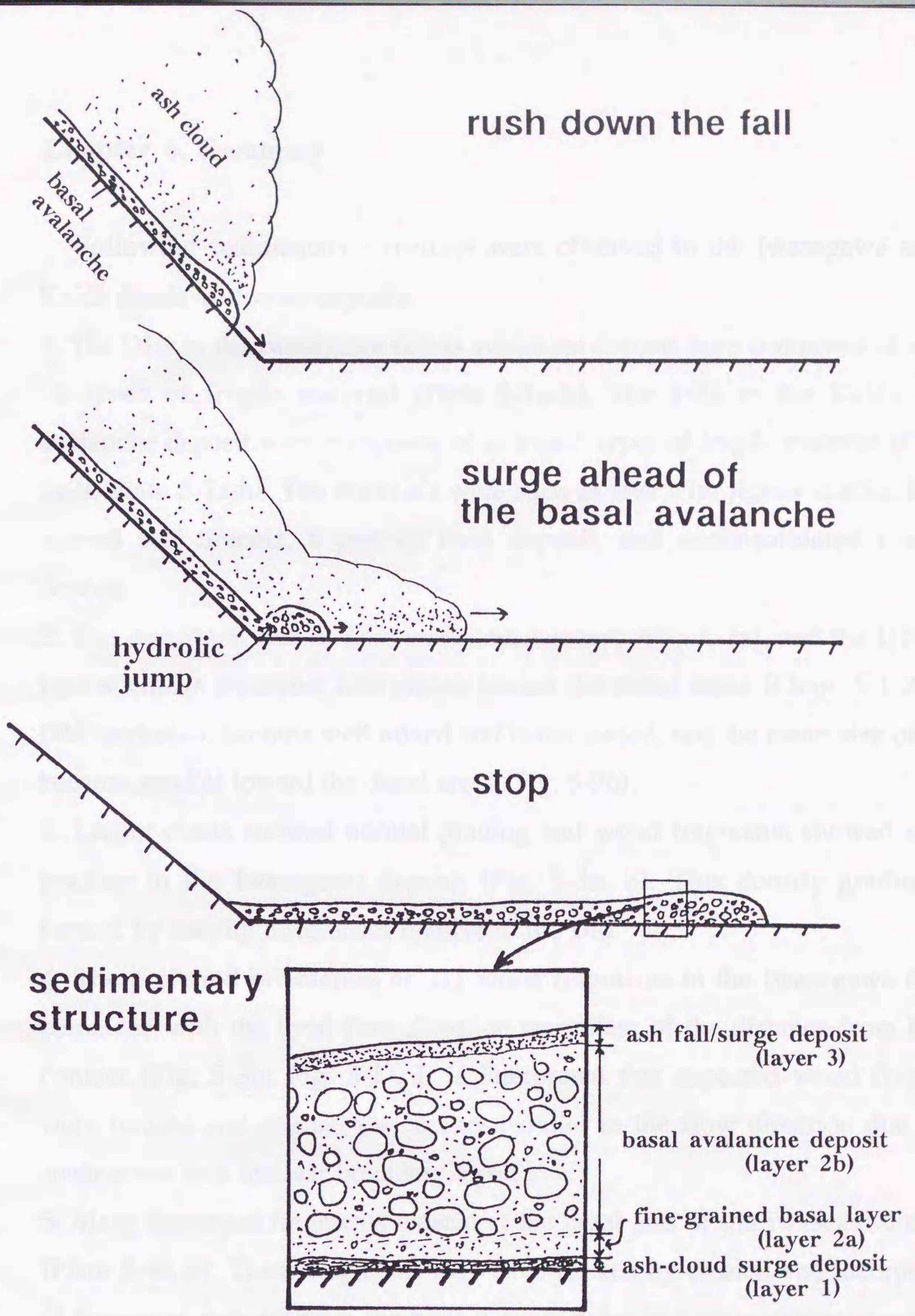

Fig. 7-8. A model to produce the ground surge deposit, layer 1. The surge deposit at the bottom of the pyroclastic flow deposit may have been formed by the ash-cloud surge which was detached from the basal avalanche at the bottom of the steep slope due to hydraulic jump and proceeded ahead of the basal avalanche. After the pyroclastic flow rushed down the steep slope, the flow velocity of the basal avalanche decreased at the bottom of the slope, due to the hydraulic jump. At this time, the upper ash-cloud surge proceeded ahead of the basal avalanche due to inertia. When delayed basal avalanche overlie on the ash-cloud surge deposit, the layer 1 formed at the bottom of the pyroclastic flow deposit.

Chapter 8. Summary

Following sedimentary structures were observed in the Iwasegawa and the Kaida debris avalanche deposits.

1. The DBs in the Iwasegawa debris avalanche deposit were composed of at least 12 types of fragile material (Plate 5-1a-k). The DBs in the Kaida debris avalanche deposit were composed of at least 5 types of fragile material (Plate 5-6a-h; Plate 5-7a-h). The materials were such as lava with jigsaw cracks, highly-altered tuff breccia, a part of river deposit, and unconsolidated reworked deposit.

2. The maximum size of DBs tended to decrease (Fig. 5-2a), and the DBs with jigsaw cracks separated into pieces toward the distal areas (Chap. 5-1-2). The DM tended to become well mixed and better sorted, and the mean size of clasts became smaller toward the distal areas (Fig. 5-2b).

3. Larger clasts showed normal grading and wood fragments showed reverse grading in the Iwasegawa deposit (Fig. 5-3a, b). This density grading was formed by density differences relative to the DM.

4. The preferred orientation of 311 wood fragments in the Iwasegawa deposit coincided with the local flow direction regardless of the distance from bottom contact (Fig. 5-3b; Fig. 5-1). It is interpreted that captured wood fragments were rotated and aligned themselves parallel to the flow direction due to the shear stress in a laminar boundary layer.

5. Many basement fragments existed at the basal part of the Iwasegawa deposit (Plate 5-4a, b). These fragments may have formed by erosion and incorporation of basement material from the bottom contact due to a strong shear stress and a high pressure during flowage.

6. A reverse grading of clasts was observed at the basal part of the Iwasegawa deposit, which may have formed by dispersive pressure (Fig. 5-4; Plate 5-5).

This reverse grading indicate that fragile DBs could not be preserved in the laminar boundary layer which has a high shear stress field. The proportion of the captured clasts within the DM was higher in the bottom level of the deposit (Fig. 5-4).

7. Elongated DBs consisting of unconsolidated material were observed at the marginal and the basal part of the Kaida deposit (Plate 5-7c, d, h). These elongated DBs may have formed by shear stress at the marginal and the basal part of the flow.

8. The lithic component within the DM in the Kaida deposit tended to have a higher proportion of the captured material which was derived from the adjacent basements (Fig. 5-6). This evidence suggest that the avalanche flowed down the slope capturing material from the basements, which immediately mixed well with DM.

The origin of the sedimentary structures observed in the debris avalanche deposits are well explained by a plug flow model. In the inner plug, the fragile DBs were transported without major rapturing due to high yield strength and viscosity of the DM. As the debris avalanches flowed down the steep slope at high speed, basement materials were eroded and incorporated into the laminar boundary layer under a strong shear stress field. The DM was produced by the shear stress between two DBs, and DBs and basement formations. Collision between DB and basement formations resulted in fracturing. Wood fragments included within the DM in the laminar boundary layer were rotated and aligned parallel to the flow direction. The density grading of clasts and wood fragments were formed by the density differences relative to the DM. The elongated DBs were formed by shear stress within the laminar boundary layer, and reverse grading of clasts was formed by the dispersive pressure on collision of each clast at the bottom of the flows. When the shear stress in the laminar boundary

layer became smaller than the yield strengths of the flows due to deceleration, the debris avalanches froze and stopped thixotropically.

Following results were obtained from the Komagatake 1929 and the Unzen 1991-93 pyroclastic flows.

1. The order of the estimated yield strengths by the measurement of widths and heights of 53 lobes and 37 natural levees of the Komagatake pyroclastic flow deposits at the northwestern slope were 10^2-10^4 Pa (Table 6-1).

2. One flow unit of the Komagatake pyroclastic flow deposits at the northern slope was subdivided into a fines-depleted layer (DL), a fines-rich layer (FL), and a pumice-concentrated layer (PL), where the deposit contains many carbonized wood fragments (Fig. 6-5).

3. Fluidization experiments using the material of the pyroclastic flow deposits and the glass beads of various sizes revealed that the formation mechanism of the DL and the FL due to concentration of fine particles toward the top through the segregation pipes. Although, particles larger than 1 mm were not affected by the upward flow at all (Plate 6-7; Plate 6-9b).

4. Observation showed that the Unzen pyroclastic flow deposit was composed of a few-meters thick, poorly-sorted, dense basal avalanche deposit and very thin, better-sorted, ash-cloud surge deposit (Fig. 6-17; Plate 6-10g).

5. Video images revealed that the Unzen pyroclastic flows descended along the channels, with developing vortices of overlying dilute ash-cloud, but ingestion of air or jetting from the flow head which were proposed by Wilson and Walker (1983) were not observed (Chap. 6-2-5).

6. Excavation by machines of the toe of the Unzen June 8, 1991, pyroclastic flow deposit revealed that the deposit was partly fines-depleted due to the gas from the heated large blocks and carbonized wood fragments. A <5 cm-thick surge deposit (layer 1) and a 15 cm-thick layer 2a were observed at the bottom of the deposit (Plate 6-11a-*l*).

7. The measured average velocities of five Unzen pyroclastic flows from May 24 to May 29, 1991, were up to 42 m/s (Table 6-5).

8. Numerical simulations of the Unzen pyroclastic flows using energy line/cone and Bingham models were made. In the simulation using the Bingham flow model, obtained yield strengths and viscosities were 850-2000 Pa and 50-90 Pa respectively (Chap. 6-2-8).

9. The maximum grain size that can be transported by the turbulence at the measured velocities of the Unzen pyroclastic flows (Table 6-5) was at most 0.1 to 1.0 cm in diameter (Fig. 7-3). Grains finer than this size can form the dilute ash-cloud surge/fall, but grains larger than this size must be concentrated on the bottom and form the poorly-sorted, dense basal avalanche (Fig. 7-6).

10. Flume experiment (Huppert et al., 1986) showed that ingestion of ambient fluid from the flow front did not observed at a high density current due to the great density difference between the current and the ambient medium (Fig. 7-4). In this case, the basal avalanche could not maintain the high pressure to continue the fluidization. Theoretical curve of fluidization (Sparks, 1976) shows that the maximum grain size can be fluidized in the basal avalanche is at most 1.0 cm, when no ingestion of air from the flow front occurs (Fig. 7-5).

These results suggest that the transport mechanism of the grains larger than ca. 1 cm is not fluidization as proposed by Wilson (1980, 1984), but grain interaction and matrix strength (density-modified grain flow; Fig. 7-6). The roundness of the grains in the both pyroclastic flow deposits indicates the severe collision of grains. The Komagatake and the Unzen pyroclastic flows had yield strengths large enough to support the large grains (10^2-10^4 Pa and 850-2000 Pa respectively). The ash cloud were the density-stratified turbulent mixing layer. The buoyant portions of the ash cloud lighter than the air produced an ash fall. The dense portions heavier than the air produced an ash-cloud surge detached from the parental avalanche. The surge deposit at the bottom of the pyroclastic

flow deposit (layer 1) may have been formed by the ash-cloud surge which was detached from the basal avalanche at the bottom of the steep slopes due to hydraulic jump and proceeded ahead of the tip of the basal avalanche (Fig. 7-8).

Acknowledgements. I wish to thank Prof. S. Aramaki and Prof. T. Ui for their encouragement and many stimulating discussions during this study. I am indebted to T. Yamamoto, J. Itoh, S. Geronimo-Catane, T. Nakano, K. Kazahaya, Y. Kawanabe, K. Sakaguchi, S. Suto, and T. Soya for their encouragements and fruitful discussions. Y. Yamamoto and T. Osawa introduced me to good outcrops in the Kaida debris avalanche deposit. C. Feebly kindly checked English of a part of this manuscript. Y. Ishikawa allowed me to use the data obtained at the excavation survey of the Unzen June 8, 1991, pyroclastic flow deposit. Unzendake Weather Station, JMA, allowed the usage of tremor records of Unzen pyroclastic flows. T. Nakano made the program and the beautiful graphics of the computer simulations using the energy cone model. I also thank S. Iwasasa and J. Kizaki and their families for kind help during my field surveys. I'd like to thank J. Kimura and T. Sawada for their help of tremor record analysis of Unzen pyroclastic flows.

References

Allen, J.R.L. (1971) Mixing at turbidity current heads, and its geological implications. *J. Sediment. Petrol.*, **41**, 97-113.

Allen, J.R.L. (1982) **Sedimentary structures -their character and physical basis**. Elsevier, 593p.

Allen, J.R.L. (1985) **Principles of physical sedimentology.** George Allen and Unwin, 272p.

American Geological Institute (1987) **Glossary of Geology**. (Bates, R.L. and Jackson, J.A. eds), 788p.

Bagnold, R.A. (1954) Experiments on a gravity-free dispersion of large solid spheres in a Newtonian fluid under shear. *Proc. Roy. Soc. London, A*, **225**, 49-63.

Bagnold, R.A. (1962) Auto-suspension of transported sediment; turbidity currents. *Proc. Roy. Soc. London, A*, **265**, 315-319.

Beget, J.E. and Limke, A.J. (1989) Density and void ratio on emplacement of a small pyroclastic flow, Mount St. Augustine, Alaska. *J. Volcanol. Geotherm. Res.*, **39**, 349-353.

Blong, R.J. (1984) **Volcanic hazards -a sorcebook on the effects of erutions**. Academic Press, 424p.

Branney, M.J. and Kokelaar, P. (1992) A reappraisal of ignimbrite emplacement: progressive aggradation and changes from particulate to non-particulate flow during emplacement of high-grade ignimbrite. *Bull. Volcanol.*, **54**, 504-520.

Campbell, C.S. (1989) Self-lubrication for long runout landslides. *J. Geology,* **97**, 653-665.

Cas, R.A.F and Wright, J.V. (1987) **Volcanic successions -modern and ancient.** Allen and Unwin, 528p.

Cattermole, P. (1989) **Planetary volcanism.** Ellis Horwood library of space science and technology, 443p.

Cole, P.D. and Scarpati, C. (1993) A facies interpretation of the eruption and emplacement mechanisms of the upper part of the Neapolitan Yellow Tuff, Campi Flegrei, southern Italy. *Bull. Volcanol.*, **55**, 311-326.

Crandell, D.R., Miller, C.D., Gliken, H.X., Christiansen, R.L. and Newhall, C.G. (1984) Catastrophic debris avalanche from ancestral Mount Shasta volcano, California. *Geology*, **12**, 143-146.

Davis, J.C. (1973) **Statistics and data analysis in geology.** John Wiley and Sons, 646p.

Denlinger, R.P. (1987) A model for generation of ash clouds by pyroclastic flows, with application to the 1980 eruptions at Mount St. Helens, Washington. *J. Geophys. Res.*, **92(B10)**, 10284-10298.

Drake, T.G. (1990) Structural features in granular flows. *J. Geophys. Res.*, **95(B6)**, 8681-8696.

Egashira, S., Ashida, K., Yajama, H. and Takahama, J. (1989) Constitutive equations of debris flow. *Annuals Disas. Prev. Res. Inst. Kyoto Univ.*, **32(B2)**, 487-501. (in Japanese with English abstract)

Fisher, R.V. (1966) Mechanism of deposition from pyroclastic flow. *Am. Jour. Sci.*, **264**, 350-363.

Fisher, R.V. (1979) Models for pyroclastic surges and pyroclastic flows. *J. Volcanol. Geotherm. Res.*, **6**, 305-318.

Fisher, R.V. (1983) Flow transformations in sediment gravity flow. *Geology*, **11**, 273-274.

Fisher, R.V. and Heiken, G. (1982) Mt. Pelee, Martinique: May 8 and 20, 1902, pyroclastic flows and surges. *J. Volcanol. Geotherm. Res.*, **13**, 339-371.

Fisher, R.V. and Schmincke, H.-U. (1984) **Pyroclastic rocks**. Springer-Verlag, 472p.

Fisher, R.V., Smith, A.L., Wright, J.V. and Roobol, M.J. (1980) Ignimbrite veneer deposits or pyroclastic surge deposits? *Nature*, **286**, 912.

Fork, R.L. and Ward, W.C. (1957) Brazos River bar: a study in the significance of grain size parameters. *J. Sediment. Petrol.* **27**, 3-26.

Foxworthy, B.L. and Hill, M. (1982) Volcanic eruptions of 1980 at Mount St. Helens -The first 100 days. *Geol. Surv. Prof. Paper*, **1249**, 1-125.

Francis, P. (1993) **Volcanoes -a planetary perspective.** Oxford, 443p.

Freundet, A. and Schmincke, H.-U. (1985) Lithic-enriched segregation bodies in pyroclastic flow deposits of Laacher See Volcano (East Eifel, Germany). *J. Volcanol. Geotherm. Res.*, **25**, 193-224.

Fritz, W.J. and Moore, J.N. (1988) **Basics of physical stratigraphy and sedimentology**. John Wiley and Sons, 371p.

Fujii, T. (1976) Flow and deposition mechnism and structures of Kisogawa mud flow deposit, Ontake Volcano. *Report of Geography, Aichi Education Univ.*, **45**, 114-120. (in Japanese)

Gliken, H. (1986 MS) Rockslide-debris avalanche of May 18, 1980, Mount St. Helens Volcano, Washington. *Ph. D. Dissertation, University of California, Santa Barbara*, 1-303.

Hampton, M.A. (1972) The role of subaqueous debris flow in generating turbidity currents. *J. Sedimemt. Petrol.*, **42**, 775-793.

Hampton, M.A. (1975) Competence of fine-grained debris flows. *J. Sediment. Petrol.*, **45**, 834-844.

Hampton, M.A. (1979) Buoyancy in debris flows. *J. Sediment. Petrol.*, **49**, 753-758.

Hayakawa, Y. (1985) Pyroclastic geology of Towada volcano. *Bull. Earthq. Res. Inst.*, **60**, 507-592.

Hayashi, J.N. and Self, S. (1992) A comparison of pyroclastic flow and debris avalanche mobility. *J. Geophys. Res.*, **97(B6)**, 9063-9071.

Heim, A. (1882) Der Bergsturs von Elm: Deutsch. *Geol. Gesell. Zeitschr.*, **34**, 74-115.

Hoblitt, R.P. (1986) Observations of the eruptions of July 22 and August 7, 1980, at Mount St. Helens, Washington. *U. S. Geol. Surv. Spec. Pap.*, **1335**, 1-44.

Honma, F. (1936) Unzendake. *Bull. Volcanol. Soc. Japan*, **3**, 73-123. (in Japanese)

Howard, K. (1973) Avalanche mode of motion: Implication from lunar examples. *Science,* **180**, 1052-1055.

Hsü, K.J. (1975) Catastrophic debris streams (Sturzstroms) generated by rockfalls. *Geol. Soc. Am. Bull.*, **86**, 129-140.

Huppert, H.E., Turner, J.S., Carey, S.N., Sparks, R.S.J. and Hallworth, M.A. (1986) A laboratory simulation of pyroclastic flows down slopes. *J. Volcanol. Geotherm. Res.*, **30**, 179-199.

Johnson, A.M. (1970) **Physical processes in geology**. Freeman, Cooper and Co. San Francisco, 576p.

Johnson, B. (1978) Blackhawk landslide, California, U.S.A. In *Rock slide and avalanche* (Voight, B. ed), Elsevier, 481-504.

Katayama, N. (1974) The Shimabara Catastorophe. *Kagaku*, **44**, 566-570. (in Japanese)

Katsui, Y., Yokoyama, I., Fujita, T. and Ehara, Y. (1975) Komagatake -volcanic geology, eruption history, present condition and hazard measures-. *Hokkaido Hazard Prevention Conference*, 1-194. (in Japanese)

Katsui, Y., Shinozawa, T., Toshimoto, Y. and Yamada, Y. (1986) Historic pyroclastic flows at the Hokkaido Komagatake. In *Characteristics and hazards of the dry particle flows from volcanic eruption*, *Report of the research of natural hazard assisted by the Ministry of Education* (Aramaki, S. ed), 91-113. (in Japanese)

Katsui, Y., Suzuki, T., Soya, T. and Yoshihisa, Y. (1989) **Geological map of Hokkido-Komagatake Volcano 1: 50,000 Geological map of volcano 5.** Geol. Surv. Japan, 10p. (in Japanese with English abstract)

Kent, P.E. (1966) The transport mechanism in catastrophic rock falls. *J. Geology,* **74**, 79-83.

Kobayashi, K. Shimizu, H., Kitazawa, K. and Kobayashi, T. (1967) The pumice-fall deposit "Pm-I" supplied from Ontake Volcano -study of the pumice-fall deposit "Pm-I" supplied from Ontake Volcano No. 1-. *J. Geol. Soc. Japan.*, **73**, 291-308. (in Japanese with English abstract)

Kobayashi, T. (1987) Geological aspect of the 1984 Denjo Landslide on Ontake Volcano. *Transactions, Japanese Geomorphological Union*, 8, 113-125. (in Japanese with English abstract)

Kobayashi, Y. (1991) Travel mechanisms of large debris avalanches. *Proc. Japan-U.S. Workshop on Snow avalanche, Landslide, Debris flow Prediction and Control*, 409-418.

Komar, P.D. (1971) Hydrulic jamps in turbidity currents. *Geol. Soc. Am. Bull.*, **82**, 1477-1488.

Komiya, M. (1993) Eruption at Unzen volcano 1991-1993. In *Volcanic disaster at Unzen Volcano*, 1-14. The Japanese Society of Soil Mechanics and Foundation Engineering. (in Japanese)

Koyaguchi, T. and Tokuno, M. (1993) Origin of the ginant eruption cloud of Pinatubo, June 15, 1991. *J. Volcanol. Geotherm. Res.*, **55**, 85-96.

Kozu, S., Watanabe, M., Yoshiki, B., Seto, K., Yagi, T., Masuda, M., Watanabe, S., Ueda, J. and Takane, K. (1932) **A report of the big eruption of the Komagatake.** Research Rep. Saito Group. 246p. (in Japanese)

Kubo, R., Nagakura, S., Inokuchi, Y. and Ezawa, H. (1987) **Dictionary of scinece and chemistry -fourth edition**. Iwanami, 1629p. (in Japanese)

Kuno, H. (1941) Characterictics of deposits formed by pumice flows and those by ejected pumice. *Bull. Earthq. Res. Inst.*, **11**, 205-215.

Kurasawa, H. and Takahashi, K. (1965) Petorology and chemistry of rocks of the Unzen Volcano and its basement, Kyushu, southwest Japan. *Bull. Geol. Surv. Japan*, **16**, 258-274. (in Japanse with English abstract)

Lowe, D.R. (1976) Grain flow and grain flow deposits. *J. Sediment. Petrol.*, **46**, 188-199.

Lowe, D.R. (1982) Sediment gravity flows: II. depositional models with special reference to the deposit of high-density turbidity currents. *J. Sediment. Petrol.*, **52**, 279-297.

Lucchitta, B.K. (1978) A large landslide on Mars. *Geol. Soc. Am. Bull.*, **89**, 1601-1609.

Machida, H. and Arai, F. (1992) **Atlas of tephra in and around Japan**. Univ. Tokyo Press. 276p. (in Japanese)

Malin, M.C. and Sheridan, M.F. (1982) Computer-assisted mapping of pyorclastic surges. *Science*, **217**, 637-640.

Matsuda, T. and Ariyama, T. (1985) Debris avalanche deposits of Ontake Volcano, caused by the 1984 western Nagano Prefecture Earthquake -on the debris spray zone-. *Bull. Earthq. Res. Inst. Univ. Tokyo*, **60**, 281-316. (in Japanese with English abstract)

McEwen, A.S. and Malin, M.C. (1989) Dynamics of Mount St. Helens' 1980 pyroclastic flows, rockslide-avalanche, lahars, and blast. *J. Volcanol. Geotherm. Res.*, **37**, 205-231.

Melosh, H.J. (1979) Acoustic fluidization : A new geologic process? *J. Geophys. Res.*, **84(B13)**, 7513-7520.

Middleton, G.V. and Hampton, M.A. (1976) Subaqueous sediment transport and deposition by sediment gravity flows. In *Marine Sediment Transport and*

Environmental Management (Stanley, D.J. and Swift, D.J.P. eds), 197-218. New York.

Mimura, K. (1985) Yatsugatake Nirasaki debris avalanche. *Gekkan Chikyu*, **73**, 379-384. (in Japanese)

Mimura, K., Kawachi, S,, Fujimoto, U., Taneichi, M., Hyuga, T., Ichikawa, S. and Koizumi, M. (1982) Debris avalanche hills and their natural remanent magnetization -Nirasaki debris avalanche, central Japan. *J. Geol. Soc. Japan*, 88, 653-663. (in Japanese with English abstract)

Mimura, K., Kano, K., Nakano, S. and Hoshizumi, H. (1988) Ontake debris avalanche in 1984 -flow and deposition mechanism inferred from the deposit-. *Bull. Geol. Surv. Japan*, **39**, 495-523. (in Japanese with English abstract)

Miyachi, M., Kobayashi, S., Sekihara, Y., Ono, K. and Akagi, Y. (1987) Geological examination of the two old maps in the Tokugawa era concerning the "Shimabara Catastrophe", western Kyushu, Japan. *Rep. Earth Science, College of General Education, Kyushu Univ.*, **25**, 39-52. (in Japanese with English abstract)

Moore, H.J., Arthur, D.W.G. and Schaber, G.G. (1978) Yield strengths of flows on the Earth, Mars and Moon. *Proc. Lunar Planet. Sci. Conf. 9th.* 3351-3378.

Moriya, I. (1983) **Volcanic landforms in Japan.** UP-Earth Science, Tokyo Univ. Press. 135p. (in Japanese)

Moriya, I. (1984a) Step-like topography at the south and the east of the Oshima Komagatake Volcano. *In Volcanic landforms in Japan by the aerial photos* (Volcanol. Soc. Japan ed.), 78-79. Tokyo Univ. Press. (in Japanese)

Moriya, I. (1984b) Topographic features of the pyroclastic flow at the west of the Osidashisawa Valley of the Oshima Komagatake Volcano. *In Volcanic landforms in Japan by the aerial photos* (Volcanol. Soc. Japan ed.), 70-71. Tokyo Univ. Press. (in Japanese)

Munson, B.R., Young, D.F. and Okiishi, T.H. (1990) **Fundamantals of fluid mechanics**. John Wiley and Sons. 843p.

Muraoka, H. and Takakura, S. (1988) **Explanatory text of the geological map of Hakkoda geothermal area (scale 1:100,000).** Geol. Surv. Japan, 27p. (in Japanese with English abstract)

Muraoka, H. and Hase, H. (1990) **Quadrangle series scale 1:50,000 Geology of the Kuroishi District.** Geol. Surv. Japan, 124p. (in Japanese with English abstract)

Muraoka, H., Yamaguchi, Y. and Hase, H. (1991) Clustered calderas found in the Hakkoda geothermal field, Northern Japan. *Rep. Geol. Sur. Japan,* **275**, 97-111. (in Japnese with English abstract)

Nairn, I.A. and Self, S. (1978) Explosive eruptions and pyroclastic avalanches from Ngauruhoe in February 1975. *J. Volcanol. Geotherm. Res.*, **3**, 39-60.

Nakada, S. (1992) Photographic records of eruption at Unzen Volcano during May 1991-May 1992. In *Unzen Volcano the 1990-1992 eruption* (Yanagi, T., Okada, H. and Ohta, K. eds), 12-20. The Nishinippon and Kyushu Unversity Press.

Nakada, S. (1993) Eruptions at Mt. Fugen (Unzen Volcano) and the lava dome growth. In *Volcanic disaster at Unzen Volcano*, 15-27. The Japanese Society of Soil Mechanics and Foundation Engineering. (in Japanese)

Nakada, S. and Tanaka, M. (1991) Magmatic processes of Unzen Volcano. *Bull. Volcanol. Soc. Japan*, **33**, 113-121. (in Japanese with English abstract)

Nakada, S. and Fujii, T. (1993) Preliminary report on the activity at Unzen Volcano (Japan), November 1990-November 1991: Dacite lava domes and pyroclastic flows. *J. Volcanol. Geotherm. Res.*, **54**, 319-333.

Nakamura, Y. (1978) Geology and petorology of Bandai and Nekoma Volcanoes. *Tohoku Univ. Sci. Rep. Ser. 3*, **14**, 67-119.

Nakamura, T., Fujii, T., Shikano, K. and Fieldwork Group of Kiso Valley Quaternary (1991) Radiocarbon ages by accelerator mass spectrometry of the buried wood trunks from Kisogawa volcanic mudflow deposits at Yaotsu-Cho, Gifu Prefecture. *The Quaternary Res.,* **31**, 29-36. (in Japanese with English abstract)

NEDO (New Energy Development Organization) (1988) **Western Region of Unzen (summary).** 15, 224p. (in Japanese)

Nishimura, Y. and Shimizu, H. (1993) Tsumanis generated by eruptions from Komagatake Volcano, Hokkaido, Japan. *Rep. Natural Hazard Science Data Center, Hokkaido,* **8**, 17-28.

Ohta, K. (1984) **Unzen Volcano -topography, geology and volcanic phenomina.** Nagasaki Prefecture, 98p. (in Japanese)

Ohta, K. (1992) Photographic records of the 1990-1992 eruption at Unzen Volcano. In *Unzen Volcano the 1990-1992 eruption* (Yanagi, T., Okada, H. and Ohta, K. eds), 5-11. The Nishinippon and Kyushu Unversity Press.

Ohta, K. (1993) The 1990-1992 eruptive activity at Unzen Volcano. *Jour. Geol. Soc. Japan*, **99**, 835-854. (in Japanese with English abstract)

Oosawa, T. (1983) Kisogawa mud flow. *Report of Earth Science Research, Nagano Prefecture*, **3**, 18-21. (in Japanese)

Oosawa, T. (1986) Kisogawa mud flow II. *Report of Earth Science Research, Nagano Prefecture*, **6**, 19-22. (in Japanese)

Oosawa, T. (1987) Kisogawa mud flow III. *Report of Earth Science Research, Nagano Prefecture*, **7**, 22-25. (in Japanese)

Pinatsubo Volcano Observatory Team (1991) Lessons from a major eruption: Mt. Pinatubo, Philippines. *EOS*, **72**, 545-555.

Saito, E., Watanabe, K., Suto, S., Hoshizumi, H., Endo, H., Kazahaya, K., Kawanabe, Y., Sakaguchi, K., Takarada, S., Yamamoto, T. and Takada, A. (1991) Ground deformation of Unzen volcano while 1990-91 eruption

measured by electro-optical distance measurement. *Volcanol. Soc. Japan Progr. Abstract*, **2**, 20. (in Japanese)

Sakai, J. (1963) Loam formations in Kiso Valley I. *Earth Science*, **67**, 13-20. (in Japanese)

Sagayama, T. (1986) **Explanatory text of the geological map of Japan scale 1: 50,000 Komagatake.** Geol. Surv. Hokkaido, 45p. (in Japanese with English abstract)

Sasaki, T., Katayama, M., Tomioka, E., Sasaki, S., Yazawa, M., Yamada, S., Yano, Y. and Kitagawa Y. (1971) Studies on chronology of humified tephras in Hokkaido. *The Quaternary Res.*, **10**, 117-123. (in Japanese with English abstract)

Sasaki, T. and Katsui, Y. (1981) A new technique for measuring density of pumice using glass beads. *Bull. Volcanol. Soc. Japan,* **26**, 117-118. (in Japanese)

Sato, H. (1969) Measurement of ^{14}C ages of recent volcanic activities in Hokkaido. *Chishitu News*, **178**, 30-35. (in Japanese)

Sato, H., Fujii, T. and Nakada, S. (1992) Crumbling of dacite dome lava and generation of pyroclastic flows at Unzen volcano. *Nature*, **360**, 664-666.

Scheidegger, A.E. (1973) On the prediction of the reach and velocity of catastrophic landslides. *Rock Mechanics*, **5**, 231-236.

Sekiya, S. and Kikuchi, Y. (1890) The eruption of Bandai-san. *Sci. Imp. Univ. Tokyo*. **3**, 91-171.

Shreve, R.L. (1968a) The Blackhawk landslide. *Geol. Soc. Am. Spec. Pap.*, **108**, 1-47.

Shreve, R.L. (1968b) Leakage and fluidization in air-layer lubricated avalanches. *Geol. Soc. Am. Bull.*, **79**, 653-658.

Sheridan, M.F. and Malin, M.C. (1983) Application of computer-assisted mapping to volcanic hazard evaluation of surge eruptions: Vulcano, Lipari, and Vesuvius. *J. Volcanol. Geotherm. Res.*, **17**, 187-202.

Siebert, L. (1984) Large volcanic debris avalanches: characteristics of source areas, deposits, and associated eruptions. *J. Volcanol. Geotherm. Res.*, **22**, 163-197.

Siebert, L., Gliken, H. and Ui, T. (1987) Volcanic hazards from Bezymianny- and Bandai-type eruptions. *Bull. Volcanol.*, **49**, 435-459.

Simpson, J.E. (1987) **Gravity currents: in the environment and the laboratory**. John Wiley and Sons, 244p.

Soh, W. and Tokuhashi, S. (1984) Story of turbidite (5) - what is sediment gravity flow? *Chishitsu News*, **359**, 6-15. (in Japanese)

Sparks, R.S.J. (1976) Grain size variations in ignimbrites and implications for the transport of pyroclastic flows. *Sedimentology*, **23**, 147-188.

Sparks, R.S.J. and Walker, G.P.L. (1973) The ground surge deposit: a third type of pyorclastic rock. *Nature*, **241**, 62-64.

Sparks, R.S.J. and Wilson, L. (1976) A model for the formation of ignimbrite by gravitational column collapse. *J. Geol. Soc. London*, **132**, 441-451.

Sparks, R.S.J., Self, S. and Walker, G.P.L. (1973) Products of ignimbrite eruptions. *Geology*, **1**, 115-118.

Sparks, R.S.J., Wilson, L. and Hulme, G. (1978) Theoretical medeling of the generation, movement, and emplacement of pyroclastic flows by column collapse. *J. Geophs. Res.*, **83(B4)**, 1727-1739.

Sugimura, A. (1978) Large geography, volcano and earthquake in Japan. *In Iwanami course Earth Science 10* (Kasahara, K. and Sugimura, A. eds), 159-181.Iwanami. (in Japanese)

Sugiyama, H., Hayashi, M. and Fujino, T. (1986) Fission Track age of the Unzen Volcanic Rocks in western Kyshu, Japan. *Bull. Volcanol. Soc. Japan*, **31**, 85-94.

Sumi, K., Ozawa, A. and Hirayama, J. (1962) **Explanatory text of the geological map of Japan (scale 1:50,000) Dairakozan.** Geol. Surv. Japan, 51p. (in Japanese with English abstract)

Suzuki, T. and Kastui, Y. (1982) Volume of the air-fall tephras in Hokkaido. *In Volcanic ash in Hokkaido* (Katsui, Y., Sasaki, T., Kitagawa, Y., Kasugai, A. and Matsushita, K. eds), 15, Nomenclature Comittee of Volcanic ash in Hokkaido. (in Japanese)

Suzuki, T., Katsui, Y. and Kamata, K. (1986) Morphology and grain size distribution of the 1929 Hokkaido Komagatake Volcano. In *Characteristics and hazards of the dry particle flows from volcanic eruption, Report of the research of natural hazard assisted by the Ministry of Education* (Aramaki, S. ed), 61-90. (in Japanese)

Takahashi, M. (1989) Unzendake. *In Volcanoes in Japan* (Aramaki, S., Shirao, M. and Nagaoka, M. eds), 196-200. Maruzen. (in Japanese)

Takahashi, T. (1982) Study on the deposition of debris flows (3) -erosion of debris fan-. *Annuals Disas. Prev. Res. Inst. Kyoto Univ.,* **25(B2)**, 327-348. (in Japanese with English abstract)

Takahashi, T. (1986) Flow mechanism of pyroclastic flow and debris avalanche. In *Characteristics and hazards of the dry particle flows from volcanic eruption, Report of the research of natural hazard assisted by the Ministry of Education* (Aramaki, S. ed), 25-41. (in Japanese)

Takarada, S. (1988 MS) Collapse and flow mechanism of the debris avalanche -a case study on Iwasegawa debris avalanche, Tashiro Volcano, northern Japan. *A graduation thesis, Kobe Univ.*, 1-93. (in Japanese with English abstract)

Takarada, S. (1990 MS) Flow and depositional mechanisms of debris avalanche - A case study of Iwasegawa debris avalanche deposit, Tashirodake Volcano, northern Japan. *A Master thesis, Kobe Univ.* 1-214. (in Japanese with English abstract)

Takarada, S. (1991) Flow and depositional mechanisms of debris avalanche -A case study of Iwasegawa debris avalanche deposit, Tashirodake Volcano, northern Japan-. *Bull. Volcanol. Soc. Japan*, **36**, 11-23. (in Japanese with English abstract)

Takarada, S., Kazahaya, K., Kawanabe, Y., Sakaguchi, K., Suto, S., Yamamoto, T., Soya, T. and Unzendake Weather Station, JMA (1993a) Volume estimation of 1991-92 eruption of Unzen Volcano, and initiation mechanisms of pyroclastic flows on June 3 and June 8, 1991. *Bull. Geol. Surv. Japan*. **44**, 11-24. (in Japanese with English abstract)

Takarada, S., Yamamoto, T., Nakano, T., Murata, Y., Kazahaya, K., Kawanabe, Y., Sakaguchi, K. and Soya, T. (1993b) Computer simulations of pyroclastic flows of the 1991-92 eruptions of Unzen Volcano. *Bull. Geol. Surv. Japan*, **44**, 25-54. (in Japanese with English abstract)

Takemoto, H., Momose, M., Hirabayashi, K. and Kobayashi, T. (1987) Stratigraphy and correlation of the younger Ontake tephra group -an implication to the late Pleistocene chronology in central Japan-. *The Quaternary Res.,* **25**, 337-352. (in Japanese with English abstract)

Tanaka, M. and Nakada, S. (1988) Geology of eastern part of Unzen Volcano. *Sci. Rep. Shimabara Earthquake Volcano Observ., Kyushu Univ.*, **14**, 1-11. (in Japanese with English abstract)

The Japanese Society of Soil Mechanics and Foundation Engineering (1993) **Volcanic disaster at Unzen Volcano**. The Japanese Society of Soil Mechanics and Foundation Engineering, 178p. (in Japanese)

The Nishinippon (1992) Photographic records of people's life during the eruption. In *Unzen Volcano the 1990-1992 eruption* (Yanagi, T., Okada, H. and Ohta, K. eds), 21-27. The Nishinippon and Kyushu Unversity Press.

The Quaternary research group of the Kiso Valley and Kigoshi, K. (1964) Radiocarbon date of the Kisogawa volcanic mudflows and its significance on the Würmian chronology of Japan. *Earth Science*, **71**, 1-7.

Uchida, Y. and Hakuno, M. (1990) Distinct element analysis of dry rock avalanches. *Structural Eng. / Earthquake Eng.*, **7**, 203s-214s.

Ui, T. (1983) Volcanic dry avalanche deposits -identification and comparison with nonvolcanic debris stream deposits. *J. Volcanol. Geotherm. Res.*, **18**, 135-150.

Ui, T. (1985) Debris avalanche deposits associated with volcanic activity. *Proc. IVth International Conf. and Field Workshop on Landslides, 1985, Tokyo*, 405-410.

Ui, T. (1987) Flow behavior of volcanic debris avalanche. *Transactions, Japanese Geomorphological Union*, **8**, 83-93. (in Japanese with English abstract)

Ui, T. and Gliken, H. (1986) Internal structural variation in a debris-avalanche deposit from ancestral Mount Shasta, California, USA. *Bull. Volcanol.*, **48**, 189-194.

Ui, T., Kawachi, S. and Neall, V.E. (1986a) Fragmentation of debris avalanche material during flowage -evidence from the Pungarehu formation, Mount Egmont, New Zealand. *J. Volcanol. Geotherm. Res.*, **27**, 255-264.

Ui, T., Yamamoto, H. and Suzuki-Kamata, K. (1986b) Characterization of debris avalanche deposits in Japan. *J. Volcanol. Geotherm. Res.*, **29**, 231-243.

Valentine, G.A. (1987) Stratified flow in pyroclastic surges. *Bull. Volcanol.*, **49**, 616-630.

Voight, B. (1981) Time scale for the first moments of the May 18 eruption. In *The 1980 eruptions of Mount St. Helens, Washington* (Lipman, P.W. and Mullineaux, D.R. eds), U. S. Geol. Surv. Prof. Pap., **1250**, 69-86.

Voight, B., Gliken, H., Janda, R.J. and Douglass, P.M. (1981) Catastrophic rockslide avalanche of May 18. In *The 1980 eruptions of Mount St. Helens, Washington* (Lipman, P.W. and Mullineaux, D.R. eds), U. S. Geol. Surv. Prof. Pap., **1250**, 347-377.

Voight, B., Janda, R.J., Gliken, H. and Douglass, P.M. (1983) Nature and mechanics of the Mount St Helens rockslide-avalanche of 18 May 1980. *Geotechnique*, **33**, 243-273.

Wadge, G. and Lopes, R.M.C. (1991) The lobes of lava flows on earth and Olympus Mons, Mars. *Bull. Volcanol.*, **54**, 10-24.

Walker, G.P.L. (1980) The Taupo pumice: product of the most powerful known (ultraplinian) eruption? *J. Volcanol. Geotherm. Res.*, 8, 69-94.

Walker. G.P.L. (1983) Ignimbrite types and ignimbrite problems. *J. Volcanol. Geotherm. Res.*, **17**, 65-88.

Walker, G.P.L., Heming, R.F. and Wilson, C.J.N. (1980a) Low aspect ratio ignimbrites. *Nature*, **283**, 286-287.

Walker, G.P.L., Wilson, C.J.N. and Froggatt, P.C. (1980b) Fines-depleted ignimbrite in New Zealand -The product of a turbulent pyrocalstic flow. *Geology*, 8, 245-249.

Walker, G.P.L., Wilson, C.J.N. and Froggatt, P.C. (1981a) An ignimbrite veneer deposit: the trail-marker of a pyroclastic flow. *J. Volcanol. Geotherm. Res.*, **9**, 409-421.

Walker, G.P.L, Self, S. and Froggatt, P.C. (1981b) The ground layer of the Taupo ignimbrite: a striking example of sedimentation from a pyroclastic flow. *J. Volcanol. Geotherm. Res.*, **10**, 1-11.

Watanabe, I., Hoshizumi, H. and Itaya, T. (1991) Geology of Mayuyama, Unzen Volcano. *In report of the research, general research (A), grant of scientific research, 1990* (Kamo, K. ed), 1-11. (in Japanese)

Watanabe, I., Ono, K., Sakaguchi, K., Takada, A. and Hoshizumi, H. (1991) Co-ignimbrite ash-fall deposits accompanied with the pyroclastic flows of May-June, 1991, eruptions, Fugen-dake, Unzen volcano.*Volcanol. Soc. Japan Progr. Abstract*, **2**, 144. (in Japanese)

Williams, H. and McBirney, A. (1979) **Volcanology**. Freeman, Cooper & Co., San Francisco, 397p.

Wilson, C.J.N. (1980) The role of fluidization in the emplacement of pyroclastic flows: an experimental approach. *J. Volcanol. Geotherm. Res.*, **8**, 231-249.

Wilson, C.J.N. (1984) The role of fluidization in the emplacement of pyroclastic flows, 2: experimental results and their interpretation. *J. Volcanol. Geotherm. Res.*, **20**, 55-84.

Wilson, C.J.N. (1985) The Taupo eruption, New Zealand II. The Taupo ignimbrite. Phil. *Trans. Roy. Soc. London, A*, **314**, 229-310.

Wilson, C.J.N. and Walker, G.P.L. (1982) Ignimbrite depositional facies: the anatomy of a pyroclastic flow. *J. Geol. Soc. London*, **139**, 581-592.

Wilson, L. and Head, J.W. (1981) Morphology and rheology of pyroclastic flows and their deposits, and guidelines for future observations. In *The 1980 eruptions of Mount St. Helens, Washington* (Lipman, P.W. and Mullineaux, D.R. eds), U. S. Geol. Surv. Prof. Pap., **1250**, 513-524.

Yamada, N., Kobayashi, T. (1988) **Quadrangle series scale 1:50,000 Geology of the Ontakesan District.** Geol. Surv. Japan, 136p. (in Japanese with English abstract)

Yamamoto, T., Takarada, S. and Suto, S. (1993) Pyroclastic flows from the 1991 eruption of Unzen volcano, Japan. *Bull. Volcanol.*, **55**, 166-175.

Yamamoto, Y. (1990 MS) A study of the debris avalanche deposit on the eastern foot of the Ontake volcano. *A graduation thesis, Kobe Univ.* 1-80. (in Japanese with English abstract)

Yamasato, H., Fukui, K., Uhira, K., Hashimoto, T. and Mori, H. (1993) Analysis of seismic and acoustic signals excited by pyroclastic flows at Unzendake Volcano. *Bull. Volcanol. Soc. Japan*, **38**, 79-90. (in Japanese with English abstract)

Yanai, S. and Ganzawa, Y. (1988) Discovery and significance of the period forest around the piedmont of Komagatake Volcano, southwestern Hokkaido. *Earth Science*, **42**, 25-28. (in Japanese)

Yanai, S., Ganzawa, Y. and Komori, Y. (1992) The stratigraphy and distribution of the Nigorikawa tephra, latest glacial age time-marker in southwest Hokkaido. *Jour. Geol. Soc. Japan*, **98**, 125-136. (in Japanese with English abstract)

Yarnold, J.C. (1993) Rock-avalanche characteristics in dry climates and the effect of flow into lakes: insights from mid-Tertiary sedimentary breccias near Artillery Peak, Arizona. *Geol. Soc. Am. Bull.*, **105**, 345-360.

Yarnold, J.C. and Lombard, J.P. (1989) A facies model for large rock-avalanche deposits formed in dry climates. In *Conglomerates in basin analysis, A sysmposium dedicate to A.O. Woodford* (Abbott, P., Colburn, I.E. eds), Society of Economic Paleontologists and Mineralogists Pacific Section., **62**, 9-31.

```
' Velocity Simulation of Pyroclastic Flow (Energy line model)
LM=2400
DIM LL(200), HH(200), L(200), H(200), S(200), A(200), V(200), T(200)
N=161
 FOR I=1 TO N
    READ LL(I)
 NEXT I
 FOR I=1 TO N
    READ HH(I)
 NEXT I
 FOR I=1 TO N-1
   L(I)=LL(I+1)-LL(I)
    H(I)=HH(I)-HH(I+1)
   SS=L(I)^2+H(I)^2
   S(I)=SQR(SS)
 NEXT I

 OPEN "CLIP:" FOR OUTPUT AS #1
LA=0: HA=0
 FOR I=1 TO N-1
    LA=LA+L(I): HA=HA+H(I)
    IF LM<L(I)  THEN GOTO 100
    IF LA>LM THEN GOTO 200
  NEXT I
100 LX=L(1)
      HM=H(1)*LM/L(1): FR=HM/LM  :GOTO 300
200 LX=L(I): HX=H(I)  : NN=I-1
     LY=LM-(LA-LX)
     HM=HY+(HA-HX)
     FR=HM/LM
300  V(0)=0: VV=0: TT=0: CLS
PRINT "  N", "Distance (m)", "  a (m/s2)", "  V(m/s)"," Time  (s)"
FOR J=1 TO NN
 A(J)=9.8*(H(J)-FR*L(J))/S(J)
 VV=2*A(J)*S(J)+V(J-1)^2
 IF VV<0 THEN GOTO 400
 V(J)=SQR(VV)
 T(J)=(V(J)-V(J-1))/A(J)
 TT=TT+T(J)
 PRINT USING "    ####"; J, TT, LL(J), LL(J+1) ;
 PRINT USING "    ###.###   "; A(J), V(J)
 WRITE #1, J, TT, LL(J)+25, A(J), V(J)
NEXT J
400 PRINT FR

CLOSE :END

DATA 50,100,150,200,250,300,350,400,450,500
DATA 550.600.650.700.750.800.850.900.950.1000
```

Appendix 1-1. Source list of the program to simulate the pyroclastic flow using the energy line model.

```
DATA 1050,1100,1150,1200,1250,1300,1350,1400,1450,1500
DATA 1550,1600,1650,1700,1750,1800,1850,1900,1950,2000
DATA 2050,2100,2150,2200,2250,2300,2350,2400,2450,2500
DATA 2550,2600,2650,2700,2750,2800,2850,2900,2950,3000
DATA 3050,3100,3150,3200,3250,3300,3350,3400,3450,3500
DATA 3550,3600,3650,3700,3750,3800,3850,3900,3950,4000
DATA 4050,4100,4150,4200,4250,4300,4350,4400,4450,4500
DATA 4550,4600,4650,4700,4750,4800,4850,4900,4950,5000
DATA 5050,5100,5150,5200,5250,5300,5350,5400,5450,5500
DATA 5550,5600,5650,5700,5750,5800,5850,5900,5950,6000
DATA 6050,6100,6150,6200,6250,6300,6350,6400,6450,6500
DATA 6550,6600,6650,6700,6750,6800,6850,6900,6950,7000
DATA 7050,7100,7150,7200,5250,7300,7350,7400,5450,7500
DATA 7550,7600,7650,7700,7750,7800,7850,7900,7950,8000
DATA 8050
DATA 1250,1225,1200,1170,1137,1110,1090,1065,1037,1010
DATA 970,950,930,900,858,815,757,742,725,715
DATA 700,690,680,670,663,653,645,637,628,620
DATA 610,600,592,585,578,565,525,497,485,470
DATA 450,445,438,425,410,397,390,387,382,377
DATA 373,367,361,349,338,327,318,308,299,293
DATA 288,282,275,268,260,257,251,248,244,239
DATA 235,230,228,225,223,220,217,212,208,205
DATA 202,198,195,192,188,184,180,178,175,171
DATA 168,166,163,160,157,153,148,145,139,137
DATA 133,130,128,125,123,120,117,114,110,108
DATA 105,102,99,97,93,89,87,85,82,79
DATA 77,74,71,68,65,62,60,58,56,53
DATA 50,48,45,42,40,38,36,34,32,30
DATA 29,27,26,24,22,21,20,18,16,15
DATA 14,12,11,9,8,7,5,4,3,1,0
```

Appendix 1-1. Continued.

```
'Velocity Simulation of  Pyroclastic Flow (Bingham Model)

DE=1300 : D=1.7: K=850 :  E=70  :  CG=.01

DIM LL(200),HH(200),L(200),H(200),SS(200),TT(200),DC(200)

GOSUB topography

OPEN "CLIP:" FOR OUTPUT AS #1
TT(0)=0:  L0=0 : H0=0 : V0=.1 : VS=.1 : V=.1 : ST=1: CLS

GOSUB parameter

FOR I=1 TO N-1
    FOR T=0 TO 100 STEP ST

      GOSUB calc

       IF S>=SS(I)  THEN GOTO 100
       IF V<.2 THEN GOTO 200
            PRINT USING "      ####";I,TT(I),L;
            PRINT USING "    ###.####  ";DC,AC,V
            WRITE #1, I, TT(I), L, DC, AC, V
     NEXT T
100      V0=VP  :  L0=L(I)+L0:  H0=H(I)+H0 : S0=0
NEXT I
200 CLOSE #1 : END

topography:

N=81
FOR I=1 TO N
READ LL(I)
NEXT I

FOR I=1 TO N
READ HH(I)
NEXT I

FOR I=1 TO N-1
     L(I)=LL(I+1)-LL(I)
     H(I)=HH(I)-HH(I+1)
     SS(I)=SQR(L(I)^2+H(I)^2)
NEXT I
RETURN

parameter:
```

Appendix 1-2. Source list of the program to simulate the pyroclastic flow using the Bingham flow model.

```
PRINT "DENSITY" DE "kg/m3"
PRINT "FLOW  DEPTH" D "m"
PRINT "YIELD STRENGTH" K "Pa"
PRINT "VISCOSITY" E "Pas"
PRINT "DRAG COEFFICIENT" CG
PRINT "          N";"    Time(s)";" Distance (m)";" Plug (m) ";"      a(m/s2)";"         V(m/s)"

RETURN


calc:
      DC=((K*D+E*V)-((K*D+E*V)^2-(K*D)^2)^.5)/K
      A=9.8*H(I)/SS(I)-2*K/(DE*(D+DC))
      B=-2*E/(DE*(D^2-DC^2))
      C=-.5*CG/D

 IF DE*V^2/K>=1000 THEN GOTO 300

' LAMINAR
      DQ=ABS(A+B*V0)
      Q=EXP(B*T+LOG(DQ))
      VP=(Q-A)/B
      GOTO 400

'TURBULENCE
300 IF (B^2-4*A*C)<0 THEN GOTO 200
      AA=(-B-(B^2-4*A*C)^.5)/(2*C)
      BB=(-B+(B^2-4*A*C)^.5)/(2*C)
      DX=ABS((V0-AA)/(V0-BB))
      IF DX=0 THEN GOTO 200
      CC=LOG(DX)/(C*(AA-BB))
      XX=EXP(C*(AA-BB)*(T+CC))
      VP=(AA-BB*XX)/(1-XX)

400 M=-4.9*DE*H(I)/SS(I)
     N=-M*D^2-K*D
       VB=((M*(D^3-DC^3)/3)+(K*(D^2-DC^2)/2)+(N*(D-DC)))/(D*E)
     V=VB+VP*DC/D
        AC=(V-VS)/ST :  VS=V
        S=V*ST+S0    : S0=S
         TT(I)=TT(I-1)+T
         L=L0+S*L(I)/SS(I)
         H=H0+S*H(I)/SS(I)
RETURN

DATA 0,100,200,300,400,500
DATA 600,700,800,900,1000
DATA 1100,1200,1300,1400,1500
DATA 1600.1700.1800.1900.2000
```

Appendix 1-2. Continued.

```
DATA 2100,2200,2300,2400,2500
DATA 2600,2700,2800,2900,3000
DATA 3100,3200,3300,3400,3500
DATA 3600,3700,3800,3900,4000
DATA 4100,4200,4300,4400,4500
DATA 4600,4700,4800,4900,5000
DATA 5100,5200,5300,5400,5500
DATA 5600,5700,5800,5900,6000
DATA 6100,6200,6300,6400,6500
DATA 6600,6700,6800,6900,7000
DATA 7100,7200,7300,7400,7500
DATA 7600,7700,7800,7900,8000

DATA 1255,1225,1170,1110,1065,1010
DATA 950,900,815,742,715
DATA 690,670,653,637,620
DATA 600,585,565,497,470
DATA 445,425,397,387,377
DATA 367,349,327,308,293
DATA 282,268,257,248,239
DATA 230,225,220,212,205
DATA 198,192,184,178,171
DATA 166,160,153,145,137
DATA 130,125,120,114,108
DATA 102,97,89,85,79
DATA 74,68,62,58,53
DATA 48,42,38,34,30
DATA 27,24,21,18,15
DATA 12,9,7,4,1
```

Appendix 1-2. Continued.

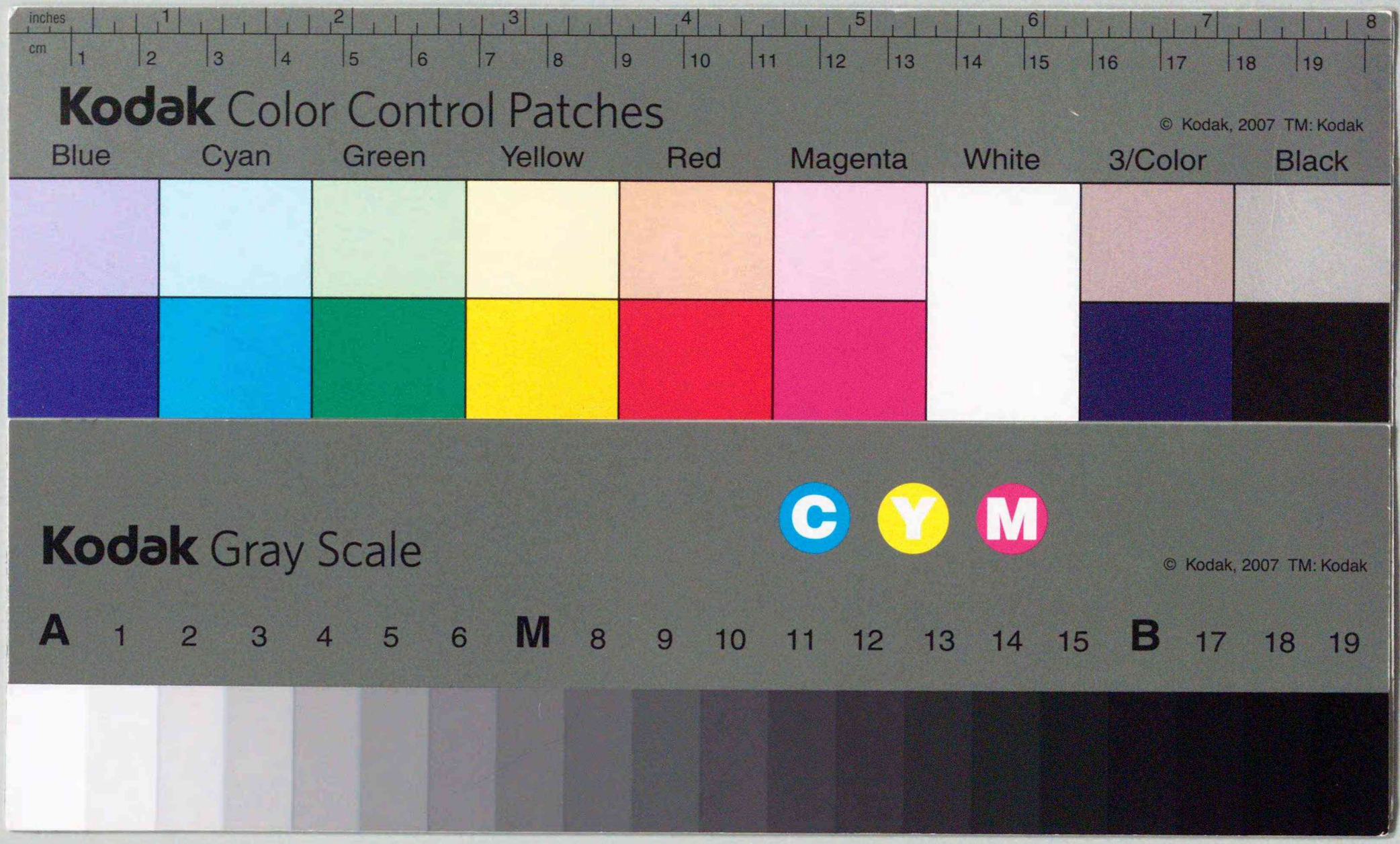
inches
cm
Kodak Color Control Patches
© Kodak, 2007 TM: Kodak
Blue
Cyan
Green
Yellow
Red
Magenta
White
3/Color
Black
Kodak Gray Scale
C
Y
M
© Kodak, 2007 TM: Kodak
A 1 2 3 4 5 6 M 8 9 10 11 12 13 14 15 B 17 18 19